A&A 523, A45 (2010)
DOI: 10.1051/0004-6361/200913359

Astronomy & Astrophysics

A survey of the Galactic center region in HCO^+, $H^{13}CO^+$, and SiO

D. Riquelme[1,2], L. Bronfman[2], R. Mauersberger[1,3], J. May[2], and T. L. Wilson[4]

[1] Instituto de Radioastronomía Milimétrica (IRAM), Av. Divina Pastora 7, Local 20, 18012 Granada, Spain
e-mail: `riquelme@iram.es`
[2] Departamento de Astronomía, Universidad de Chile, Casilla 36-D, Santiago, Chile
[3] Joint ALMA Observatory, Av. Alonso de Córdova 3107, Vitacura, Santiago de Chile, Chile
[4] Naval Research Laboratory, Code 7210, Washington, DC 20375, USA

Received 26 September 2009 / Accepted 7 June 2010

ABSTRACT

Aims. A large-scale survey of the Galactic center region in the 3 mm rotational transitions of SiO, HCO^+ and $H^{13}CO^+$ (beamsize ∼3.′6) was conducted to provide an estimate of cloud conditions, heating mechanisms, chemistry, and other properties.

Methods. Using the NANTEN 4 m telescope from Nagoya University, a region between $-5.°75 < l < 5.°6$ and $-0.°68 < b < 1.°3$ was mapped in the $J = 1 \rightarrow 0$ lines of HCO^+ and $H^{13}CO^+$ and in the $J = 2 \rightarrow 1$ line of SiO with a spacing of 3.′75 (HCO^+) and 1.′875 (SiO and $H^{13}CO^+$).

Results. Velocity channel maps, longitude-velocity maps, and latitude-velocity maps are presented. We identify 51 molecular clouds; 33 of them belong to the Galactic center and 18 to disk gas. We derive an average of the luminosity ratio of SiO($J = 2 \rightarrow 1$)/CO($J = 1 \rightarrow 0$) in clouds belonging to the Galactic center of 4.9×10^{-3} and for disk clouds of 3.4×10^{-3}. The luminosity ratio of HCO^+($J = 1 \rightarrow 0$)/CO($J = 1 \rightarrow 0$) in the Galactic center is 3.5×10^{-2}, and for disk clouds it is 1.5×10^{-2}. We can distinguish clearly between regions where the SiO or HCO^+ dominate.

Key words. ISM: clouds – ISM: molecules – Galaxy: center – surveys

1. Introduction

To understand the evolution, dynamics, and constitution of our Galaxy, it is crucial to explore its central kiloparsec. This region is obscured by intervening dust in the optical, but not in the millimeter to far infrared wavelength range. It contains a large amount ($\sim 3 \times 10^7\ M_\odot$, see Dahmen et al. 1998) of molecular gas, the Central Molecular Zone[1] (CMZ, Morris & Serabyn 1996), which is traced by the mm-emission of CO and its isotopomers (e.g. Bitran et al. 1997; Dahmen et al. 1998; Bally et al. 1987). The distribution and mass of the components of the interstellar medium (ISM) in the central part of the Galaxy is discussed by Ferrière et al. (2007).

Clouds in the Galactic center region are influenced by large potential gradients, and the proximity to the center of our Galaxy, which may lead to frequent cloud-cloud collisions and exposes the clouds to enhanced magnetic fields, cosmic ray fluxes, X-rays, and explosive events. As a consequence, in the CMZ, the lines are first, typically wider than 10 km s^{-1} (e.g. Morris & Serabyn 1996). Second, the thermal emission of SiO is extended, finding it over parsec-size regions (e.g. Martín-Pintado et al. 1997; Hüttemeister et al. 1998), which is also seen in the central regions of external galaxies (Mauersberger & Henkel 1991). In contrast, in the Galactic disk, SiO is observed mainly at the leading edges of outflows, which has been interpreted as a signature of shocked gas (e.g. Ziurys et al. 1990). In general, Galactic disk sources are compact with sizes of <0.1 pc or at most 1 pc (Jiménez-Serra et al. 2010). Third, a substantial amount of the gas has a kinetic temperature of ∼200 K (e.g. Hüttemeister et al. 1993), while the bulk of the dust has a much lower temperature of $T_{\rm dust} < 40$ K (Rodríguez-Fernández et al. 2002; Odenwald & Fazio 1984; Cox & Laureijs 1989). Our survey results provide additional information about the heating and chemistry of Galactic center clouds that cannot be easily obtained from an analysis of CO data alone.

HCO^+ is a molecule known to vary considerably in abundance relative to neutral molecules with similar dipole moments and rotational constants, such as HCN, within a galaxy and from galaxy to galaxy (Nguyen et al. 1992; Seaquist & Frayer 2000; Krips et al. 2008). Seaquist & Frayer (2000) argue that, in the environment of circumnuclear galactic or extragalactic gas, the abundance of HCO^+ decreases with increasing CR ionization rates. However, Krips et al. (2008) observe that the HCO^+ abundance tends to be higher in galaxies with nuclear starbursts than in galaxies with active galactic nuclei (AGN), which would be unexpected if HCO^+ is destroyed by the CRs produced by SNRs. Using chemical model computations for photon-dominated regions (PDRs), Bayet et al. (2009) found that the molecular fractional abundance of HCO^+ is insensitive to changes in both the CR ionization rate and the far-UV radiation. Loenen et al. (2008) also point out that in PDRs the ratios of HCO^+ to HCN or HNC decrease with increasing density and that a change in the UV flux of two orders of magnitude only produces modest changes in the line ratio because the UV field is attenuated at the high column densities. To provide information about the chemistry of HCO^+ in circumnuclear regions and to relate this to CR ionization rates and to heating mechanisms, we mapped this molecule and its rare $H^{13}CO^+$ isotopomer in its $J = 1{-}0$ transition throughout the Galactic center. These results can be combined with CO data to provide insight into conditions

---

[1] Following the notation of Morris & Serabyn (1996), we refer to the "CMZ" as the region about $-0.°5 < l < 1.°5$, and to the "Galactic center region" as the region between $-5° < l < 5°$, which is the region observed in this work.

Table 1. Atomic and molecular surveys of the Galactic bulge.

Species	Frequ. [GHz]	Observed Area l [°]	b [°]	Sampling interval	*FWHM*	Ref.
H i	1.4	$-11 \leq l \leq 13$	$-10 \leq b \leq 10$	30′	21′	1
C i	492	$-0.5 \leq l \leq 1.5$	0	3′	2′	2
C ii	1900	$-100 \leq l \leq 60$	$-3 \leq b \leq 3$		15′	3
^{12}CO (1–0)	115	$-10 \leq l \leq 25$	0^{b}	$30'^{c}$	65′	4
^{12}CO (1–0)	115	$-12 \leq l \leq 13$	$-2 \leq b \leq 2$	$7.'5^{a}$	8.′8	5
^{12}CO (1–0)	115	$-12 \leq l \leq 12$	$-5 \leq b \leq 5$	4′	2.′7	6
^{12}CO (2–1)	231	$-3 \leq l \leq 3$	0	7.′5	9′	7
^{12}CO (2–1)	231	$-6 \leq l \leq 6$	$-2 \leq b \leq 2$	7.′5	9.′2	8
^{12}CO (3–2)	345	$-1.5 < l < +1.0$	$-0.2 < b < +0.2$	34″	22″	9
^{13}CO (1–0)	110	$-5 \leq l \leq 5$	$-0.6 \leq b \leq 0.6$	1.′7	6′	10
^{13}CO (1–0)	110	$-6 \leq l \leq 8$	$-1 \leq b \leq 1$	2′	2.′6	6
^{13}CO (2–1)	220	$-1.5 \leq l \leq 3.25$	0	7.′5	9.′2	8
C^{18}O (1–0)	110	$-1.05 \leq l \leq 3.6$	$-0.9 \leq b \leq 0.9$	9′	9′	11
NH_3 (1, 1)–(3, 3)	24	$-2 \leq l \leq 2$	0	1.′7	5.′3	12
SiO (1–0)	43	$-0.8 \leq l \leq 0.9$	$-0.25 \leq b \leq 0.2$	2′	2′	13
OH	1.7	$-6 \leq l \leq 8$	$-1 \leq b \leq 1$	12′	10′	14
H_2CO	4.8	$0.5 \leq l \leq 4$	$-0.5 \leq b \leq 0.9$	3′	3′	15
CS (2–1)	98	$-1 \leq l \leq 3.7$	$-0.4 \leq b \leq 0.4$	1′	2′	10
HNCO($5_{0,5}$–$4_{0,4}$)	110	$-1.05 \leq l \leq 3.6$	$-0.9 \leq b \leq 0.9$	9′	9′	11
HCN (1–0)	89	$-0.2 \leq l \leq 0.7$	$-0.2 \leq b^{d} \leq 0.1$	2′	2′	16
HCN (1–0)	89	$-2.15 \leq l \leq 2.15$	$-0.3 \leq b \leq 0.2$	0.′8	1′	17
HCN (1–0)	89	$-6 \leq l \leq 6$	$-0.8 \leq b \leq 0.87$	$4'^{e}$	1′	18

References. 1) Burton & Liszt (1983); 2) Jaffe et al. (1996); 3) Nakagawa et al. (1995); 4) Bania (1986); 5) Bitran et al. (1997); 6) Fukui et al. (2006); 7) Oka et al. (1996); 8) Sawada et al. (2001); 9) Oka et al. (2007); 10) Bally et al. (1987); 11) Dahmen et al. (1997); 12) Morris et al. (1983); 13) Martín-Pintado et al. 1997, 2000; 14) Boyce & Cohen (1994); 15) Zylka et al. (1992); 16) Fukui et al. (1977); 17) Jackson et al. (1996); 18) Lee (1996).

Notes. $^{(a)}$ for $-1° \leq l \leq 1°$; $^{(b)}$ also 4 strips in latitude at ±10′ and ±20′; $^{(c)}$ at $b = 0$, $\Delta l = 6'$; $^{(d)}$ few positions towards SgrB; $^{(e)}$ 8′ in regions of weak emission.

in the Galactic center. SiO emission, on the other hand, is a tracer of hot, shocked gas, since it can be formed from silicon that is liberated from dust grains, either by low-velocity shock waves or by evaporation at high temperatures. Such shocks are expected, e.g., at the foot points of the giant molecular loops detected by Fukui et al. (2006), who explain such features by the magnetic buoyancy caused by a Parker instability.

Large-scale surveys have been made in $^{12}C^{16}O$ and its isotopomers in the $J = 1 \rightarrow 0$, as well as in $J = 2 \rightarrow 1$ spectral lines (e.g. Bitran et al. 1997; Dahmen et al. 1998; Oka et al. 2001). Up to now, there are few complete maps in species that are less abundant than CO (e.g. CS: Bally et al. 1987, 1988; HNCO: Dahmen et al. 1997; NH_3: Handa et al. 2006; OH: Boyce & Cohen 1994). A compilation of existing spectral line surveys updated from Mauersberger & Bronfman (1998) is given in Table 1. There have been two previous surveys of SiO in the Galactic center region. Martín-Pintado et al. (1997) mapped the $J = 1 \rightarrow 0$ spectral line, but did not cover the entire CMZ. Hüttemeister et al. (1998) measured a number of SiO and CO spectral line transitions toward 33 cloud maxima, to investigate the excitation of the SiO and estimate SiO/H_2 ratios for the clouds. There is a map of the $J = 1 \rightarrow 0$ spectral line of main isotopic HCO$^+$ by Linke et al. (1981), which does not, however, extend far beyond the Sgr A* region. Fukui et al. (1980) also present HCO$^+$ ($J = 1 \rightarrow 0$) observations, but only toward Sgr A and a few positions in Sgr B2. In the following, we present maps of the $J = 2 \rightarrow 1$ spectral line of SiO and the $J = 1 \rightarrow 0$ spectral lines of HCO$^+$ and H^{13}CO$^+$. These are the first complete maps of both species in the Galactic center region.

In Sect. 2 the observations and data reduction are described. In Sect. 3, the survey data are presented. These consist of the full set of the spatial maps of the integrated intensity, longitude-velocity diagrams, and latitude-velocity diagrams for each molecule. We present an analysis in Sect. 4. Four appendices are also included, beginning with Appendix A which presents complementary figures for the paper. Also, Appendices B–D present the complete data set in HCO$^+$, SiO, and H^{13}CO$^+$, respectively, showing velocity channel maps of 10 km s^{-1} velocity width, longitude-velocity, and latitude-velocity diagrams. Appendix E contains the Gaussian fits for each cloud in the survey, identifying the temperature peaks, velocity center, and velocity width. In a subsequent paper, the results will be discussed in the context of other available data.

2. Observations and data reduction

2.1. Observations

This survey was carried out with the NANTEN 4 m telescope operated by Nagoya University at the Las Campanas Observatory, Chile. With its southern location and moderate angular resolution, this instrument is well-suited to large-scale mapping of the Galactic center region. It has a 3.′5 beamwidth at the HCO$^+$ frequency (89.188518 GHz, Lovas et al. 1979) and a 3.′6 beamwidth at the SiO frequency (86.846998 GHz, Lovas et al. 1979), which corresponds to a spatial resolution of about 9 pc at a distance of 8.5 kpc (Blitz et al. 1993). The front end was a 4 K cryogenically cooled NbN superconductor-insulator-superconductor (SiS) mixer receiver that provided a typical system temperature of ~280 K (single side band). The spectrometer was an acousto-optical spectrometer (AOS) with 2048 channels. The frequency coverage and resolution were 250 MHz and 250 kHz, corresponding to a velocity coverage of 840 km s^{-1}

Table 2. Parameters of the survey.

	HCO^+	SiO	$H^{13}CO^+$
Velocity resolution	$1\ km\ s^{-1}$	$1\ km\ s^{-1}$	$1\ km\ s^{-1}$
Rms sensitive	28 mK	20 mK	20 mK
Spatial range:			
CMZ	$-1.^{\circ}5 \leq l \leq 2.^{\circ}25$	$-1.^{\circ}375 \leq l \leq 2.^{\circ}0$	$-1.^{\circ}375 \leq l \leq 2.^{\circ}0$
	$-0.^{\circ}5625 \leq b \leq 0.^{\circ}5625$	$-0.^{\circ}5 \leq b \leq 0.^{\circ}5$	$-0.^{\circ}5 \leq b \leq 0.^{\circ}5$
M+3.2+0.3 (Clump 2)	$2.^{\circ}5625 \leq l \leq 3.^{\circ}5$	$2.^{\circ}5625 \leq l \leq 3.^{\circ}4375$	$2.^{\circ}5625 \leq l \leq 3.^{\circ}4375$
	$-0.^{\circ}3125 \leq b \leq 0.^{\circ}8125$	$-0.^{\circ}25 \leq b \leq 0.^{\circ}875$	$-0.^{\circ}25 \leq b \leq 0.^{\circ}875$
M−5.3+0.4	$-5.^{\circ}75 \leq l \leq -4.^{\circ}6875$	$-5.^{\circ}8125 \leq l \leq -4.^{\circ}6875$	$-5.^{\circ}8125 \leq l \leq -4.^{\circ}6875$
	$-0.^{\circ}125 \leq b \leq 0.^{\circ}5625$	$-0.^{\circ}125 \leq b \leq 0.^{\circ}5625$	$-0.^{\circ}125 \leq b \leq 0.^{\circ}5625$
M−4.4+0.6	$-4.^{\circ}75 \leq l \leq -4.^{\circ}25$	$-4.^{\circ}75 \leq l \leq -4.^{\circ}3125$	$-4.^{\circ}75 \leq l \leq -4.^{\circ}3125$
	$0.^{\circ}25 \leq b \leq 0.^{\circ}8125$	$0.^{\circ}1875 \leq b \leq 0.^{\circ}84375$	$0.^{\circ}1875 \leq b \leq 0.^{\circ}84375$
M−3.8+0.9	$-4.^{\circ}0 \leq l \leq -3.^{\circ}625$	$-4.^{\circ}0625 \leq l \leq -3.^{\circ}625$	$-4.^{\circ}0625 \leq l \leq -3.^{\circ}625$
	$0.^{\circ}5625 \leq b \leq 1.^{\circ}1875$	$0.^{\circ}5625 \leq b \leq 1.^{\circ}21875$	$0.^{\circ}5625 \leq b \leq 1.^{\circ}21875$
M+5.3−0.3	$5.^{\circ}125 \leq l \leq 5.^{\circ}625$	$5.^{\circ}0625 \leq l \leq 5.^{\circ}6875$	$5.^{\circ}0625 \leq l \leq 5.^{\circ}6875$
	$-0.^{\circ}6875 \leq b \leq 0.^{\circ}125$	$-0.^{\circ}8125 \leq b \leq 0.^{\circ}125$	$-0.^{\circ}8125 \leq b \leq 0.^{\circ}125$
Sampling interval:	$3.'75$	$3.'75$	$3.'75$
		$1.'875^{a}$	$1.'875^{a}$
Velocity range:			
CMZ	$-350\ km\ s^{-1} \leq v \leq 350\ km\ s^{-1}$	$-280\ km\ s^{-1} \leq v \leq 300\ km\ s^{-1}$	$-300\ km\ s^{-1} \leq v \leq 250\ km\ s^{-1}$
M+3.2+0.3	$-300\ km\ s^{-1} \leq v \leq 300\ km\ s^{-1}$	$-150\ km\ s^{-1} \leq v \leq 350\ km\ s^{-1}$	$-180\ km\ s^{-1} \leq v \leq 200\ km\ s^{-1}$
M−5.3+0.4	$-350\ km\ s^{-1} \leq v \leq 350\ km\ s^{-1}$	$-150\ km\ s^{-1} \leq v \leq 210\ km\ s^{-1}$	$-190\ km\ s^{-1} \leq v \leq 260\ km\ s^{-1}$
M−4.4+0.6	$-350\ km\ s^{-1} \leq v \leq 350\ km\ s^{-1}$	$-150\ km\ s^{-1} \leq v \leq 210\ km\ s^{-1}$	$-190\ km\ s^{-1} \leq v \leq 260\ km\ s^{-1}$
M−3.8+0.9	$-350\ km\ s^{-1} \leq v \leq 350\ km\ s^{-1}$	$-320\ km\ s^{-1} \leq v \leq 190\ km\ s^{-1}$	$-190\ km\ s^{-1} \leq v \leq 130\ km\ s^{-1}$
M+5.3−0.3	$-300\ km\ s^{-1} \leq v \leq 300\ km\ s^{-1}$	$-100\ km\ s^{-1} \leq v \leq 270\ km\ s^{-1}$	$-190\ km\ s^{-1} \leq v \leq 280\ km\ s^{-1}$

Notes. [a] In the most intense zones, see Fig. 2. M+3.2+0.3, M−5.3+0.4, M−4.4+0.6, M−3.8+0.9, M+5.3−0.3, are the clouds observed by Bitran et al. (1997) and the positions of the cloud are defined by them.

and a velocity resolution of $0.84\ km\ s^{-1}$ at the HCO^+ frequency, and a velocity coverage of $863\ km\ s^{-1}$ and a velocity resolution of $0.86\ km\ s^{-1}$ at the SiO frequency. The data were calibrated using the standard chopper-wheel method (Kutner & Ulich 1981). The measured quantity, $T_{\rm obs}$, was converted to antenna temperature, using $T_{\rm A}^{*} = T_{\rm obs}/(2 \times 0.89) = T_{\rm obs}/1.78$. The factor of 2 is needed because our raw NANTEN data were calibrated as double sideband, while the receiver used was single sideband. The factor of 0.89 is a measured correction arising from the less-than-perfect image band suppression. Throughout this work, all values are given in $T_{\rm A}^{*}$. The main beam temperature scale, $T_{\rm MB}$, can be obtained using $T_{\rm MB} = T_{\rm A}^{*}/\eta_{\rm MB}$, where the main beam efficiency is $\eta_{\rm MB} = 0.87$ at 86 GHz (value provided by the Nanten team).

The data were observed between 1999 and 2003. The area mapped is from about $l = -5.^{\circ}7$ to $l = 5.^{\circ}6$ and from $b = -0.^{\circ}7$ to $b = 1.^{\circ}3$. The survey contains about 1500 positions in the $J = 1 \rightarrow 0$ spectral line of HCO^+, at a uniform spacing of $3.'75$. Each map point was observed for at least 1 min on source, for an rms noise antenna temperature of 28 mK at a velocity resolution of $1\ km\ s^{-1}$. More than 3000 positions were observed in the $J = 2 \rightarrow 1$ spectral line of the vibrational ground state of SiO, fully sampling at $1.'875$ spacing in the most intense regions (see Fig. 2). Each map point was observed for 2.5 min on source, for an rms noise antenna temperature of 20 mK at a $1\ km\ s^{-1}$ velocity resolution. The survey consisted of the CMZ, and five molecular clouds observed in CO by Bitran et al. (1997) with large velocity widths that we call here "Peripheral Molecular Zone" (PMZ). We also observed the presumably optically thin formyl ion isotopic $H^{13}CO^+$ $J = 1 \rightarrow 0$ line (86.754330 GHz, Lovas et al. 1979), which is in the same spectrometer range as SiO (see Table 2 for parameters of the survey)[2].

2.2. Data reduction

The data were reduced using the NDRS (Nanten Data Reduction Software) package. Each data point was reduced individually, fixing the velocity emission interval, and the order of the polynomial to fit the spectrum baseline. Most baselines were polynomials of first order, but a few spectra required second and third order baselines to produce flat spectra where no spectral line emission was expected. To determine the emission interval, we used the velocity intervals where CO($1 \rightarrow 0$) emission appears in the Galactic center (Bitran et al. 1997).

For the reduction of spectra belonging to the CMZ and M+3.2+0.3 cloud, we used the longitude-velocity diagrams of CO (Bitran et al. 1997) as a guide to determine the range of possible molecular emission required for baseline subtraction. The reduction and evaluation of HCO^+ data was straightforward since this spectral line is not blended with other strong molecular emission. The SiO reduction was more difficult since within the SiO band, spectra are offset by $+320\ km\ s^{-1}$ from the $H^{13}CO^+$ ($1 \rightarrow 0$) spectral line. Given the large linewidths present in the CMZ, these spectra are sometimes nearly blended. These two spectral lines were reduced independently. In most of the spectra, the SiO and $H^{13}CO^+$ emission are clearly separated, but toward $l < -0.^{\circ}5$ in CMZ, the SiO spectrum shows high-velocity emission ($\sim 170\ km\ s^{-1}$, see Fig. 4 middle), and a priori is not clear whether this emission corresponds to a high velocity clouds in SiO, or to a low velocity cloud in $H^{13}CO^+$ ($\sim -150\ km\ s^{-1}$). In most cases, a comparison with (unblended) main isotopic HCO^+ could settle this ambiguity. For very few spectra ($\sim$10 spectra), we had to study adjacent spectra to distinguish between emission from SiO and $H^{13}CO^+$. This kind of problem was only found in the CMZ in longitudes lower than $-0.^{\circ}5$. In most cases ($\sim$90%), the emission appears to come from high-velocity SiO cloud, rather than $H^{13}CO^+$.

---

[2] The data cubes are available at `http://www.das.uchile.cl/galcendata`

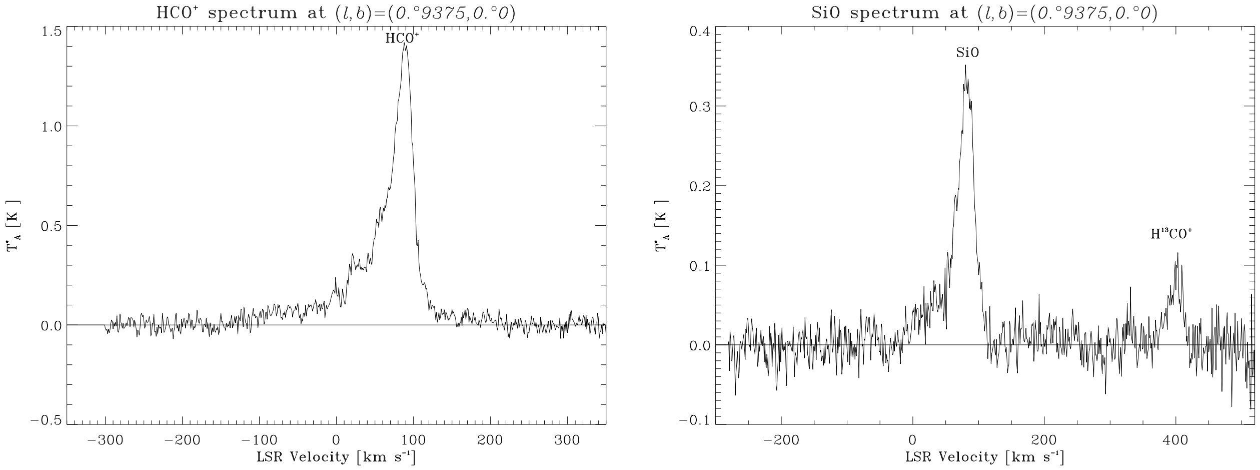

Fig. 1. Typical spectra of HCO$^+$ (*left*) and SiO and H^{13}CO$^+$ (*right*) at *l* and *b* ($0\fdg9375, 0\fdg0$).

In the PMZ, the data reduction was more difficult owing to the low signal-to-noise ratios in the spectra (~5 and even less in M−3.8+0.9 cloud in H^{13}CO$^+$) and the high linewidths. In these cases, we used the CO data from Bitran (1987) to define the velocity interval range where the emission is possible. We first obtained a summed spectrum over the total cloud and from that defined the velocity range of emission. To establish the baseline, we subsequently reduced each spectrum individually. To reduce the HCO$^+$ spectra we interpolated the CO data, which have a sampling of $7\farcm5$, to the same grid as the HCO$^+$ ($3\farcm75$), and then compared spectrum by spectrum. For SiO, we interpolated the HCO$^+$ data to the SiO sampling ($1\farcm875$), and finally, for H^{13}CO$^+$, we used HCO$^+$ and SiO data to define the velocity range where emission might be present. The polynomial order of the subtracted baselines was typically higher than for the CMZ. Most spectra required a polynomial order below 3, but in a few cases, we had to use fourth grade. The basic result of the survey are data cubes, i.e. only, spectra obtained point by point in longitude and latitude, forming a three-dimensional array of $T_{\rm A}^*$. We obtained three data sets with coordinates galactic longitude-galactic latitude-radial velocity for each observed molecule.

3. Results

In this section we present the results of the HCO$^+$ (1 → 0), SiO (2 → 1), and H^{13}CO$^+$ (1 → 0) Galactic center survey. Figure 1 shows typical spectra of HCO$^+$, H^{13}CO$^+$, and SiO. The HCO$^+$ spectrum shows emission over a very broad velocity range between −150 km s^{-1} and 100 km s^{-1}.

3.1. The integrated intensity maps

In Fig. 2, we show the integrated intensity maps, $\int T_{\rm A}^* {\rm d}v$, of the entire observed region in the HCO$^+$, SiO, and H^{13}CO$^+$ spectral lines. For a better display of the observations, we chose the velocity integration range in each spectral line to cover only the emission visible in the respective longitude-velocity diagram, which is indicated in the figure captions. The lowest contour level is at 3σ. The value of σ was calculated as

$$\sigma_{lb} = \sqrt{N_{\rm v}} \times \Delta v \times T_{\rm A}^*({\rm rms}), \tag{1}$$

where $N_{\rm v}$ is the number of velocity channels covered by the emission (for example, in HCO$^+$, the emission is within −230 to 270 km s^{-1}, therefore $N_{\rm v} = 501$), Δv is the velocity resolution (1 km s^{-1}), and $T_{\rm A}^*$(rms) is 28 mK for HCO$^+$ and 20 mK for SiO and H^{13}CO$^+$. In Fig. 2, we can distinguish both the CMZ and the PMZ. In the SiO and H^{13}CO$^+$ maps, the spacing of the observations was variable ($1\farcm875$ in the most intense regions and $3\farcm75$ for the remaining of the maps, see top of Fig. 2). We therefore interpolated the map to the positions with no observations.

For an easy comparison with previous work, most of which include only the CMZ and the cloud at $l \sim 3\fdg2$, in Appendix A, we plot the integrated intensity emission only in this region in all spectral lines observed (Fig. A.1). In this figure we can see the well-known asymmetry of molecular distribution with respect to the Galactic center, with the emission concentrated on the positive longitude side (e.g. Sawada et al. 2001; Oka et al. 1996), and the broad features of the CMZ such as Sgr A ($l \sim 0°$), Sgr B ($l \sim 0\fdg6$), Sgr C ($l \sim -0\fdg5$), Sgr D ($l \sim 1\fdg1$), Sgr E ($l \sim -1\fdg1$, v − 200 km s^{-1}, see e.g. Liszt 2006), and the $1\fdg3$ complex. In the HCO$^+$ spectral line, both in the velocity-integrated map and in the channel maps (Appendix B), the most intense source corresponds to $l = 0\fdg0625$ and $b = -0\fdg0625$ (in Sgr A region). In SiO emission, the intensity peak of the whole map is at $l = 0\fdg75$ and $b = -0\fdg0625$, i.e. the Sgr B2 region. In H^{13}CO$^+$, the highest intensity is toward Sgr B and Sgr A; the other CMZ features are less intense. In the Appendices B.1, C.1, and D.1, we present integrated intensity maps in these spectral lines in 10 km s^{-1} wide velocity intervals.

3.2. Longitude-velocity plots

In Fig. 3, we plot the intensity integrated in latitude for the survey ($\int T_{\rm A}^* {\rm d}b$), covering all the observed range as a function of *l*. In HCO$^+$ and SiO maps, we can clearly see the CMZ and the PMZ, which appear as broad features. In H^{13}CO$^+$, the CMZ is weak as seen, and the only cloud clearly seen is the M−3.8+0.9. The lowest level of the contours is 3σ, which was calculated using

$$\sigma_{l{\rm v}} = \sqrt{N_b} \times \Delta b \times T_{\rm A}^*({\rm rms}), \tag{2}$$

where N_b is the number of latitude points with latitude emission (e.g., 17 pixels for HCO$^+$ in the CMZ), and Δb the spacing in latitude ($0\fdg0625$ for HCO$^+$ data and $0\fdg03125$ for SiO and H^{13}CO$^+$ data).

In Appendix A, we plot the integrated intensity in latitude for the CMZ and M+3.2+0.3 cloud (Fig. A.2). We see the well known asymmetry in longitude and velocity as a parallelogram

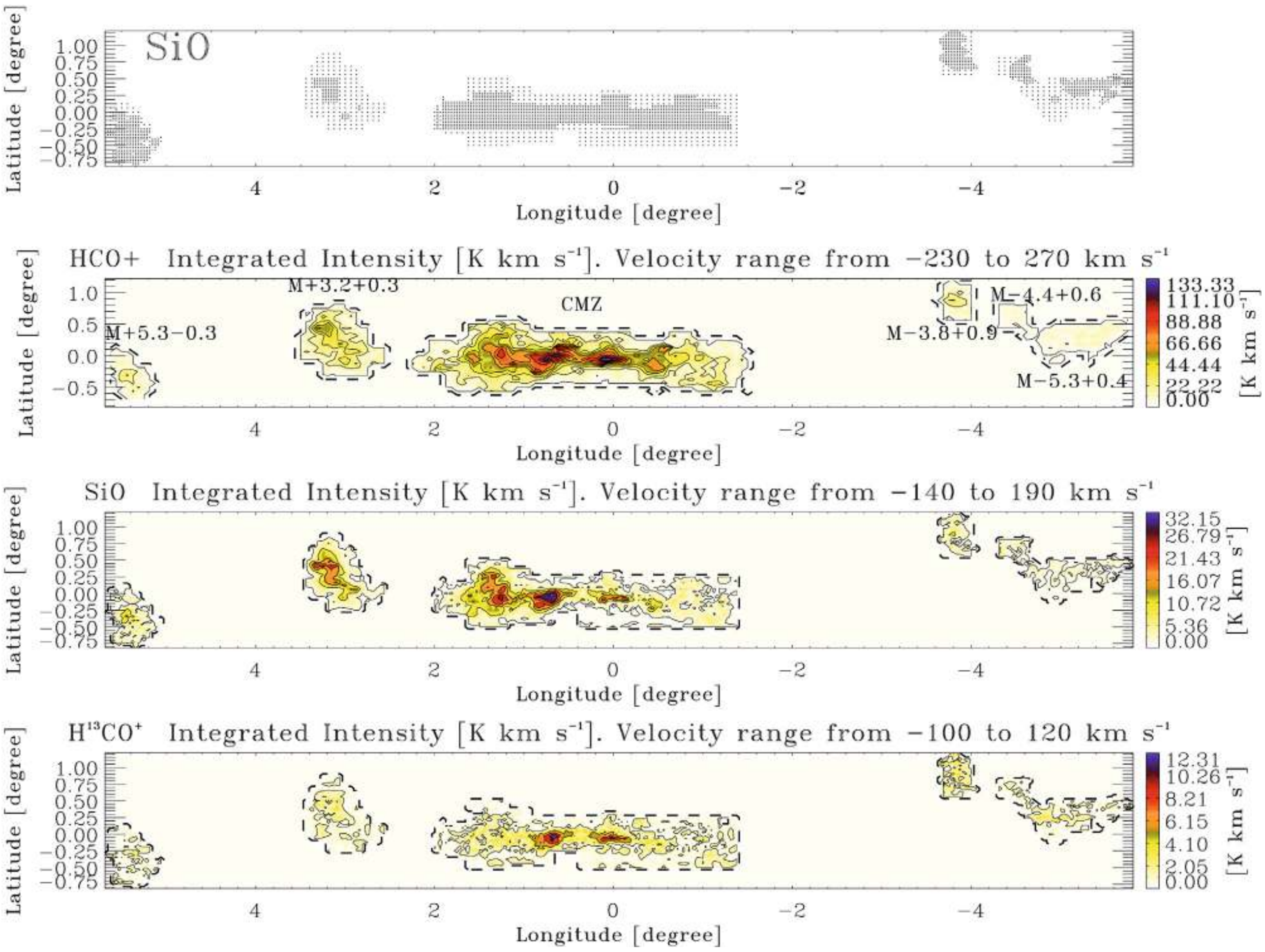

Fig. 2. *From top to bottom*: spatial coverage of the observations in SiO and H^{13}CO$^+$ (HCO$^+$ has uniform sampling of $3\overset{\prime}{.}5$). Emission integrated over velocity from −230 to 270 km s^{-1} for the region measured in HCO$^+$. The solid contour levels start at 1.9 K km s^{-1} (3σ) and increase in steps of 12.53 K km s^{-1} (20σ). Emission integrated over velocity from −140 to 190 km s^{-1} for the region measured in SiO. The solid contours start at 1.09 K km s^{-1} (3σ) and increase in steps of 5.46 K km s^{-1} (15σ). Emission integrated over velocity from −100 to 120 km s^{-1} for the region measured in H^{13}CO$^+$. The solid contours start at 0.89 K km s^{-1} (3σ) and increase in steps of 2.97 K km s^{-1} (10σ). In all plots, the dashed line shows the coverage of the survey in each molecule. For a better display of the observations, we choose the velocity integration range in each spectral line to cover only the emission visible in the respective longitude-velocity diagram.

shape, with the emission placed primarily at positive velocities for $l > 0°$ and at negative velocities for $l < 0°$. We see the large molecular complex features, such as Sgr C ($l \sim -0\overset{\circ}{.}7$ to $-0\overset{\circ}{.}1$; $v < 0$ km s^{-1}), Sgr A ($l \sim 0°$, $v \sim 50$ km s^{-1}; Fukui et al. 1977), Sgr B ($l \sim 0\overset{\circ}{.}6$, $v \sim 50$ km s^{-1}), and Sgr D ($l \sim 0\overset{\circ}{.}9$, $v \sim 80$ km s^{-1}) and the $1\overset{\circ}{.}3$ complex, with a strong peak at $l \sim 1\overset{\circ}{.}25$ and $v \sim 90$ km s^{-1}. The molecular gas complex associated to Sgr E is barely seen toward $l \sim -1.1°$, $v \sim -200$ km s^{-1} (e.g., Liszt 2006). As already noted in previous surveys of CO and HI (e.g. Bitran et al. 1997; Burton & Liszt 1983), the molecular gas at the Galactic center shows non-circular movements with velocities forbidden for galactic rotation, negative for $l > 0°$, and positive for $l < 0°$.

In the HCO$^+$ map, the foreground spiral arms appear as narrow absorption features at $l = 0°$ with $v_{\rm LSR} \sim -50$ km s^{-1} (3 kpc arm), $v_{\rm LSR} \sim -30$ km s^{-1} (Norma arm), and $v_{\rm LSR} \sim 0$ km s^{-1} (Crux am). These absorption features were previously observed in HCO$^+$ and HCN (Fukui et al. 1977, 1980; Linke et al. 1981). In SiO we do not detect any absorption. The SiO emission appears to be more fragmented than HCO$^+$. Sgr E is weaker than other features. At $l \sim 0°$, we detect the well-known clouds associated with Sgr A. Compared with the others features, Sgr B is very intense. The $1\overset{\circ}{.}3$ complex is the most intense feature in this map. In SiO, there is less emission with forbidden velocities than in HCO$^+$. One example of a region where it is not immediately clear whether the emission arises from high-velocity (forbidden) SiO or from H^{13}CO$^+$ can be seen in the mid panel of Fig. 3 (or with more detail in Fig. A.2) at $l \sim -0\overset{\circ}{.}8$ and $v \sim 150$ km s^{-1}. A comparison with the unblended HCO$^+$ emission (top panel) clearly suggests that this feature arises from a forbidden velocity component of SiO. In H^{13}CO$^+$, we can see the features of the CMZ, but these are much weaker than in the other molecular lines. Sgr C shows a very weak emission, and we can barely detect the cloud at $l = -0\overset{\circ}{.}5$ and $v = -50$ km s^{-1}. Sgr A is more intense, and one can see three clouds at $(l, v) \sim (0°, -15$ km s$^{-1})$, $(l, v) \sim (-0\overset{\circ}{.}125, 15$ km s$^{-1})$, and at $(l, v) \sim (0.125°, 50$ km s$^{-1})$. The last two could correspond to the molecular complex M−0.13−0.08 y M−0.02−0.07, with velocities of +20 km s^{-1} and +50 km s^{-1}, respectively (Martín-Pintado et al. 1997). Sgr B2 is the most intense feature, with an intensity peak at $l = 0\overset{\circ}{.}65625$ and $v = 50$ km s^{-1}. Sgr D is less intense than in the other molecular lines, and the $1\overset{\circ}{.}3$ complex is very weak. In this spectral line, M+3.2+0.3 is barely visible. In Appendices B.2, C.2, and D.2, we present a set

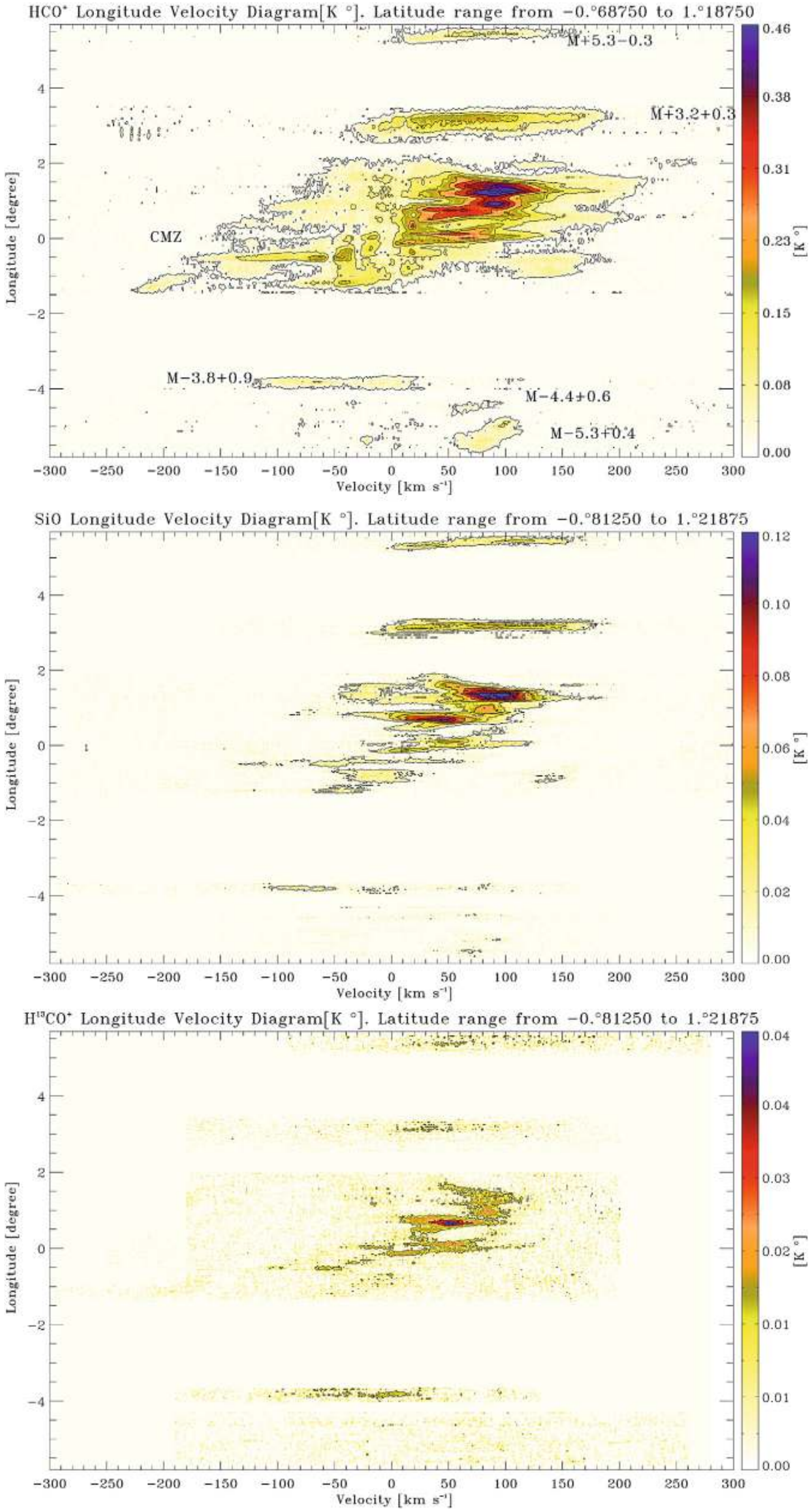

Fig. 3. *Top*: longitude-velocity diagram of HCO$^+$ emission from the CMZ and PMZ covering the whole survey in the latitude range between $b = -0\overset{\circ}{.}6875$ to $b = 1\overset{\circ}{.}1875$. The contour levels start at 0.021 K (3σ), and increase in steps of 0.058 K (8σ). *Middle*: longitude-velocity diagram of SiO emission from the CMZ and PMZ covering the whole survey in the latitude range between $b = -0\overset{\circ}{.}8125$ to $b = 1\overset{\circ}{.}21875$. The contour levels start at 0.01 K (3σ), and increase in steps of 0.018 K (5σ). *Bottom*: longitude-velocity diagram of H^{13}CO$^+$ emission from the CMZ and PMZ covering the whole survey in the latitude range between $b = -0\overset{\circ}{.}8125$ to $b = 1\overset{\circ}{.}21875$. The contour levels start at 0.009 K (3σ), and increase in steps of 0.016 K (5σ).

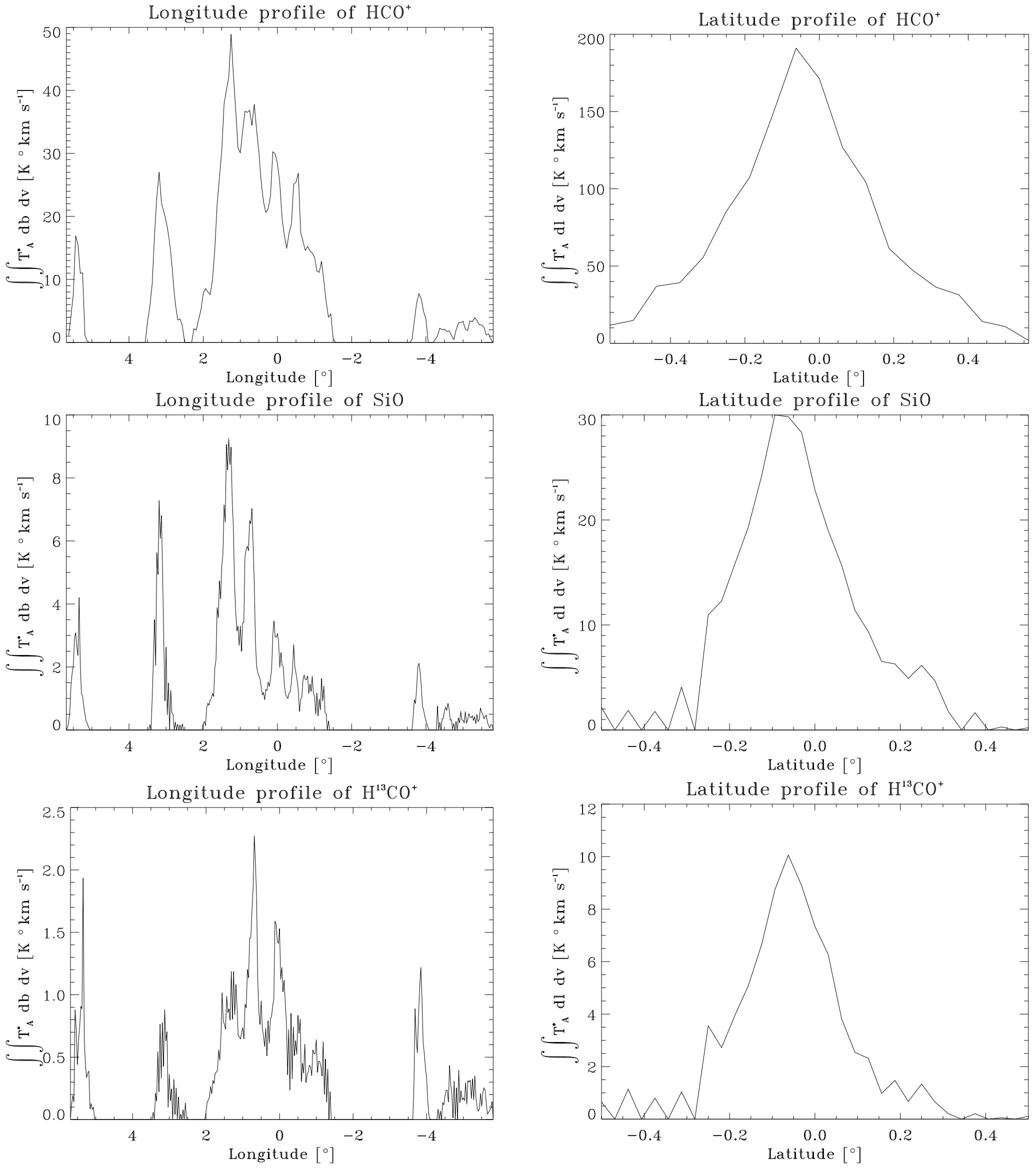

Fig. 4. *Left*: longitude profile for the entire latitude range observed in HCO^+ (*top*), SiO (*middle*) and $H^{13}CO^+$ (*bottom*) emission. *Right*: latitude profile for entire longitude range observed of the CMZ ($-1.^\circ5 < l < 2.^\circ25$) in HCO^+ (*top*), SiO (*middle*) and $H^{13}CO^+$ (*bottom*) emission.

of longitude-velocity diagrams, one for each observed latitude in HCO^+, SiO, and $H^{13}CO^+$.

We show the longitudinal distribution of the molecular emission in Fig. 4, $I(l) = \int\int T^*_A \mathrm{d}b\mathrm{d}v$, integrated over the whole observed latitude. We can see that, in the longitude corresponding to the CMZ, the emission appears asymmetrically distributed toward $l > 0^\circ$, and the 5 clouds in the PMZ clearly appear as intensity peaks at $l \sim 3^\circ$, $5.^\circ5$, $-3.^\circ8$, $-4.^\circ4$, and $-5.^\circ3$. In the CMZ, most of the emission is found toward $l > 0^\circ$, obtaining an average longitude weighted by intensity of $0.^\circ5$ for HCO^+, $0.^\circ7$ for SiO, and $0.^\circ4$ for $H^{13}CO^+$.

3.3. Latitude-velocity plots

We present the intensity integrated in longitude ($\int T^*_A \mathrm{d}l$), covering all observed range for the CMZ and M+3.2+0.3 cloud. Figure 5 shows the CMZ, integrated in all observed longitude corresponding to this region. In Fig. 6, we show the integrated intensity in longitude from HCO^+, SiO, and $H^{13}CO^+$ for the M+3.2+0.3 cloud. In the HCO^+ map, the absorption produced by the spiral arms in ~ -50 km s^{-1}, ~ -30 km s^{-1}, and ~ 0 km s^{-1} is apparent.

We present the latitude profile of the CMZ, $I(b) = \int\int T^*_A \mathrm{d}l\mathrm{d}v$ (Fig. 4), integrated over the entire observed longitude. The average latitude weighted by intensity in HCO^+ emission is $-0.^\circ04$ (which agrees with the value of $-0.^\circ05$ obtained by Bitran 1987 for CO emission), in SiO, $-0.^\circ04$, and in $H^{13}CO^+$ is $-0.^\circ06$.

In the Appendices B.3, C.3, and D.3 we show the latitude-velocity diagrams, one for each observed longitude.

4. Discussion

As mentioned in the previous section, all molecules observed by us are widely distributed throughout the Galactic center region. To distinguish between the dominant heating mechanism for the molecular gas in well-determined space and velocity regions, we compare the maps of SiO and HCO^+ and the maps of SiO and $H^{13}CO^+$.

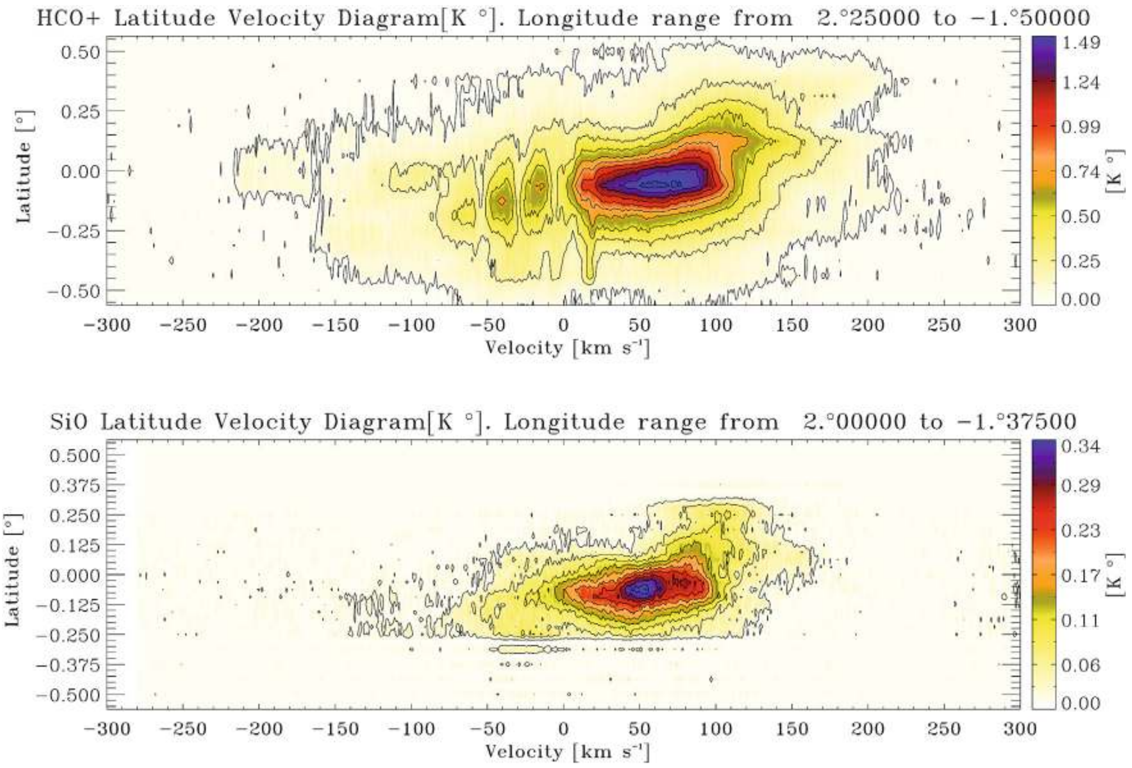

Fig. 5. Latitude-velocity diagram of the CMZ. *Top*: HCO$^+$. The contours start at 0.041 K (3σ value) and increase in steps of 0.136 K (10σ). *Bottom*: SiO. The contours start at 0.02 K (3σ value) and increase in steps of 0.03 K (5σ).

4.1. The spatial and velocity distributions of the spectral line emission ratios

To compare SiO and HCO$^+$ emission, we plot the logarithm of the integrated intensity ratio for all positions where the emission of both spectral lines is above 3σ and in different velocity channels. In regions where the emission is below this value we use the 3σ threshold. We also compare the SiO emission with the H^{13}CO$^+$ emission, and use the 3σ threshold in both transitions.

The H^{13}CO$^+$ is useful since it is optically thin and therefore traces the deeper regions of the clouds. Because it has a high critical density of $\sim 10^5$ cm^{-3} (Wilson et al. 2009), it picks out the densest regions in our maps. In Fig. 7 we plot the logarithm of the integrated intensity ratio for SiO and HCO$^+$ in the velocity range from 30 to 130 km s^{-1}, and for SiO and H^{13}CO$^+$ in the velocity range from −110 to −50 km s^{-1}. In Appendix A, we plot the logarithm of the integrated intensity ratio for velocity intervals of 50 km s^{-1} (Figs. A.3 and A.4). We can clearly identify regions where the HCO$^+$ (blue regions), or where SiO dominates (yellow and red regions). The SiO-dominated regions are, M−3.8+0.9 cloud (Fig. 7, and in the velocity range from $v_{\rm LSR} = -100$ to -50 km s^{-1} in Fig. A.4), M+3.2+0.3 cloud, and M+5.3−0.3 cloud (Fig. 7, and in the velocity range from $v_{\rm LSR}$ = 50 to 150 km s^{-1} in Fig. A.3), the 1.°3 complex ($v > 0$ km s^{-1}) and toward Sgr E region, both in negative velocity and in forbidden velocity between $100 < v < 150$ km s^{-1} (Fig. A.4). The HCO$^+$ is dominant toward Sgr A ($-50 < v < 100$) and Sgr C ($-150 < v < 0$) in the CMZ. In the velocity range of $v_{\rm LSR} = 0$ to 50 km s^{-1}, we observe a very intense SiO zone toward Sgr B, but this velocity range could be contaminated by local gas seen by absorption in HCO$^+$, toward $v \sim 0$ km s^{-1} (see e.g. top of Fig. A.2), which could increase the SiO to HCO$^+$ ratio emission (as can be seen in the Fig. 8 at $v \sim 0$ km s^{-1}.

In Fig. 8, we plot the logarithm of the ratio of the intensities integrated in latitude between SiO and HCO$^+$ emission, using the 3σ threshold. In the region toward Sgr C, Sgr A and Sgr D are dominated by HCO$^+$, and the region toward the 1.3° complex, Sgr B, M+3.2+0.3, and M+5.3−0.3 are dominated by SiO.

To relate the observed line intensities and intensity ratios to molecular column densities and abundance ratios, assumptions on the excitation conditions of the gas are required. First of all, it is necessary to estimate whether the observed transitions are optically thick or optically thin. In the case of HCO$^+$, we have measurements of its rarer isotopomere H^{13}CO$^+$. The ^{12}C/^{13}C isotopic ratio in the Galactic center region is about 20 (Wilson & Matteucci 1992). If both, HCO$^+$ and H^{13}CO$^+$ are optically thin in its $J = 1 \rightarrow 0$ transitions one would expect that their line intensity ratio is close to 20. On average, the measured line intensity ratio in the observed region is typically between 10 and 30, with an average of 19.8 (see Fig. A.5). This indicates that the HCO$^+$ (1−0) emission is indeed optically thin or just moderately optically thick in most of the positions measured by us. This cannot be taken for granted for other galactic centers; for example, in the nearby starbust galaxy NGC 253, the HCO$^+$ emission is on average optically thick (Henkel et al. 1993).

This allows column densities of the levels involved in the transition to be determined (see e.g. Mauersberger & Henkel 1991, for the corresponding equations). More difficult is the task of determining the total column densities of the corresponding molecules since, depending on the excitation conditions $T_{\rm kin}$, $n({\rm H_2})$), the observed levels may represent only a small fraction of the total column density. However, SiO and HCO$^+$ have very similar dipole moments, namely 3.1 (Raymonda et al. 1970) and 3.9 Debye (Botschwina et al. 1993), and therefore

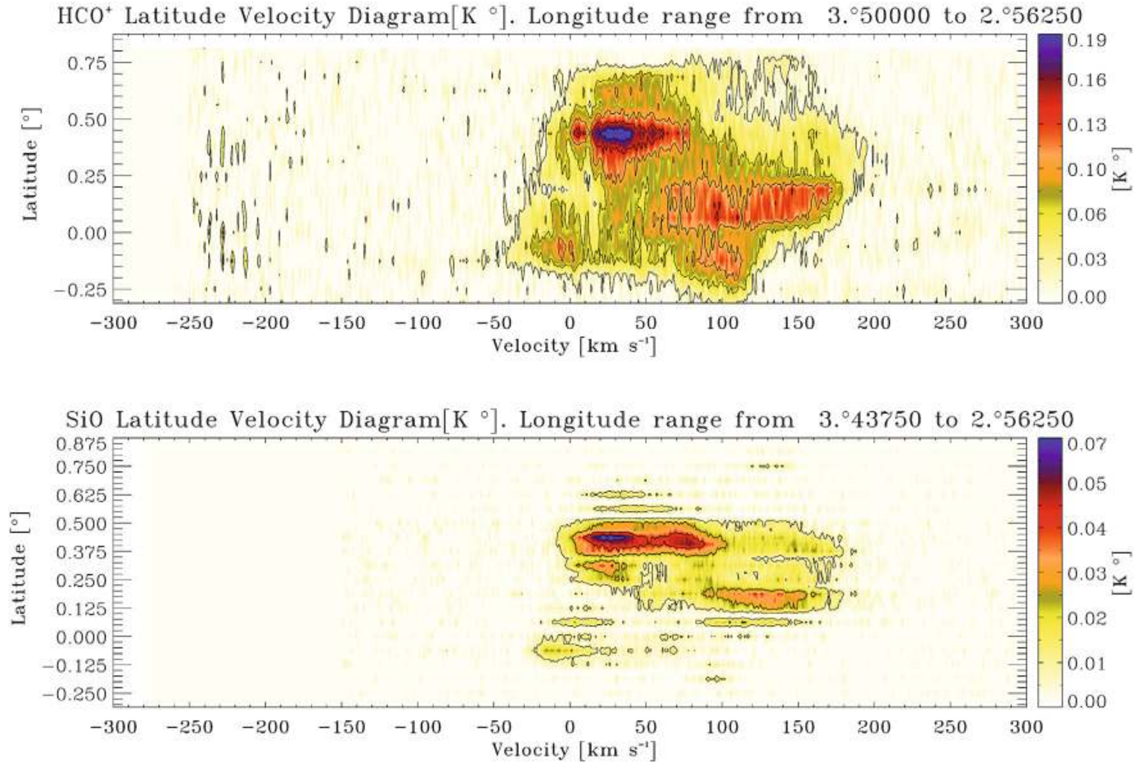

Fig. 6. Latitude-velocity diagram of M+3.2+0.3. *Top*: HCO^+. The contours start at 0.021 K (3σ value) and increase in steps of 0.035 K (5σ). *Bottom*: SiO. The contours start at 0.009 K (3σ value) and increase in steps of 0.015 K (5σ).

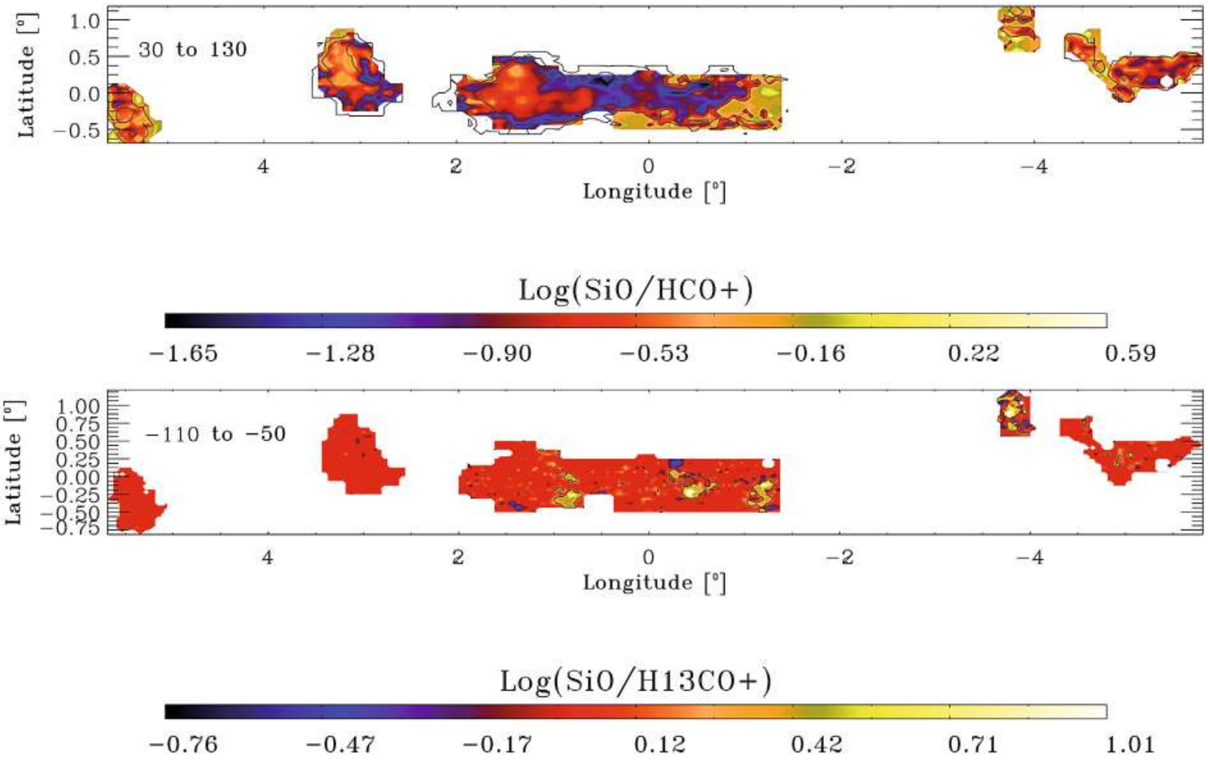

Fig. 7. Logarithm of the integrated intensity ratio. *Top*: $\log(\int T(\mathrm{SiO})\mathrm{d}v/\int T(\mathrm{HCO}^+)\mathrm{d}v)$ in the velocity range from 30 to 130 $\mathrm{km\,s}^{-1}$. The contours correspond to the HCO^+ emission at 3σ and 30σ. We can identify clearly regions where either the SiO (e.g. in the 1.3 Complex and in the M+3.2+0.3 cloud) or HCO^+ (e.g. towards Sgr A region) dominate. *Bottom*: $\log(\int T(\mathrm{SiO})\mathrm{d}v/\int T(\mathrm{H}^{13}\mathrm{CO+})\mathrm{d}v)$ in the velocity range from −110 to −50 $\mathrm{km\,s}^{-1}$. The contours correspond to the SiO emission at 3σ and 30σ. In this velocity range, we can see the enhacement of the SiO toward the M−3.8+0.9 cloud.

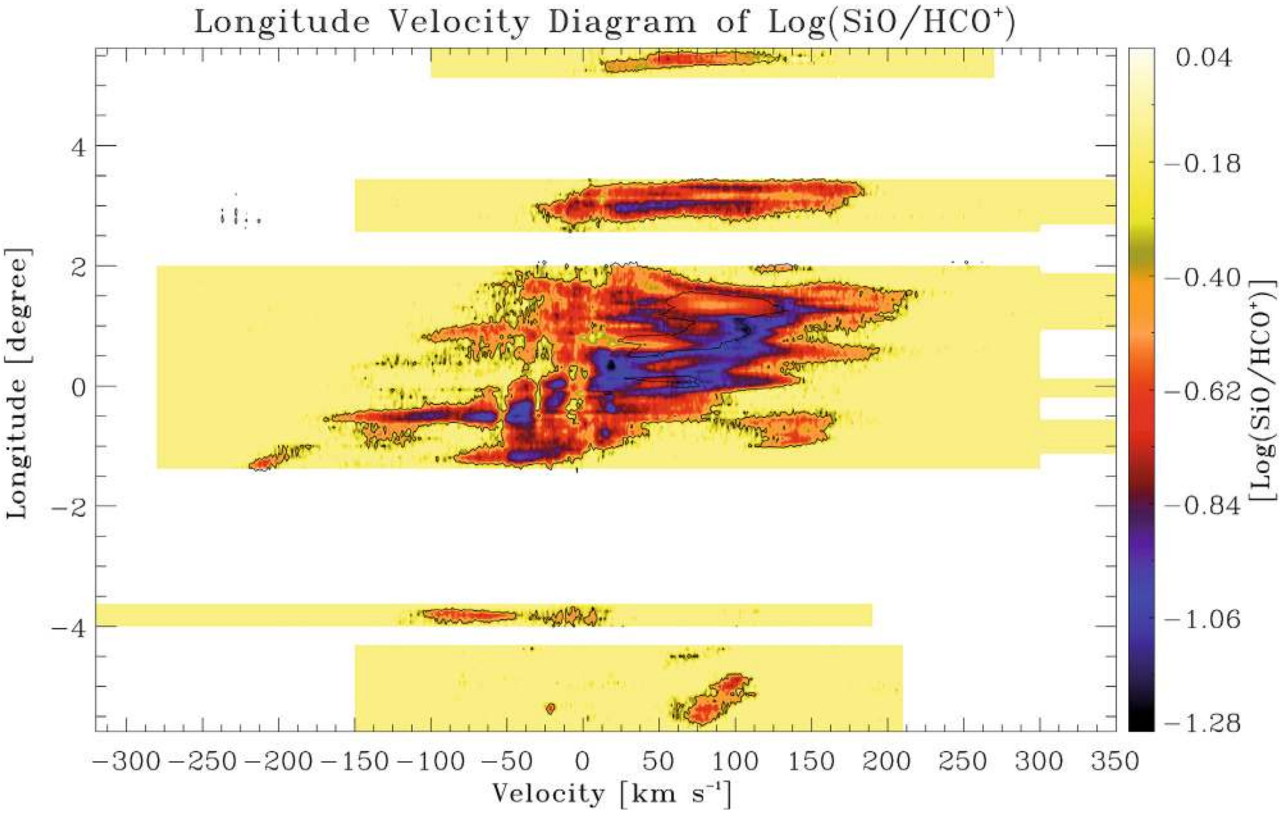

Fig. 8. Longitude-velocity emission comparison between the SiO and HCO+ emission. We plot $\log(\int T(\mathrm{SiO}(J=2\rightarrow 1))\mathrm{d}b/\int T(\mathrm{HCO}^{+}(J=1\rightarrow 0))\mathrm{d}b)$. In the region toward Sgr C, Sgr A, and Sgr D are dominated by HCO+, and the region toward the 1.3 deg complex, Sgr B, M+3.2+0.3, and M+5.3−0.3 are dominated by SiO.

their excitation conditions expressed in terms of critical density should be similar.

4.2. Intensity ratio of molecular emission

We also determined the ratio of the apparent luminosity S between the molecular emissions of HCO$^+$ to CO, SiO to CO, and HCO$^+$ to SiO, integrated over the observed regions to characterize the physical properties of different clouds. The apparent luminosity S is defined as the total emission integrated over velocity and solid angle, in units of K km s^{-1} deg^2 (Dame et al. 1986). The HCO$^+$($J = 1 \rightarrow 0$)/CO($J = 1 \rightarrow 0$) ratio can be related to the ionization fraction of the gas, and the intensity ratio SiO($J = 2 \rightarrow 1$)/CO($J = 1 \rightarrow 0$) is a measure of the amount of material subject to shocks compared to "quiescent" gas. We also plot the apparent luminosity ratio SiO($J = 2 \rightarrow 1$)/HCO$^+$($J = 1 \rightarrow 0$). To define the molecular clouds, we use the average spectrum of each region in HCO$^+$, SiO, H^{13}CO$^+$, and CO from Bitran et al. (1997). In the average spectrum, we perform Gaussian fits to identify each molecular cloud. Different molecular clouds can be distinguished by one dimensional Gaussian fits (Online Appendix E), which yield temperature peaks (T_o), velocity centers, and velocity widths (*FWHM*) of the average spectra of the different regions (Table 3). Also, we list central positions for the clouds. All the values and errors in the Table 3 come from the Gaussian fits. Also, we assign locations to the clouds in this table. In cases where the Gaussian fits did not give unique results or did not converge, the values were obtained by visual inspection. Such cases are marked with an asterisk.

Clump-finding algorithms, such as "Clumpfind" (Williams et al. 1994), have shown to be themselves useful for identifying clumps in Galactic molecular cloud. In the present work, we aim to identify the different velocity molecular clouds (with 10^5–10^6 M_o) along the line of sight toward the Galactic center region. It is not intended to derive the internal substructure within every molecular cloud identified. That is why we only fit Gaussians in the velocity dimension. We identified 51 molecular clouds, 33 of them belonging to the Galactic center region and 18 to the Galactic disk, local gas, or clouds along the line of sight. The molecular clouds classified as outside the Galactic center are characterized by narrow linewidths (<10 km s^{-1}). However, there are still some clouds classified as outside the Galactic center, which present large linewidths. A possible reason is that the clouds could be under the strong influence of the Galactic center tidal forces (e.g. cloud numbers 44 and 48, see Table 3). For example, cloud number 51 has a large linewidth in HCO$^+$. This cloud belongs to the 135 km s^{-1} arm (Bania 1980), which is supposedly located outside from the Galactic center, but it is strongly influenced by it.

The apparent luminosity for each molecular component was obtained using

$$S = \int_{\Omega_s}\int_{v} T^{*}_{\mathrm{A}}\mathrm{d}v\mathrm{d}\Omega, \tag{3}$$

where T^{*}_{A} is the antenna temperature. Figure 9 shows an example of the average spectra and the Gaussian fit. In this cloud the different intensities of the emission in the main velocity component ($v \sim -79$ km s^{-1}) belonging to the Galactic center are evident. The HCO$^+$ and SiO emission in the main velocity component have a noticeable increase of the intensity when compared with, e.g., the gas at velocities $v \sim 0$ km s^{-1}, which, presumably

Table 3. Gaussian fits of the each component of the molecular clouds.

Region	Cloud number	Line	Central velocity [km s^{-1}]	Velocity width[a] [km s^{-1}]	T_0 [K]	Luminosity [K km s^{-1} degree^2]	Associated Object
Sgr A	1	CO	–126 ± 8	60 ± 18	1.3 ± 0.2	56.5 ± 19.6	EMR
Sgr A	1	HCO$^+$	–76 ± 2	127 ± 3	0.032	2.57 ± 0.10	EMR
Sgr A	1	SiO	–110 ± 3	108 ± 8	0.0045 ± 0.0003	0.17 ± 0.02	EMR
Sgr A	2	CO	–34 ± 18	68 ± 42	1.9 ± 0.3	95.7 ± 61.0	
Sgr A	2	HCO$^+$	–39 ± 1	12 ± 1	0.066	0.5	
Sgr A	2	HCO$^+$	–18 ± 1	13 ± 1	0.10	0.85	
Sgr A	2	H^{13}CO$^+$	–26 ± 10	74± 11	0.004 ± 0.002	0.12 ± 0.05	
Sgr A	3	CO	11 ± 5	36 ± 14	2.5 ± 1.6	65.7 ± 50.9	MM
Sgr A	3	HCO$^+$	17 ± 1	24 ± 1	0.12	1.9	MM
Sgr A	4	CO	66 ± 8	71 ± 38	2.3 ± 0.2	124 ± 67	Sgr A cloud
Sgr A	4	HCO$^+$	61 ± 1	72 ± 1	0.19	8.4	Sgr A cloud
Sgr A	4	SiO	44 ± 1	94 ± 1	0.035	1.16	Sgr A cloud
Sgr A	4	H^{13}CO$^+$	40 ± 5	96 ± 6	0.016 ± 0.001	0.55 ± 0.05	Sgr A cloud
Sgr A	5	CO	147 ± 31	72 ± 49	0.8 ± 0.3	44 ± 35	EMR
Sgr A	5	HCO$^+$	135 ± 4	79 ± 5	0.027 ± 0.001	1.3 ± 0.1	EMR
Sgr B	6	CO	–61 ± 7	100 ± 15	1.8 ± 0.1	110 ± 17	EMR
Sgr B	6	HCO$^+$	–56 ± 1	115 ± 3	0.046	2.47	EMR
Sgr B	6	SiO	–49 ± 3	83 ± 7	0.0053	0.092	EMR
Sgr B	7*	CO	30 ± 5	60 ± 5	4.1 ± 0.1	147 ± 12	Sgr B cloud
Sgr B	7	HCO$^+$	42 ± 1	63 ± 1	0.26	7.56	Sgr B cloud
Sgr B	7	SiO	38 ± 1	59 ± 1	0.12	1.43	Sgr B cloud
Sgr B	7	H^{13}CO$^+$	43 ± 1	55 ± 1	0.044	0.505	Sgr B cloud
Sgr B	8*	CO	90 ± 5	35 ± 5	2.75 ± 0.05	58 ± 8	
Sgr B	8	HCO$^+$	95 ± 1	47 ± 1	0.16	3.4	
Sgr B	8	SiO	93 ± 1	37 ± 1	0.028	0.214	
Sgr B	8	H^{13}CO$^+$	94 ± 1	26 ± 1	0.013	0.070	
Sgr B	9	CO	170 ± 12	56 ± 19	1.0 ± 0.3	33 ± 15	
Sgr B	9	HCO$^+$	144 ± 3	97 ± 4	0.056	2.6	
Sgr C	10	CO	–123 ± 5	80 ± 14	1.8 ± 0.2	88 ± 18	EMR
Sgr C	10	HCO$^+$	–103 ± 1	91 ± 1	0.095	2.8	EMR
Sgr C	10	SiO	–116 ± 1	50 ± 2	0.012	0.109	EMR
Sgr C	10	H^{13}CO$^+$	–99 ± 1	29 ± 1	0.006	0.031	EMR
Sgr C	11	CO	–64 ± 4	16 ± 11	1.1 ± 0.5	11 ± 9	Sgr C cloud
Sgr C	11	CO	–41 ± 3	15 ± 8	1.6 ± 0.7	14 ± 10	Sgr C cloud
Sgr C	11	CO	–24 ± 3	6 ± 7	0.9 ± 0.8	3 ± 4	Sgr C cloud
Sgr C	11	HCO$^+$	–65 ± 1	15 ± 1	0.079	0.38	Sgr C cloud
Sgr C	11	HCO$^+$	–41 ± 1	15 ± 1	0.16	0.79	Sgr C cloud
Sgr C	11	HCO$^+$	–21 ± 1	11 ± 1	0.067	0.235	Sgr C cloud
Sgr C	11	SiO	–50 ± 1	43 ± 2	0.019 ± 0.002	0.15 ± 0.02	Sgr C cloud
Sgr C	11	H^{13}CO$^+$	–54 ± 1	33 ± 2	0.011 ± 0.001	0.064 ± 0.007	Sgr C cloud
Sgr C	12*	CO	10 ± 5	40 ± 5	4.1	99 ± 12	
Sgr C	12	HCO$^+$	22 ± 1	73 ± 1	0.099	2.37	
Sgr C	12	SiO	3 ± 2	73 ± 10	0.016	0.21 ± 0.03	
Sgr C	12	H^{13}CO$^+$	–14 ± 4	75 ± 10	0.0063	0.09 ± 0.01	
Sgr C	13*	CO	60 ± 5	30 ± 5	1.3 ± 0.1	24 ± 4	3 kpc far
Sgr C	13	SiO	57 ± 1	29 ± 4	0.007 ± 0.001	0.034 ± 0.007	3 kpc far
Sgr C	13	H^{13}CO$^+$	57 ± 1	33 ± 3	0.0026 ± 0.0002	0.015 ± 0.002	3 kpc far
Sgr C	14	CO	126 ± 6	76 ± 14	1.5 ± 0.2	68 ± 16	EMR
Sgr C	14	HCO$^+$	132 ± 1	85 ± 1	0.057	1.57	EMR
Sgr C	14	SiO	153 ± 1	26 ± 2	0.0064	0.030	EMR
Sgr D	15	CO	–53 ± 48	62 ± 73	2.2 ± 1.6	59 ± 83	
Sgr D	15	HCO$^+$	–56 ± 2	73 ± 4	0.043	1.35	
Sgr D	15	SiO	–48 ± 3	65 ± 4	0.009	0.118	
Sgr D	16	CO	8 ± 26	56 ± 70	3.0 ± 1.8	74 ± 104	
Sgr D	16	HCO$^+$	–10 ± 1	32 ± 2	0.054	0.75 ± 0.07	
Sgr D	16	SiO	18 ± 1	58 ± 3	0.019	0.23	
Sgr D	16	H^{13}CO$^+$	4 ± 2	79 ± 5	0.0048	0.077	
Sgr D	17	CO	86 ± 8	65 ± 28	5.4 ± 0.8	157 ± 71	Sgr D cloud
Sgr D	17	HCO$^+$	27 ± 1	31 ± 2	0.062	0.83	Sgr D cloud
Sgr D	17	HCO$^+$	88 ± 1	71 ± 1	0.31	9.6	Sgr D cloud
Sgr D	17	SiO	81 ± 1	55 ± 1	0.085	0.941	Sgr D cloud
Sgr D	17	H^{13}CO$^+$	83 ± 1	40 ± 1	0.026	0.216	Sgr D cloud
Sgr D	18	CO	176 ± 26	60 ± 62	1.3 ± 0.8	35 ± 42	EMR
Sgr D	18*	HCO$^+$	180 ± 5	50 ± 5	0.045 ± 0.005	1.0 ± 0.1	EMR

Table 3. continued.

Region	Cloud number	Line	Central velocity [km s^{-1}]	Velocity width^a [km s^{-1}]	T_0 [K]	Luminosity [K km s^{-1} degree^2]	Associated Object
Sgr E	19	CO	–201± 14	33 ± 34	0.7± 0.6	20.7 ± 27.9	Sgr E cloud
Sgr E	19	HCO$^+$	–203± 1	29± 1	0.024	0.477	Sgr E cloud
Sgr E	19	SiO	–180 ± 3	40 ± 7	0.0030 ± 0.0003	0.040 ±0.008	Sgr E cloud
Sgr E	19	H^{13}CO$^+$	–185 ± 1	40 ± 2	0.0032	0.042	Sgr E cloud
Sgr E	20	CO	–128 ± 23	83 ± 96	0.76± 0.37	57 ± 71	EMR
Sgr E	20	HCO$^+$	–124 ±1	103 ± 4	0.03	2	EMR
Sgr E	20	SiO	–124 ±2	40 ± 4	0.005	0.063 ±0.008	EMR
Sgr E	20	H^{13}CO$^+$	–123 ± 1	22 ± 2	0.0016± 0.0001	0.012 ±0.002	EMR
Sgr E	21	CO	–59 ± 25	28± 43	1.2 ± 1.6	31± 62	
Sgr E	21	CO	–26 ± 9	33 ± 44	2.7 ±0.6	79± 108	
Sgr E	21	CO	–3 ±4	11± 11	2.1± 2.2	22± 32	
Sgr E	21	HCO$^+$	–31 ± 1	49 ± 1	0.096	3.2	
Sgr E	21	SiO	–23 ± 1	67 ± 1	0.021	0.47	
Sgr E	21	H^{13}CO$^+$	–23 ± 1	81± 1	0.007	0.19	
Sgr E	22	CO	13 ± 5	16 ± 11	2.1 ±0.9	30± 25	MM
Sgr E	22*	HCO$^+$	12 ± 5	25 ± 5	1.1 0.2		MM
Sgr E	23*	CO	140 ± 5	55 ± 5	0.50 ± 0.05	24.7±3.3	EMR
Sgr E	23	HCO$^+$	131 ± 1	68 ± 1	0.028	1.28	EMR
Sgr E	23	SiO	134 ± 1	36 ± 1	0.009	0.114	EMR
Sgr E	23	H^{13}CO$^+$	105 ± 1	60 ± 2	0.002	0.048	EMR
1.3 complex	24	CO	–1 ± 8	88 ± 17	2.9 ± 0.2	265 ± 55	
1.3 complex	24	HCO$^+$	–22 ± 1	75 ± 1	0.048	2.99	
1.3 complex	24	SiO	–16 ± 1	54 ± 1	0.018	0.462	
1.3 complex	24	H^{13}CO$^+$	–24 ± 1	47 ± 2	0.0046	0.102	
1.3 complex	25	CO	85 ± 6	64 ± 18	3.1 ± 1.0	206 ± 89	1.3 complex cloud
1.3 complex	25	HCO$^+$	83 ± 0	90 ± 1	0.18	13.6	1.3 complex cloud
1.3 complex	25	SiO	81 ± 1	76 ± 1	0.076	2.735	1.3 complex cloud
1.3 complex	25	H^{13}CO$^+$	75 ± 1	82 ± 1	0.01	0.388	1.3 complex cloud
1.3 complex	26	CO	167 ± 43	121 ± 73	1.1 ± 0.3	143 ± 93	EMR
1.3 complex	26	HCO$^+$	178 ± 2	86 ± 3	0.031	2.19	EMR
M+3.2+0.3	27	CO	–42 ± 18	35 ± 42	0.5 ± 0.4	29 ± 41	3 kpc
M+3.2+0.3	27	H^{13}CO$^+$	–45 ± 3	48 ± 7	0.0025 ± 0.0002	0.033 ± 0.006	3 kpc
M+3.2+0.3	28	CO	11 ± 4	40 ± 14	2.3 ± 0.5	150 ± 62	
M+3.2+0.3	28	HCO$^+$	32 ± 1	84 ± 2	0.09	6.4	
M+3.2+0.3	28	SiO	23 ± 1	51 ± 1	0.045	0.64	
M+3.2+0.3	28	H^{13}CO$^+$	24 ± 2	55 ± 5	0.0094	0.14	
M+3.2+0.3	29	CO	93 ± 10	97 ± 49	1.7 ± 0.3	276 ± 146	Clump 2
M+3.2+0.3	29	HCO$^+$	103 ± 1	68 ± 3	0.074	4.4	Clump 2
M+3.2+0.3	29	SiO	80 ± 1	54 ± 2	0.039	0.59	Clump 2
M+3.2+0.3	29	H^{13}CO$^+$	85 ± 6	63 ± 9	0.0042	0.07 ± 0.01	Clump 2
M+3.2+0.3	30	CO	159 ± 11	27 ± 37	0.6 ± 0.6	24 ± 45	
M+3.2+0.3	30	HCO$^+$	159 ± 1	38 ± 1	0.037	1.21	
M+3.2+0.3	30	SiO	139 ± 1	61 ± 2	0.031	0.52 ± 0.02	
M+3.2+0.3	31	CO	237 ± 32	55 ± 76	0.3 ± 0.3	25 ± 45	EMR
M+3.2+0.3	31	HCO$^+$	219 ± 13	137 ± 24	0.0055	0.6 ± 0.1	EMR
M−5.3+0.4	32	CO	–81 ± 3	14 ± 7	1.0 ± 0.4	12 ± 8	3 kpc
M−5.3+0.4	32	HCO$^+$	–78 ± 4	29 ± 7	0.012 ± 0.002	0.19 ± 0.06	3 kpc
M−5.3+0.4	32	SiO	–91 ± 1	8 ± 3	0.0027 ± 0.0008	0.006 ± 0.003	3 kpc
M−5.3+0.4	32	H^{13}CO$^+$	–80 ± 1	8 ± 3	0.0025 ± 0.0008	0.005 ± 0.003	3 kpc
M−5.3+0.4	33	CO	–44 ± 8	25 ± 21	0.7 ± 0.3	16 ± 15	Norma
M−5.3+0.4	33	HCO$^+$	–43 ± 5	33 ± 23	0.008 ± 0.001	0.15 ± 0.1	Norma
M−5.3+0.4	33*	SiO	–50 ± 5	20 ± 5	0.008	0.04 ± 0.01	Norma
M−5.3+0.4	33	H^{13}CO$^+$	–55 ± 4	33 ± 16	0.0019 ± 0.0004	0.018 ± 0.009	Norma
M−5.3+0.4	34	CO	–18 ± 3	17 ± 7	1.6 ± 0.4	24 ± 12	Crux
M−5.3+0.4	34	HCO$^+$	–21 ± 1	9 ± 2	0.021 ± 0.003	0.11 ± 0.03	Crux
M−5.3+0.4	34*	SiO	–20 ± 5	10 ± 5	0.0078	0.02 ± 0.01	Crux
M−5.3+0.4	34	H^{13}CO$^+$	–23 ± 2	17 ± 4	0.0037 ± 0.0006	0.017 ± 0.005	Crux
M−5.3+0.4	35	CO	3 ± 1	10 ± 2	3.0 ± 0.5	27 ± 7	MM
M−5.3+0.4	35*	HCO$^+$	5 ± 5	10 ± 5	0.030 ± 0.003	0.18 ± 0.09	MM
M−5.3+0.4	35	SiO	12 ± 3	37 ± 9	0.004 ± 0.0004	0.04 ± 0.01	MM
M−5.3+0.4	35	H^{13}CO$^+$	11 ± 2	26 ± 7	0.0024 ± 0.0004	0.017 ± 0.005	MM
M−5.3+0.4	36	CO	87 ± 3	42 ± 7	1.7 ± 0.2	65 ± 13	Clump 1
M−5.3+0.4	36	HCO$^+$	86 ± 1	41 ± 1	0.069	1.65	Clump 1
M−5.3+0.4	36	SiO	72 ± 1	51 ± 2	0.015	0.206	Clump 1
M−5.3+0.4	36	H^{13}CO$^+$	83 ± 2	92 ± 5	0.0061	0.15 ± 0.01	Clump 1

Table 3. continued.

Region	Cloud number	Line	Central velocity [km s^{-1}]	Velocity width^a [km s^{-1}]	T_0 [K]	Luminosity [K km s^{-1} degree^2]	Associated Object
M−4.4+0.6	37	CO	–75 ± 1	28 ± 3	1.2 ± 0.1	8 ± 1	3 kpc
M−4.4+0.6	37*	HCO$^+$	–70 ± 5	10 ± 5	0.014 ± 0.003	0.025 ± 0.01	3 kpc
M−4.4+0.6	37	SiO	–75 ± 1	14 ± 2	0.0062 ± 0.0009	0.009 ± 0.002	3 kpc
M−4.4+0.6	37	H^{13}CO$^+$	–70 ± 2	22 ± 4	0.0047 ± 0.0006	0.011 ± 0.002	3 kpc
M−4.4+0.6	38	CO	–34 ± 1	16 ± 2	1.3 ± 0.1	5 ± 0.9	Norma
M−4.4+0.6	38*	HCO$^+$	–45 ± 5	20 ± 5	0.018 ± 0.003	0.06 ± 0.02	Norma
M−4.4+0.6	38	SiO	–40 ± 5	15 ± 5	0.008	0.012 ± 0.004	Norma
M−4.4+0.6	38	H^{13}CO$^+$	–37 ± 1	10 ± 2	0.006 ± 0.001	0.006 ± 0.002	Norma
M−4.4+0.6	39*	CO	–20 ± 5	10 ± 5	0.72 ± 0.05	1.8 ± 0.9	Crux
M−4.4+0.6	39*	HCO$^+$	–30 ± 5	10 ± 5	0.036 ± 0.003	0.06 ± 0.03	Crux
M−4.4+0.6	39	SiO	–20 ± 5	20 ± 5	0.0092	0.018 ± 0.005	Crux
M−4.4+0.6	39	H^{13}CO$^+$	–23 ± 1	6 ± 2	0.005 ± 0.001	0.003 ± 0.001	Crux
M−4.4+0.6	40*	CO	0 ± 5	10 ± 5	2.75	7 ± 3	MM
M−4.4+0.6	40	H^{13}CO$^+$	–1 ± 2	27 ± 6	0.0041 ± 0.0006	0.012 ± 0.003	MM
M−4.4+0.6	41*	CO	18 ± 5	20 ± 5	1.25 ± 0.05	6 ± 2	
M−4.4+0.6	41	SiO	25 ± 2	30 ± 4	0.011 ± 0.001	0.033 ± 0.005	
M−4.4+0.6	42	CO	70 ± 2	55 ± 6	1.55 ± 0.08	21 ± 2	M−4.4+0.6 cloud
M−4.4+0.6	42	HCO$^+$	71 ± 1	49 ± 1	0.048	0.42	M−4.4+0.6 cloud
M−4.4+0.6	42	SiO	72 ± 1	51 ± 3	0.014	0.073	M−4.4+0.6 cloud
M−4.4+0.6	42	H^{13}CO$^+$	65 ± 1	39 ± 3	0.0073	0.031 ± 0.003	M−4.4+0.6 cloud
M−3.8+0.9	43	CO	–67 ± 6	81 ± 14	1.0 ± 0.1	28 ± 5	M−3.8+0.9 cloud
M−3.8+0.9	43	HCO$^+$	–79 ± 1	61 ± 1	0.067	1.05	M−3.8+0.9 cloud
M−3.8+0.9	43	SiO	–80 ± 2	79 ± 4	0.014	0.2	M−3.8+0.9 cloud
M−3.8+0.9	43	H^{13}CO$^+$	–60 ± 4	73 ± 7	0.0097	0.13 ± 0.01	M−3.8+0.9 cloud
M−3.8+0.9	44	CO	0 ± 2	37 ± 5	2.1 ± 0.2	26 ± 4	MM
M−3.8+0.9	44	HCO$^+$	–4 ± 1	55 ± 2	0.058	0.83	MM
M−3.8+0.9	44	SiO	–5 ± 1	43 ± 3	0.014	0.109	MM
M−3.8+0.9	44	H^{13}CO$^+$	5 ± 2	54 ± 4	0.012	0.12 ± 0.01	MM
M−3.8+0.9	45	CO	60 ± 13	53 ± 51	0.3 ± 0.1	5 ± 5	3 kpc far
M−3.8+0.9	45*	HCO$^+$	60 ± 5	15 ± 5	0.013 ± 0.002	0.05 ± 0.02	3 kpc far
M−3.8+0.9	45	SiO	40 ± 2	16 ± 5	0.004 ± 0.001	0.013 ± 0.005	3 kpc far
M−3.8+0.9	45	H^{13}CO$^+$	60 ± 1	8 ± 2	0.004 ± 0.001	0.005 ± 0.002	3 kpc far
M−3.8+0.9	46	CO	106 ± 3	19 ± 7	0.74 ± 0.20	5 ± 2	135 km s^{-1}
M−3.8+0.9	46	HCO$^+$	108 ± 1	17 ± 2	0.019 ± 0.003	0.08 ± 0.02	135 km s^{-1}
M−3.8+0.9	46*	SiO	80 ± 5	20 ± 5	0.012	0.04 ± 0.01	135 km s^{-1}
M−3.8+0.9	46	H^{13}CO$^+$	95 ± 1	7 ± 1	0.006 ± 0.001	0.008 ± 0.002	135 km s^{-1}
M+5.3−0.3	47	CO	–27 ± 1	9 ± 2	1.4 ± 0.2	9 ± 2	3 kpc
M+5.3−0.3	47	HCO$^+$	–28 ± 1	15 ± 2	0.013 ± 0.001	0.06 ± 0.01	3 kpc
M+5.3−0.3	48	CO	9 ± 1	12 ± 2	2.9 ± 0.2	25 ± 4	MM
M+5.3−0.3	48	CO	23 ± 3	11 ± 6	0.7 ± 0.2	6 ± 4	MM
M+5.3−0.3	48	HCO$^+$	23 ± 2	39 ± 3	0.05	0.61	MM
M+5.3−0.3	48*	SiO	26 ± 1	48 ± 1	0.014	0.207	MM
M+5.3−0.3	48	H^{13}CO$^+$	8 ± 13	49 ± 14	0.003 ± 0.001	0.043 ± 0.02	MM
M+5.3−0.3	49	CO	40 ± 12	62 ± 15	1.3 ± 0.5	55 ± 26	
M+5.3−0.3	49	HCO$^+$	59 ± 1	32 ± 3	0.062 ± 0.007	0.6 ± 0.1	
M+5.3−0.3	49*	SiO	65 ± 5	35 ± 5	0.017	0.18 ± 0.03	
M+5.3−0.3	49	H^{13}CO$^+$	54 ± 5	51 ± 11	0.0068 ± 0.0009	0.11 ± 0.03	
M+5.3−0.3	50	CO	104 ± 28	83 ± 52	0.8 ± 0.2	45 ± 31	M+5.3−0.3 cloud
M+5.3−0.3	50	HCO$^+$	98 ± 2	47 ± 8	0.061 ± 0.007	0.81 ± 0.13	M+5.3−0.3 cloud
M+5.3−0.3	50*	SiO	105 ± 5	60 ± 5	0.021	0.38 ± 0.03	M+5.3−0.3 cloud
M+5.3−0.3	50	H^{13}CO$^+$	120 ± 4	61 ± 9	0.0045	0.08 ± 0.01	M+5.3−0.3 cloud
M+5.3−0.3	51	CO	190 ± 6	38 ± 15	0.4 ± 0.1	10 ± 5	135 km s^{-1}
M+5.3−0.3	51	HCO$^+$	150 ± 6	50 ± 8	0.020 ± 0.002	0.31 ± 0.06	135 km s^{-1}
M+5.3−0.3	51	H^{13}CO$^+$	173 ± 1	12 ± 2	0.0041 ±0.0004	0.015 ± 0.003	135 km s^{-1}

Notes. In most, the nominal Gaussian fits do the data give uncertainties smaller that 10%, the estimated relative calibration uncertainty of our data, only in cases where the errors from the Gaussian fit exceed 10%, these uncertainties are indicated. The size of each region is given in Table 2. $^{(a)}$ Gaussian *FWHM*. Central velocity, Velocity width and temperature peaks (T_0) derived by the average spectrum shown in Appendix D. EMR: "Expanding Molecular Ring" (Bitran 1987); MM: "Main Maximum" (Bitran 1987); 3 kpc: "3 kpc Arm" (Bitran 1987; Sawada et al. 2001); Norma: "Norma Arm" (Bitran 1987; Sawada et al. 2001); Crux: "Crux Arm" (Bitran 1987; Sawada et al. 2001); 135 km s^{-1}: "135 km s^{-1} Arm" (Bitran 1987; Bania 1980); Clump 1 (Bania 1977; Bania et al. 1986; Bitran 1987); Clump 2 (Bania 1977; Bitran 1987). The cloud number 15 is formed by the 3 kpc, Crux and Norma arms. M−4.4+0.6 cloud, identifyed by Bitran (1987). M−3.8+0.9 cloud, identifyed by Bitran (1987). M+5.3−0.3 cloud, identifyed by Bitran (1987).

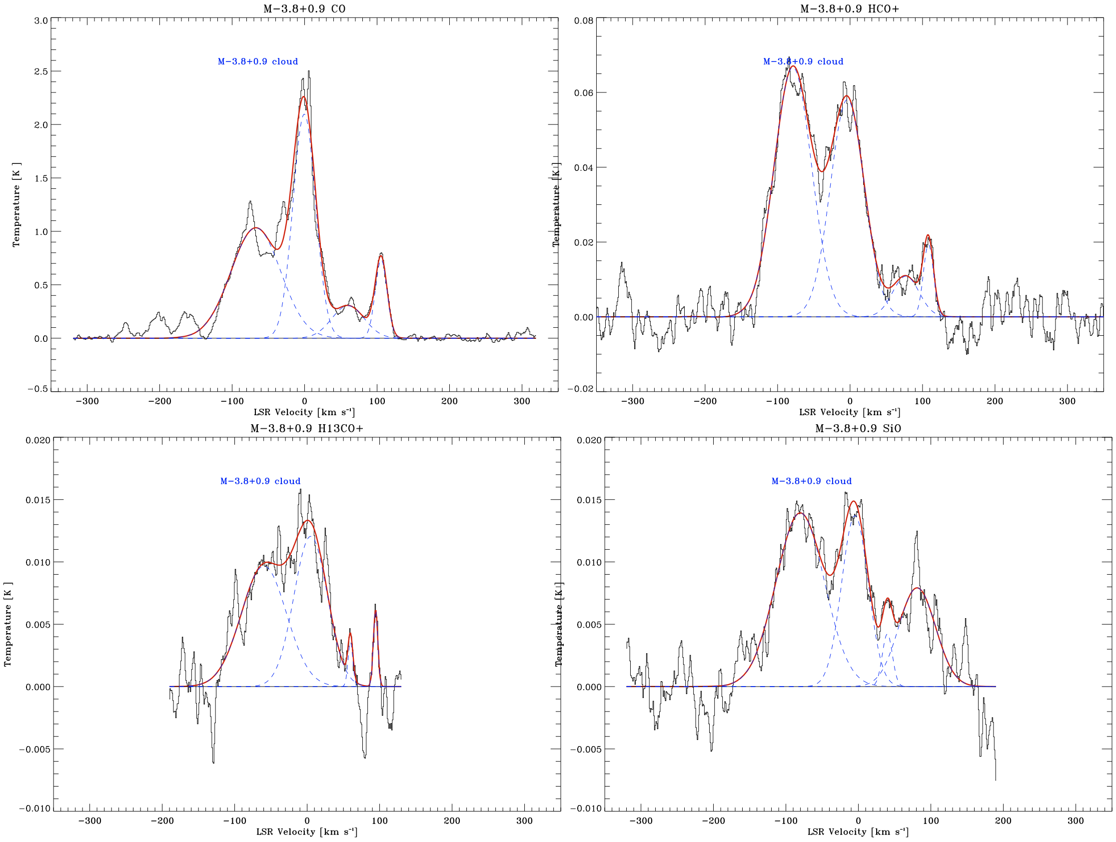

Fig. 9. CO, HCO^+, SiO, and $H^{13}CO^+$ average spectra over the angular size of M−3.8+0.9 cloud (from $l = -4\overset{\circ}{.}0$ to $-3\overset{\circ}{.}625$, and from $b = 0\overset{\circ}{.}5625$ to $1\overset{\circ}{.}1875$). The angular size considered for each region is listed in Table 2. The red lines indicate the Gaussian fit for the complete region and blue dashed lines show the Gaussian fits of each velocity components.

correspond to gas in the line of sight[3]. In the CO emission, the main component ($v \sim -79$ km s^{-1}) show less emission when compared with the gas in the line of sight at $v \sim 0$ km s^{-1}. This plot clearly shows the differences in the molecular gas in the Galactic center and in the disk. In the Appendix D, we show the Gaussian fits for all the molecular complexes.

Figures A.6 and A.7 show the ratio of HCO^+ and SiO to CO luminosities, respectively, while Fig. A.8 shows the ratio of SiO to HCO^+ luminosities for each molecular cloud. The "main component" is the most prominent Galactic center cloud in the region (see Table 4), and it was identified by Bitran (1987). It is noticeable that we could identify some SiO clouds as belonging to the local gas and/or spiral arms, while it is supposed that SiO only traces the gas belonging to the Galactic center. From their velocities and line shape these clouds appear to be in the Galactic disk rather than in the Galactic center. That they are emitting SiO radiation would, however, indicate a location within the Galactic center region. A more detailed study of these clouds would be interesting, since they are either Galactic center clouds with an unusual velocity footprint or they are disk clouds with unusual chemistry and/or excitation conditions. The average of the ratio of HCO^+ to CO luminosity in clouds belonging to the Galactic center is 0.035 ± 0.003 and for disk clouds is 0.015 ± 0.004. The higher intensity ratios are found toward cloud 9 in Sgr B, cloud 4 in Sgr A, cloud 17 in Sgr D, cloud 23 in Sgr E, and cloud 25 in the $1\overset{\circ}{.}3$ complex. In the same way, we display the ratio between SiO and CO. The average of the ratio of SiO to CO luminosity in clouds belonging to the Galactic center is 0.0049 ± 0.0005 and for disk cloud is 0.0034 ± 0.0009. A higher abundances of SiO($J = 2 \rightarrow 1$)/CO($J = 1 \rightarrow 0$) is observed in the M+3.2+0.3 cloud, $1\overset{\circ}{.}3$ complex, and in the M+5.3−0.3 cloud. The luminosity ratio of SiO($J = 2 \rightarrow 1$)/HCO^+($J = 1 \rightarrow 0$) in Fig. A.8, gives an average of 0.15 ± 0.002 for the Galactic center and 0.26 ± 0.05 for the disk clouds. The higher ratios in the Galactic center are found in the M+3.2+0.3 cloud, M+5.3−0.3 cloud, and Sgr D region, and the lower in Sgr A, Sgr C, and Sgr B. For the clouds belonging to the Galactic disk, the average was obtained without considering the clouds with large linewidths discussed before (clouds number 44, 48, and 51), and for the cloud belonging to the Galactic center we did not consider the clouds that present self absorption in HCO^+ and CO, which would decrease the integrated intensity of the cloud (clouds number 2, 11, and 21).

We also investigated the relationship between the HCO^+($J = 1 \rightarrow 0$)/CO($J = 1 \rightarrow 0$) and SiO($J = 2 \rightarrow 1$)/CO($J = 1 \rightarrow 0$) luminosity ratio and the velocity width of the respective clouds in Fig. 10. Here we show disk clouds, clouds in the Galactic center, and cloud that presumably belong to the Galactic disk but they present large linewidth, probably because of the strong Galactic center tidal forces in this region. It is evident, in general, that Galactic center clouds show higher HCO^+($J = 1 \rightarrow 0$)/CO($J = 1 \rightarrow 0$) and SiO($J = 2 \rightarrow 1$)/CO($J = 1 \rightarrow 0$) luminosity ratios and larger linewidths than disk clouds.

---

[3] The line of sight components are shown in the Appendix A, Fig. A2.2 as a narrow emission (~5−10 km s^{-1}), whereas the Galactic center emission is characterized by broad velocity width lines ($\gtrsim$50 km s^{-1}). Thus, the emission coming from the region at $l \sim -0\overset{\circ}{.}4$ to $l \sim 0\overset{\circ}{.}6$ and $b \sim -0\overset{\circ}{.}4375$ to $b \sim -0\overset{\circ}{.}375$ at ~0 km s^{-1} corresponds to local gas.

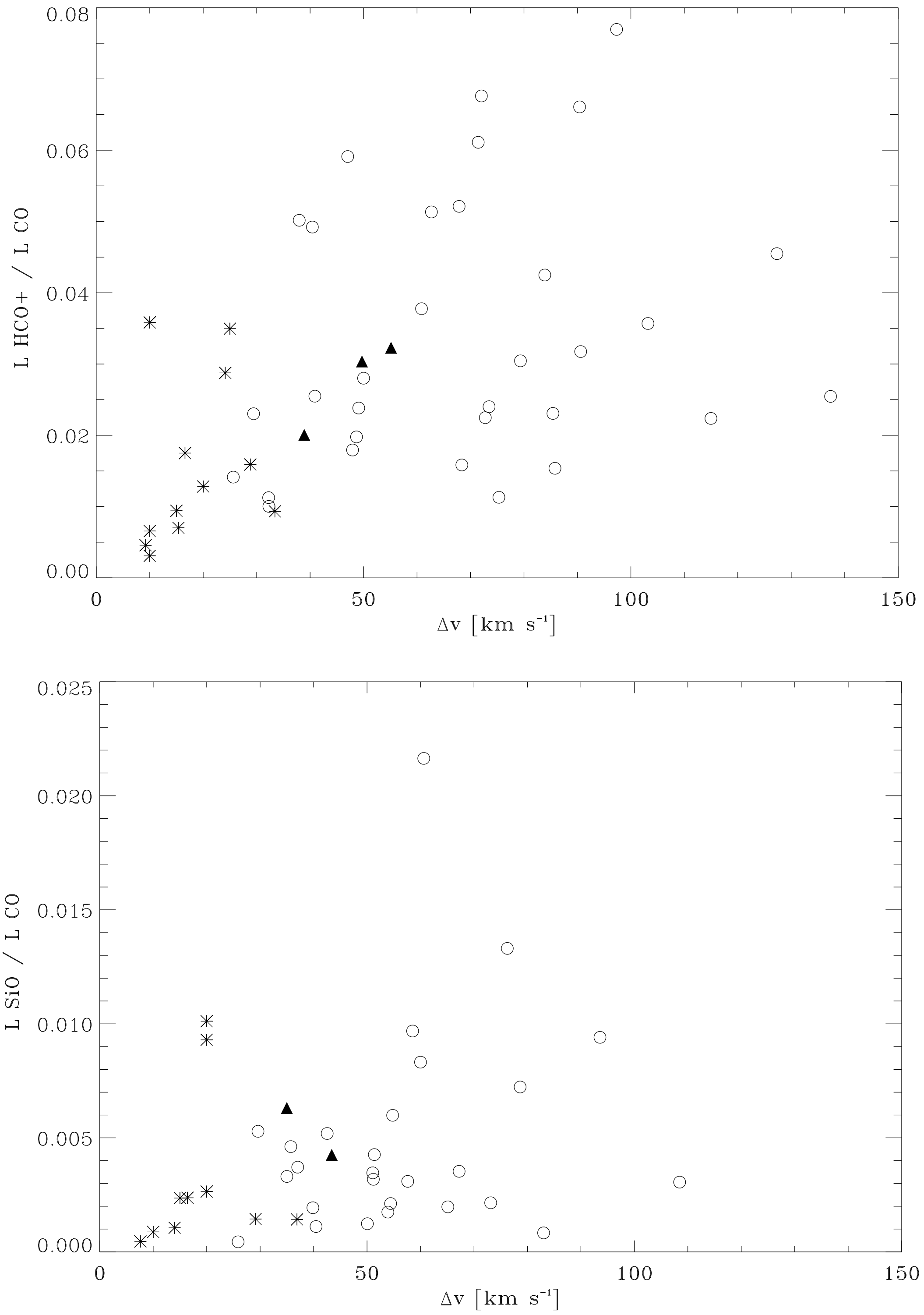

Fig. 10. Relationship between the luminosity ratio HCO^+ to CO (*top*) and the HCO^+ velocity width, and the luminosity ratio SiO to CO (*bottom*) and the SiO velocity width for each molecular cloud of the survey. Open circles denote Galactic center clouds, an asterisk the disk clouds, and filled triangles are clouds that probably are in an intermediate region, influenced by a bar, and that present large linewidth, probably due the strong Galactic center tidal forces in this region. There is a cloud (number 35 in SiO) with a large linewidth (~35 km s^{-1}) in the bottom plot. This cloud is also not considered in our analysis owing the poor fit (see Fig. E.8).

4.3. Comparison with previous work

As shown before, we can distinguish regions where either SiO or HCO^+ dominates. Roughly, in the CMZ at longitudes lower than $l \sim 0\fdg6$, HCO^+ dominates, and at longitudes $l > 0\fdg6$, SiO prevails, indicating shock. Nevertheless, we find clouds with an enhancement of SiO toward lower longitudes in the CMZ. For cloud 4 in Sgr A and cloud 7 in Sgr B, the SiO is also intense. In the PMZ, the clouds M+3.2+0.3, M+5.3−0.3, and M−3.8+0.9 show an enhancement of SiO, which is a clear signal of shocks.

The SiO abundance can be increased, e.g., as a consequence of cloud-cloud collisions, interactions with supernova remnants,

Table 4. Velocity components of each region with the longitude and latitude ranges used to defined different regions.

Zone	Region	Longitude [deg]	Latitude [deg]	Velocity center [km s^{-1}]				
				$v_{\rm LSR}$	$v_{\rm LSR}$	$v_{\rm LSR}$	$v_{\rm LSR}$	$v_{\rm LSR}$
CMZ	Sgr A	$-0.3125 < l < 0.3125$	$-0.5 < b < 0.5$	−76	−28^{a}	17	**61**	135
CMZ	Sgr B	$0.375 < l < 0.8125$	$-0.5 < b < 0.5$	−56	**42**	95	144	
CMZ	Sgr C	$-0.6875 < l < -0.375$	$-0.5 < b < 0.5$	−103	**−43**^{b}	22	132	
CMZ	Sgr D	$0.875 < l < 1.1875$	$-0.5625 < b < 0.5625$	−56	−10	27	**88**	180
CMZ	Sgr E	$-0.75 < l < -1.5$	$-0.5 < b < 0.5$	**−203**	−124	−31	17	131
CMZ	$1.^{\circ}3$ complex	$1.25 < l < 2.0$	$-0.5625 < b < 0.5625$	−22	**83**	178		
PMZ	M+3.2+0.3	$2.5625 < l < 3.5$	$-0.25 < b < 0.875$	32	**103**	159	219	
PMZ	M−5.3+0.4	$-5.75 < l < -4.75$	$-0.125 < b < 0.5625$	−78	−43	−21	5	**86**
PMZ	M−4.4+0.6	$-4.6875 < l < -4.3125$	$0.4375 < b < 0.8125$	−70	−45	−30	**71**	
PMZ	M−3.8+0.9	$-4.0 < l < -3.6875$	$0.5625 < b < 1.1875$	**−79**	−4	77	108	
PMZ	M+5.3−0.3	$5.125 < l < 5.5625$	$-0.6875 < b < 0.125$	−28	23	59	**98**	150

Notes. The velocity component are defined by HCO$^+$ Gaussian fits, see Appendix E. The main cloud is indicated in bold face. $^{(a)}$ Has 2 velocity components; $^{(b)}$ has 3 velocity components.

expanding bubbles, and large-scale dynamics in the Galactic center. The SiO predominance that we find in clouds 4 and 7 has been noted by other authors. Martín-Pintado et al. (1997) show that SiO emission is detected throughout the whole Galactic center region. They related the intense SiO emission that they found toward the Sgr A molecular complex (M−0.13−0.08 which is the 20 km s^{-1} cloud, M−0.02−0.07 which correspond to the 50 km s^{-1} cloud, and a condensation close to Sgr A*) to the interaction of the molecular clouds with nearby supernova remnants. Their SiO emission spots could correspond to our cloud number 4 in Sgr A region, but in our data they are blended because of our lower resolution (see Table 4). Minh et al. (1992) also found high abundances of SiO and HCO$^+$ toward Sgr A region, which indicate that shock chemistry and ion-molecule reactions are important in this region.

The enhancement of SiO that we found toward greater longitudes ($l > 0.^{\circ}6$ and in the PMZ) has been also reported by Hüttemeister et al. (1998). They performed multiline observations of the C^{18}O and also SiO isotopes in the Galactic center region toward 33 selected positions from the CS survey of Bally et al. (1987). All the sources were easily detected in SiO, where the higher abundances are found at $l > 0.^{\circ}8$. They found two regimens of densities and temperatures, one dense and cool, and other thin and hot, which are in pressure equilibrium, where the SiO emission arise in a cool, moderately dense component (Hüttemeister et al. 1998). The enhancement of the SiO emission was related to the large-scale gas dynamics in the Galactic center region where the movement of the gas can be understood as the response of a rapidly rotating bar potential (Binney et al. 1991), and the higher abundances of SiO can be identified with the collision region. This molecular cloud has also been studied by Tanaka et al. (2007). They identified 9 expanding shells with broad-velocity-width features in their HCN and HCO$^+$ maps and isolated SiO clouds that should be related to the expanding shells. They propose that the expanding shells may be in the early stage of supperbubble formation caused by massive cluster formation or continuous star formation $10^{6.8-7.6}$ years ago. Both Hüttemeister et al. (1998) and Martín-Pintado et al. (1997) observed a decrease of X(SiO) in the CMZ (between Sgr B2 and Sgr C, $-0.^{\circ}35 < l < 0.^{\circ}6$) with respect to higher longitudes ($l > 0.9$), which is also seen in our data. Figures A.6 and A.7 show that the SiO emission mainly comes from $l > 0.^{\circ}6$ and that HCO$^+$ emission is dominant in this region, which shows the densest zones where star formation is ongoing.

In this work we relate the SiO enhancement throughout the Galactic center region to the Giant molecular loops scenario proposed by Fukui et al. (2006). Fukui et al. (2006) observed an area of 240 square degrees toward $-12^{\circ} < l < 12^{\circ}$ and $-5^{\circ} < b < 5^{\circ}$ in ^{12}CO(1−0) using the NANTEN 4 m telescope from Nagoya University (the NANTEN Galactic plane survey, GPS). They find huge structures in loop shapes, and propose that there are "giant molecular loops" (huge loops of dense molecular gas with strong velocity dispersions) at the Galactic center, formed by a magnetic buoyancy caused by the Parker instability. The loops have two "foot points", one at each end, which are produced when the gas inside the loops flows down to the disk by stellar gravity and forms shock fronts above the disk. This scenario is supported by numerical simulations (Matsumoto et al. 1988; Machida et al. 2009; Takahashi et al. 2009) and by the broad velocity features of ~40 to 80 km s^{-1} observed by Fukui et al. (2006). The shocked regions detected in SiO in the present work are correlated with the foot points they found. The enhancement of SiO emission, in comparison with the HCO$^+$ emission that we found in the M−3.8+0.9 cloud (Figs. A.3, A.4), is correlated with the foot point of the loop 1 (toward $l \sim -4^{\circ}$ to -2°, in the velocity range from −180 to −90 km s^{-1}) and loop 2 (toward $l \sim -5^{\circ}$ to -4°, in the velocity range of −90 to −40 km s^{-1}). Those features are studied in detail by Torii et al. (2010b,a). The enhancement of SiO in M+3.2+0.3 and M+5.3−0.3 clouds are correlated with the foot point of the loop at positive longitudes, shown in the Fig. S6 on the "Supporting Online Material" in Fukui et al. (2006). This feature is placed at positive longitudes between $l \sim 3^{\circ}$ to 5°. The enhancement of SiO found toward $l \sim -1^{\circ}$ corresponds to the location of loop 3, which has recently been discovered by Fujishita et al. (2009). This loop is located toward $l \sim -5^{\circ}$ to -1° in the velocity range of 20 to 200 km s^{-1} (Fujishita et al. 2009). The coincidence of the enhancement of SiO to the HCO$^+$ in the "foot point", together with the high-velocity width of the clouds belonging to the Galactic center (see Table 3), support Fukui's scenario. This association will be addressed in more detail in a subsequent paper.

5. Conclusions

1. All of the species measured in this work, HCO$^+$, SiO, and H^{13}CO$^+$, have been detected throughout the Galactic center region. We find the characteristic asymmetry in longitude found for many other species, with most of the emission

toward $l > 0$ and $v > 0$. We identify 51 molecular clouds, where 33 belong to the Galactic center region and 18 to the Galactic disk or local gas.
2. The luminosity ratios SiO($J = 2 \rightarrow 1$)/CO($J = 1 \rightarrow 0$) and HCO^+($J = 1 \rightarrow 0$)/CO($J = 1 \rightarrow 0$), as well as the velocity widths, are higher for Galactic center clouds than for typical disk clouds. The highest SiO($J = 2 \rightarrow 1$)/CO($J = 1 \rightarrow 0$) luminosity ratios for the Galactic center region correspond, in general, to the highest velocity widths. The average of the luminosity ratio of SiO($J = 2 \rightarrow 1$)/CO($J = 1 \rightarrow 0$) in clouds belonging to the Galactic center region is 0.0049 ± 0.0005 and for disk clouds is 0.0034 ± 0.0009. The luminosity ratio of HCO^+($J = 1 \rightarrow 0$)/CO($J = 1 \rightarrow 0$) in the Galactic center is 0.035 ± 0.003, and for disk clouds is 0.015 ± 0.004.
3. The clouds M+3.2+0.3, M−3.8+0.9, M+5.3−0.3, and 1.3° complex show high SiO to HCO^+ ratios, which may indicate the importance of shocks as heating sources. Toward the densest regions, the SiO($J = 2 \rightarrow 1$)/HCO^+($J = 1 \rightarrow 0$) ratio is low (Sgr A and Sgr B regions).
4. The SiO emission can be correlated with several phenomena. The SiO predominance over the HCO^+ emission could be related to the molecular loops, formed by a Parker instability, where the shocks are ongoing.

Acknowledgements. We acknowledge support by the Chilean Center for Astrophysics FONDAP N 15010003 and by Center of Excellence in Astrophysics and Associated Technologies PFB 06. D.R. and R.M. were supported by DGI grant AYA 2008-06181-C02-02. We thank Fernando Olmos for help with the observations. We are grateful to the personnel and students from Nagoya University who supported observations at the telescope and keep the data reduction pack at Cerro Calán. We also want to thanks Jesús Martín-Pintado for helpful discussions. We thank the referee, Y. Fukui, and the editor of A&A, M. Walmsley, for valuable comments.

References

Bally, J., Stark, A. A., Wilson, R. W., & Henkel, C. 1987, ApJS, 65, 13
Bally, J., Stark, A. A., Wilson, R. W., & Henkel, C. 1988, ApJ, 324, 223
Bania, T. M. 1977, ApJ, 216, 381
Bania, T. M. 1980, ApJ, 242, 95
Bania, T. M. 1986, ApJ, 308, 868
Bania, T. M., Stark, A. A., & Heiligman, G. M. 1986, ApJ, 307, 350
Bayet, E., Viti, S., Williams, D. A., Rawlings, J. M. C., & Bell, T. 2009, ApJ, 696, 1466
Binney, J., Gerhard, O. E., Stark, A. A., Bally, J., & Uchida, K. I. 1991, MNRAS, 252, 210
Bitran, M. E. 1987, Ph.D. Thesis, University of Florida
Bitran, M., Alvarez, H., Bronfman, L., May, J., & Thaddeus, P. 1997, A&AS, 125, 99
Blitz, L., Binney, J., Lo, K. Y., Bally, J., & Ho, P. T. P. 1993, Nature, 361, 417
Botschwina, P., Horn, M., Flugge, J., & Seeger, S. 1993, J. Chem. Soc., Faraday Trans., 623, 2219
Boyce, P. J., & Cohen, R. J. 1994, A&AS, 107, 563
Burton, W. B., & Liszt, H. S. 1983, A&AS, 52, 63
Cox, P., & Laureijs, R. 1989, in The Center of the Galaxy, ed. M. Morris, IAU Symp, 136, 121
Dahmen, G., Hüttemeister, S., Wilson, T. L., et al. 1997, A&AS, 125, 1
Dahmen, G., Hüttemeister, S., Wilson, T. L., & Mauersberger, R. 1998, A&A, 331, 959
Dame, T. M., Elmegreen, B. G., Cohen, R. S., & Thaddeus, P. 1986, ApJ, 305, 892
Ferrière, K., Gillard, W., & Jean, P. 2007, A&A, 467, 611
Fujishita, M., Torii, K., Kudo, N., et al. 2009, PASJ, 61, 1039
Fukui, Y., Iguchi, T., Kaifu, N., et al. 1977, PASJ, 29, 643
Fukui, Y., Kaifu, N., Morimoto, M., & Miyaji, T. 1980, ApJ, 241, 147
Fukui, Y., Yamamoto, H., Fujishita, M., et al. 2006, Science, 314, 106
Handa, T., Omodaka, T., Nagayama, T., Bebe lahak, H., & Matsuyama, N. 2006, J. of Phys. Conf. Ser., 54, 42
Henkel, C., Mauersberger, R., Wiklind, T., et al. 1993, A&A, 268, L17
Hüttemeister, S., Wilson, T. L., Bania, T. M., & Martín-Pintado, J. 1993, A&A, 280, 255
Hüttemeister, S., Dahmen, G., Mauersberger, R., et al. 1998, A&A, 334, 646
Jackson, J. M., Heyer, M. H., Paglione, T. A. D., & Bolatto, A. D. 1996, ApJ, 456, L91
Jaffe, D. T., Plume, R., Evans, II, N. J., & Bally, J. 1996, in The Galactic Center, ed. R. Gredel, ASP Conf. Ser., 102, 16
Jiménez-Serra, I., Caselli, P., Tan, J. C., et al. 2010, MNRAS, 661
Krips, M., Neri, R., García-Burillo, S., et al. 2008, ApJ, 677, 262
Kutner, M. L., & Ulich, B. L. 1981, ApJ, 250, 341
Lee, C. W. 1996, ApJS, 105, 129
Linke, R. A., Stark, A. A., & Frerking, M. A. 1981, ApJ, 243, 147
Liszt, H. S. 2006, A&A, 447, 533
Loenen, A. F., Spaans, M., Baan, W. A., & Meijerink, R. 2008, A&A, 488, L5
Lovas, F. J., Johnson, D. R., & Snyder, L. E. 1979, ApJS, 41, 451
Machida, M., Matsumoto, R., Nozawa, S., et al. 2009, PASJ, 61, 411
Martín-Pintado, J., de Vicente, P., Fuente, A., & Planesas, P. 1997, ApJ, 482, L45
Martín-Pintado, J., de Vicente, P., Rodríguez-Fernández, N. J., Fuente, A., & Planesas, P. 2000, A&A, 356, L5
Matsumoto, R., Horiuchi, T., Shibata, K., & Hanawa, T. 1988, PASJ, 40, 171
Mauersberger, R., & Henkel, C. 1991, A&A, 245, 457
Mauersberger, R., & Bronfman, L. 1998, in Rev. Mod. Astron. 11, ed. R. E. Schielicke, 209
Minh, Y. C., Irvine, W. M., & Friberg, P. 1992, A&A, 258, 489
Morris, M., & Serabyn, E. 1996, ARA&A, 34, 645
Morris, M., Polish, N., Zuckerman, B., & Kaifu, N. 1983, AJ, 88, 1228
Nakagawa, T., Doi, Y., Yui, Y. Y., et al. 1995, ApJ, 455, L35
Nguyen, Q.-R., Jackson, J. M., Henkel, C., Truong, B., & Mauersberger, R. 1992, ApJ, 399, 521
Odenwald, S. F., & Fazio, G. G. 1984, ApJ, 283, 601
Oka, T., Hasegawa, T., Handa, T., Hayashi, M., & Sakamoto, S. 1996, ApJ, 460, 334
Oka, T., Hasegawa, T., Sato, F., et al. 2001, ApJ, 562, 348
Oka, T., Nagai, M., Kamegai, K., Tanaka, K., & Kuboi, N. 2007, PASJ, 59, 15
Raymonda, J. W., Muenter, J. S., & Klemperer, W. A. 1970, J. Chem. Phys., 52, 3458
Rodríguez-Fernández, N. J., Martín-Pintado, J., de Vicente, P., & Fuente, A. 2002, Ap&SS, 281, 331
Sawada, T., Hasegawa, T., Handa, T., et al. 2001, ApJS, 136, 189
Seaquist, E. R., & Frayer, D. T. 2000, ApJ, 540, 765
Takahashi, K., Nozawa, S., Matsumoto, R., et al. 2009, PASJ, 61, 957
Tanaka, K., Kamegai, K., Nagai, M., & Oka, T. 2007, PASJ, 59, 323
Torii, K., Kudo, N., Fujishita, M., et al. 2010a, PASP, 62, 675
Torii, K., Kudo, N., Fujishita, M., et al. 2010b, PASJ, 62, 1307
Williams, J. P., de Geus, E. J., & Blitz, L. 1994, ApJ, 428, 693
Wilson, T. L., & Matteucci, F. 1992, A&A Rev., 4, 1
Wilson, T. L., Rohlfs, K., & Hüttemeister, S. 2009, Tools of Radio Astronomy, ed. T. L. Wilson, K. Rohlfs, S. Hüttemeister (Springer-Verlag)
Ziurys, L. M., Wilson, T. L., & Mauersberger, R. 1990, ApJ, 356, L25
Zylka, R., Güsten, R., Henkel, C., & Batrla, W. 1992, A&AS, 96, 525

Appendix A: Complementary figures

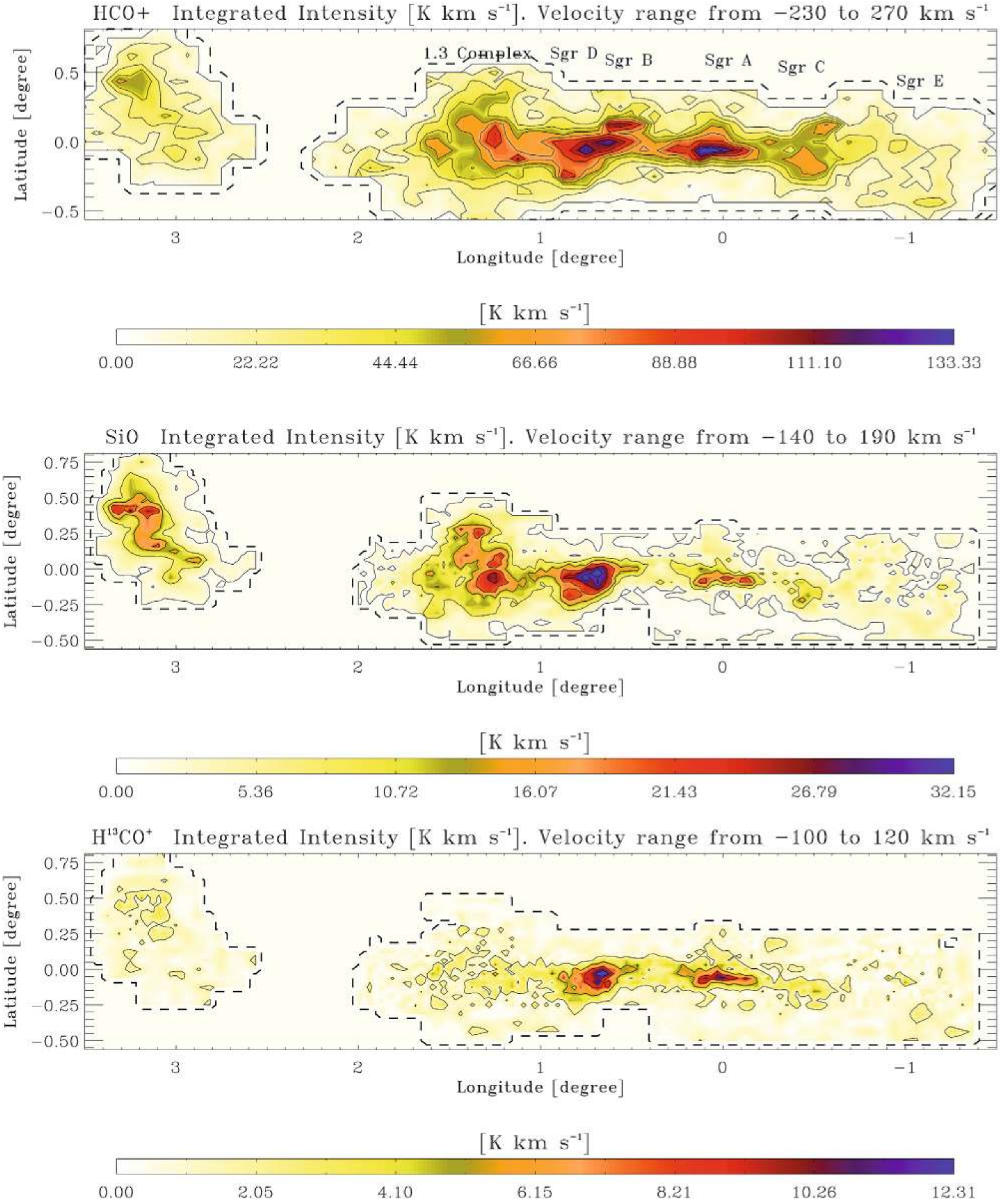

Fig. A.1. *Top*: emission from the CMZ and M+3.2+0.3 integrated over velocity from −230 to 270 km s^{-1}. This plot shows the more northerly part of the CMZ in more detail and includes source names. The solid contour levels start at 1.9 K km s^{-1} (3σ) and increase in steps of 12.53 K km s^{-1} (20σ). *Middle*: emission integrated over the velocity range listed above this plot in SiO. The solid contours start at 1.09 K km s^{-1} (3σ) and increase in steps of 5.46 K km s^{-1} (10σ). *Bottom*: emission from the CMZ and M+3.2+0.3 integrated over the velocity range listed above this plot in $H^{13}CO^+$. The solid contours start at 0.89 K km s^{-1} (3σ) and increase in steps of 2.97 K km s^{-1} (10σ). In all plot, the dashed line show the coverage of the survey in each molecule.

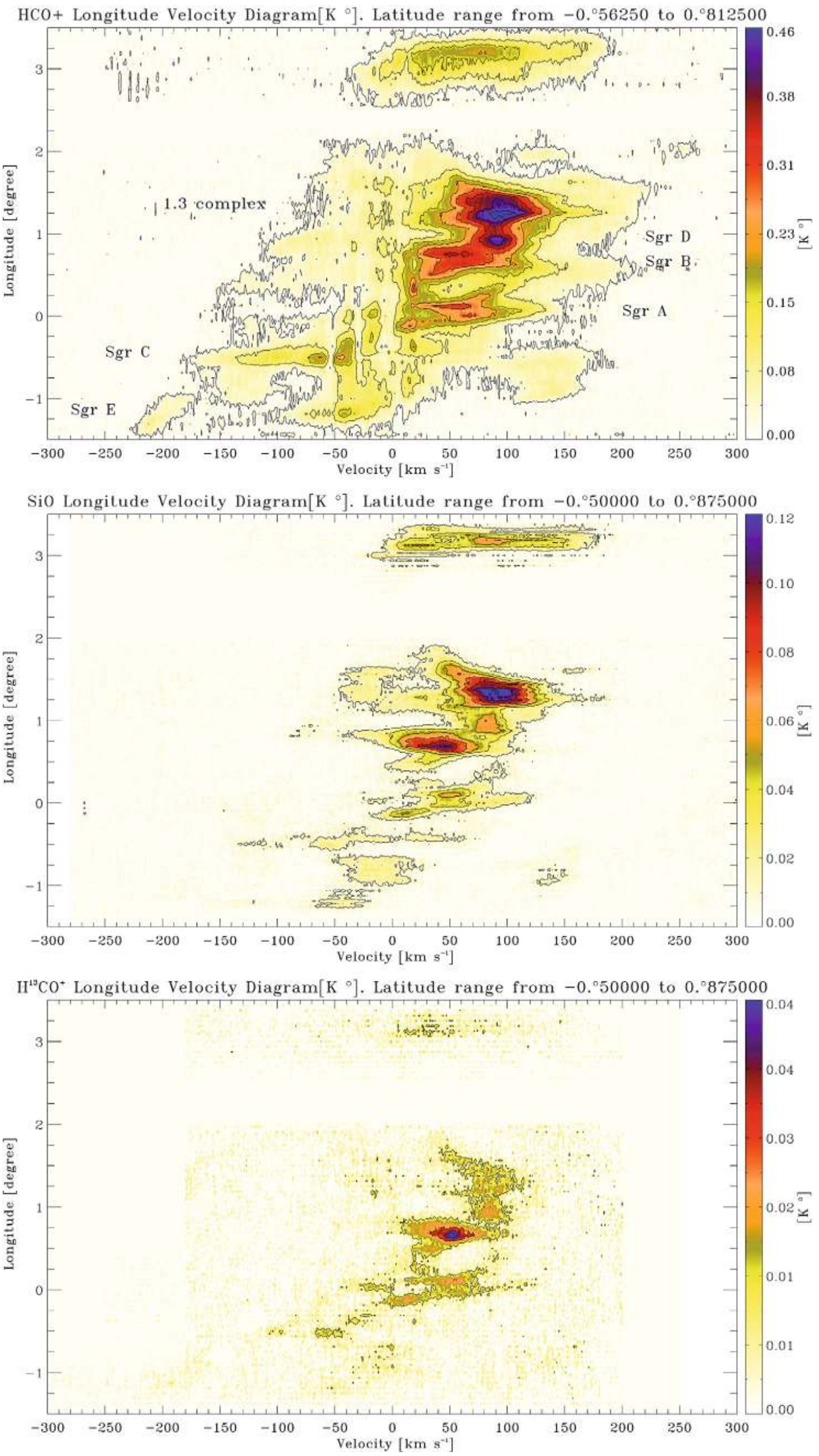

Fig. A.2. *Top*: longitude-velocity diagram of HCO$^+$ emission in the CMZ and M+3.2+0.3 in the latitude range between $b = -0\overset{\circ}{.}5625$ to $b = 0\overset{\circ}{.}8125$. The contour levels start at 0.021 K (3σ) and increase in steps of 0.058 K (8σ). *Middle*: longitude-velocity diagram of SiO emission in the CMZ and M+3.2+0.3 in the latitude range between $b = -0\overset{\circ}{.}5$ to $b = 0\overset{\circ}{.}875$. The contour levels start at 0.01 K (3σ) and increase in steps of 0.018 K (5σ). *Bottom*: longitude-velocity diagram of H^{13}CO$^+$ emission in the CMZ and M+3.2+0.3 in the latitude range between $b = -0\overset{\circ}{.}5$ to $b = 0\overset{\circ}{.}875$. The contour levels start at 0.009 K (3σ) and increase in steps of 0.016 K (5σ).

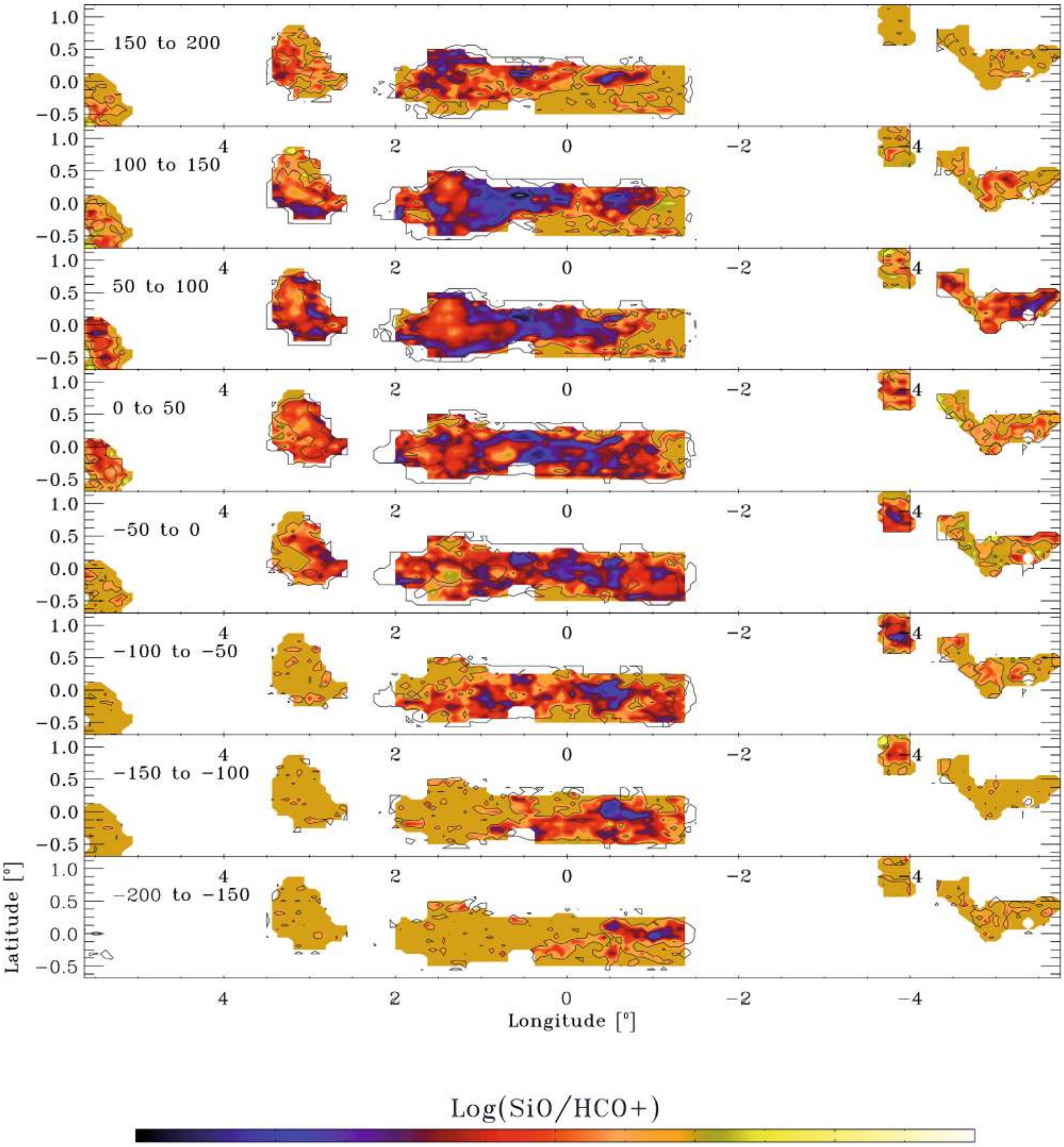

Fig. A.3. Spatial comparison in channel maps of $\log(\int T(\mathrm{SiO})\mathrm{d}v/\int T(\mathrm{HCO^+})\mathrm{d}v)$. The velocity intervals are indicated in each frame. The contours correspond to the $\mathrm{HCO^+}$ emission at 3σ and 30σ. We can identify clearly regions where either the SiO (e.g. in the 1.3 complex and in the M+3.2+0.3 cloud) or $\mathrm{HCO^+}$ (e.g. towards Sgr A region) dominate.

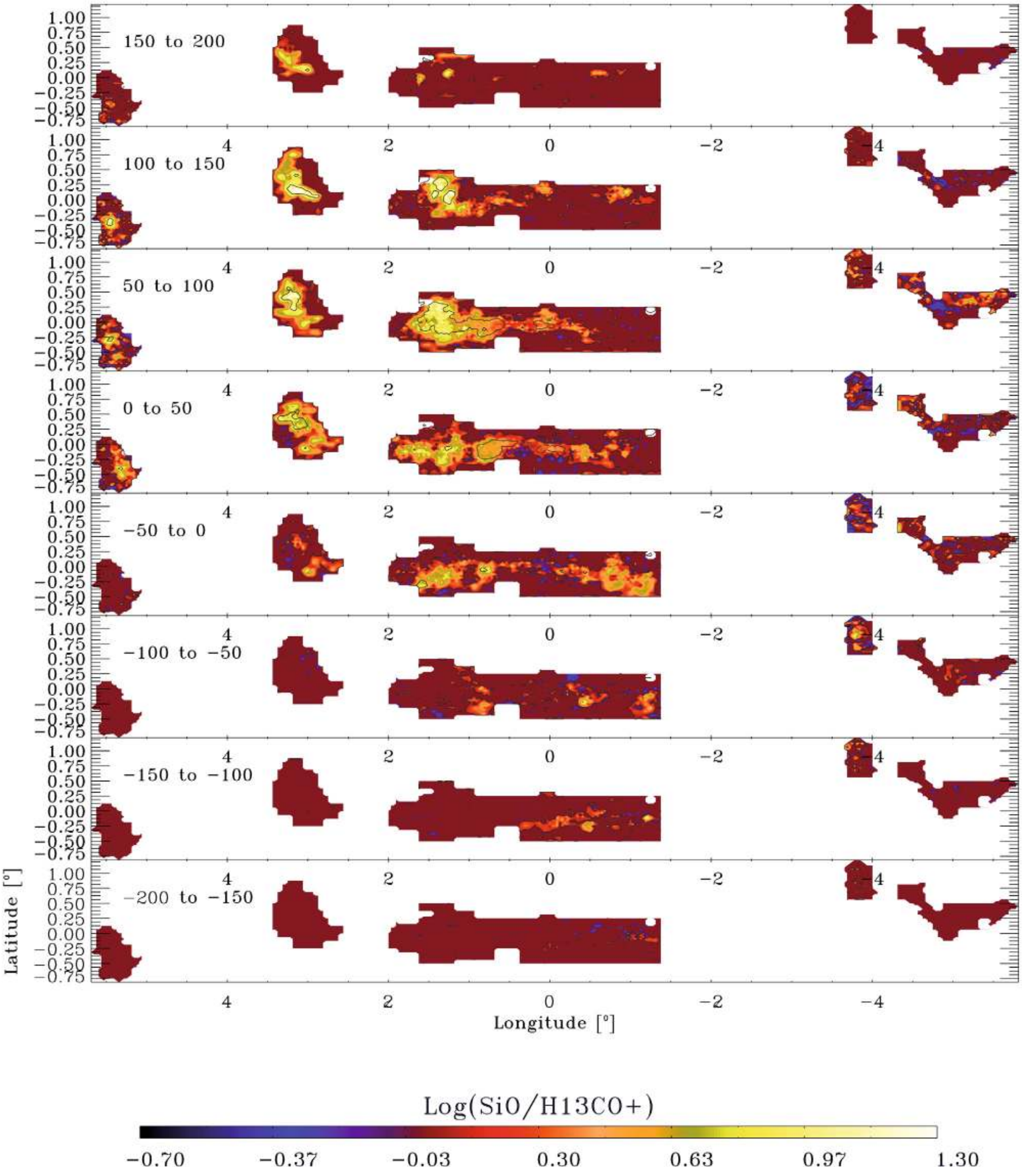

Fig. A.4. Spatial comparison in channel maps of $\log(\int T(\mathrm{SiO})\mathrm{d}v/\int T(\mathrm{H^{13}CO^+})\mathrm{d}v)$. The velocity intervals are indicated in each frame. The contours correspond to the SiO emission at 3σ and 30σ.

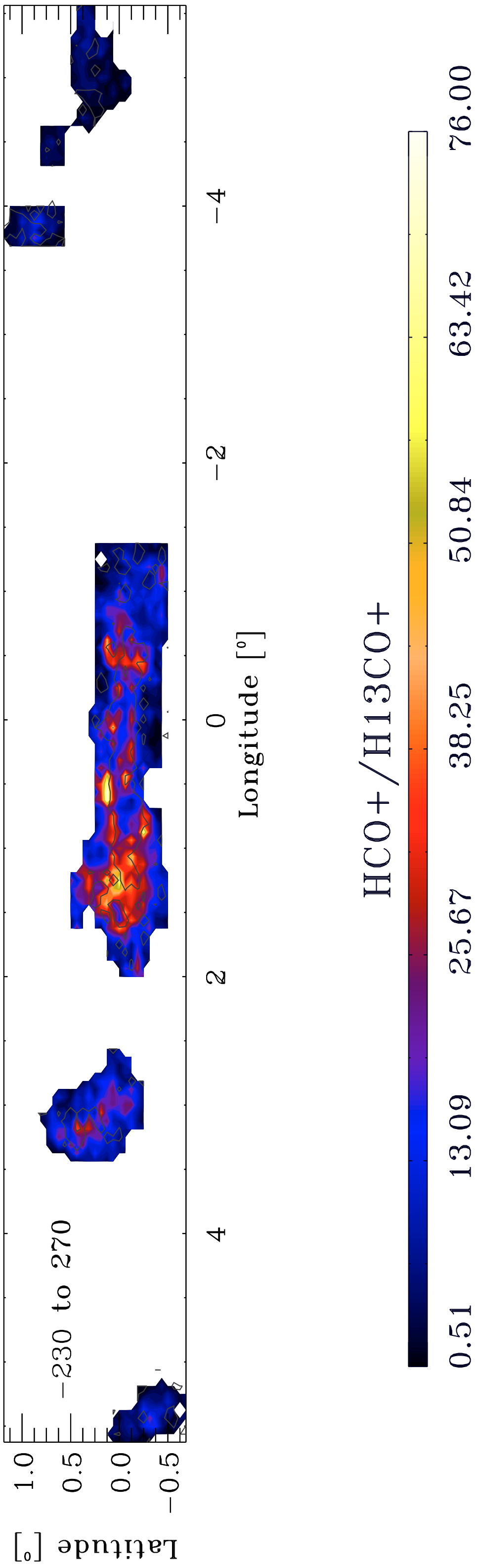

Fig. A.5. Spatial comparison of $\int T(\mathrm{HCO^+})\mathrm{d}v / \int T(\mathrm{H^{13}CO^+})\mathrm{d}v)$ in the velocity range from −230 to 270 km s^{-1}. The line intensity ratio typically range from 10 to 30 whith an average of 19.8.

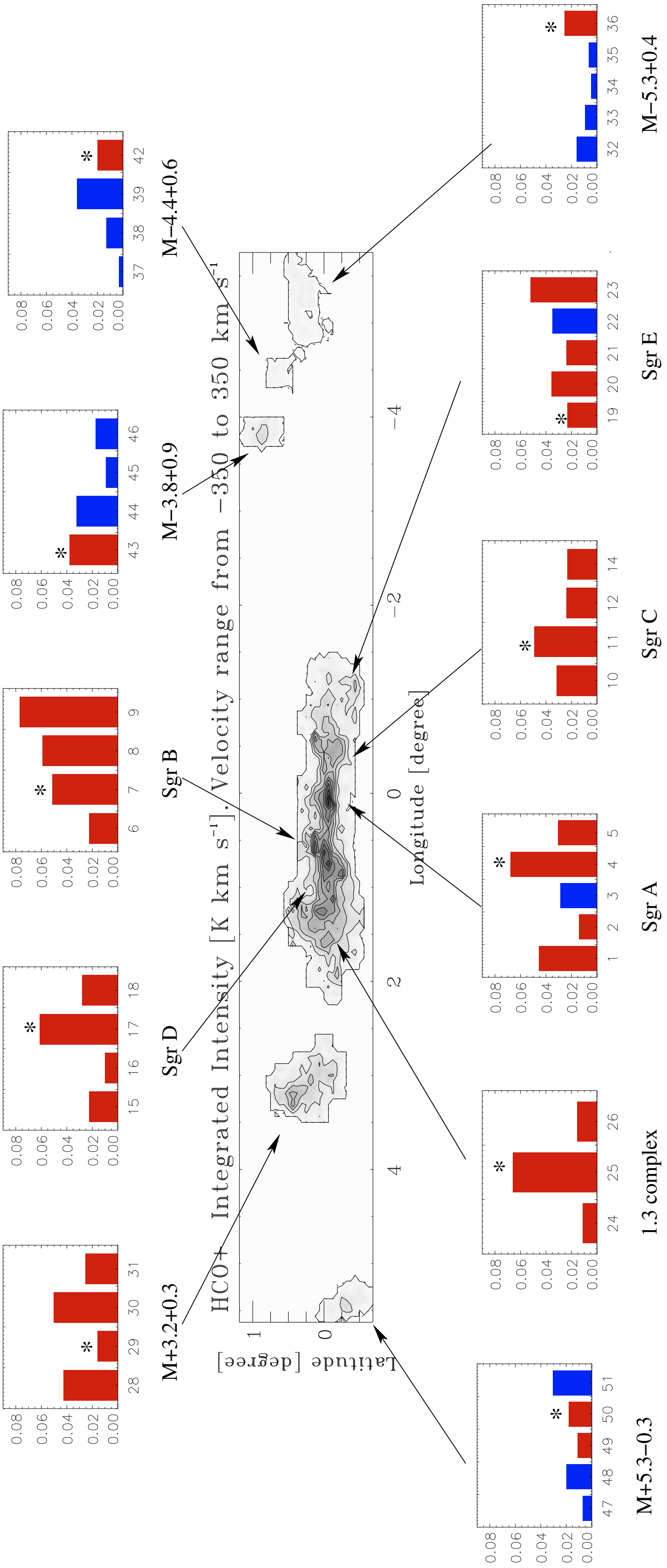

Fig. A.6. Luminosity ratio of HCO$^+$ to CO for each molecular complex. We show one plot for each region. The *x*-labels indicate the number of each velocity componet as defined by Gaussian fit (see Table 3). The main component is indicated by an asterisk. In blue we show the luminosity ratio for disk clouds and in red we show the luminosity ratio for Galactic center clouds. Each region is located in the HCO$^+$ integrated intensity map with an arrow. The highest intensities ratio belong to the Galactic center cloud (for example in Sgr B region).

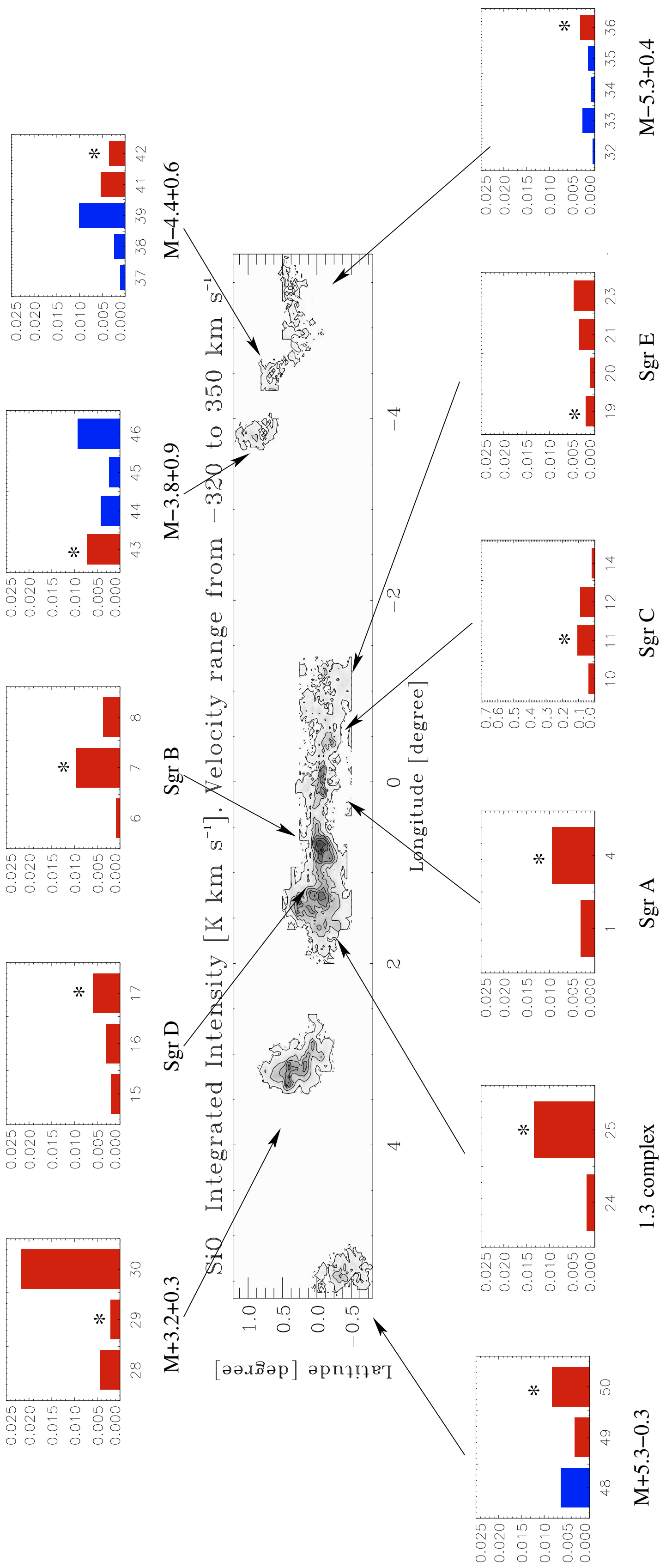

Fig. A.7. Same as Fig. A.6, but for the luminosity ratio of SiO to CO for each molecular complex. We show one plot for each region. The *x*-labels indicate the number of each velocity componet as defined by Gaussian fit (see Table 3). The main component is indicated by an asterisk. In blue we show the luminosity ratio for disk clouds and in red we show the luminosity ratio for Galactic center clouds. The ubication of each region is shown in the SiO integrated intensity map with an arrow. The highest intensities ratio are placed at $l > 1°$.

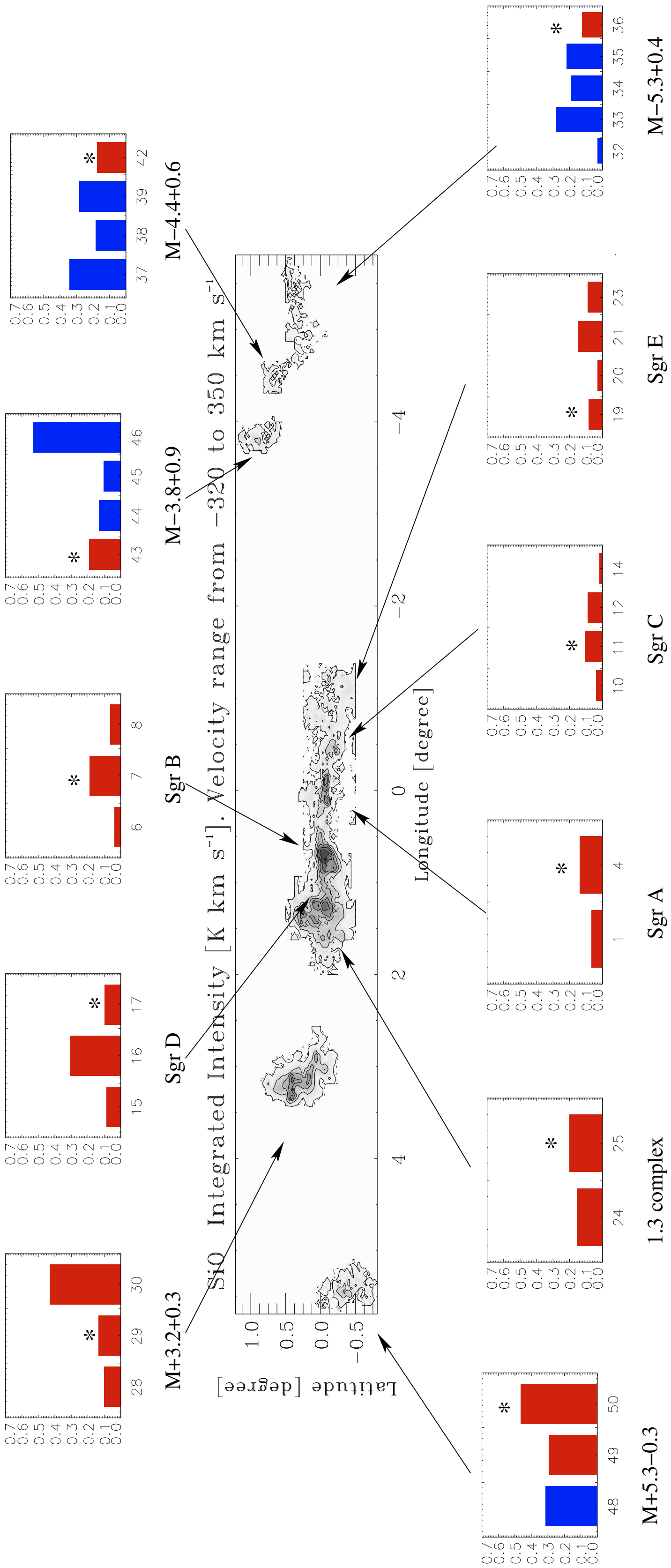

Fig. A.8. Same as Fig. A.6, but for SiO to HCO$^+$ luminosity ratio for each molecular complex. We show one plot for each region. The x-labels indicate the number of each velocity componet as defined by Gaussian fit (see Appendix E). The main component is indicated by an asterisk. In blue we show the luminosity ratio for disk clouds and in red we show the luminosity ratio for Galactic center clouds. Each region is located in the SiO integrated intensity map with an arrow.

Appendix B: HCO$^+$ Galactic center survey

This Appendix presents the HCO$^+$ data. In Fig. B.1, we show the channel maps of the HCO$^+$ emission in the Galactic center region integrated over velocity channels of 10 km s^{-1}. The maps at negative velocities range, show emission coming from Sgr C complex at $l < 0$. M−3.8+0.9 is the only molecular complex observed at negative longitude. Other clouds at negative longitudes are barely detectable with 5σ. In the −60 to 60 km s^{-1} range, the emission is contaminated by spiral arms in absorption. The molecular complexes Sgr A, Sgr B, Sgr D, and the 1$^\circ\!\!.$3 complex, the M+5.3−0.3 cloud and M+3.2+0.3 cloud are visible. At greater velocities, Sgr A, Sgr B. M+3.2+0.3, M−5.3+0.4, M−4.4+0.6 and M+5.3−0.3 show a very intense emission.

In Fig. B.2, we present $l - v$ diagrams for each observed latitude. We show 31 maps covering $b = -0^\circ\!\!.6875$ to $b = 1^\circ\!\!.1875$ with an spacing of 0$^\circ\!\!.$0625. We can clearly see in 0 km s^{-1} the emission from the local gas emission superimpose to the Galactic center emission. The local gas components are shown in Fig. B2.2 as a narrow emission (~5−10 km s^{-1}) while the Galactic center emission is characterized by broad velocity widh lines ($\gtrsim$50 km s^{-1}).

Figure B.3 shows a set of latitude-velocity diagram for each observed longitude. The contours levels start at 0.0021 K (3σ) and increase them in step of 0.0042 K (6σ).

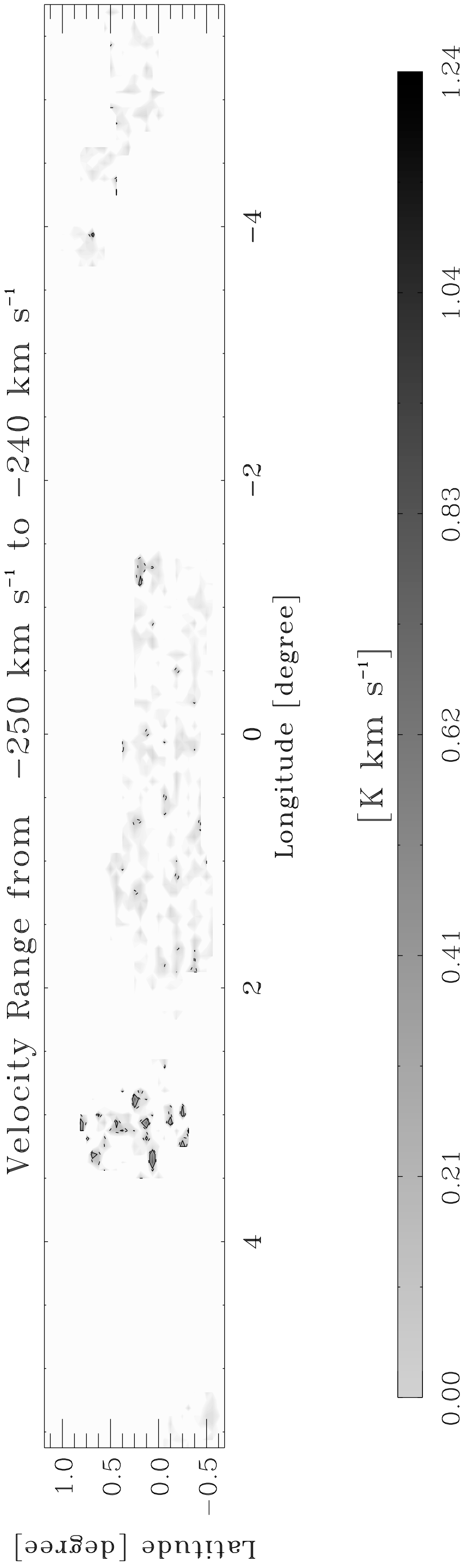

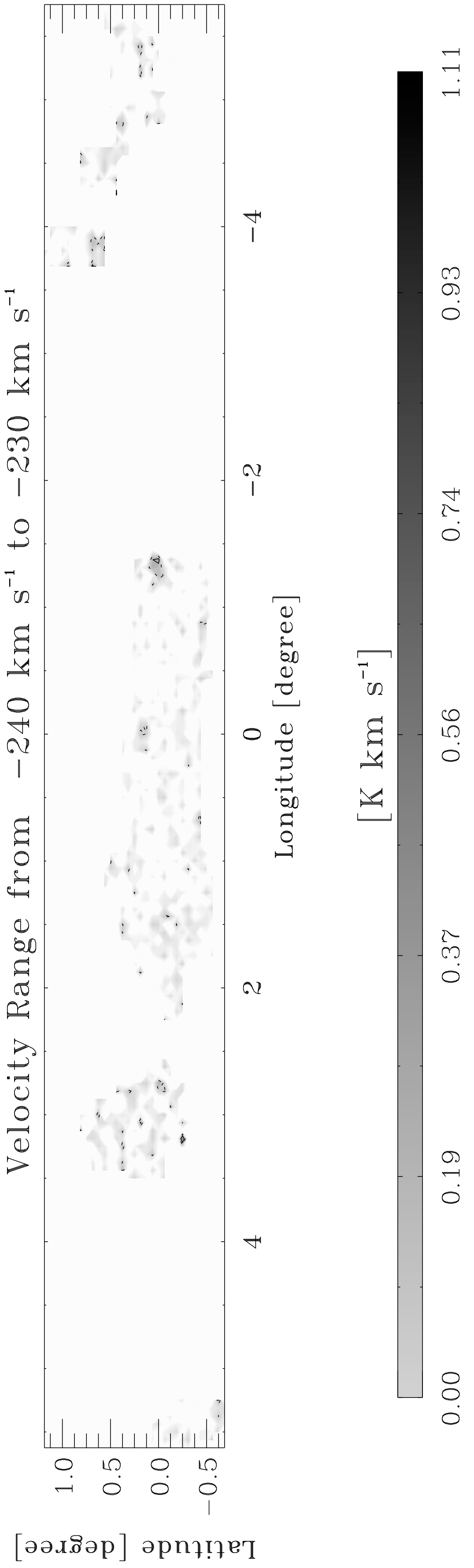

Fig. B1.1. The integrated intensity of the Galactic center region in HCO$^+$ (1−0) in velocity intervals of 10 km s^{-1} width. The solid contour levels start at 0.46 K km s^{-1}, which is the 5σ-level, and increase in steps of 1.4 K km s^{-1} (15σ). The dotted contours is at 0.28 K km s^{-1} (3σ).

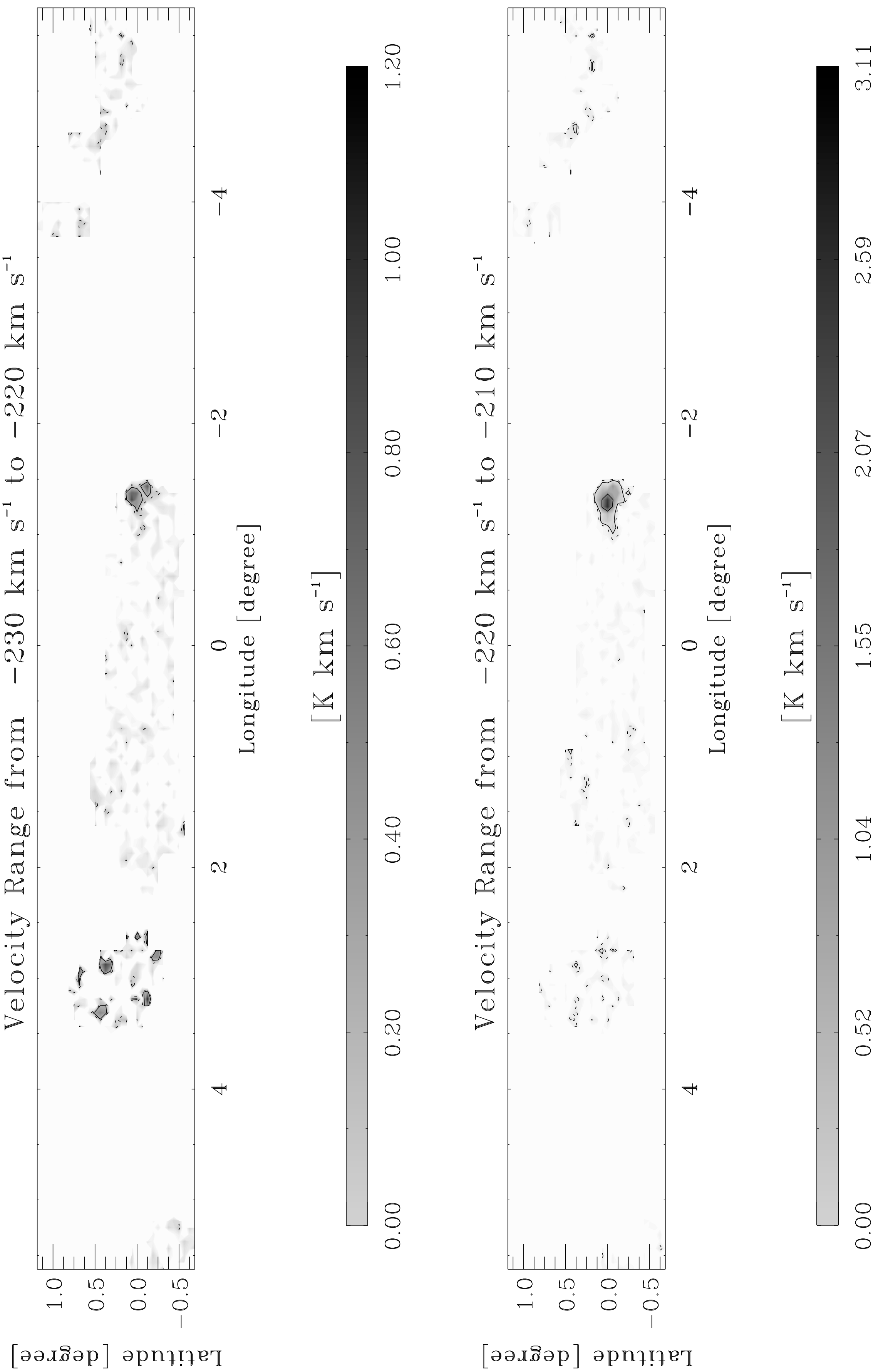

Fig. B1.2. continued.

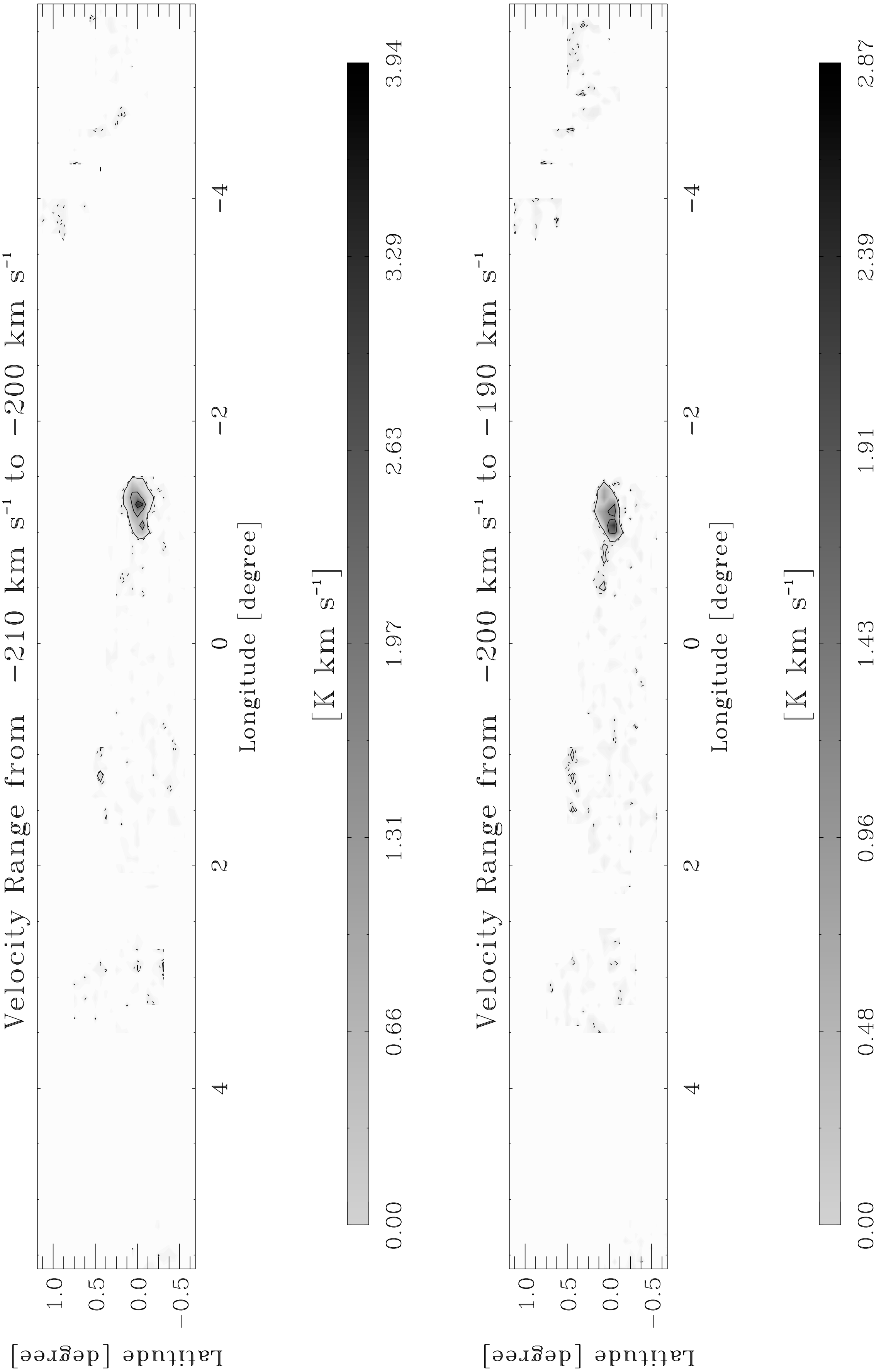

Fig. B1.3. continued.

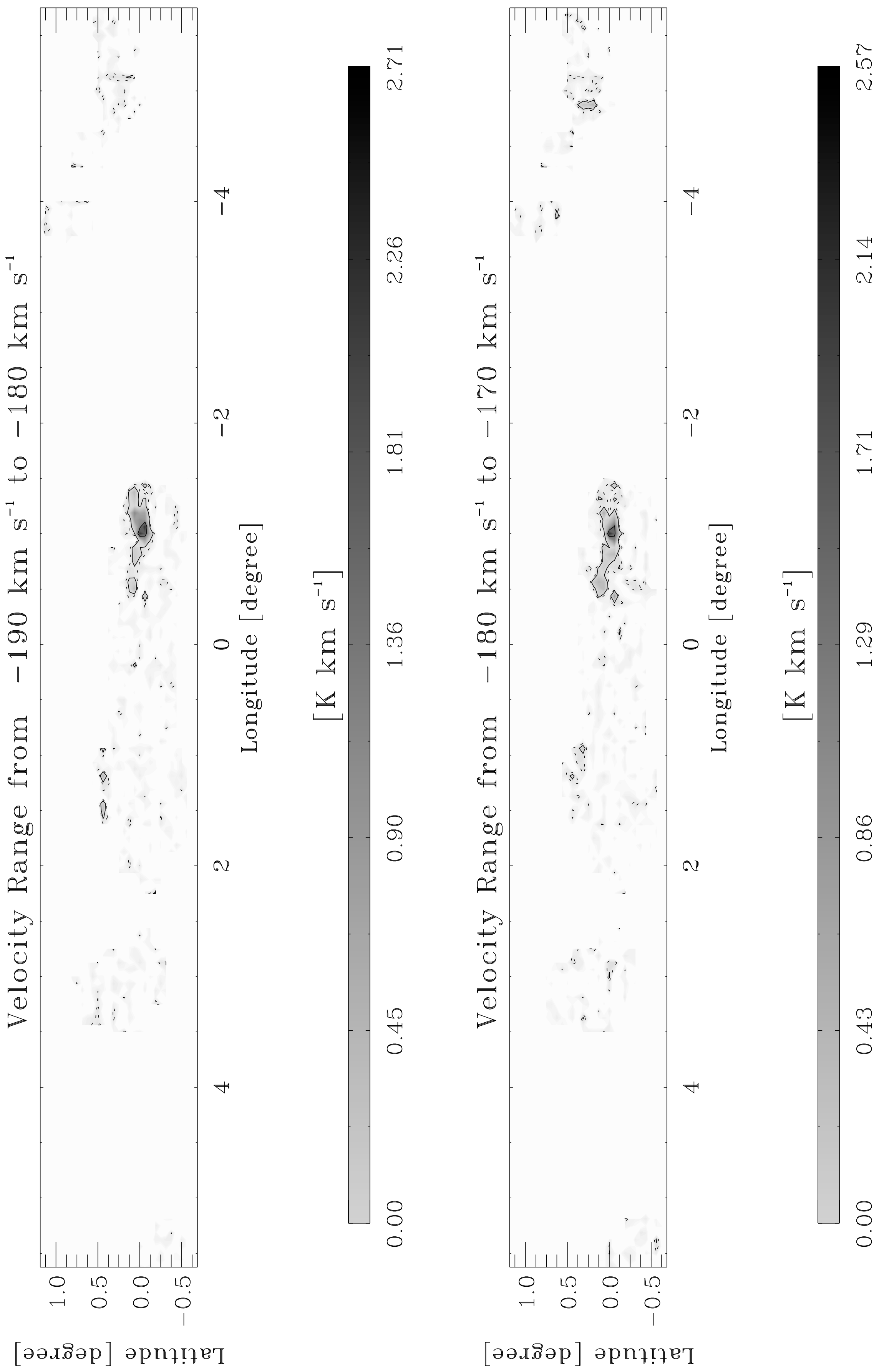

Fig. B1.4. continued.

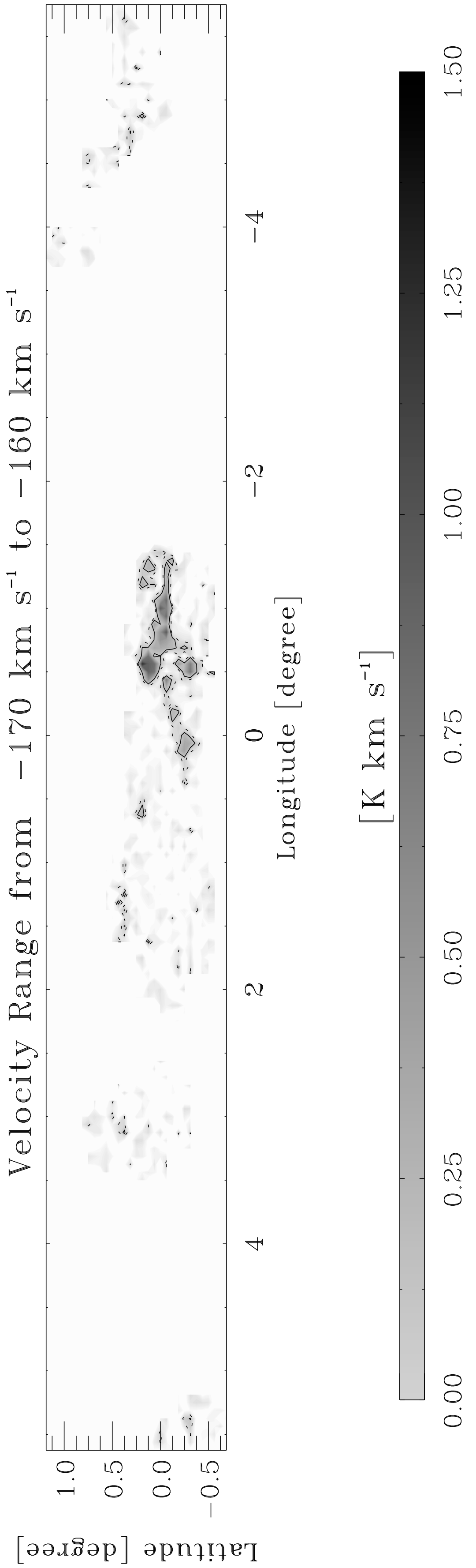

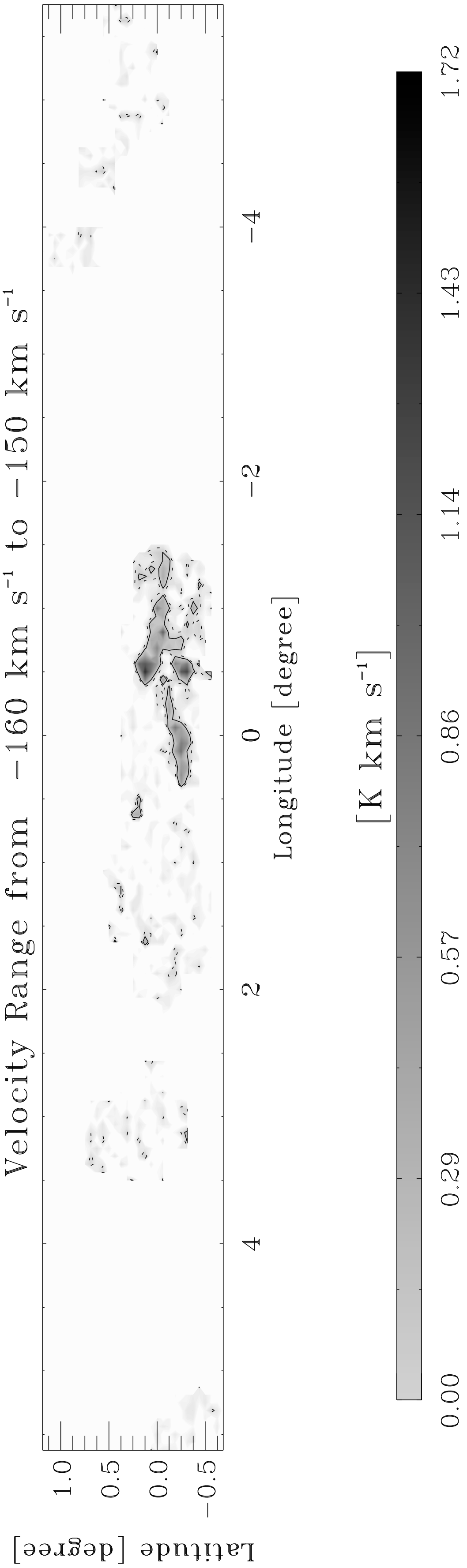

Fig. B1.5. continued.

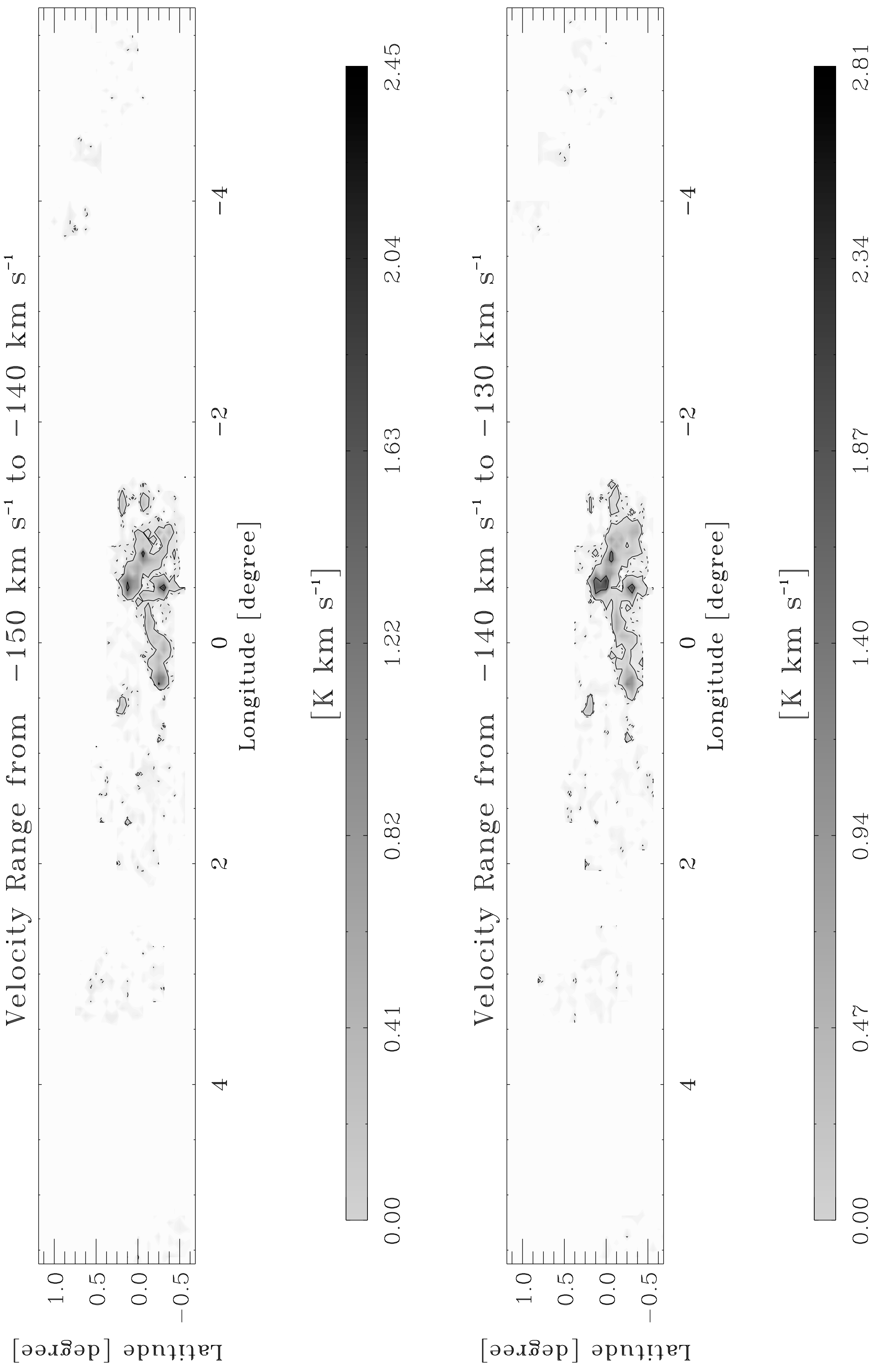

Fig. B1.6. continued.

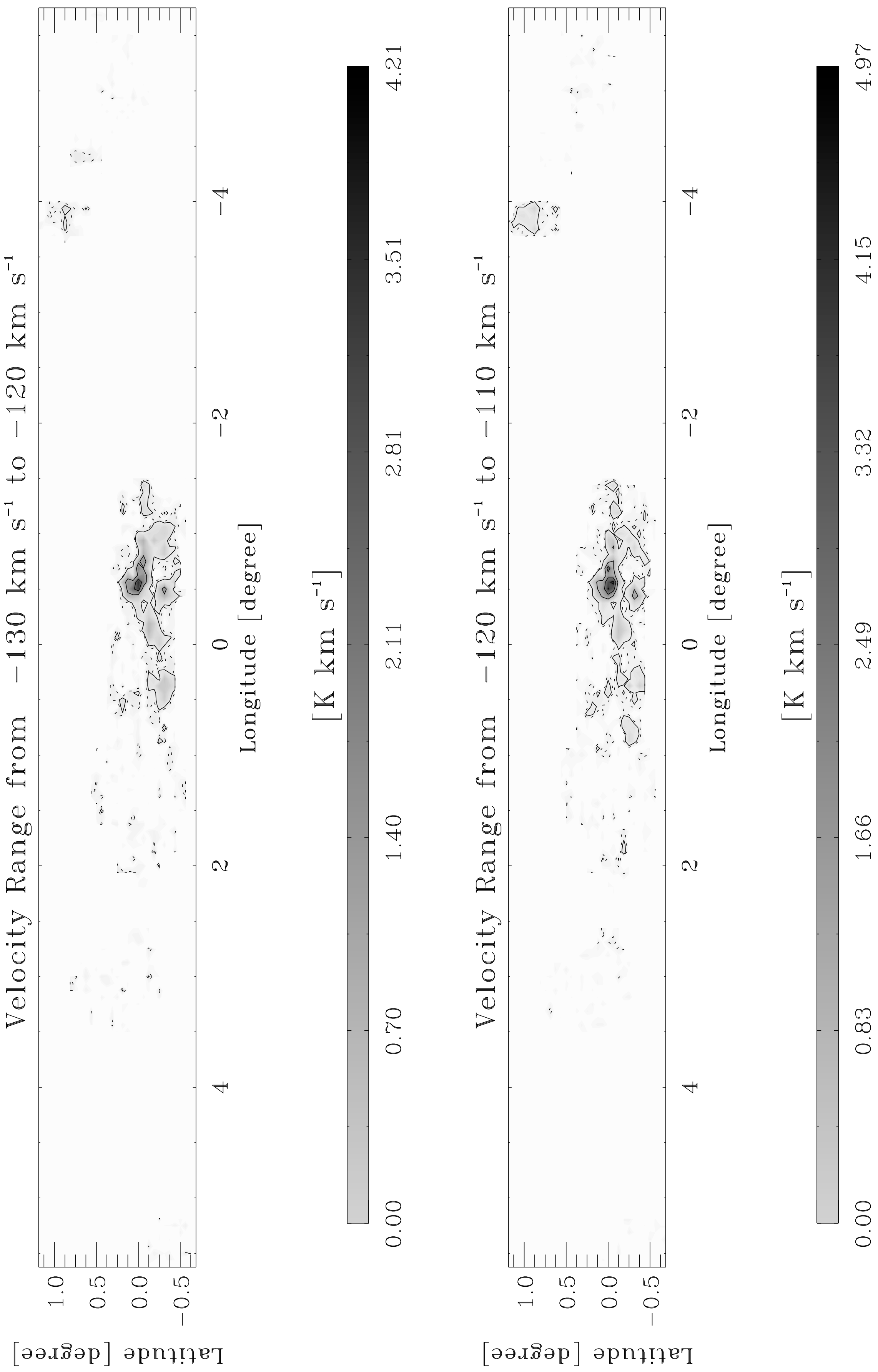

Fig. B1.7. continued.

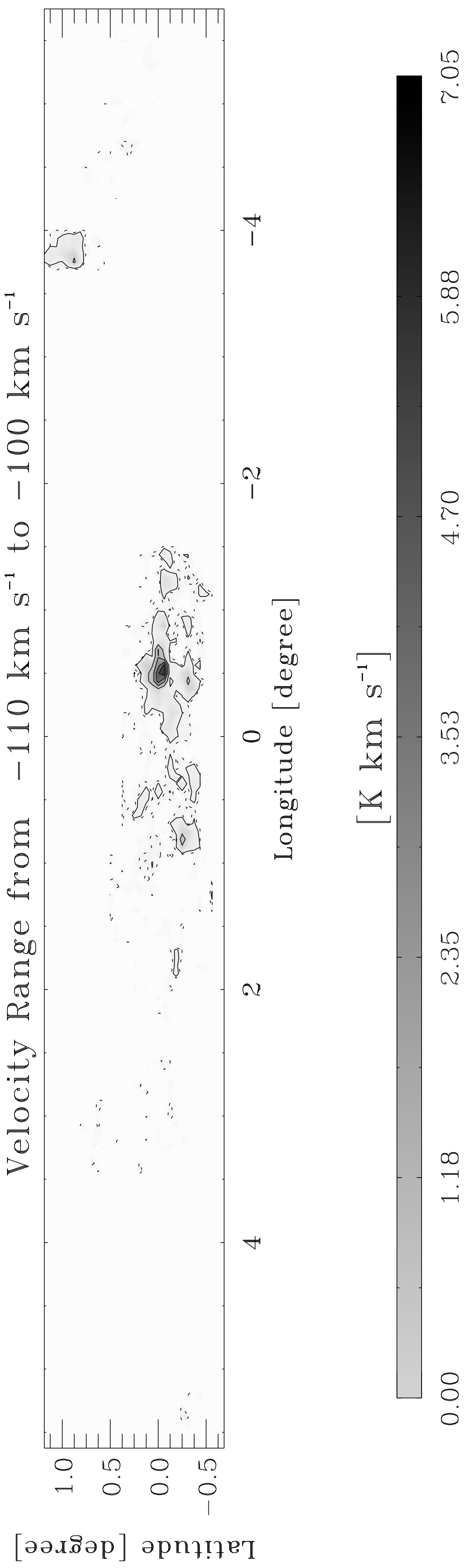

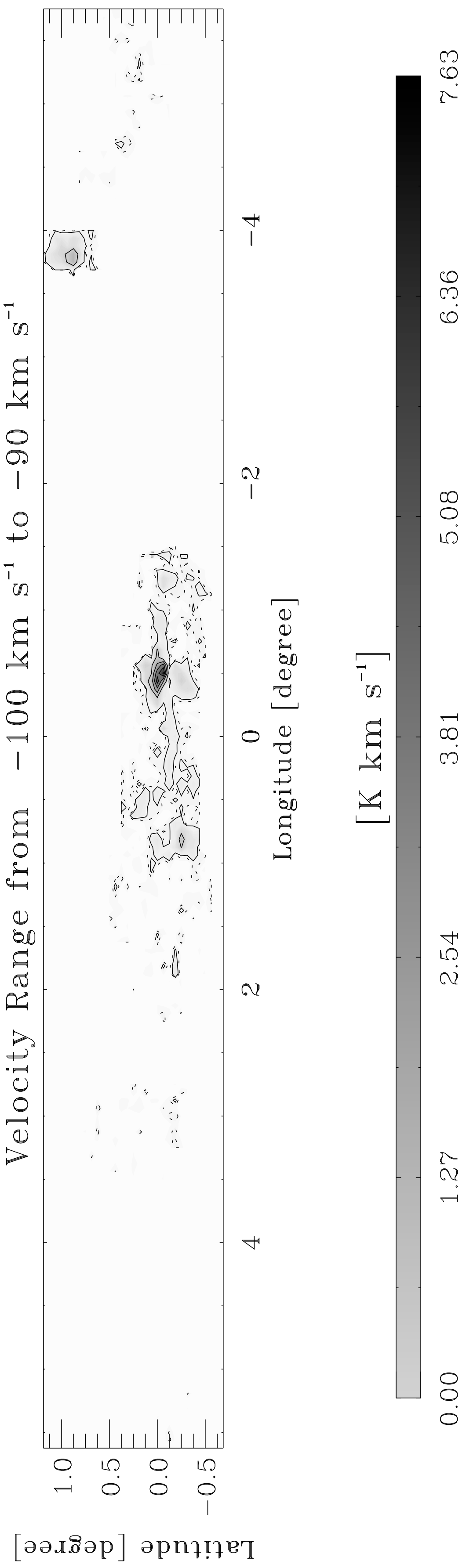

Fig. B1.8. continued.

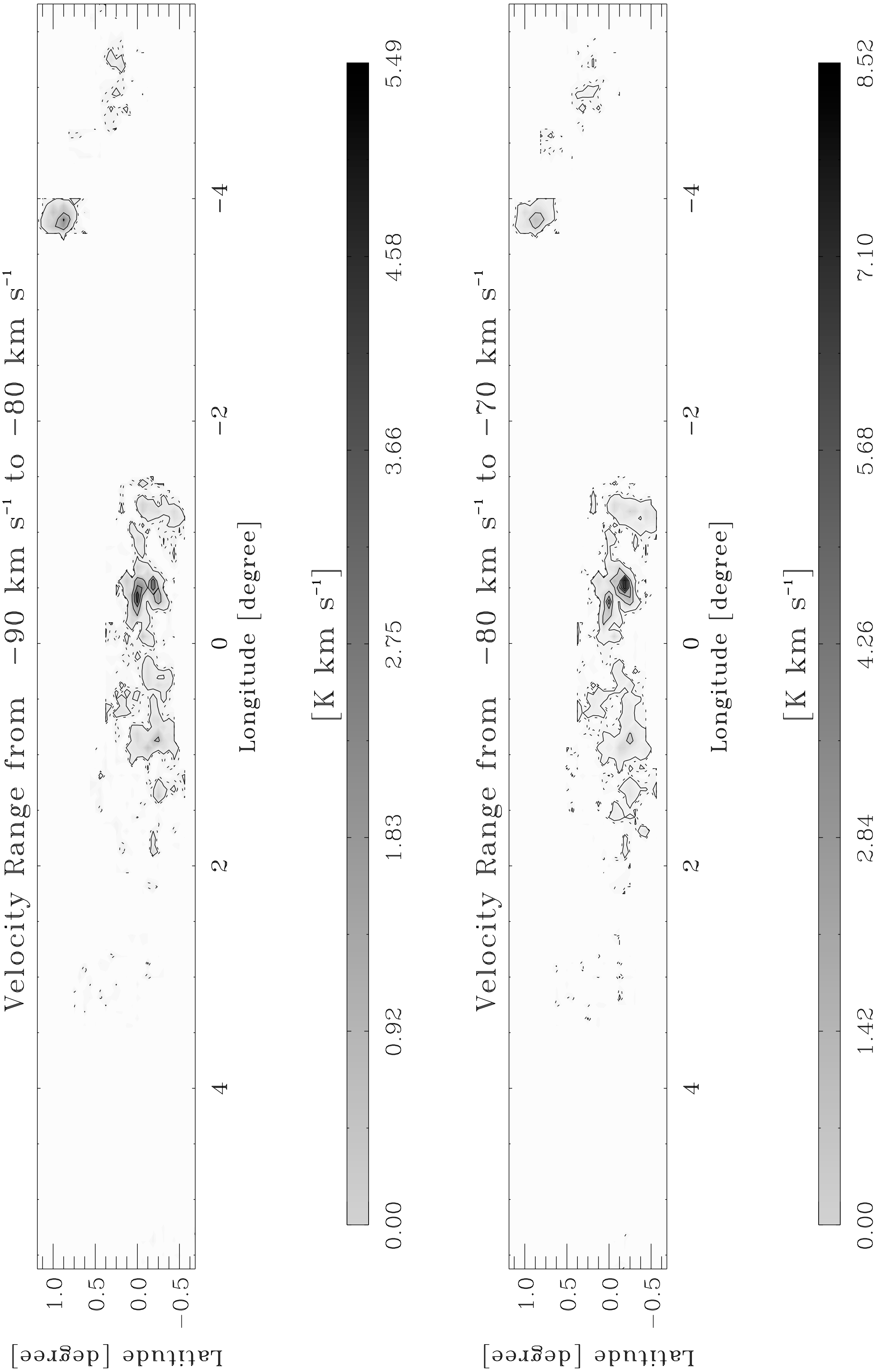

Fig. B1.9. continued.

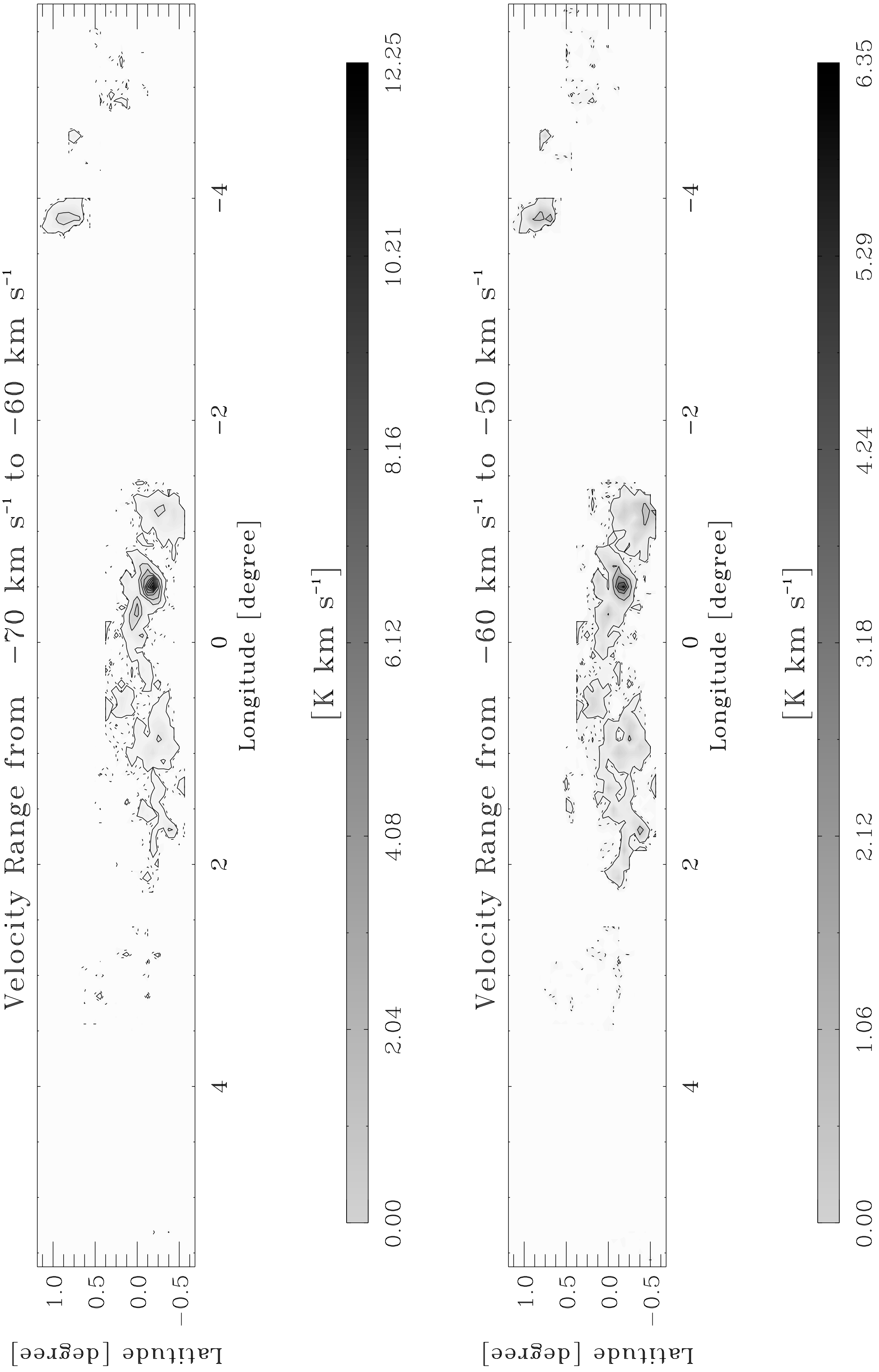

Fig. B1.10. continued.

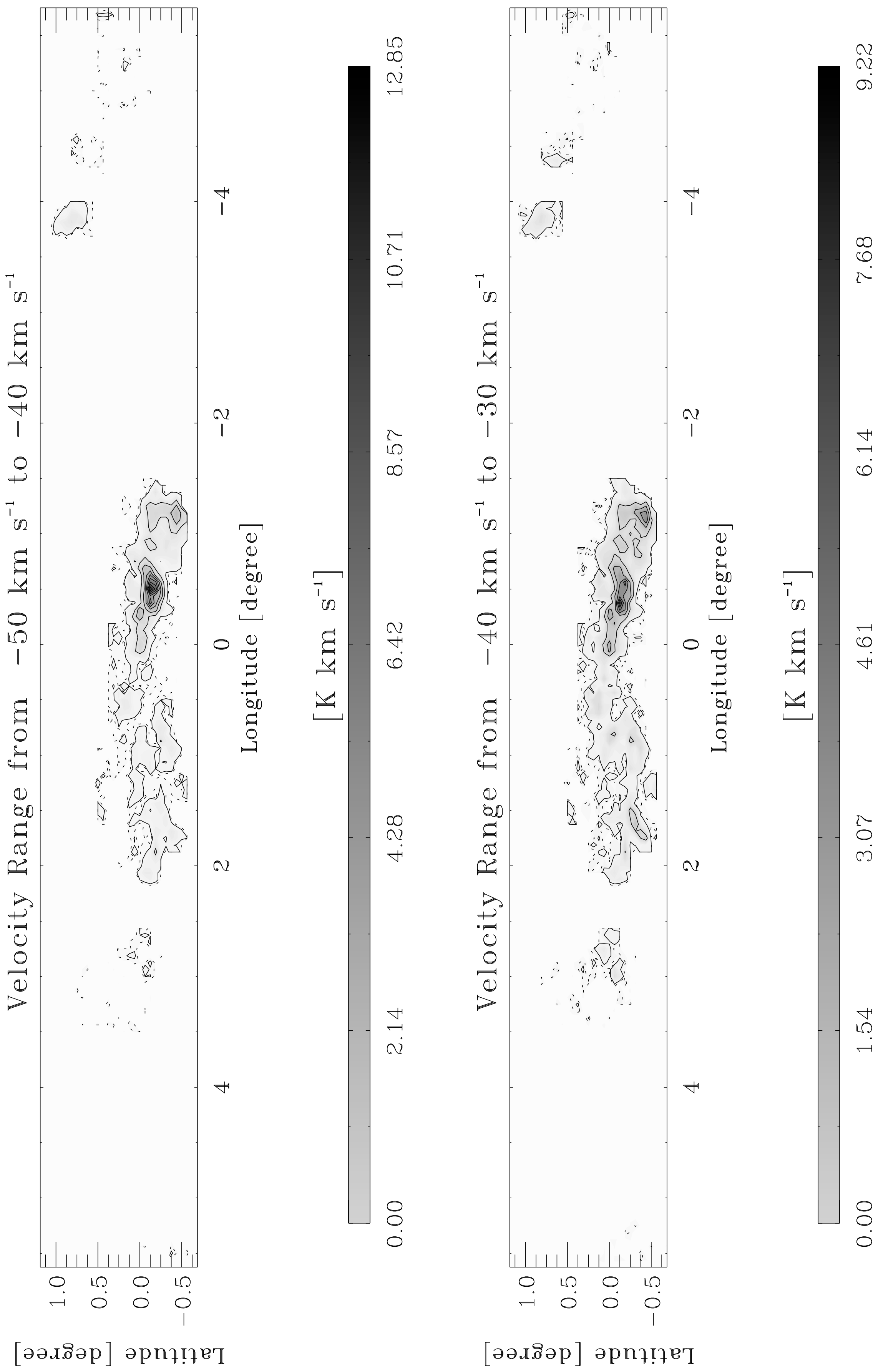

Fig. B1.11. continued.

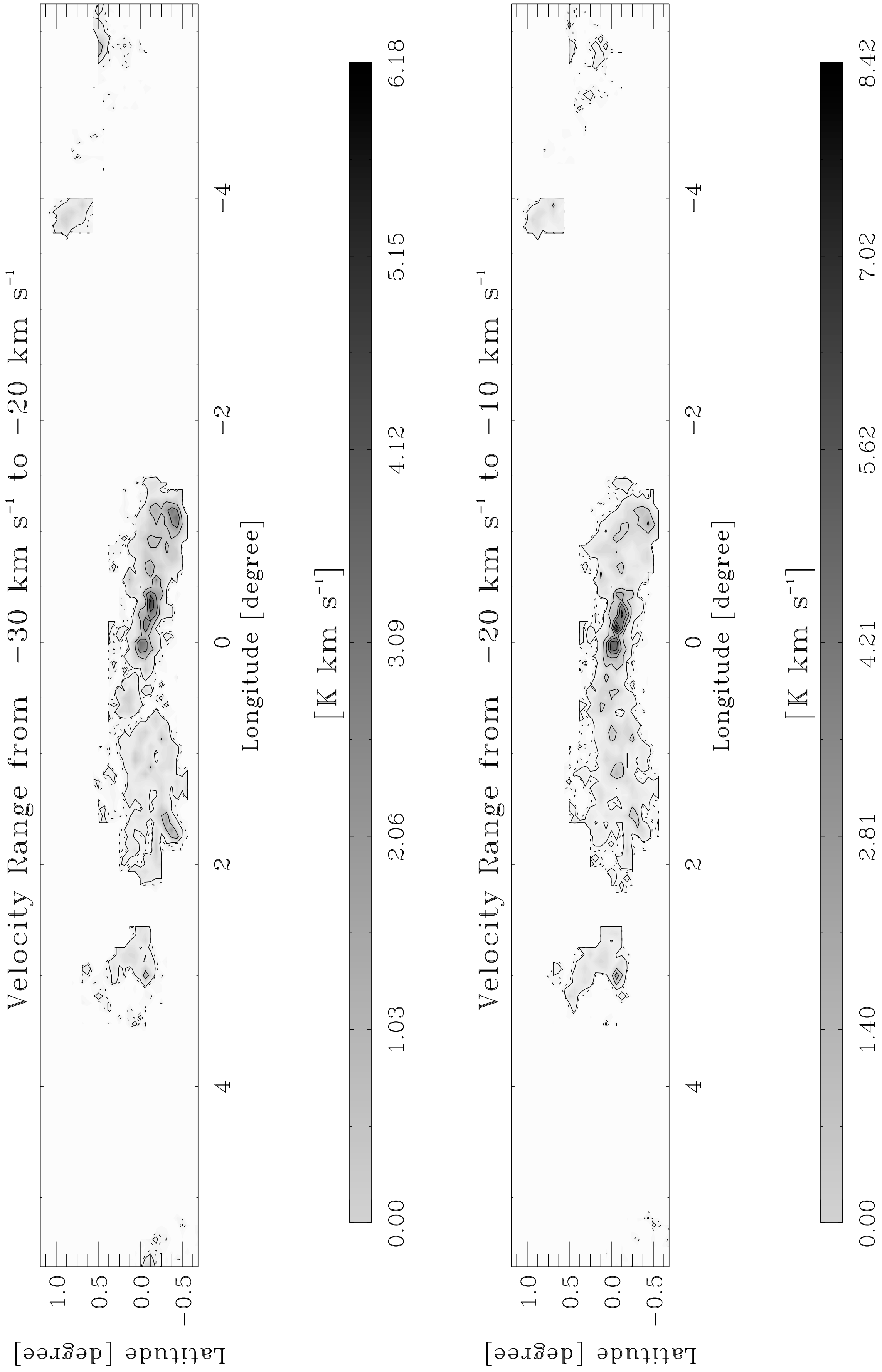

Fig. B1.12. continued.

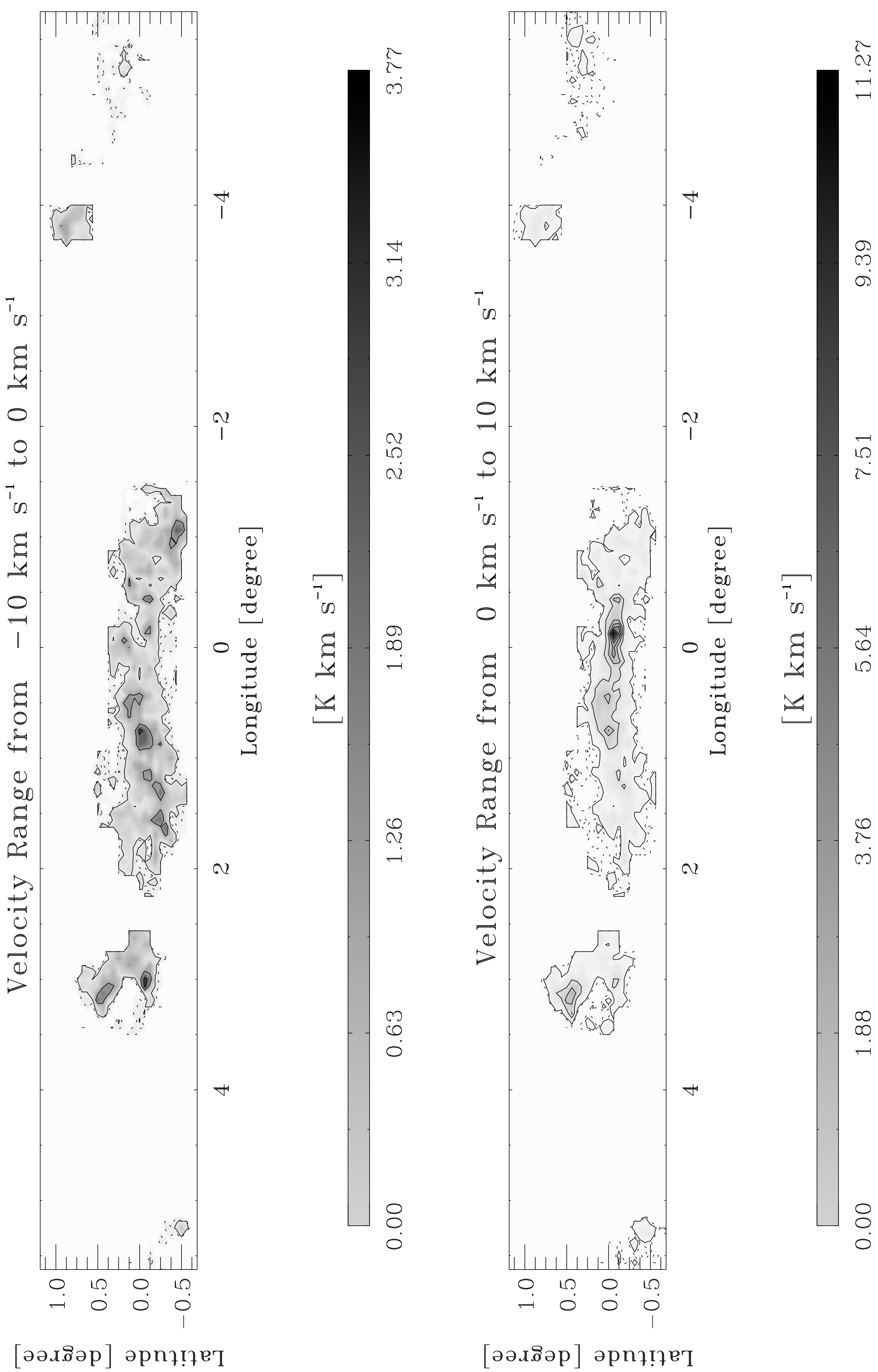

Fig. B1.13. continued.

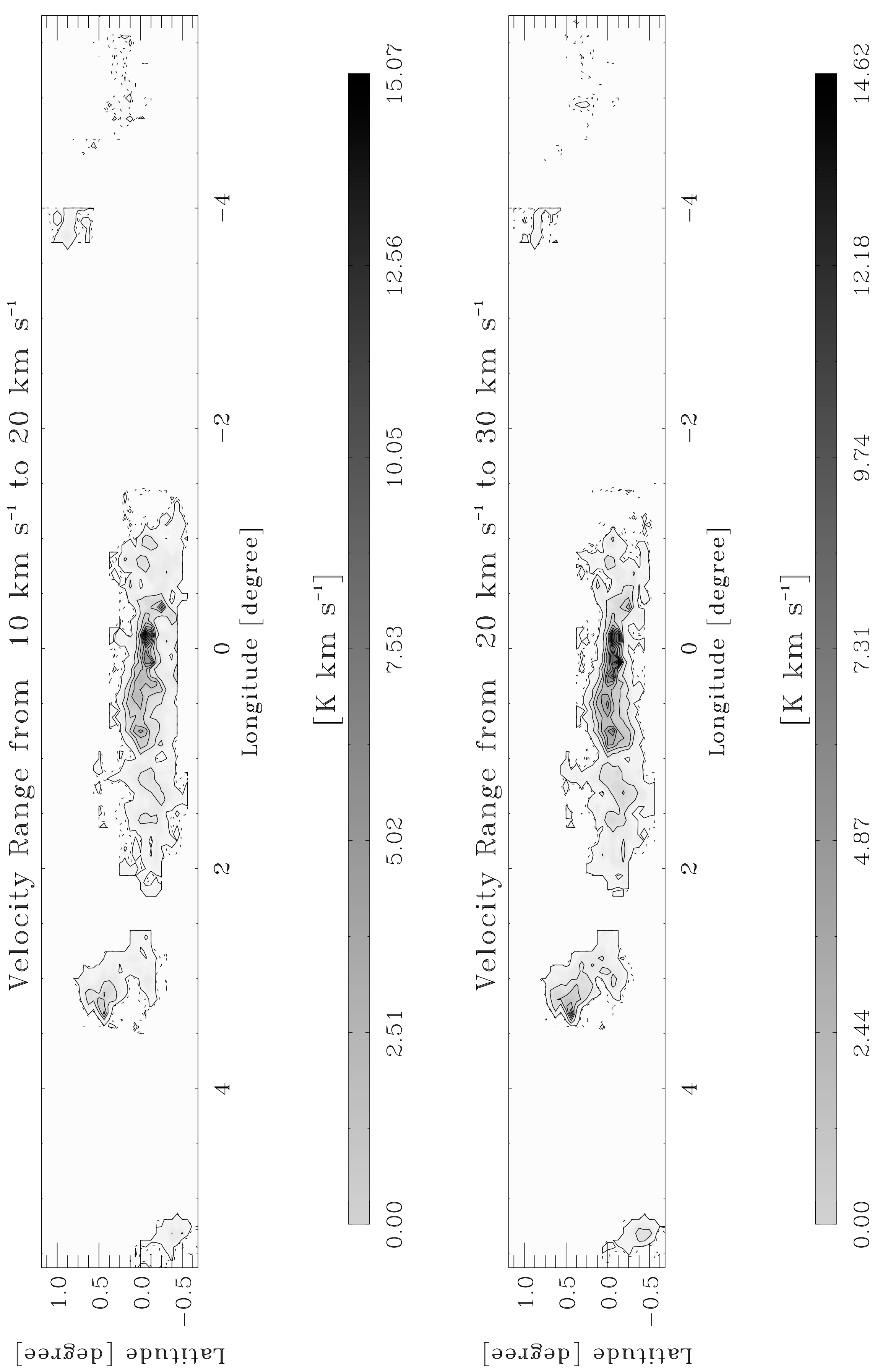

Fig. B1.14. continued.

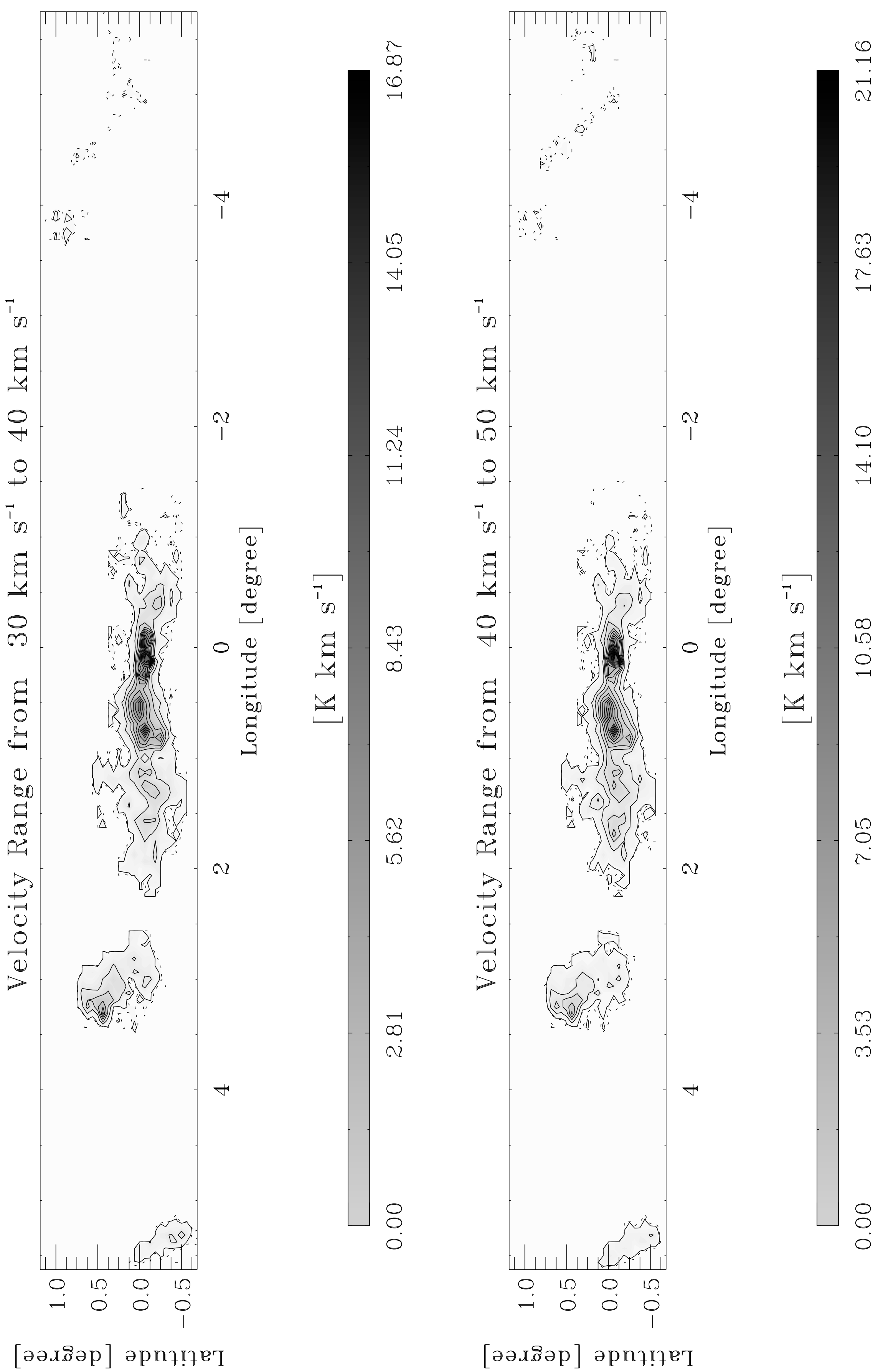

Fig. B1.15. continued.

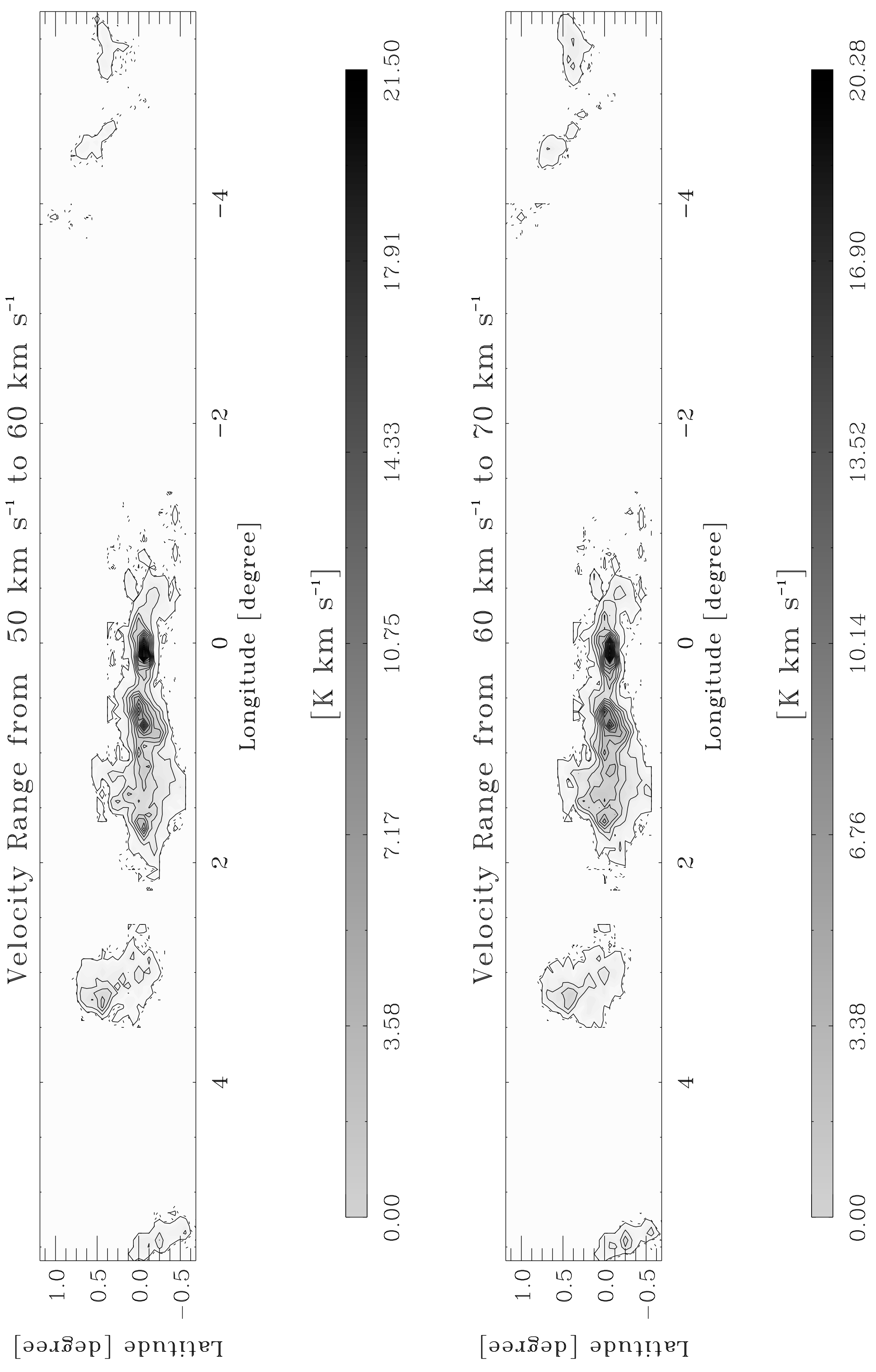

Fig. B1.16. continued.

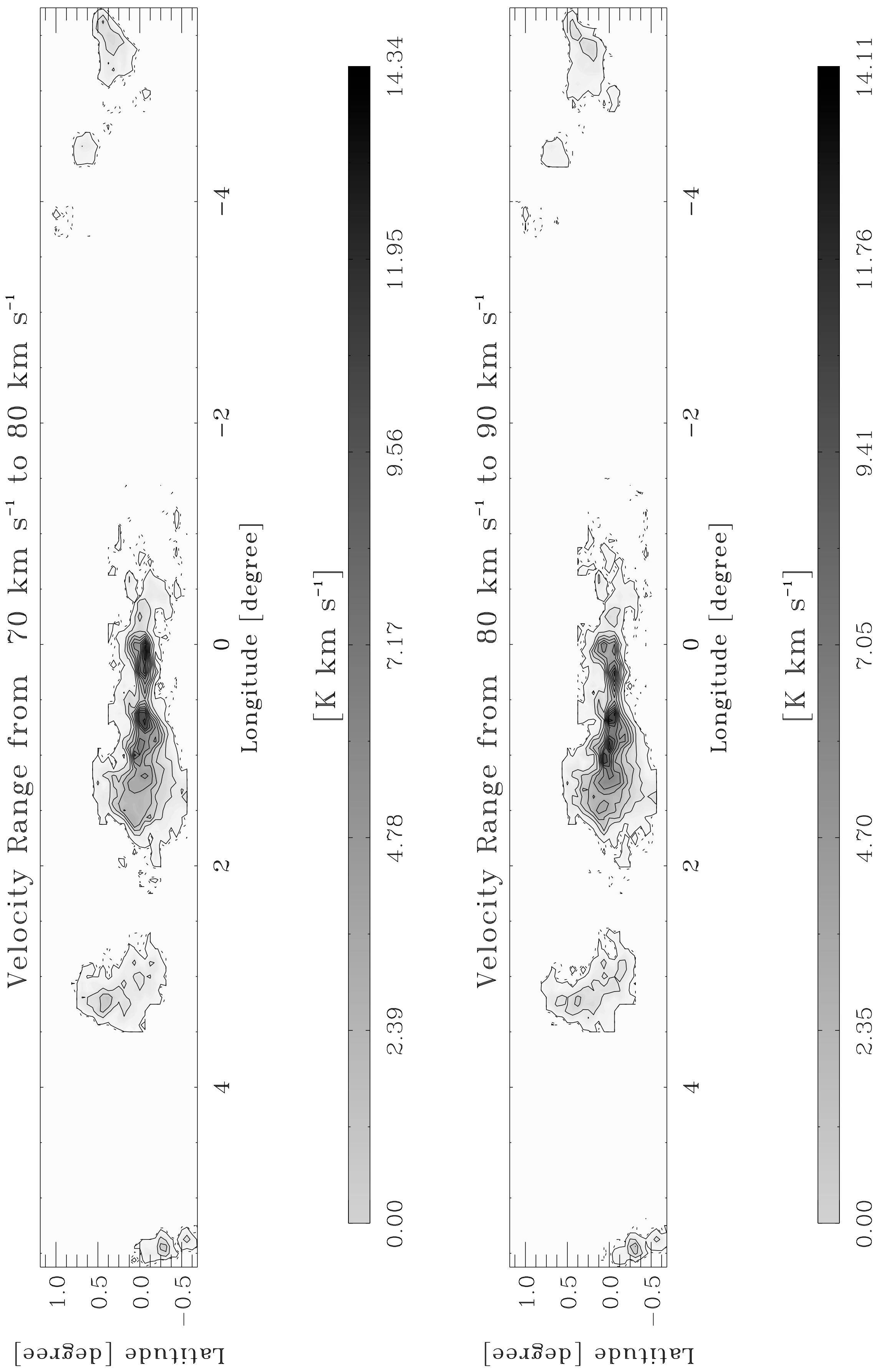

Fig. B1.17. continued.

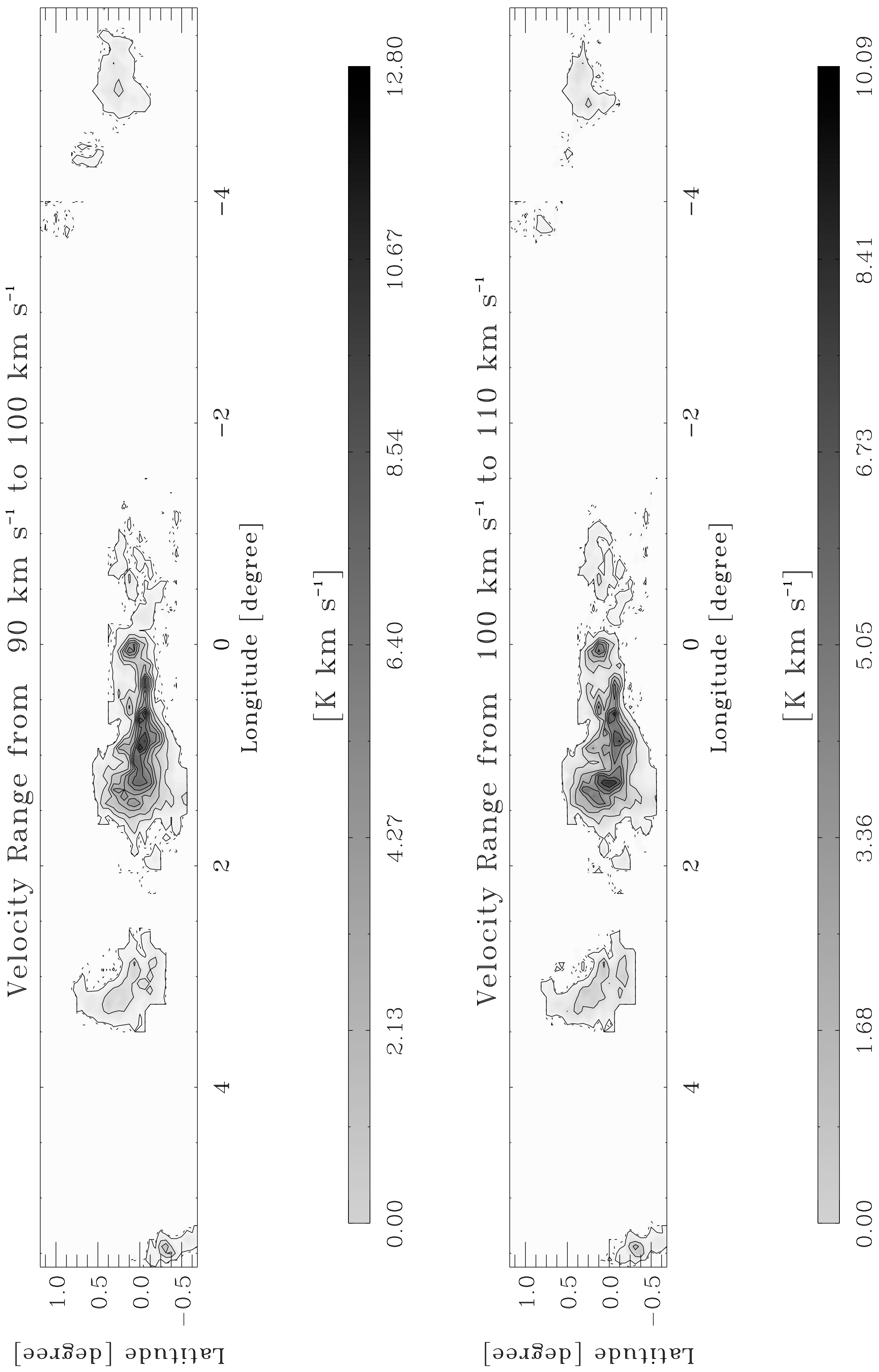

Fig. B1.18. continued.

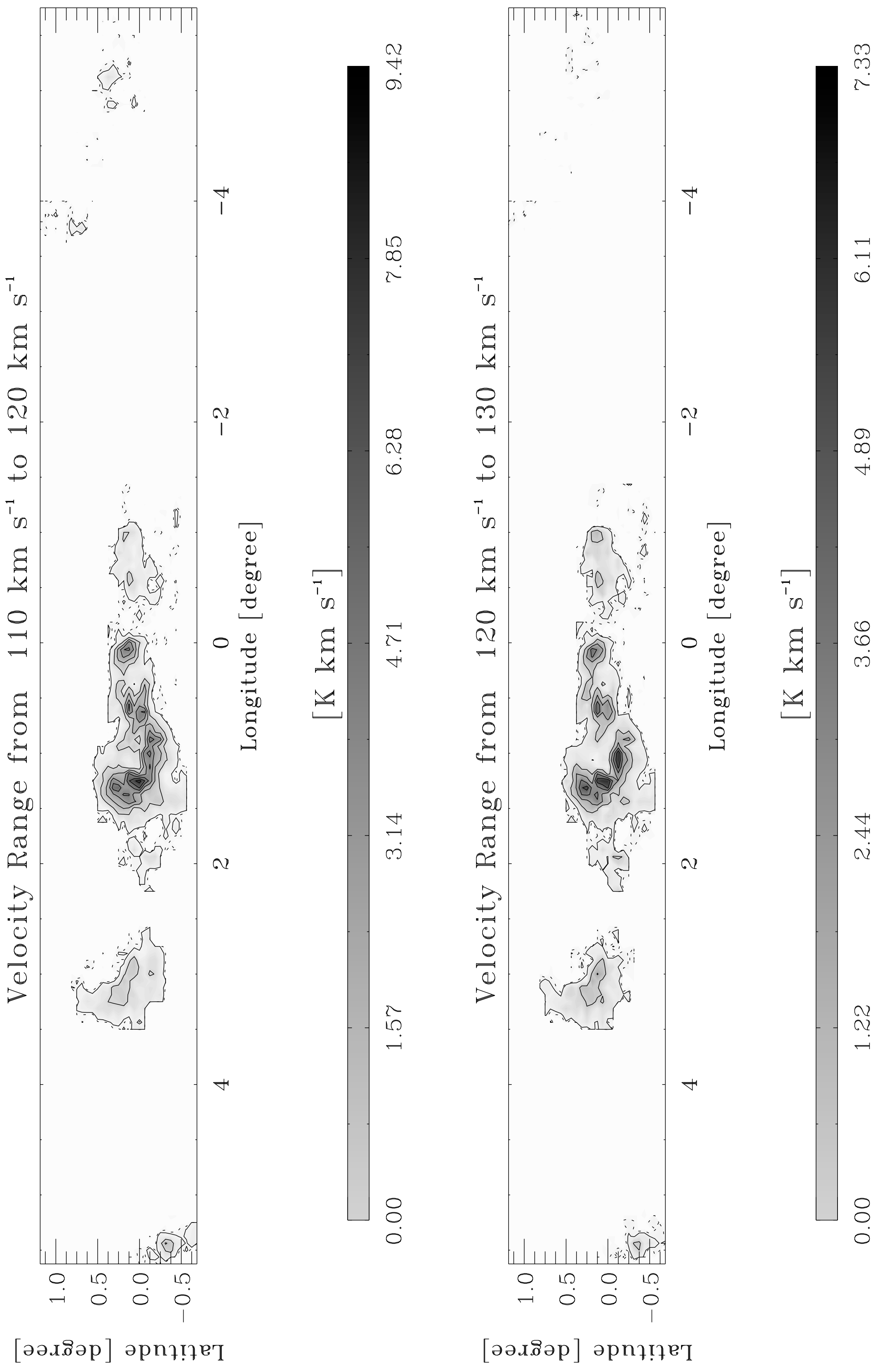

Fig. B1.19. continued.

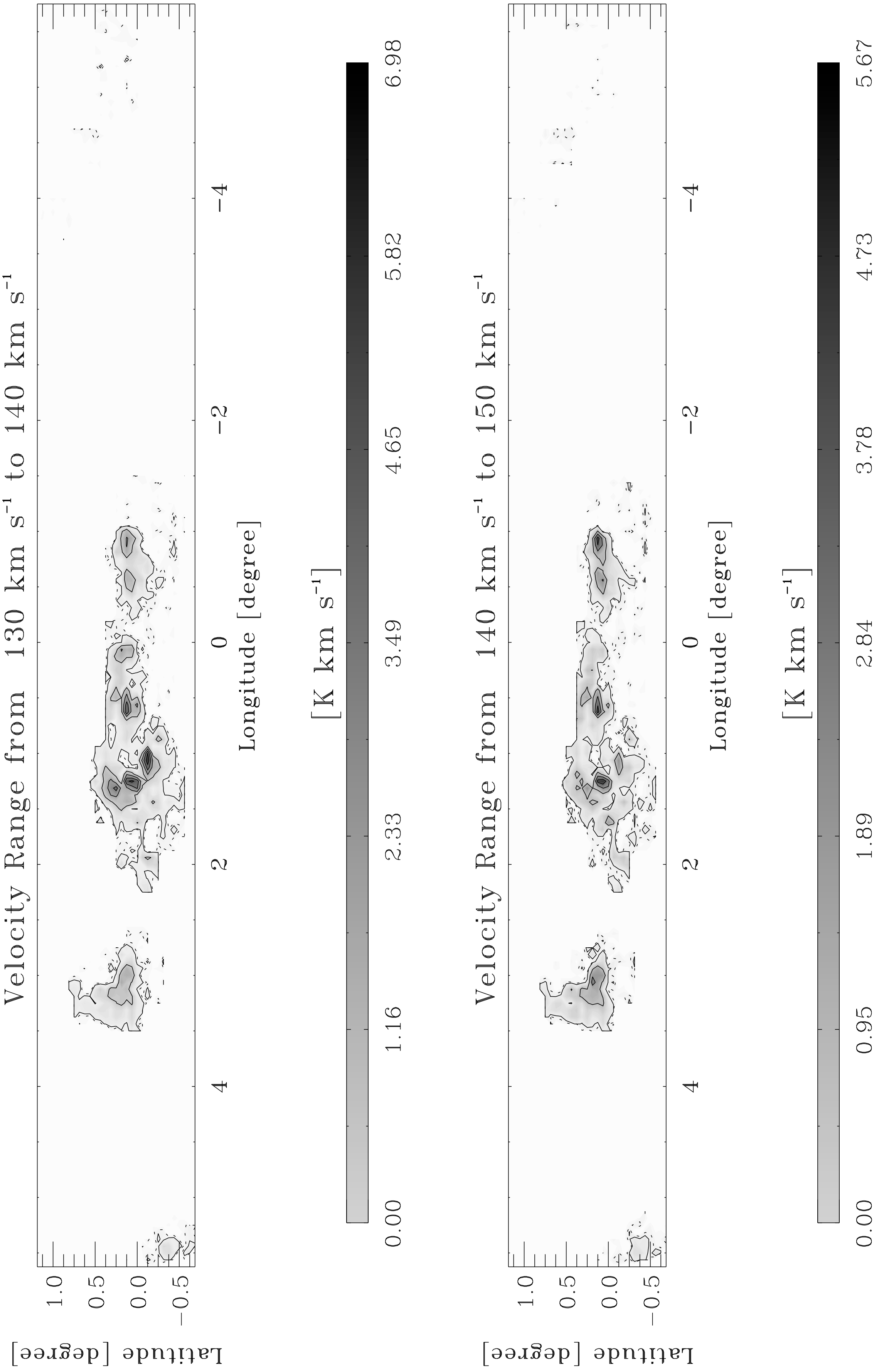

Fig. B1.20. continued.

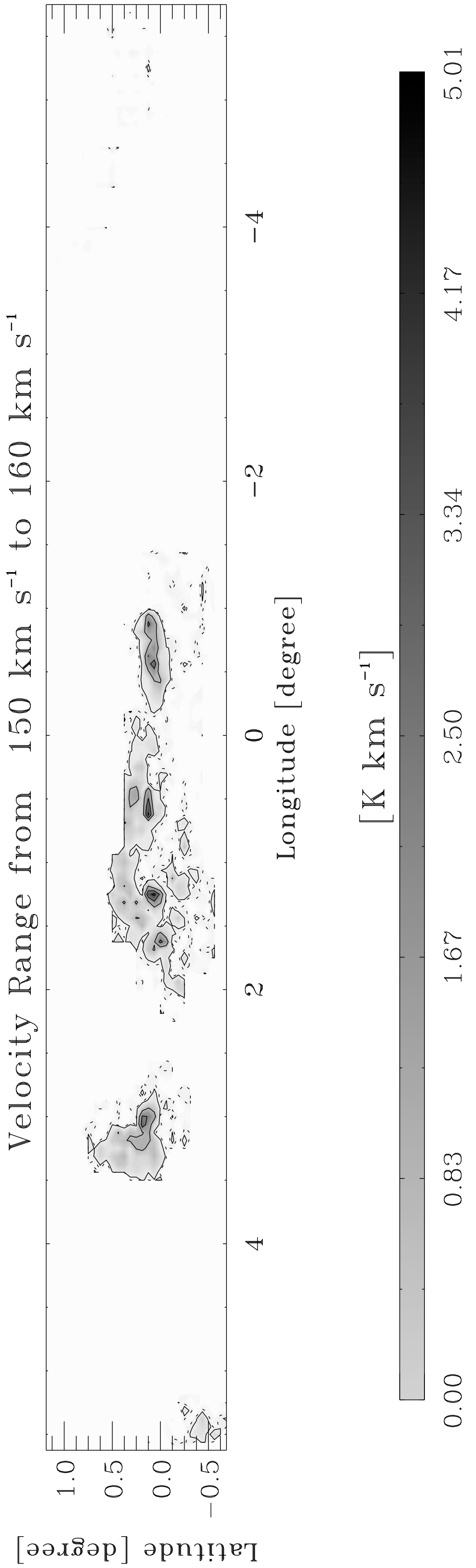

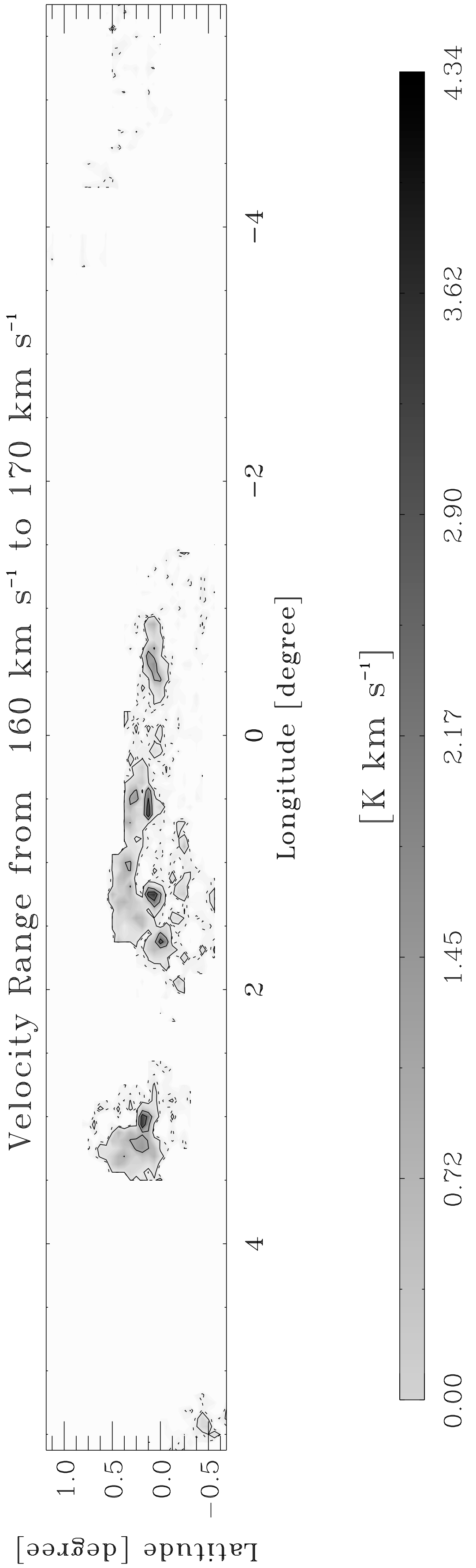

Fig. B1.21. continued.

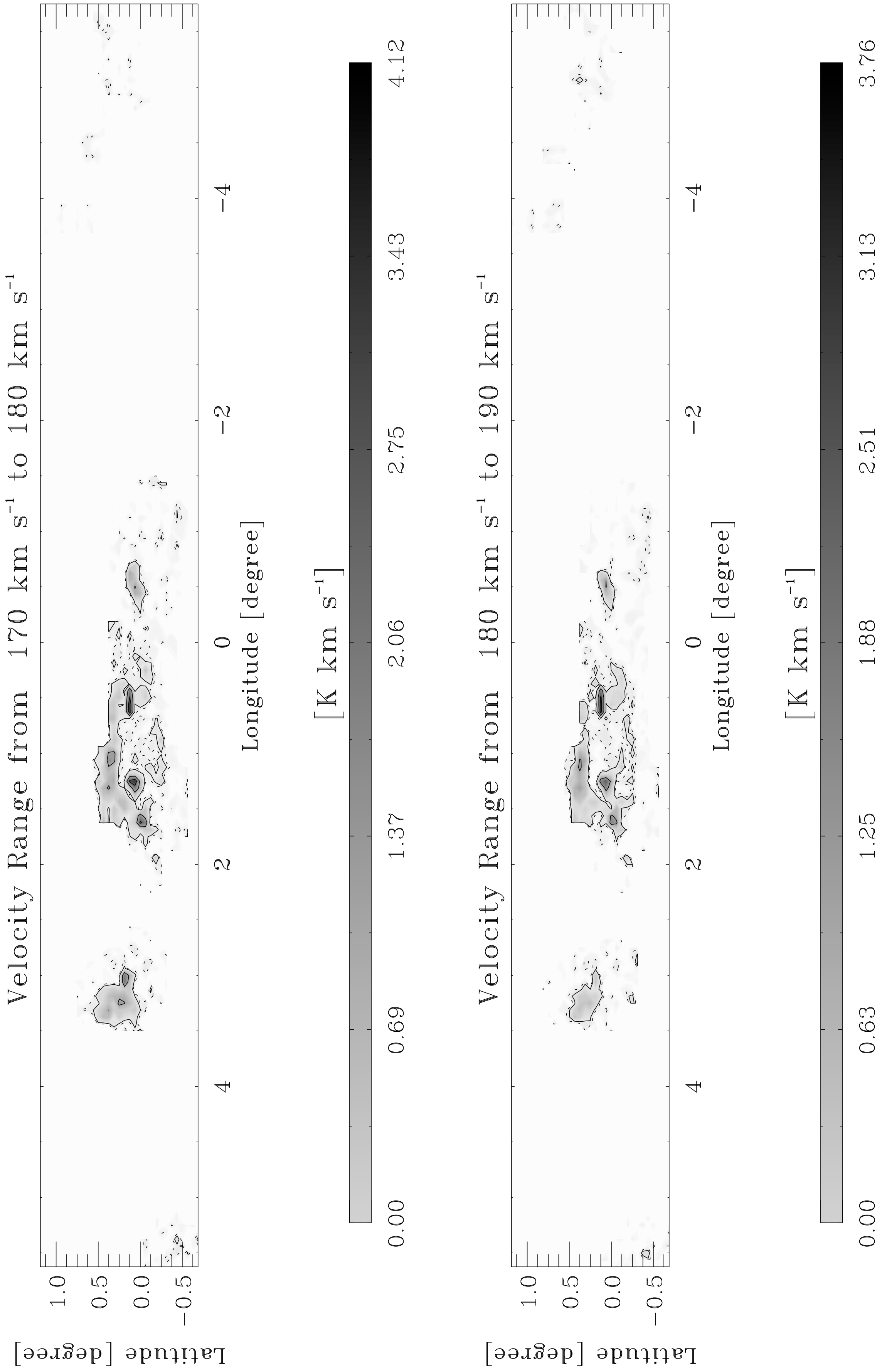

Fig. B1.22. continued.

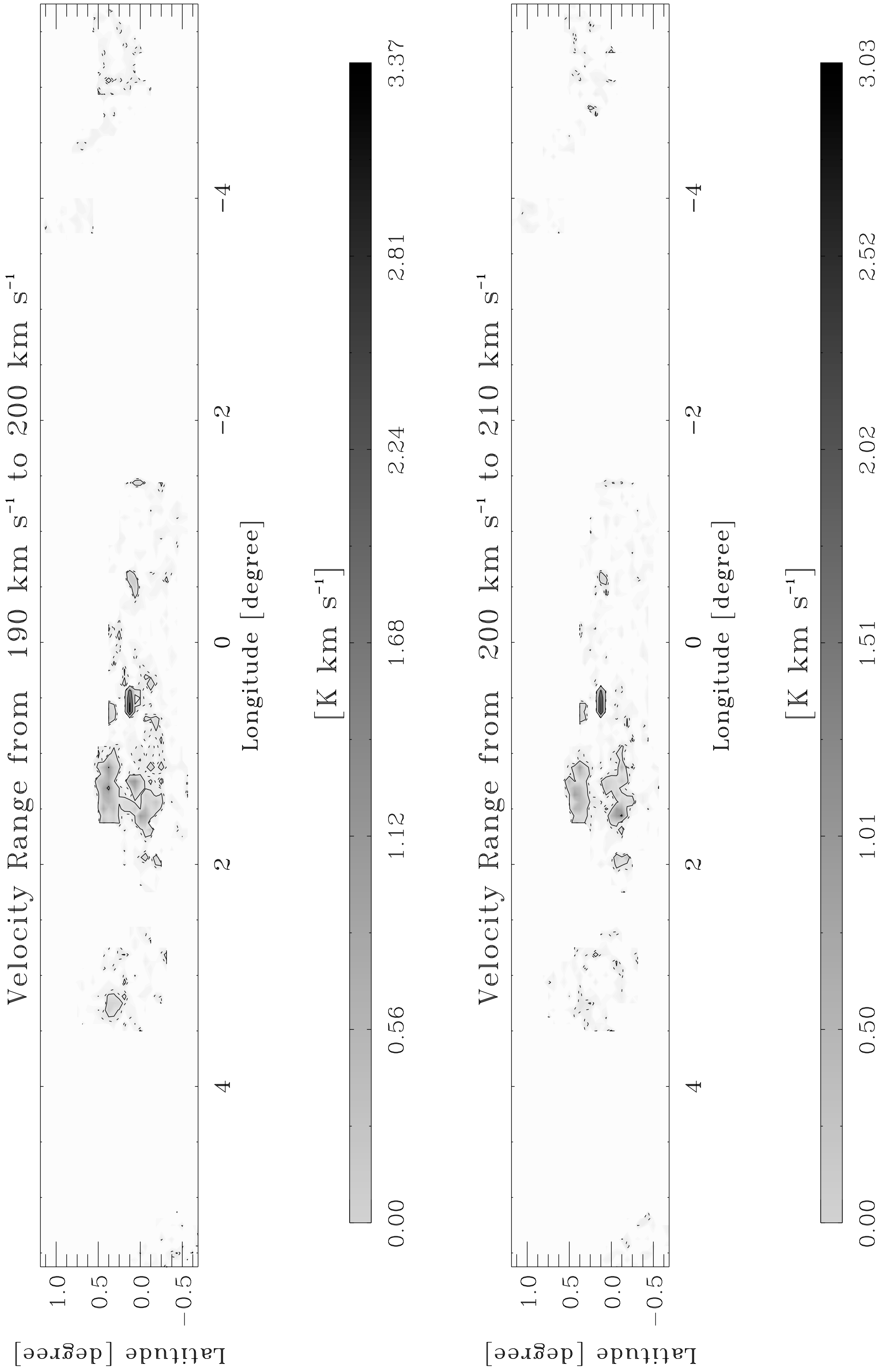

Fig. B1.23. continued.

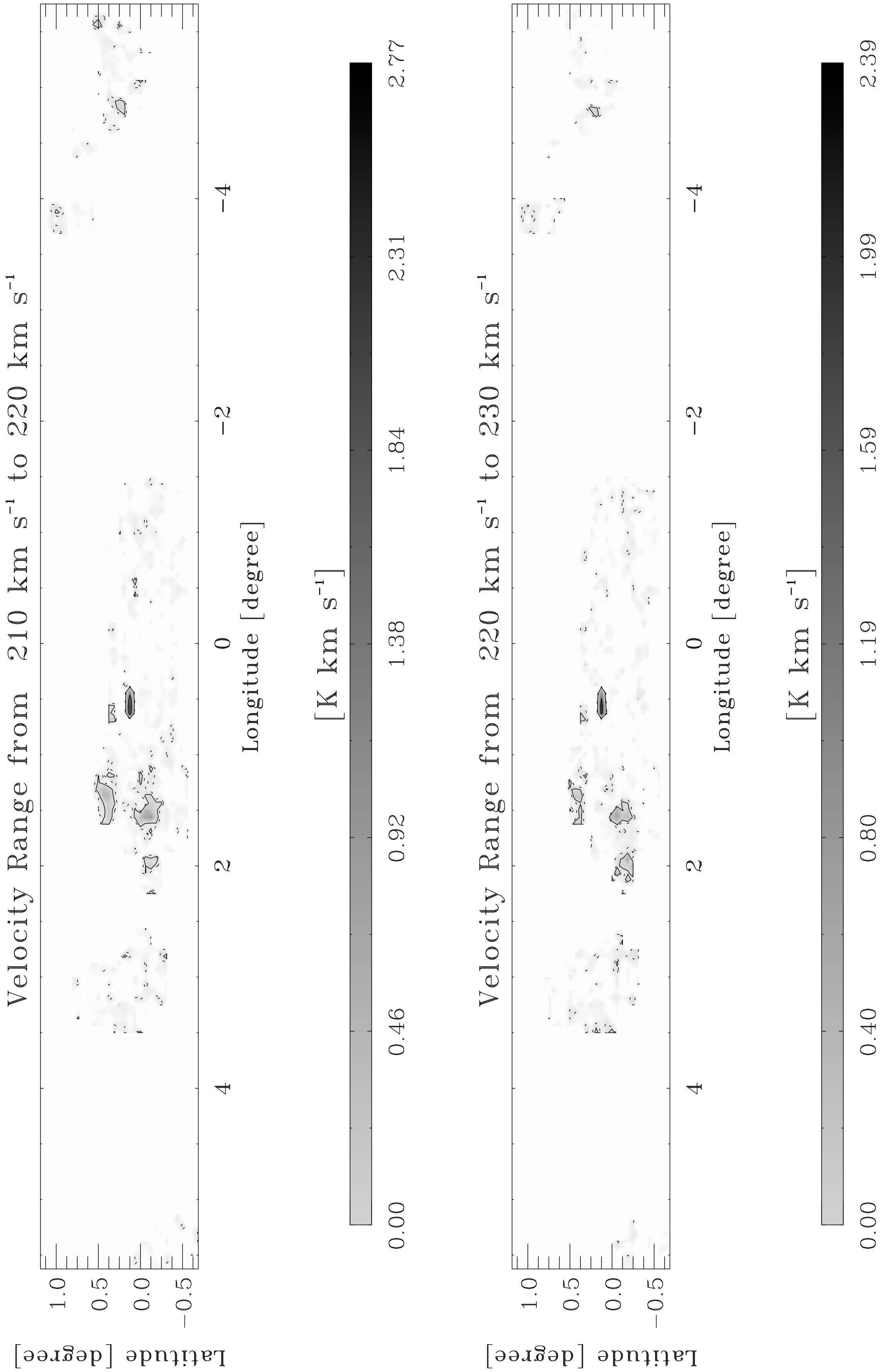

Fig. B1.24. continued.

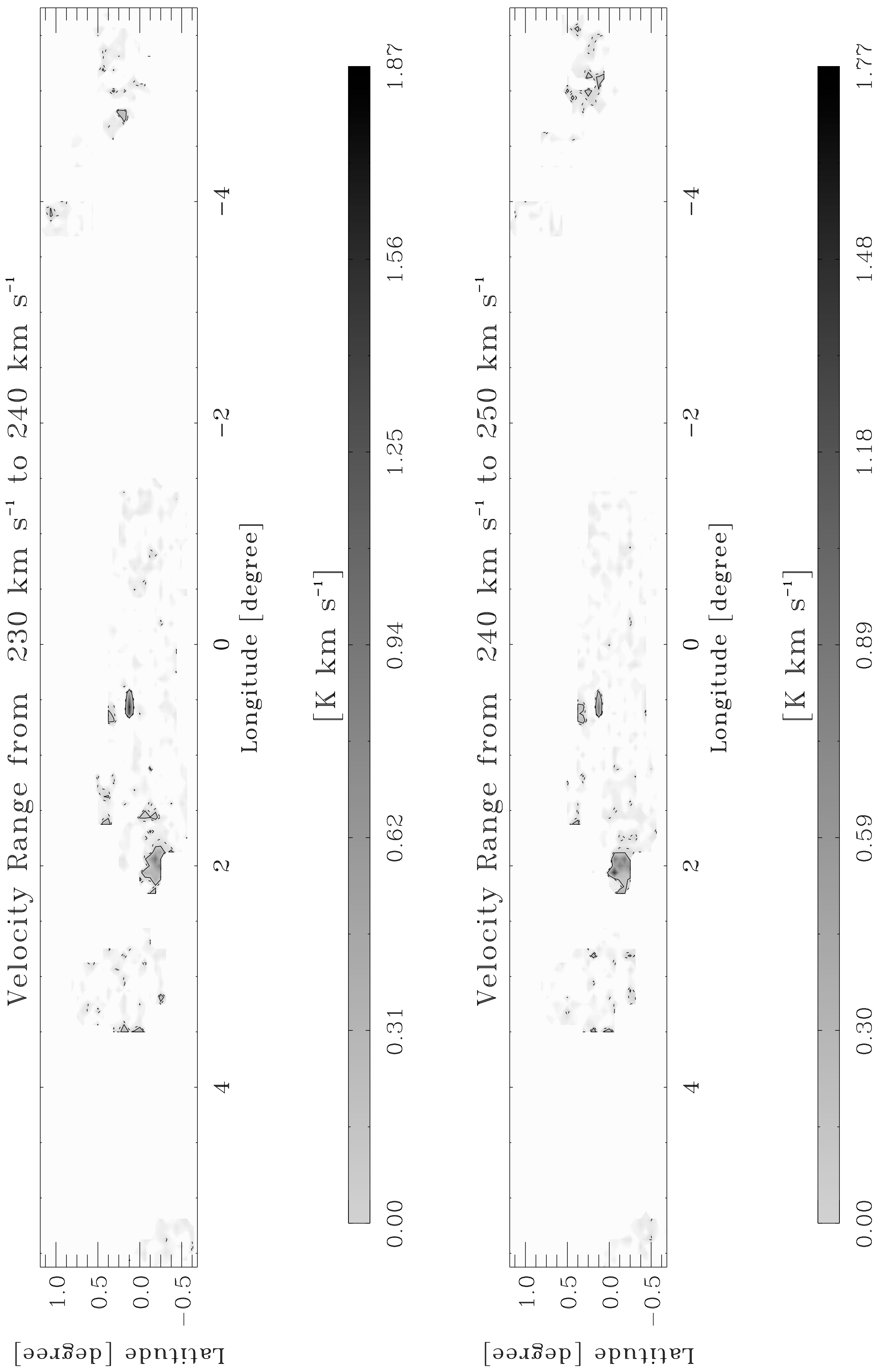

Fig. B1.25. continued.

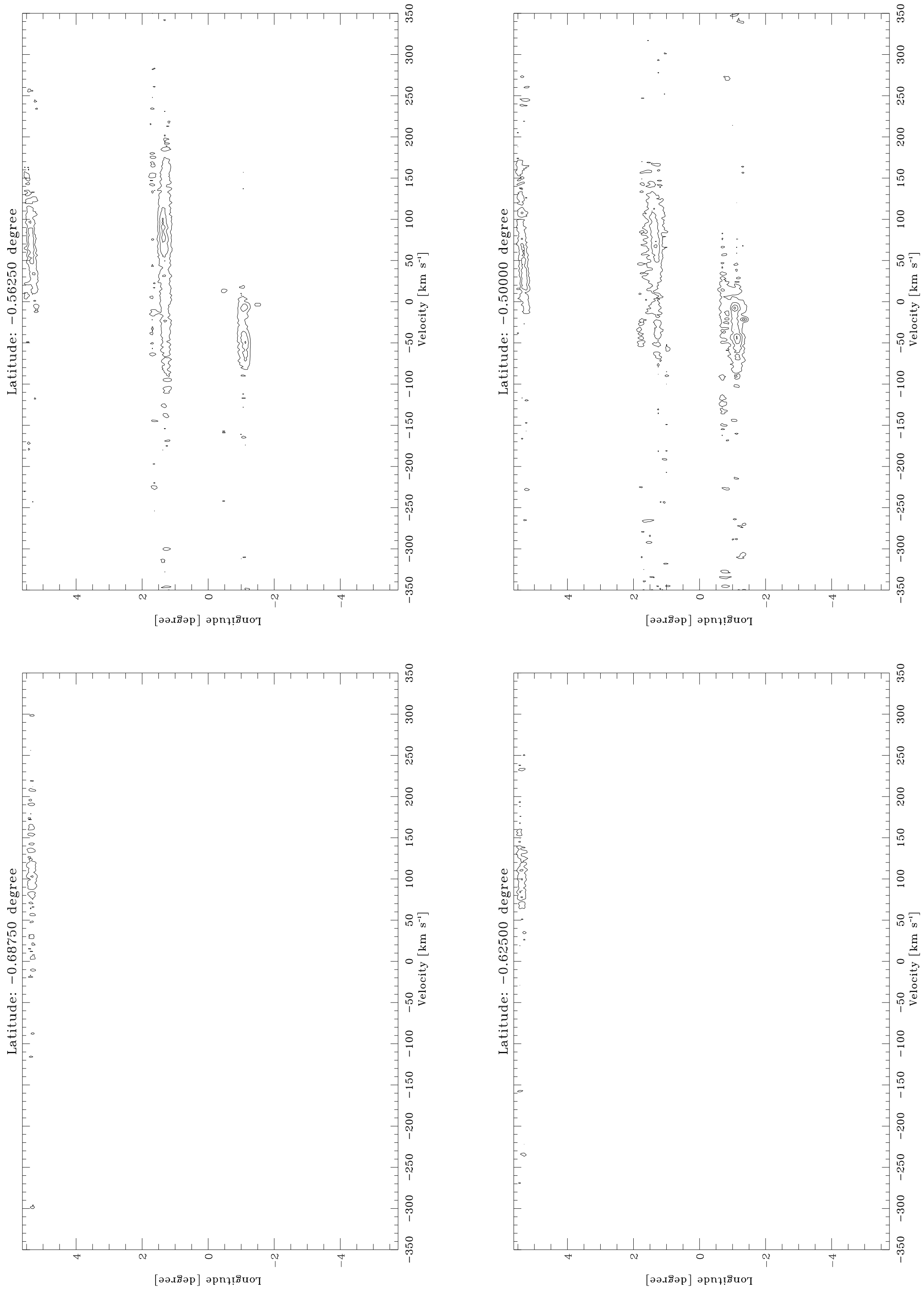

Fig. B2.1. Longitude-velocidad contour diagrams for each observed latitude in HCO$^+$. The lowest contour is at 0.0021 K (3σ). The following contours increase them in step of 0.0042 K, which correspond to 6σ.

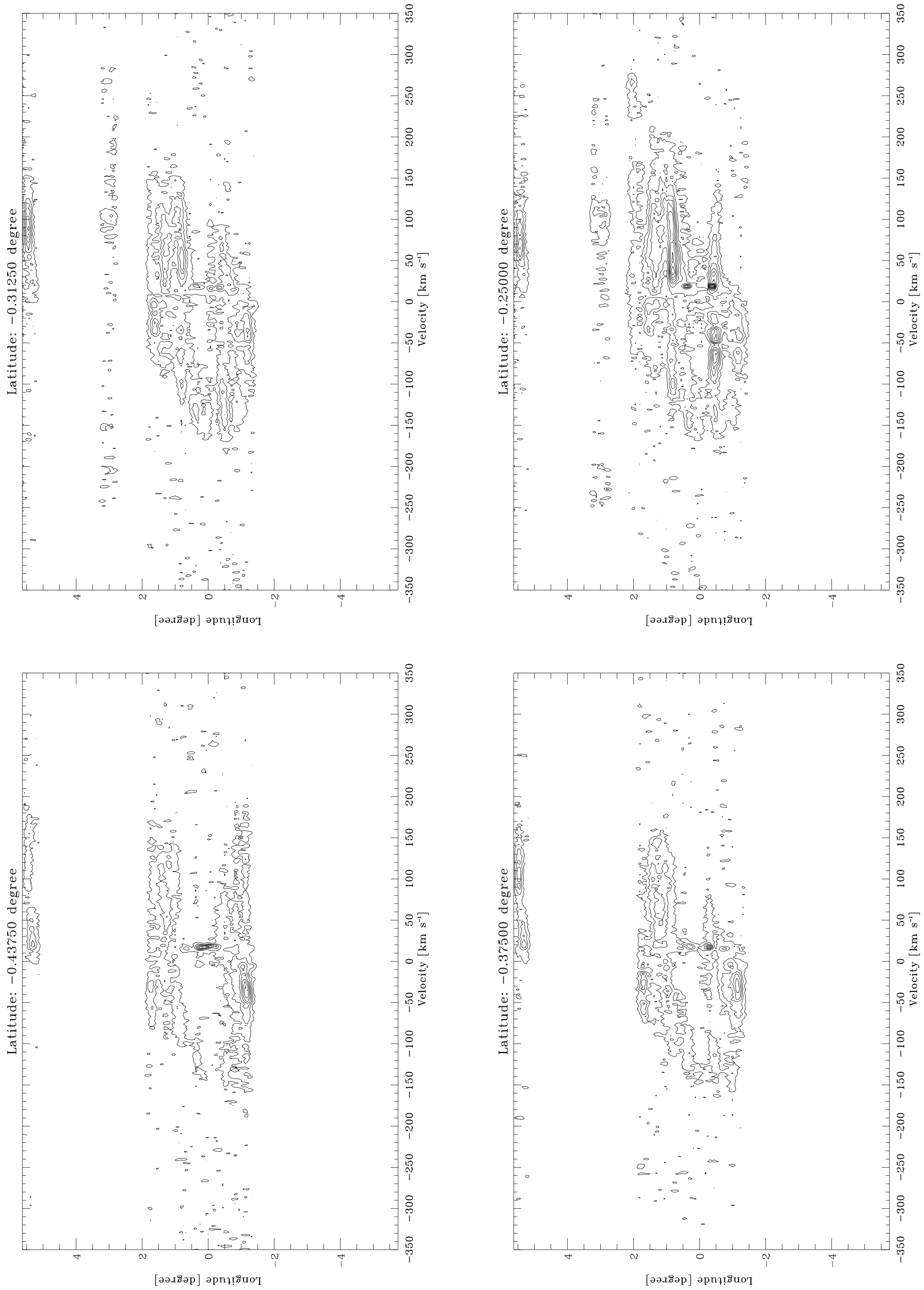

Fig. B2.2. continued.

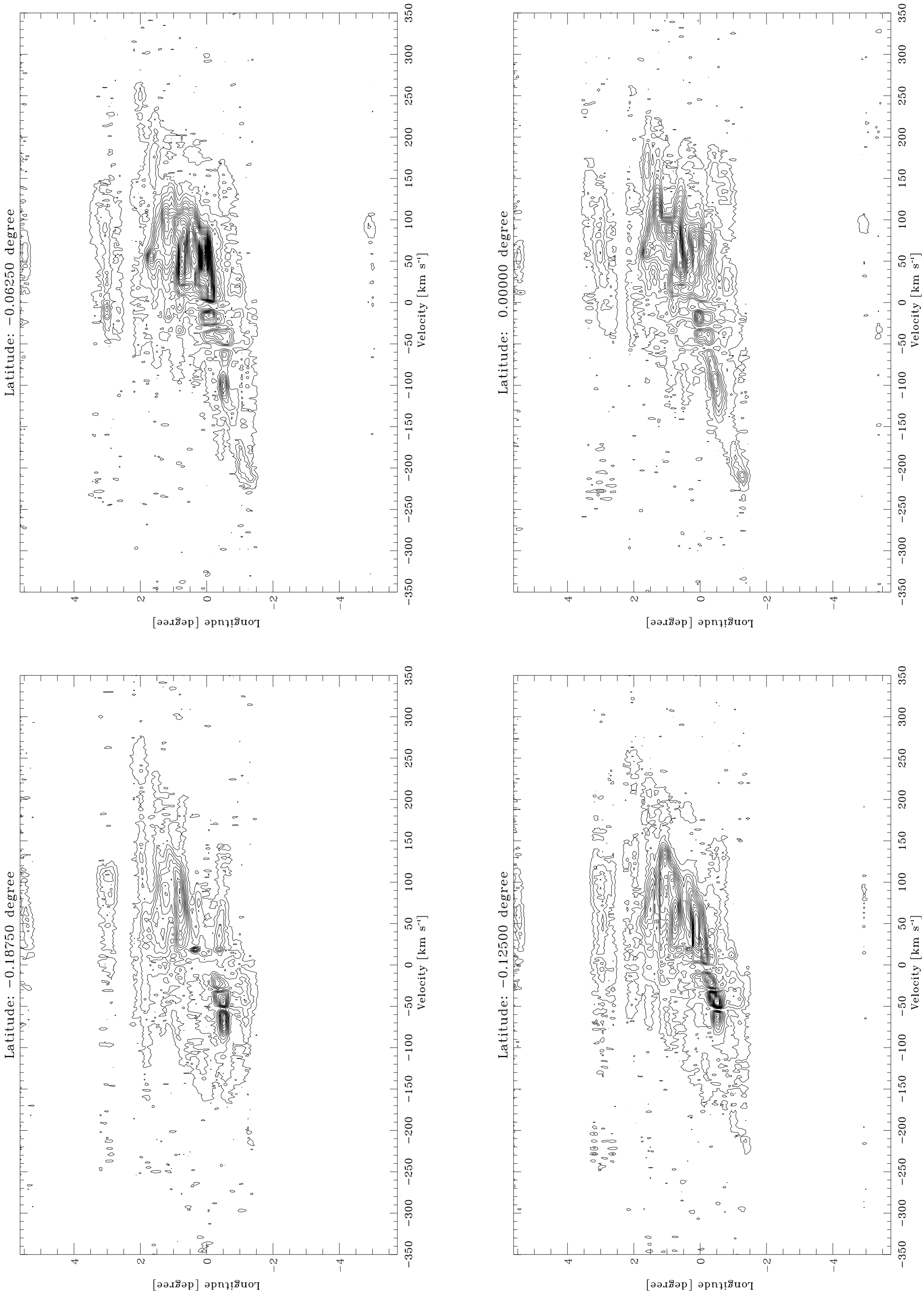

Fig. B2.3. continued.

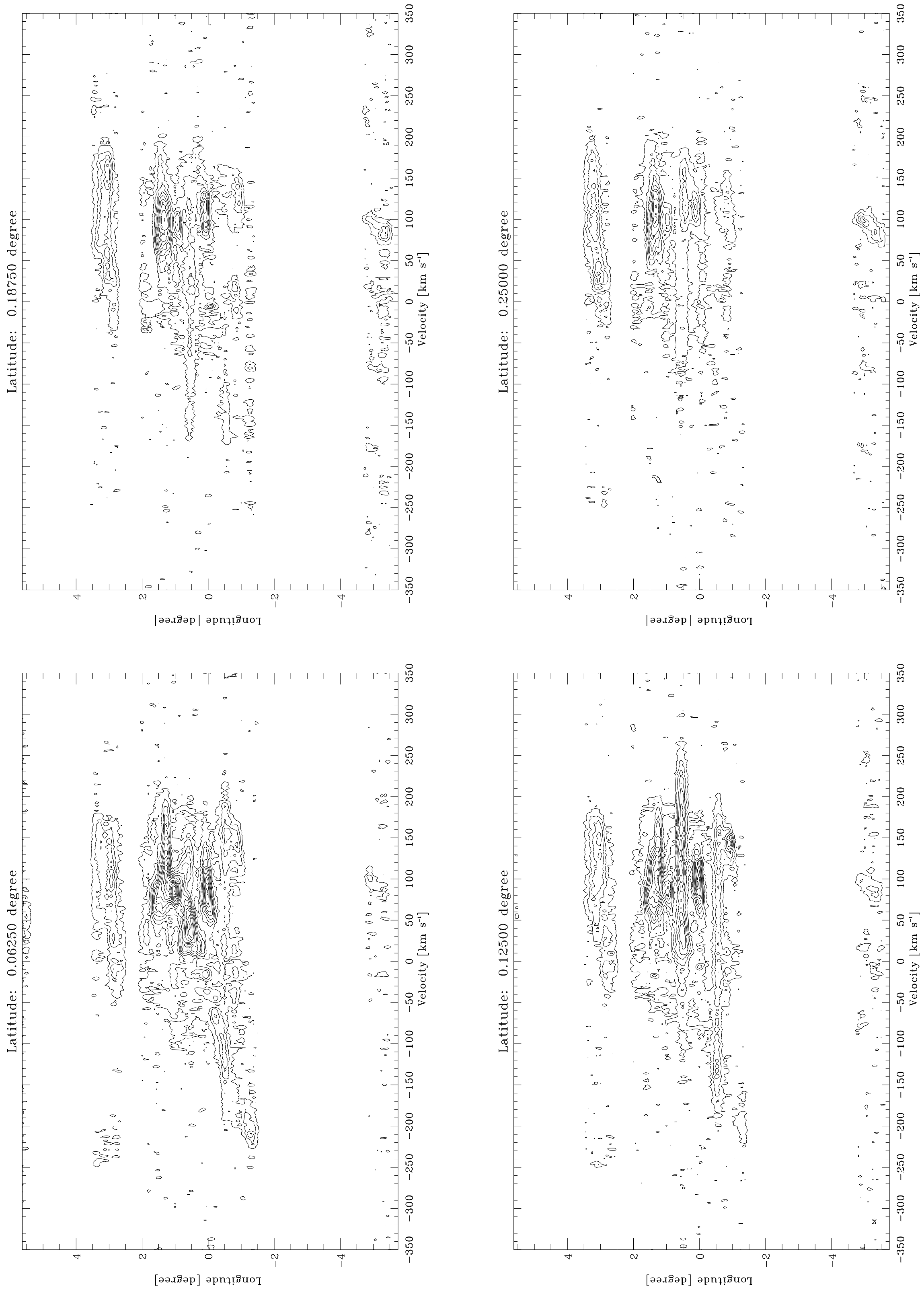

Fig. B2.4. continued.

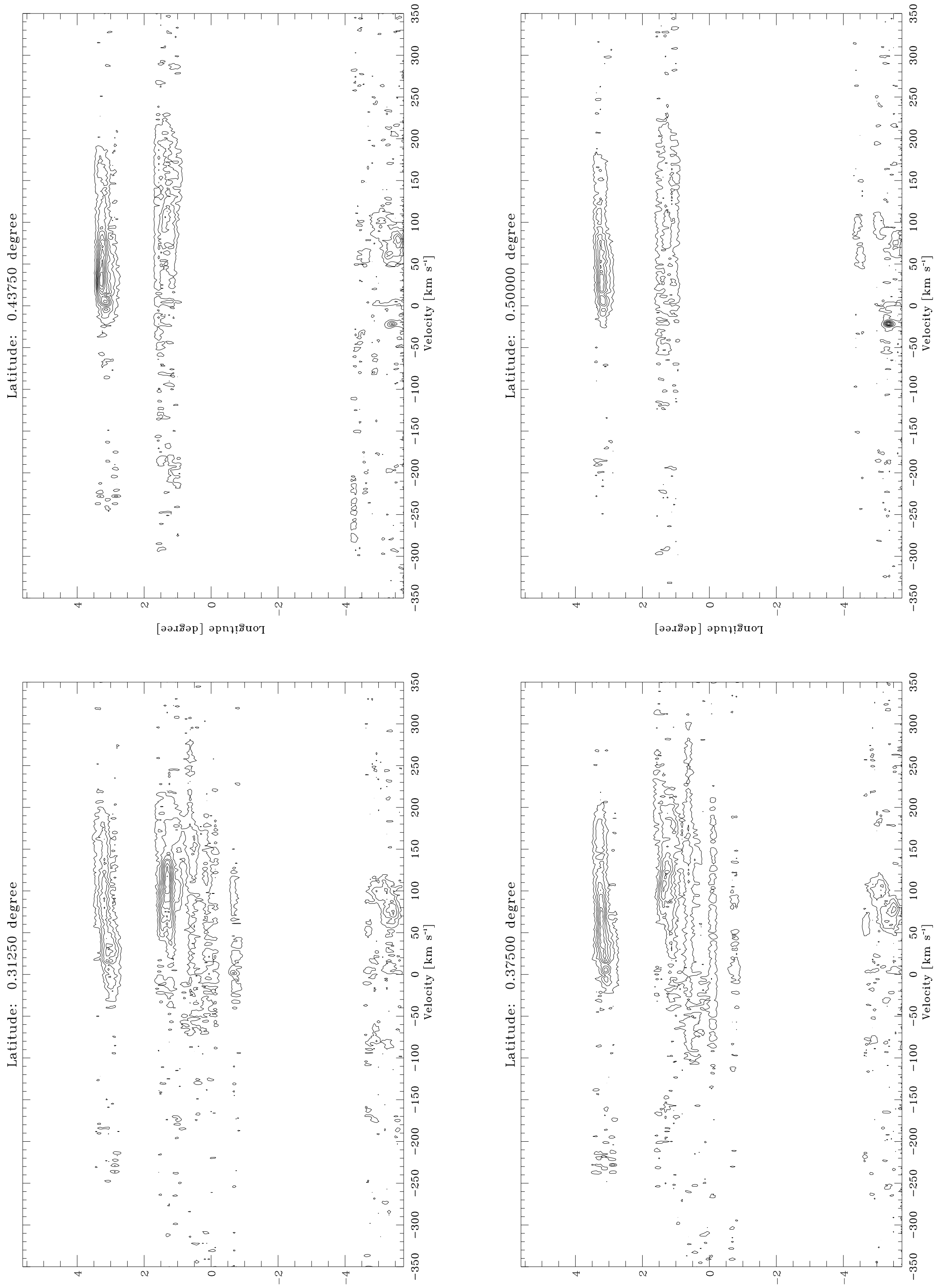

Fig. B2.5. continued.

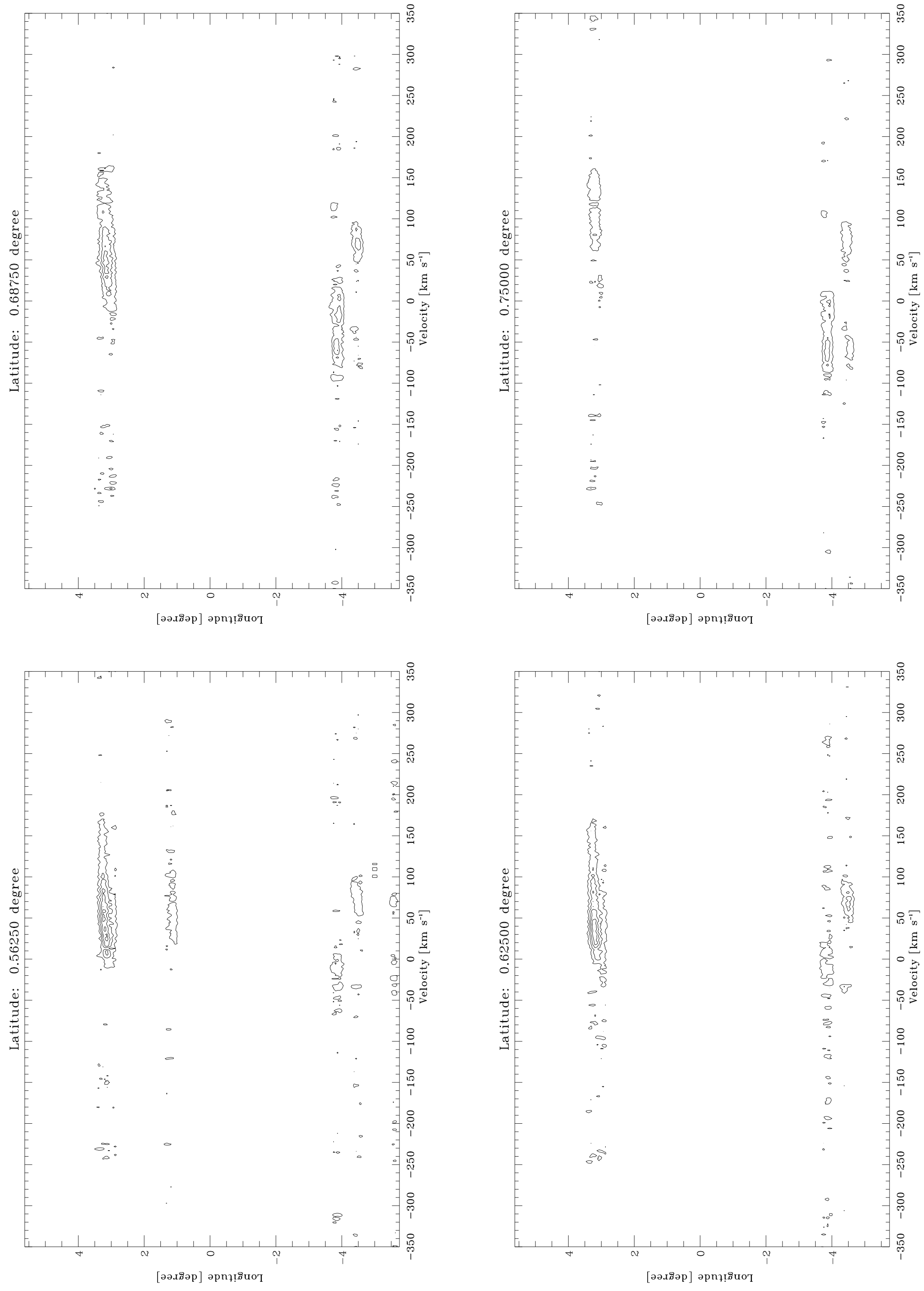

Fig. B2.6. continued.

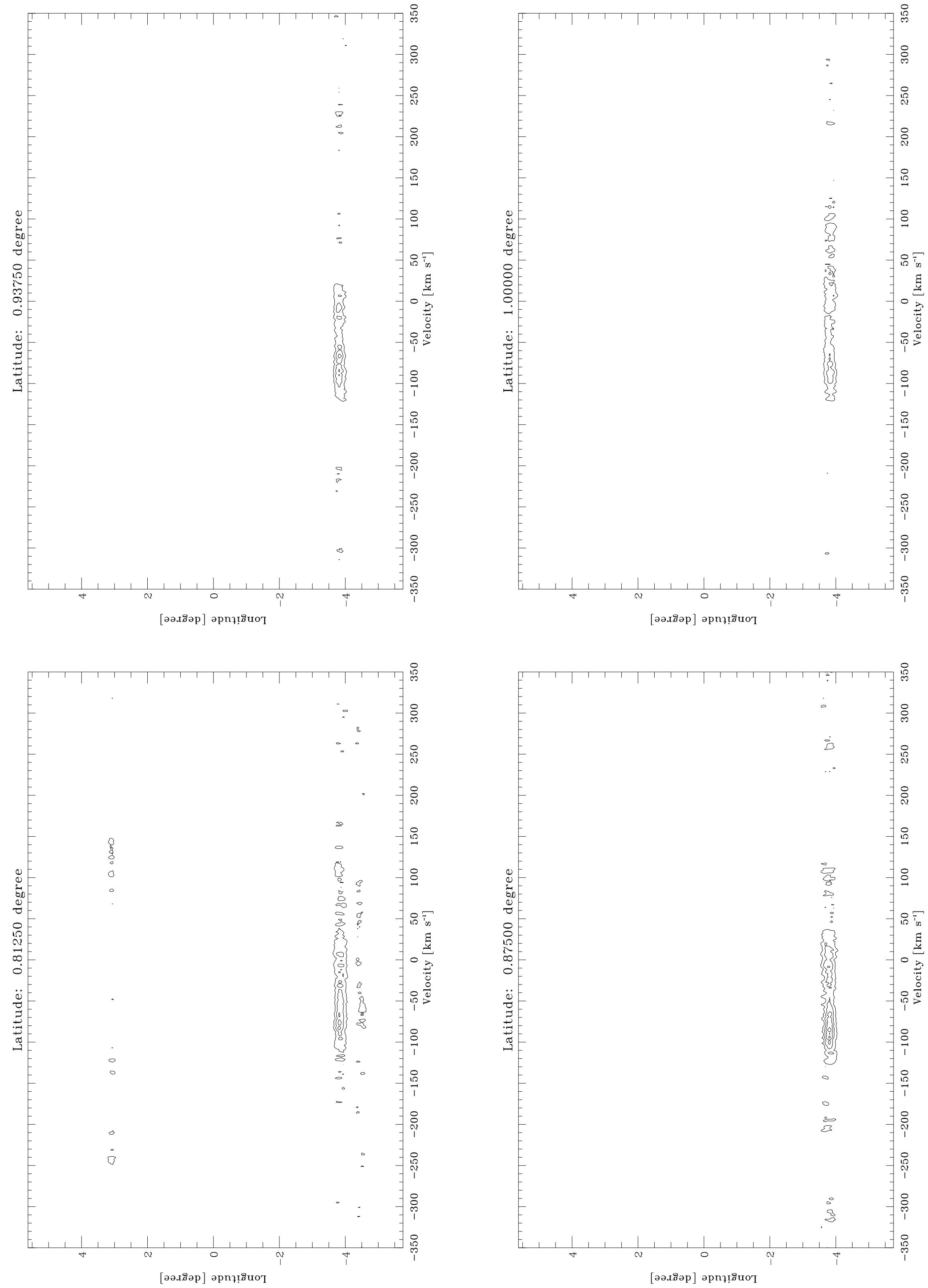

Fig. B2.7. continued.

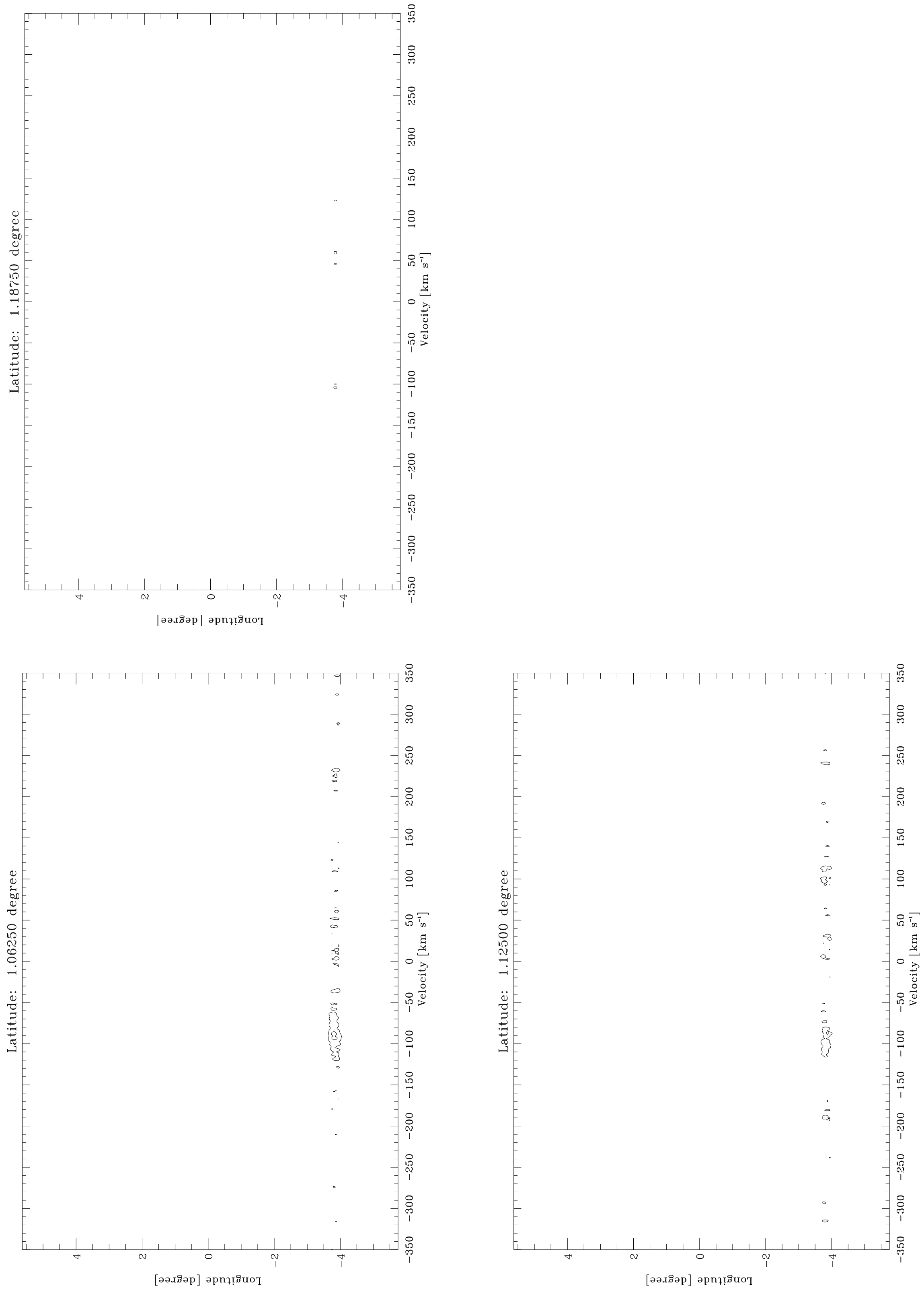

Fig. B2.8. continued.

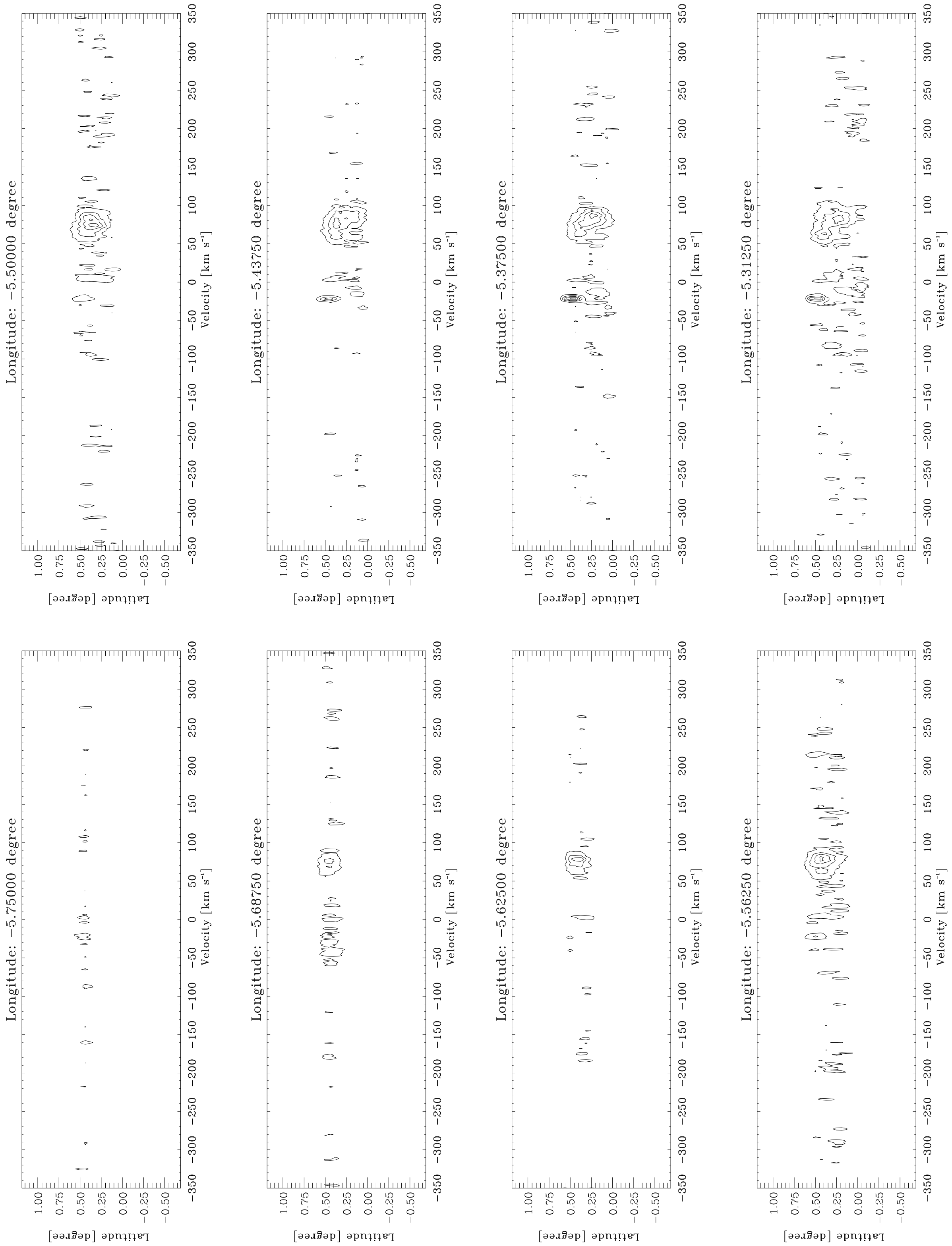

Fig. B3.1. Latitude-velocity diagrams for each observed longitude in HCO$^+$. The lowest contour is at 0.0021 K (3σ). The following contours increase them in step of 0.0042 K, which correspond to 6σ.

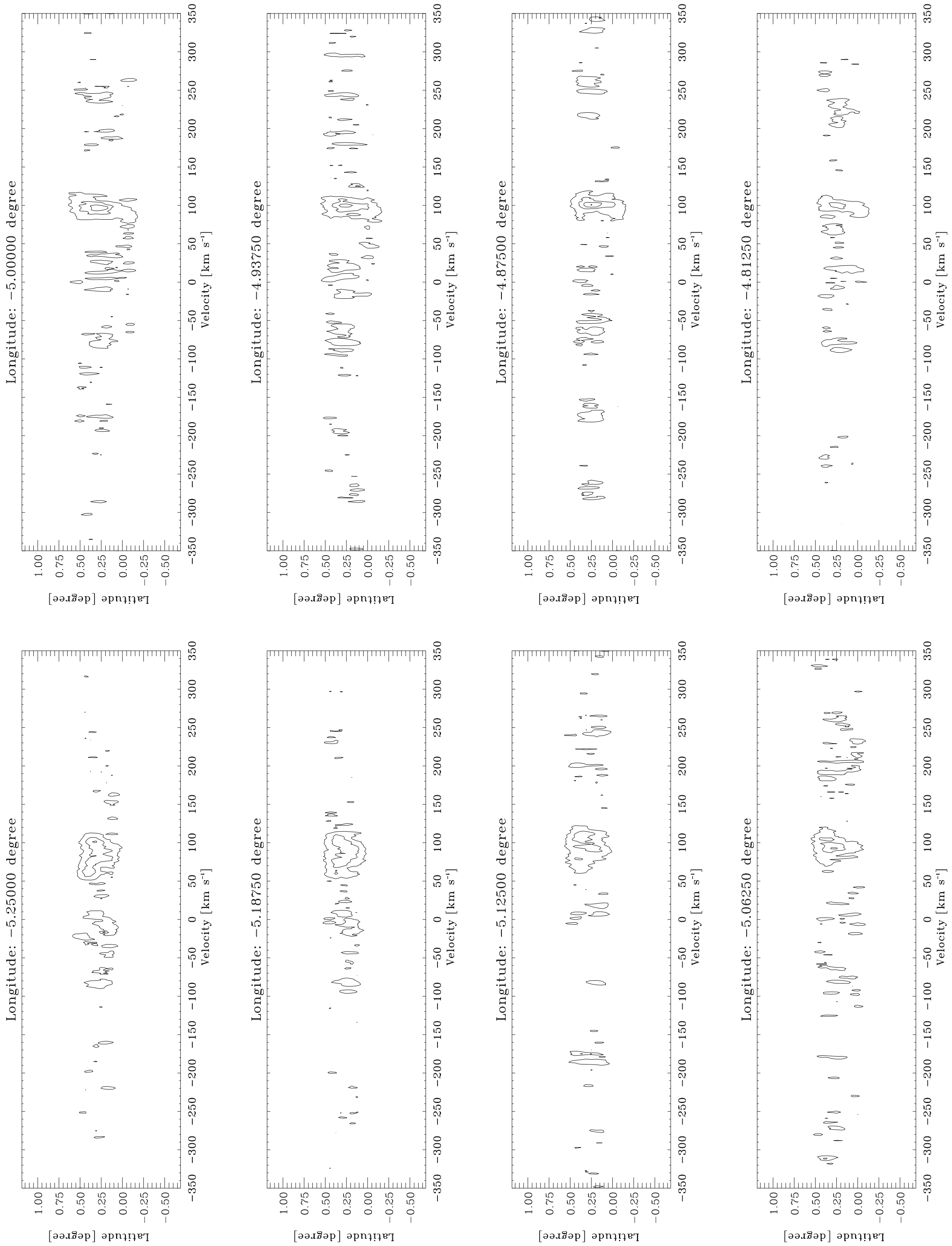

Fig. B3.2. continued.

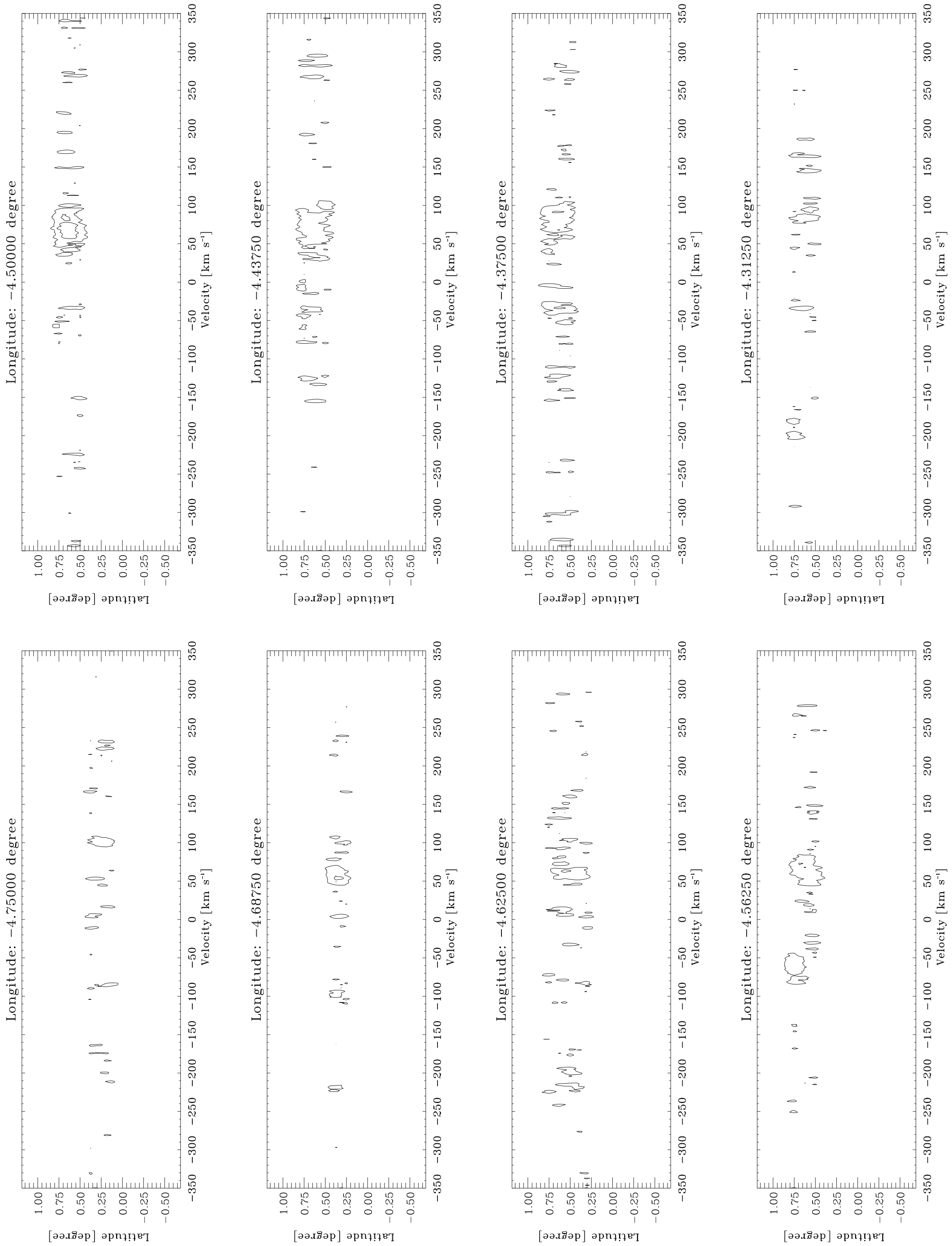

Fig. B3.3. continued.

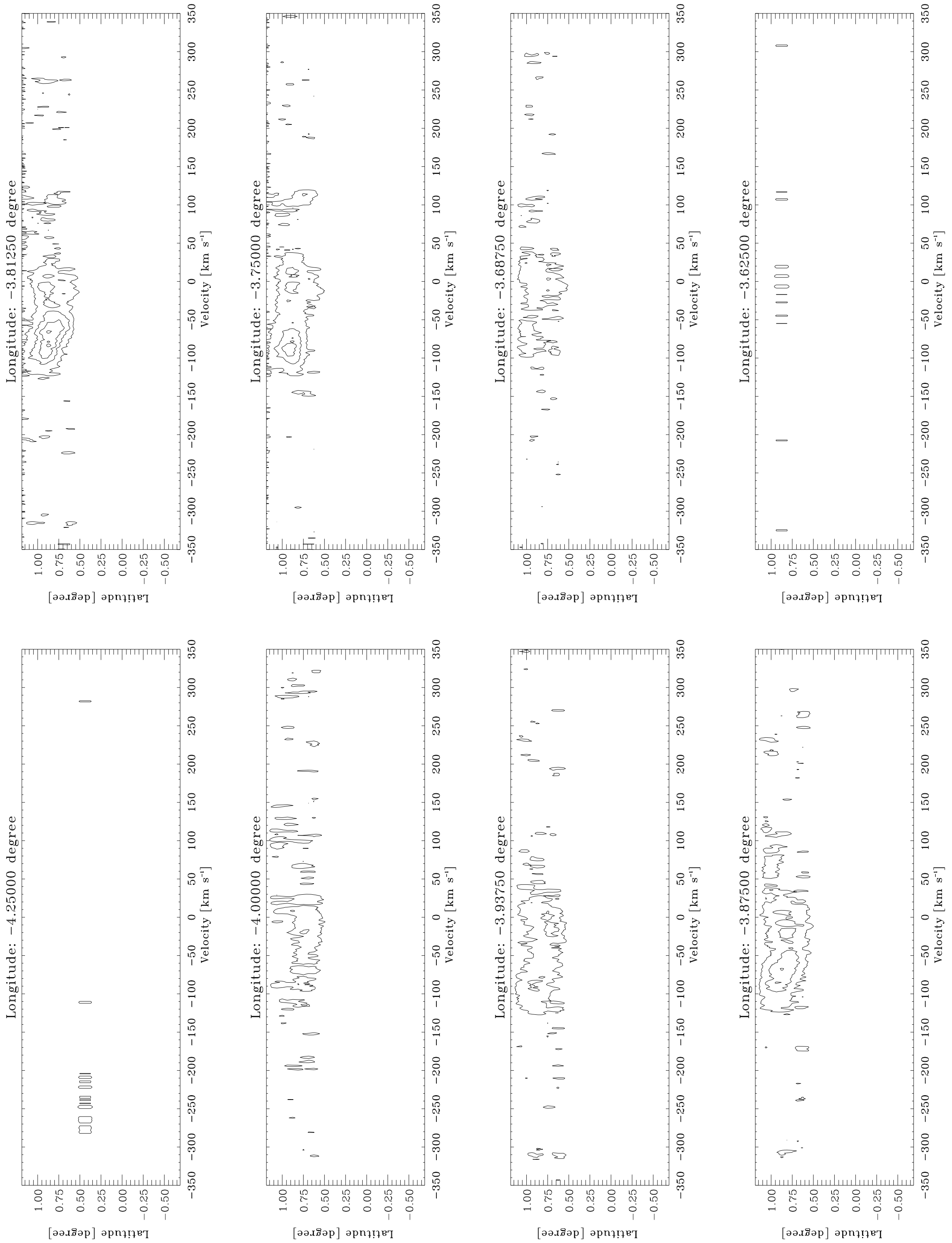

Fig. B3.4. continued.

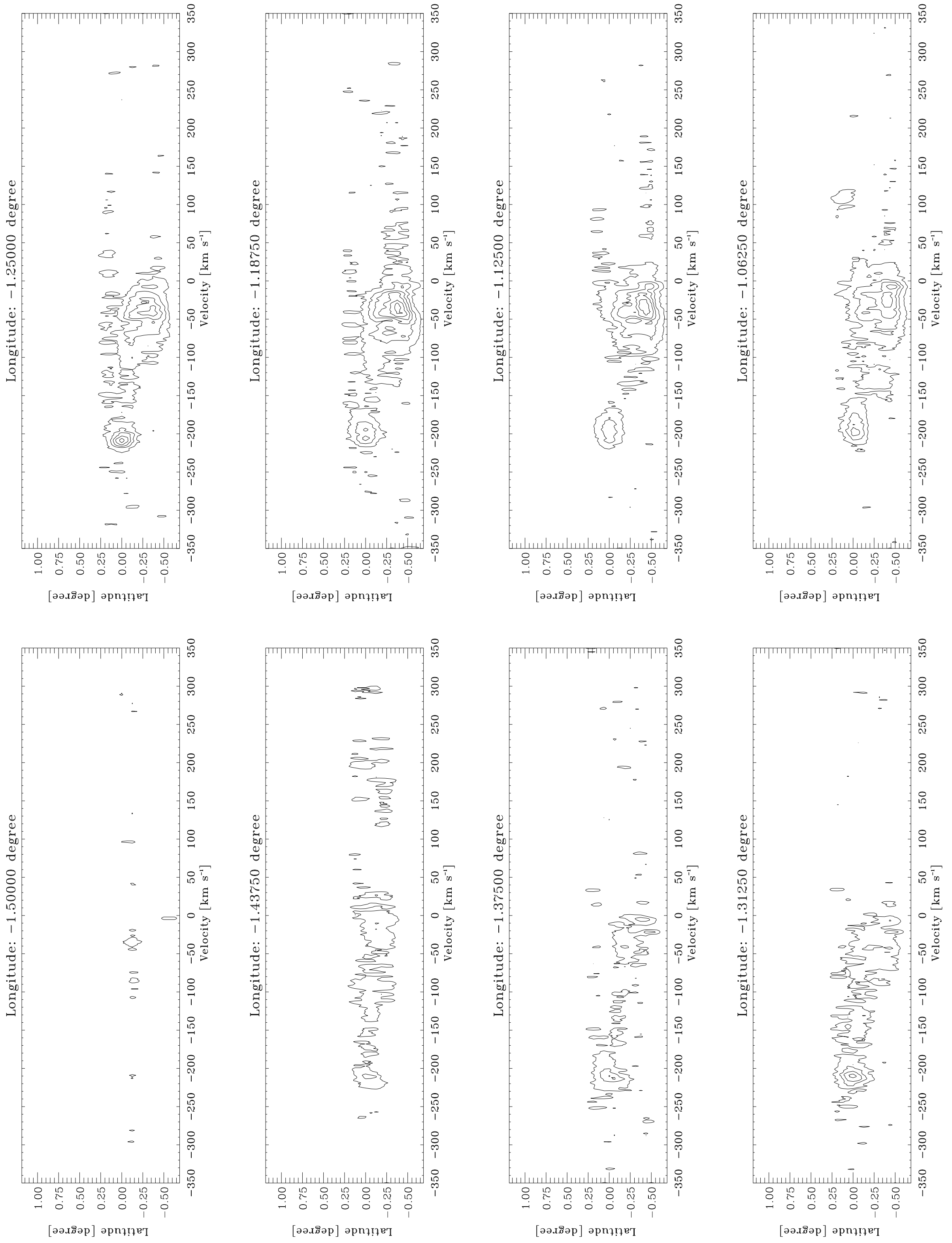

Fig. B3.5. continued.

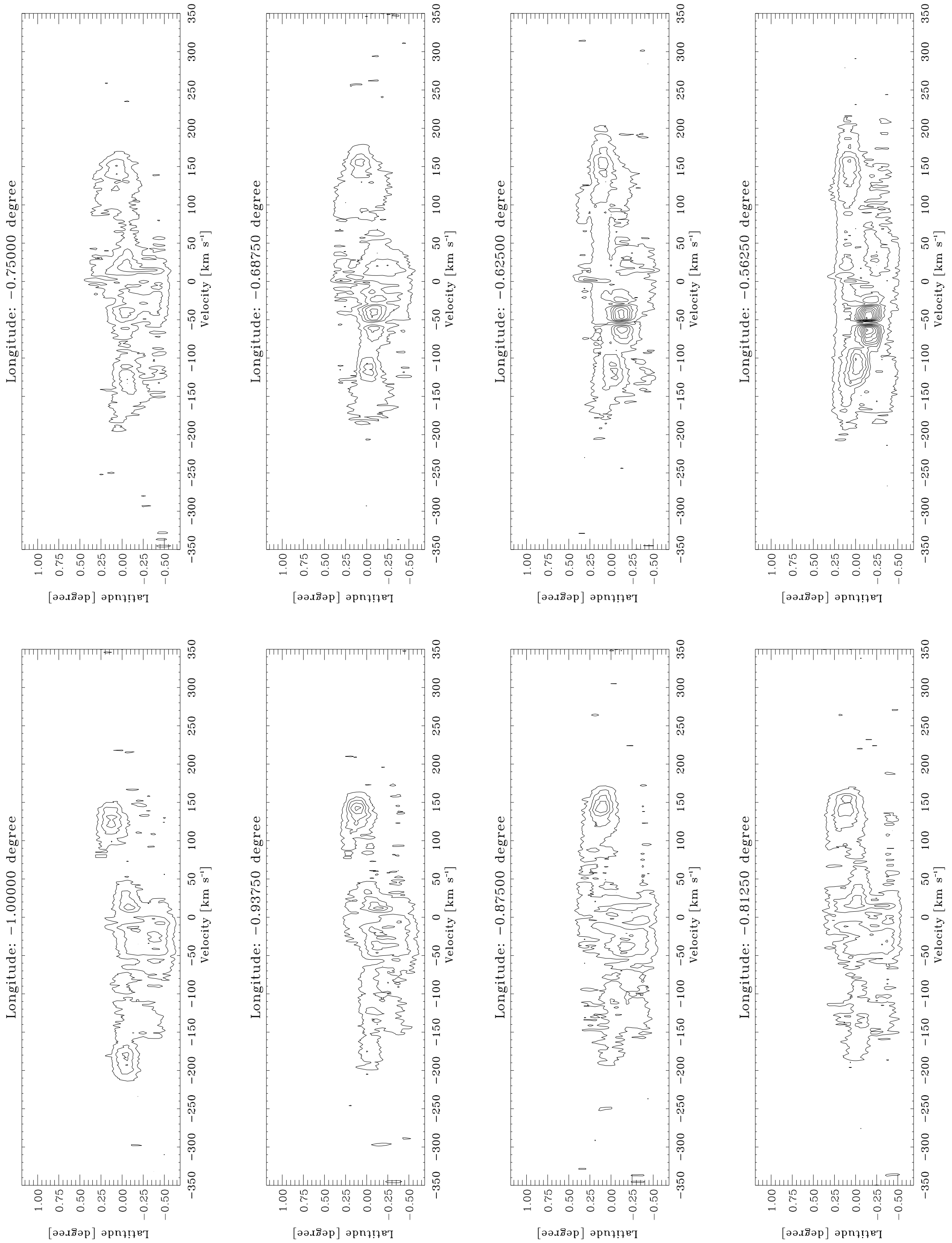

Fig. B3.6. continued.

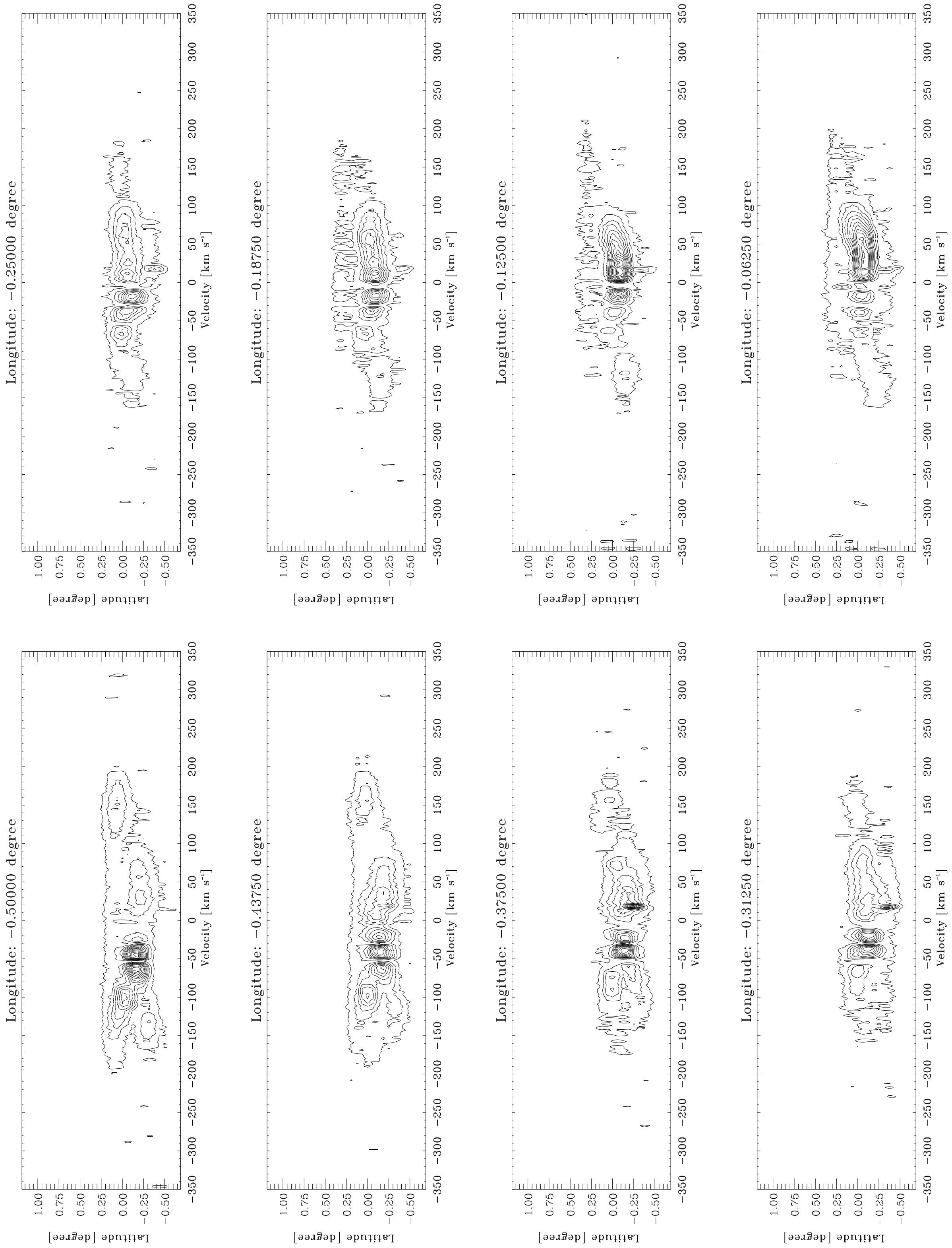

Fig. B3.7. continued.

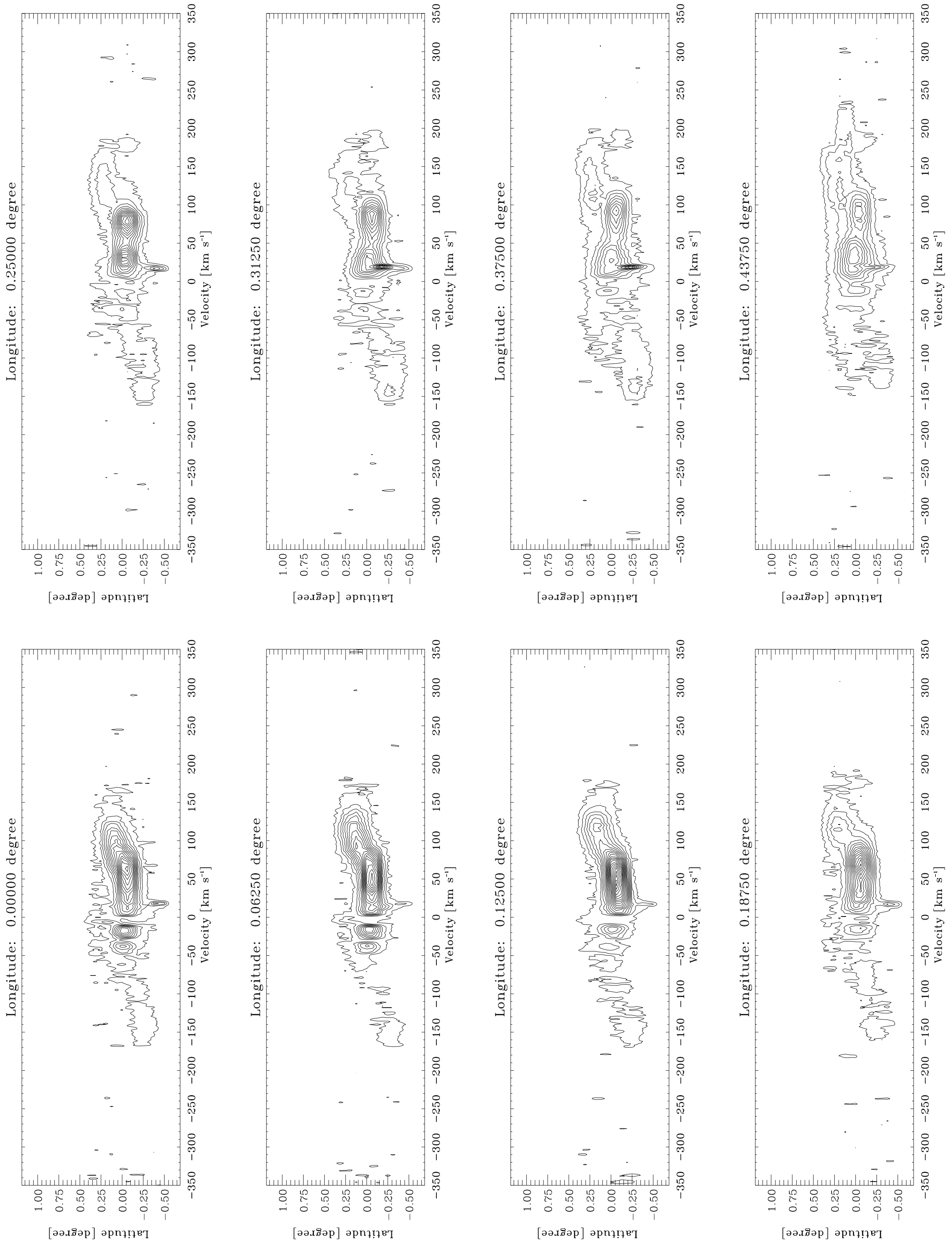

Fig. B3.8. continued.

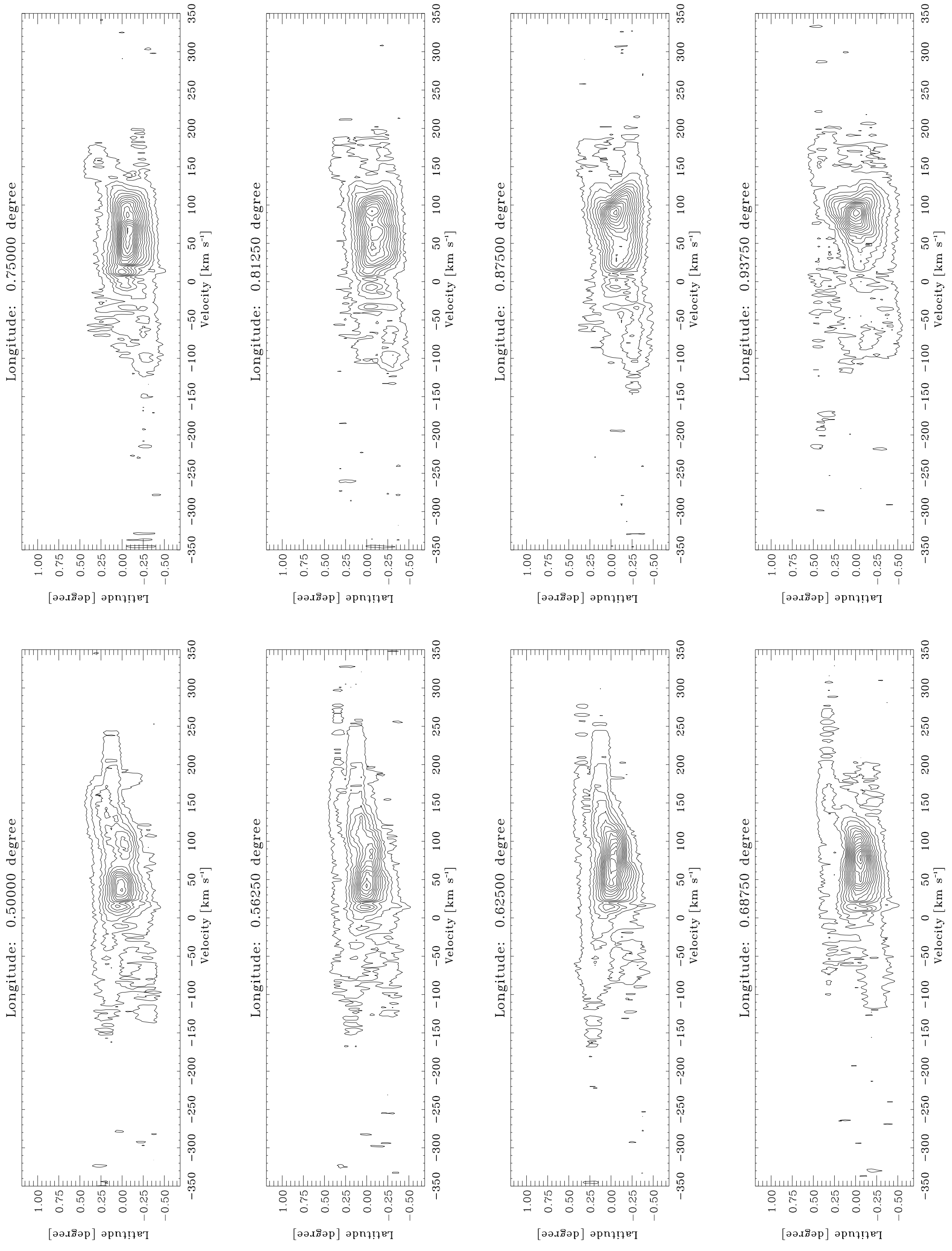

Fig. B3.9. continued.

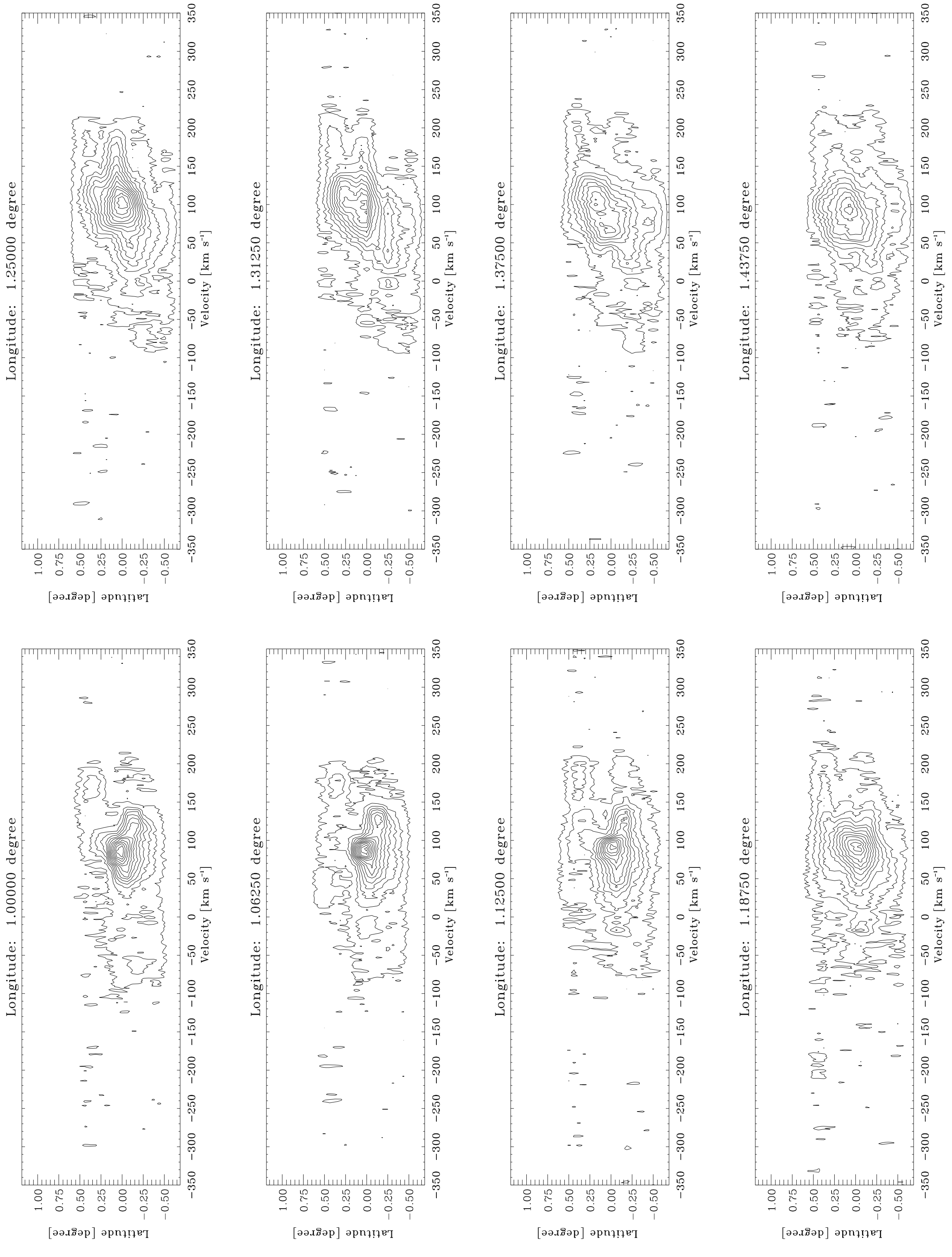

Fig. B3.10. continued.

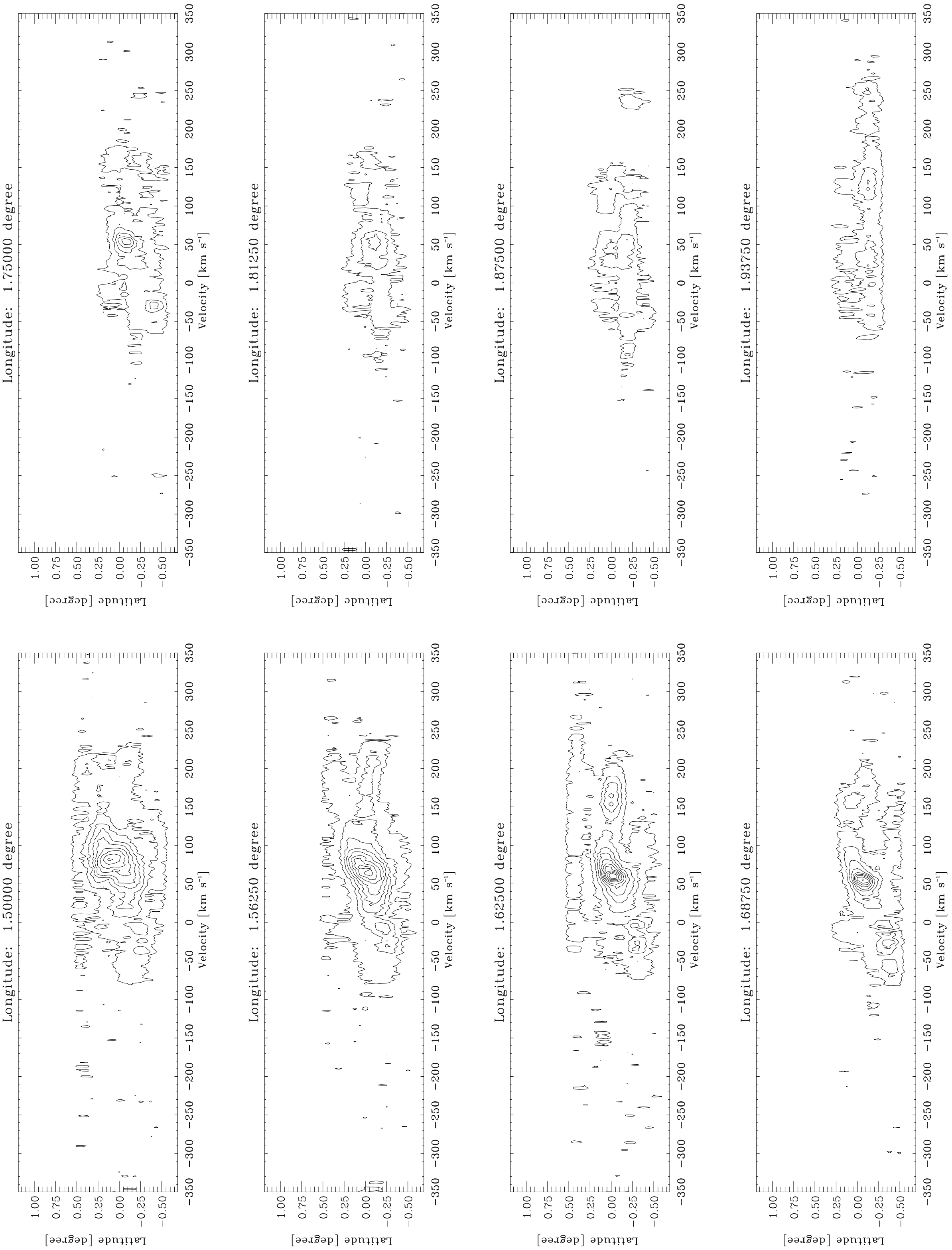

Fig. B3.11. continued.

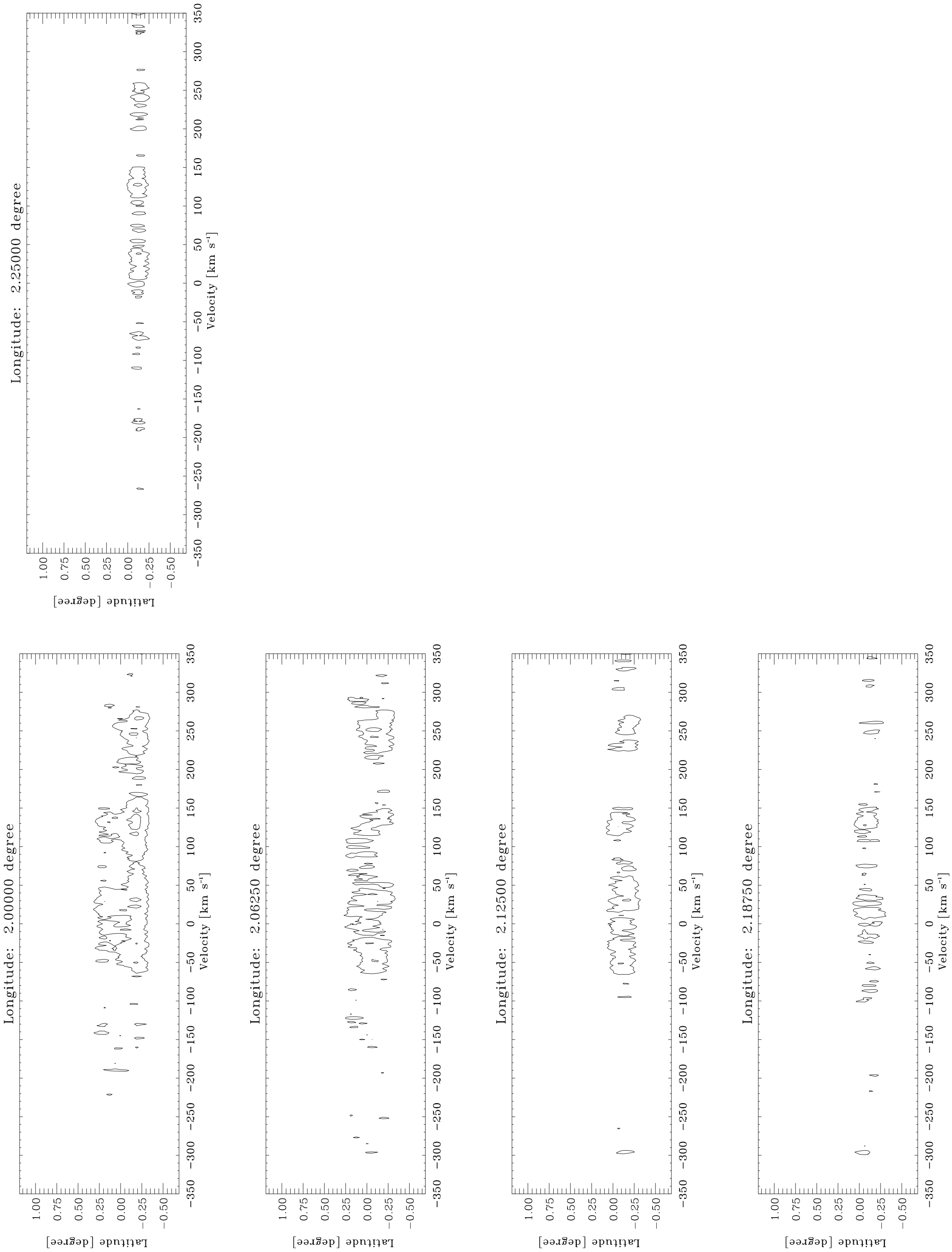

Fig. B3.12. continued.

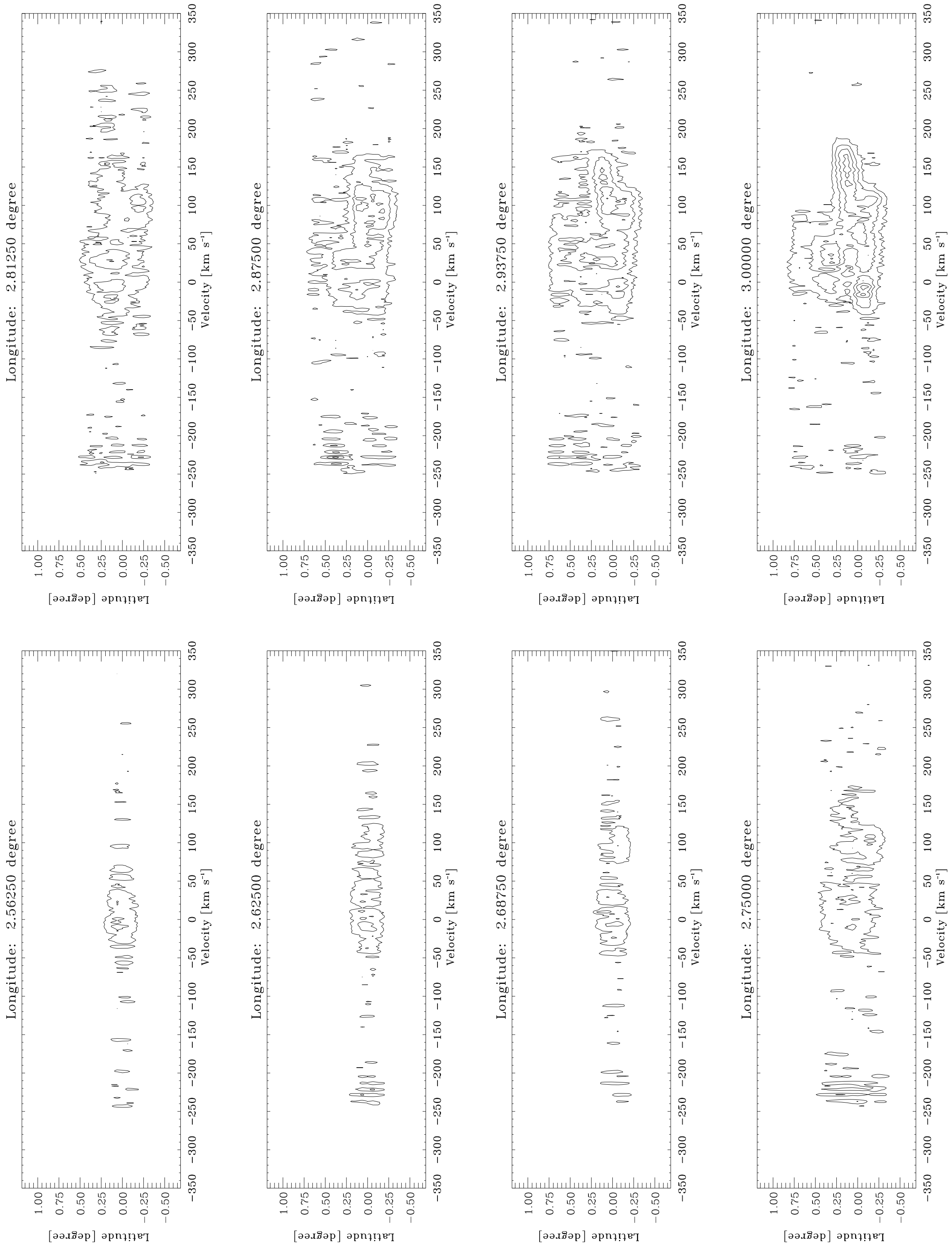

Fig. B3.13. continued.

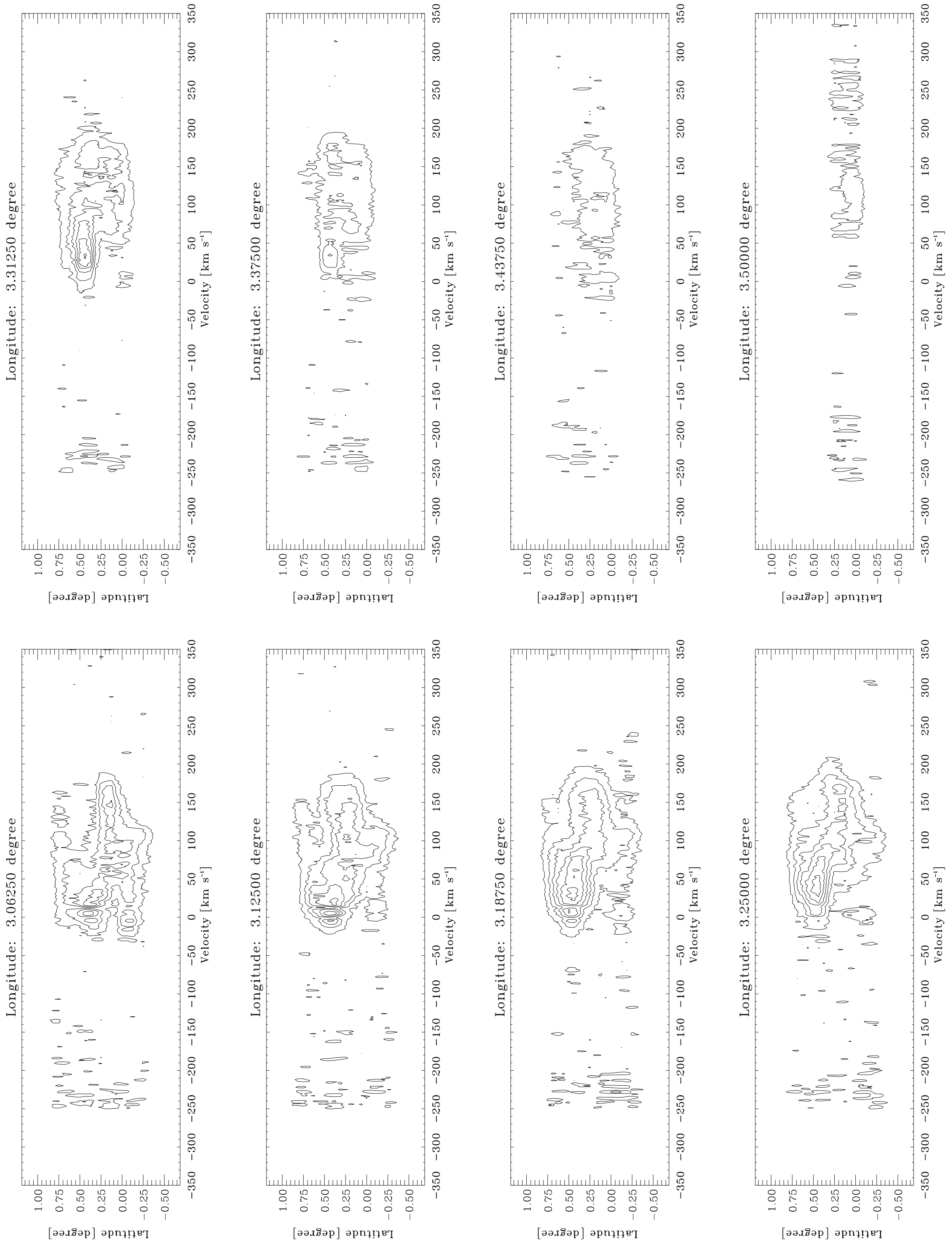

Fig. B3.14. continued.

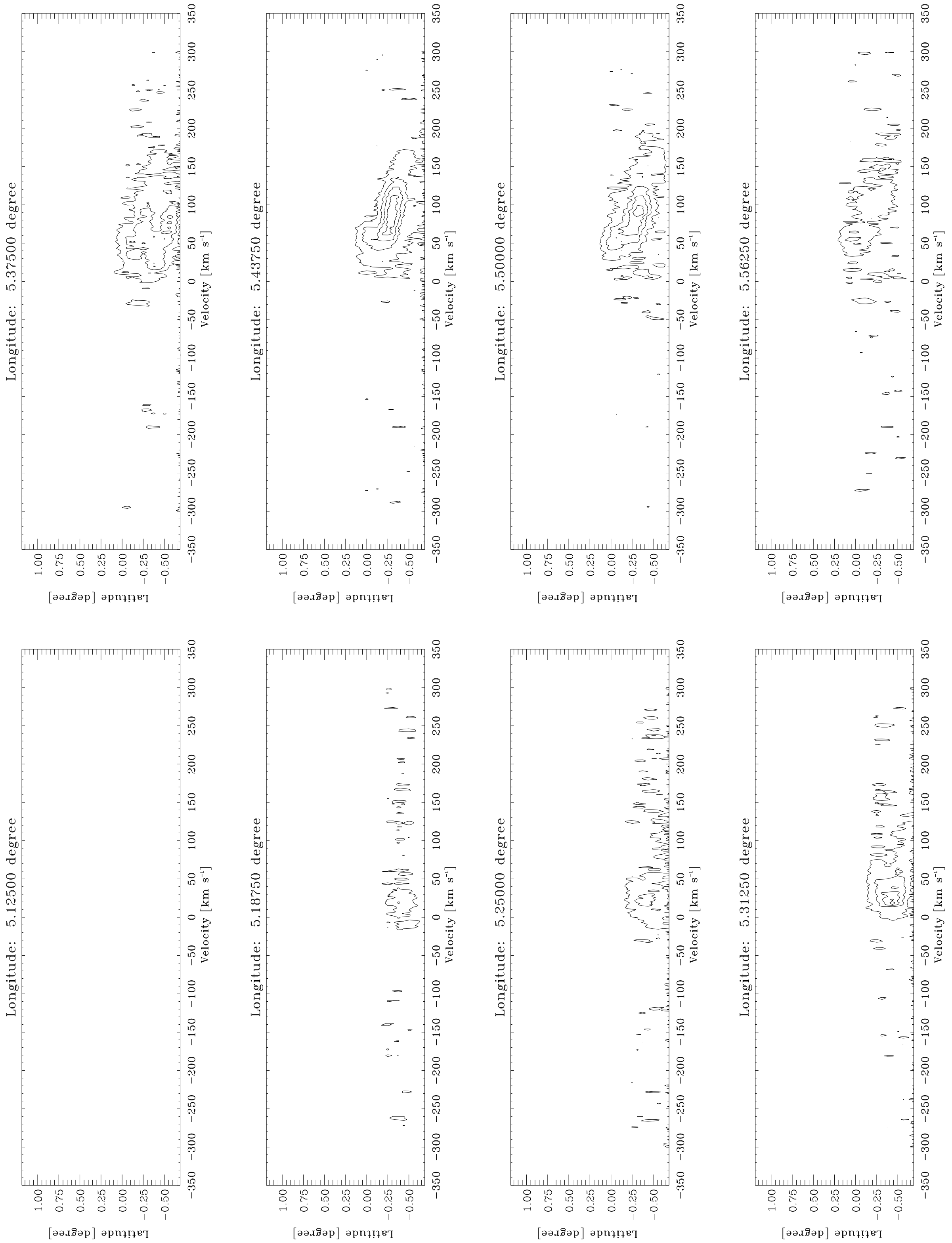

Fig. B3.15. continued.

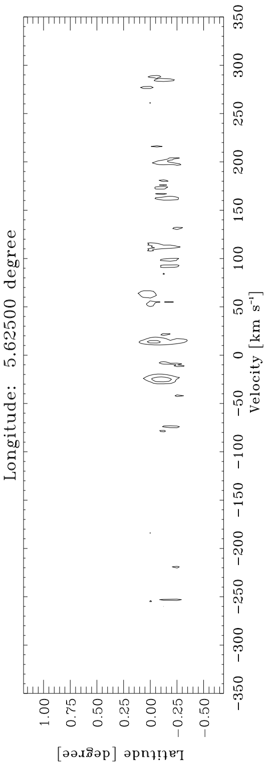

Fig. B3.16. continued.

Appendix C: SiO Galactic center survey

In this section we present the channel maps of the SiO emission in the Galactic center region integrated in velocity over 10 km s^{-1} wide channels. The contour levels start at 0.2 K km s^{-1} (3σ) and increase in steps of 0.66 K km s^{-1} (10σ). The dotted contour is at 0.13 K km s^{-1} (2σ).

Figure C.2 shows $l-v$ diagrams integrated in latitude in steps of $0\overset{\circ}{.}0625$ in SiO. The contours levels start at 0.0013 K (3σ) and increase them in steps of 0.0018 K (4σ).

Figure C.3 is a set of latitude-velocity diagrams integrated in steps of $0\overset{\circ}{.}0625$. The contours levels start at 0.0013 K (3σ) and increase them in step of 0.0026 K (6σ).

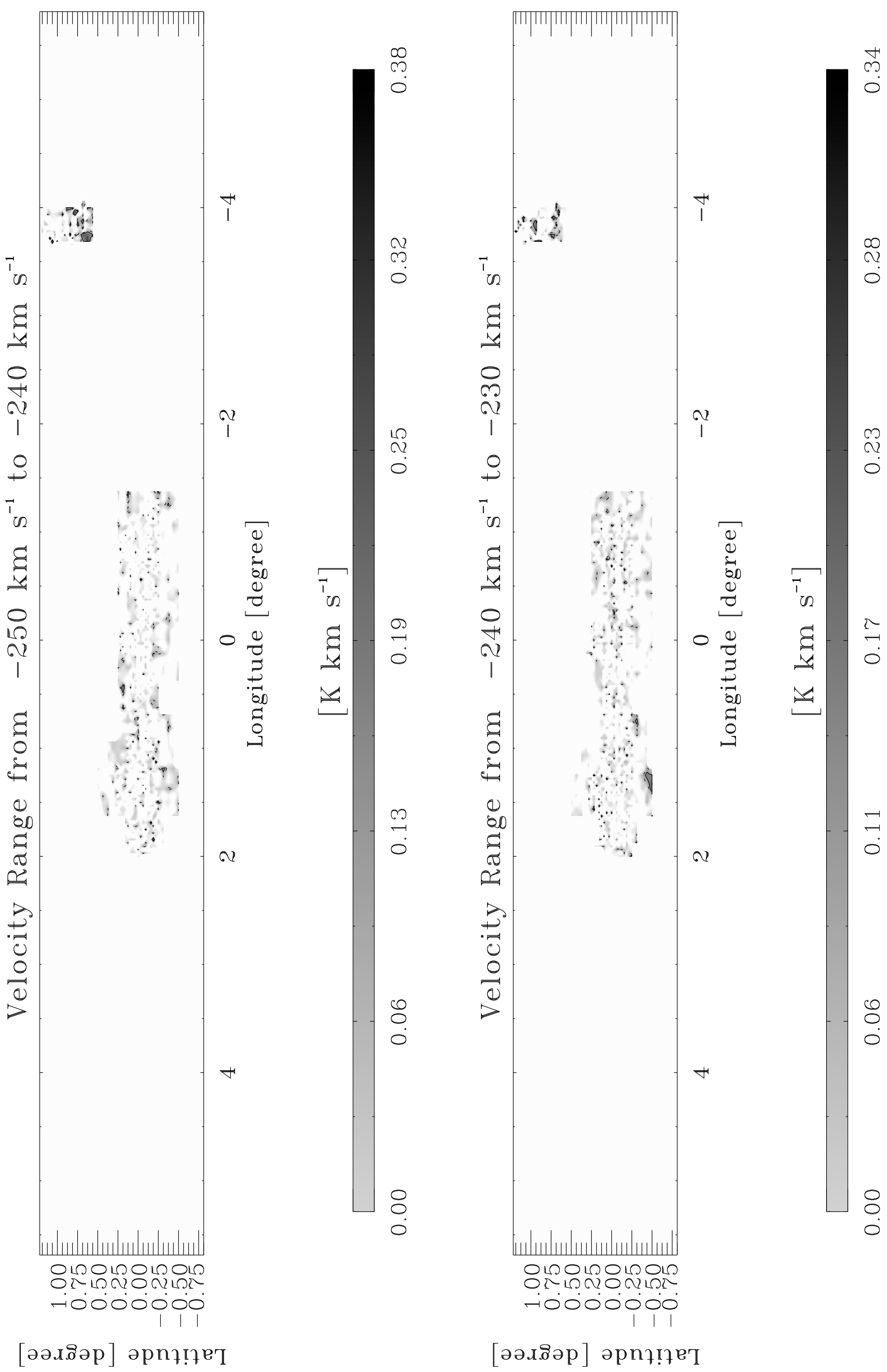

Fig. C1.1. The integrated intensity of the Galactic center region in SiO (1−0) in velocity intervals of 10 km s^{-1} width. The solid contour levels start at 0.2 K, which is the 3σ-level, and increase in steps of 0.66 K km s^{-1} (10σ). The dotted contour is at 0.13 K km s^{-1} (2σ).

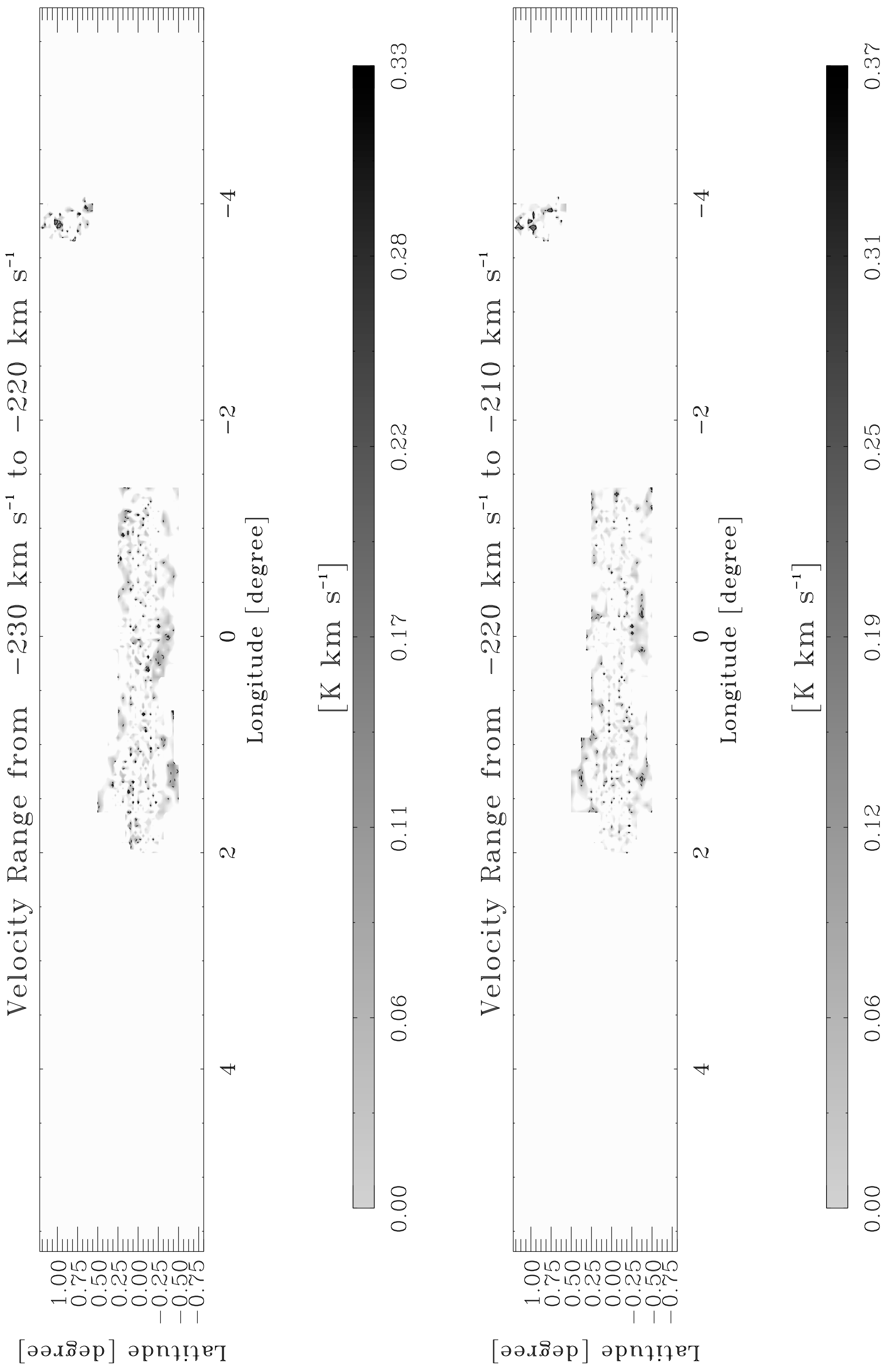

Fig. C1.2. continued.

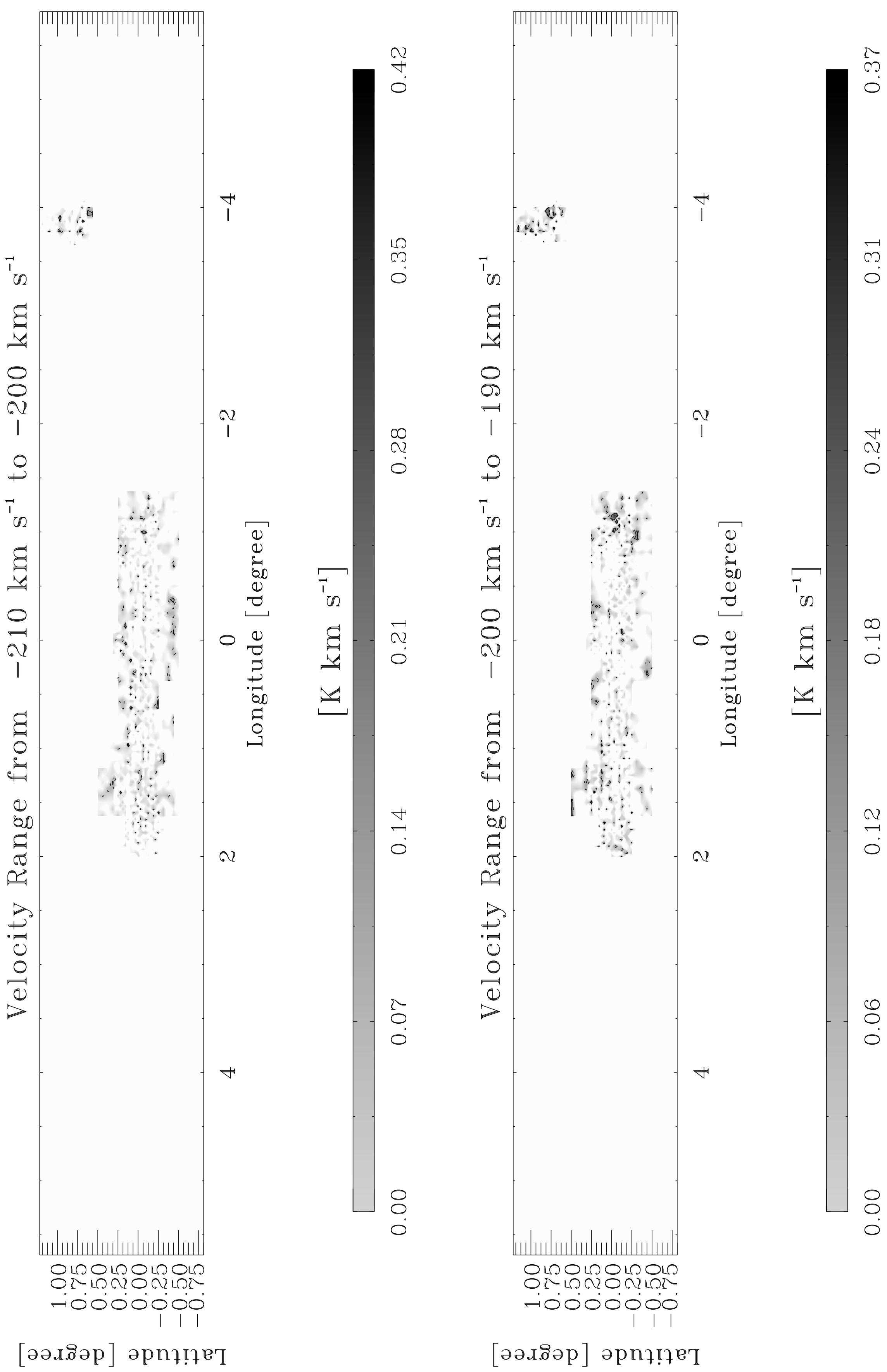

Fig. C1.3. continued.

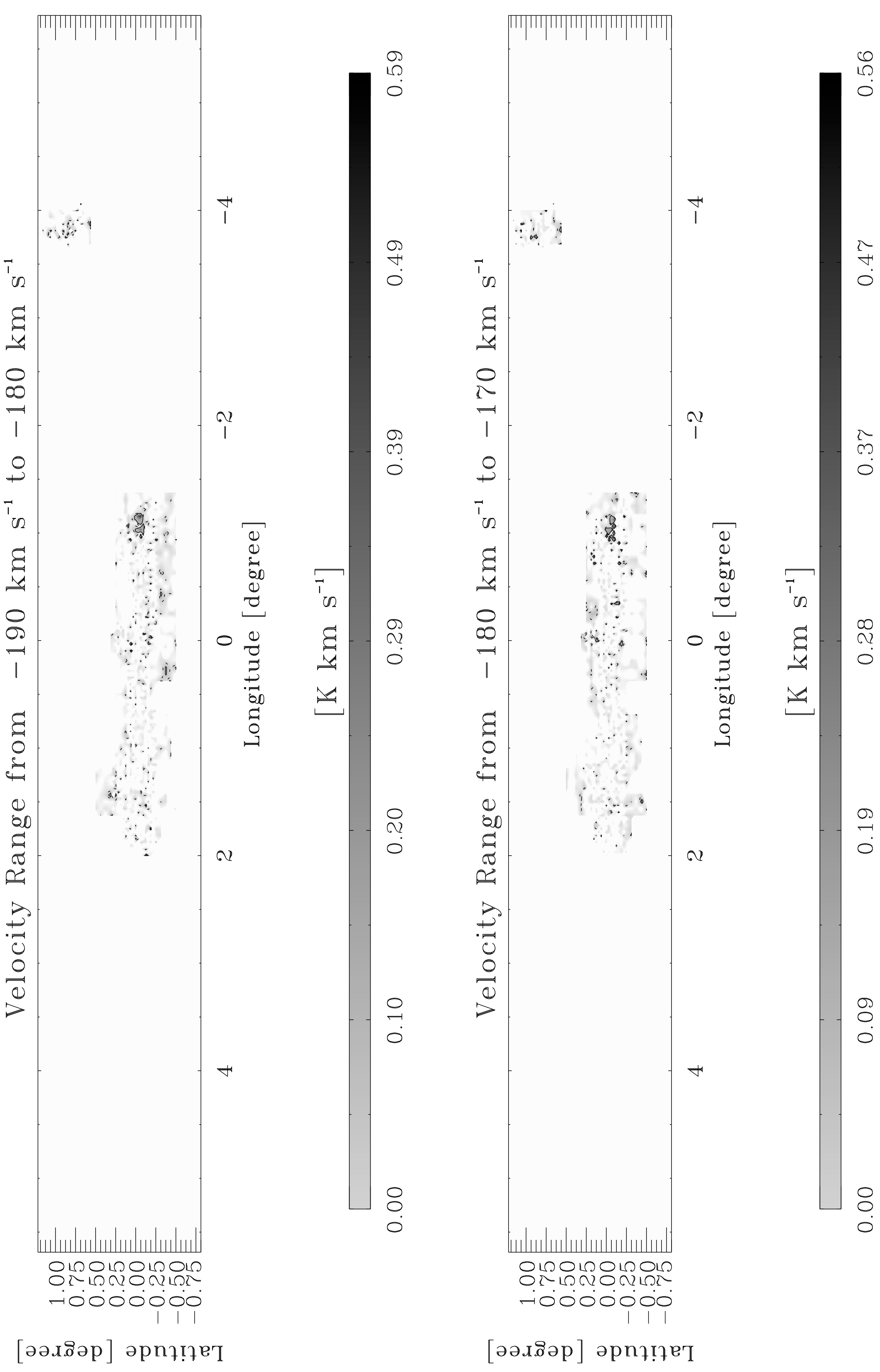

Fig. C1.4. continued.

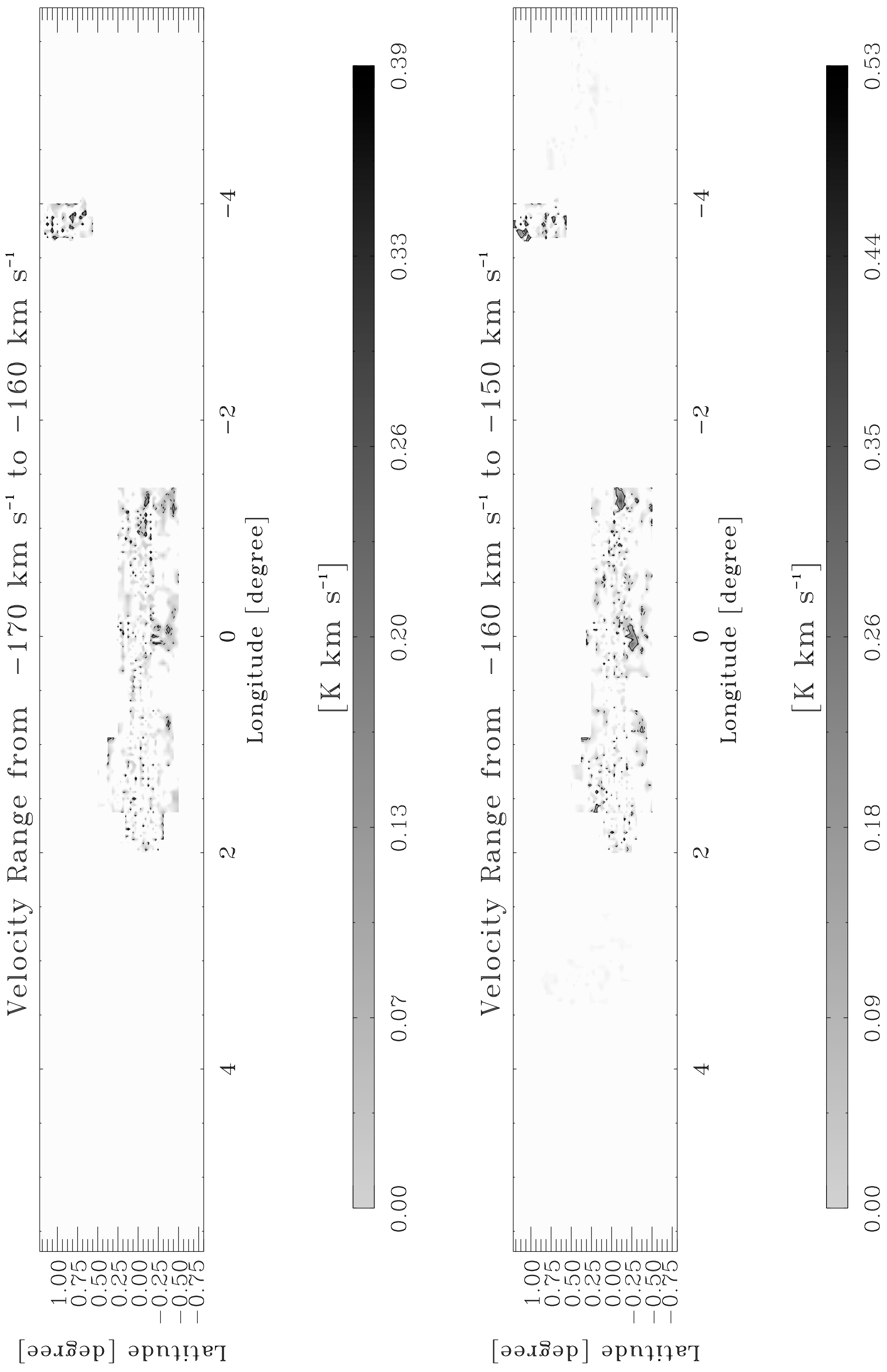

Fig. C1.5. continued.

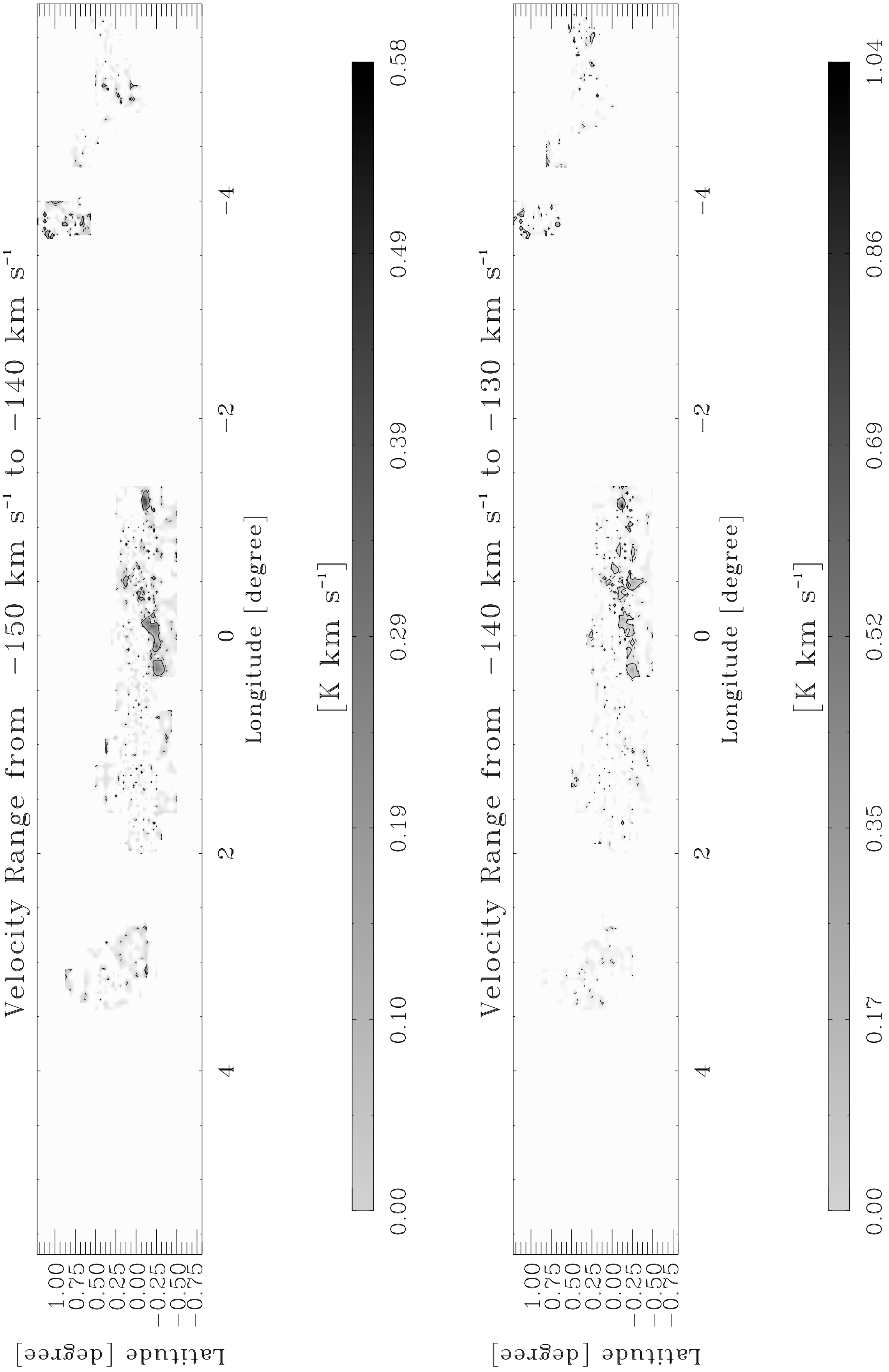

Fig. C1.6. continued.

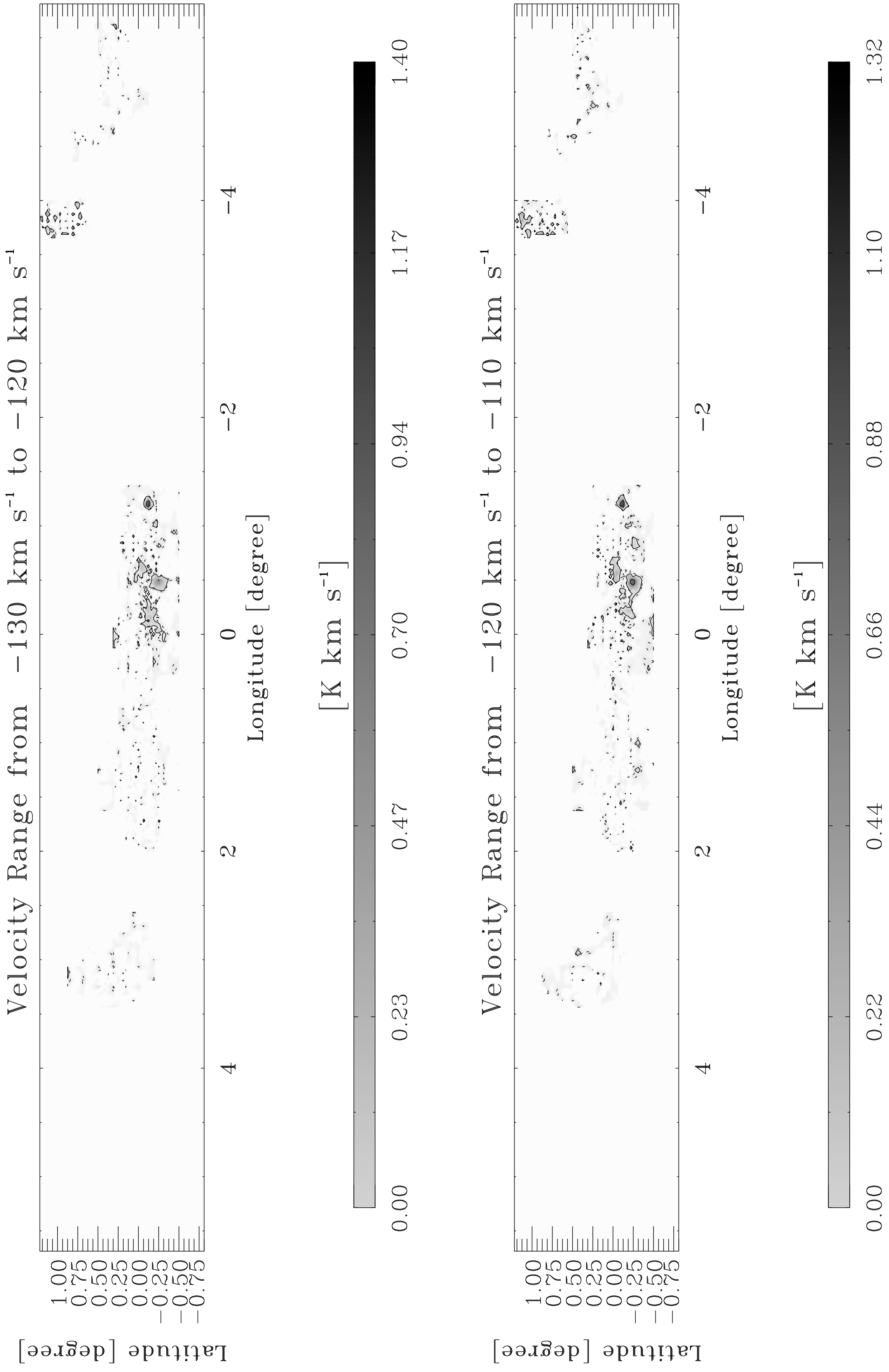

Fig. C1.7. continued.

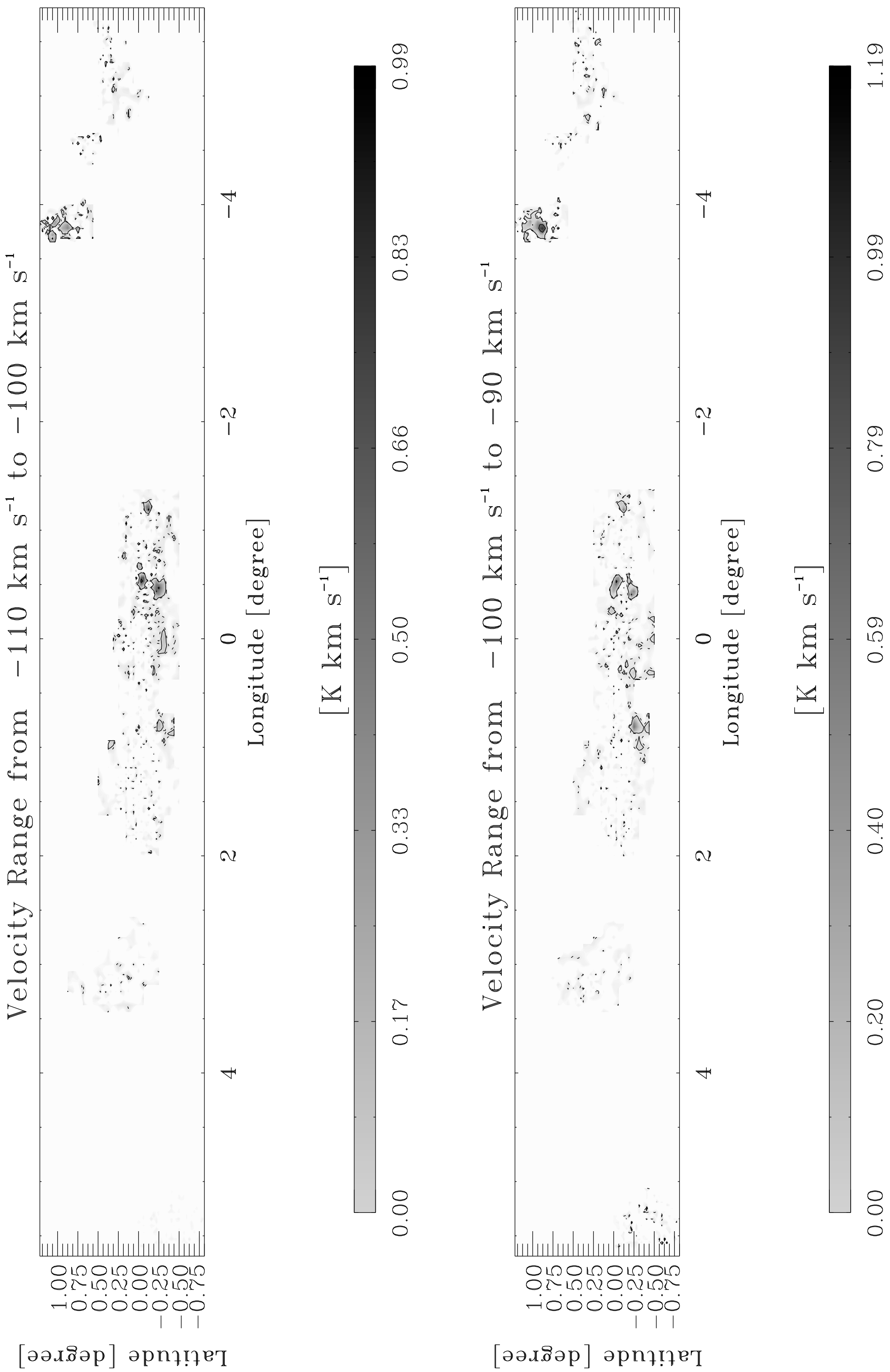

Fig. C1.8. continued.

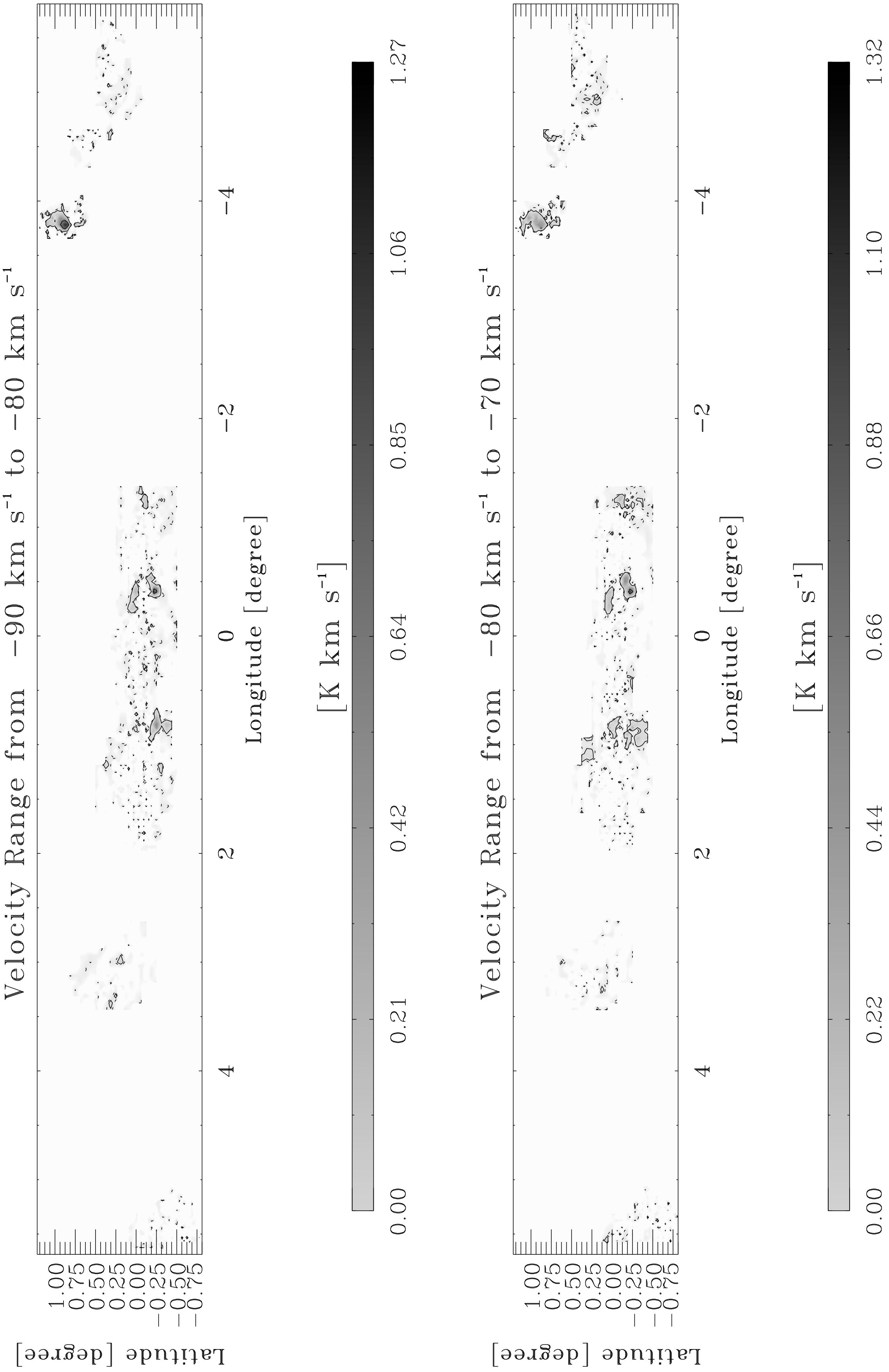

Fig. C1.9. continued.

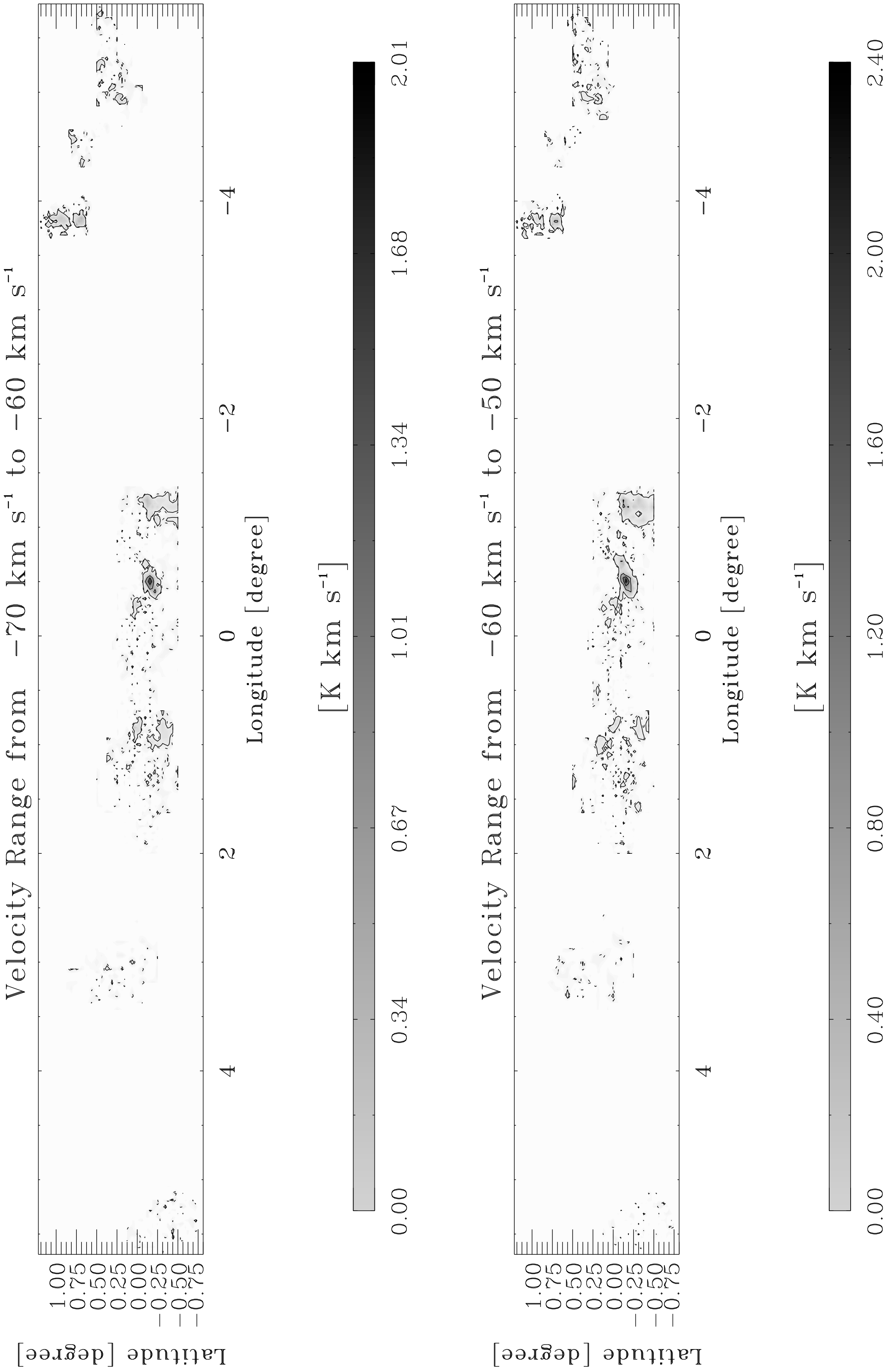

Fig. C1.10. continued.

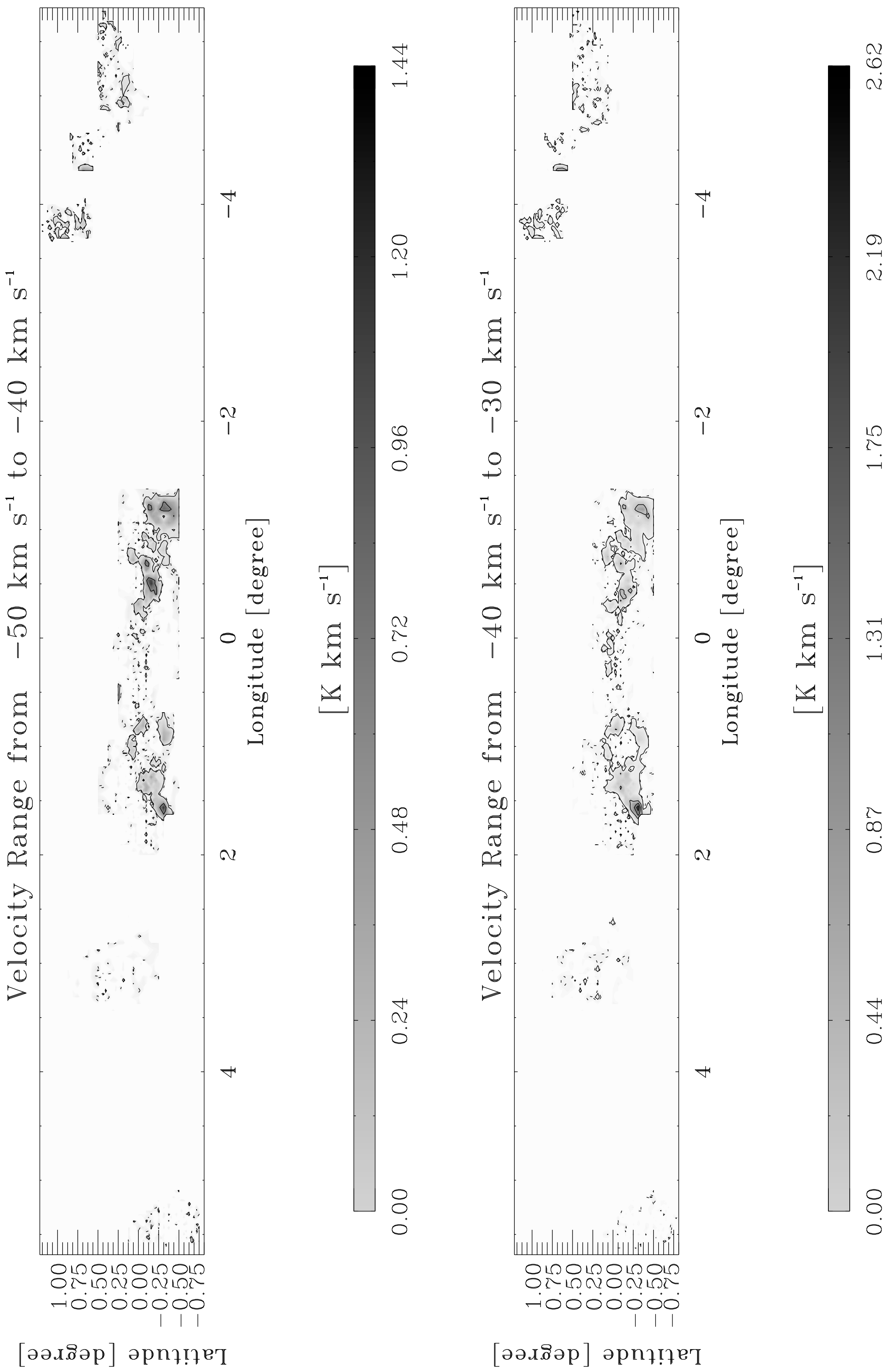

Fig. C1.11. continued.

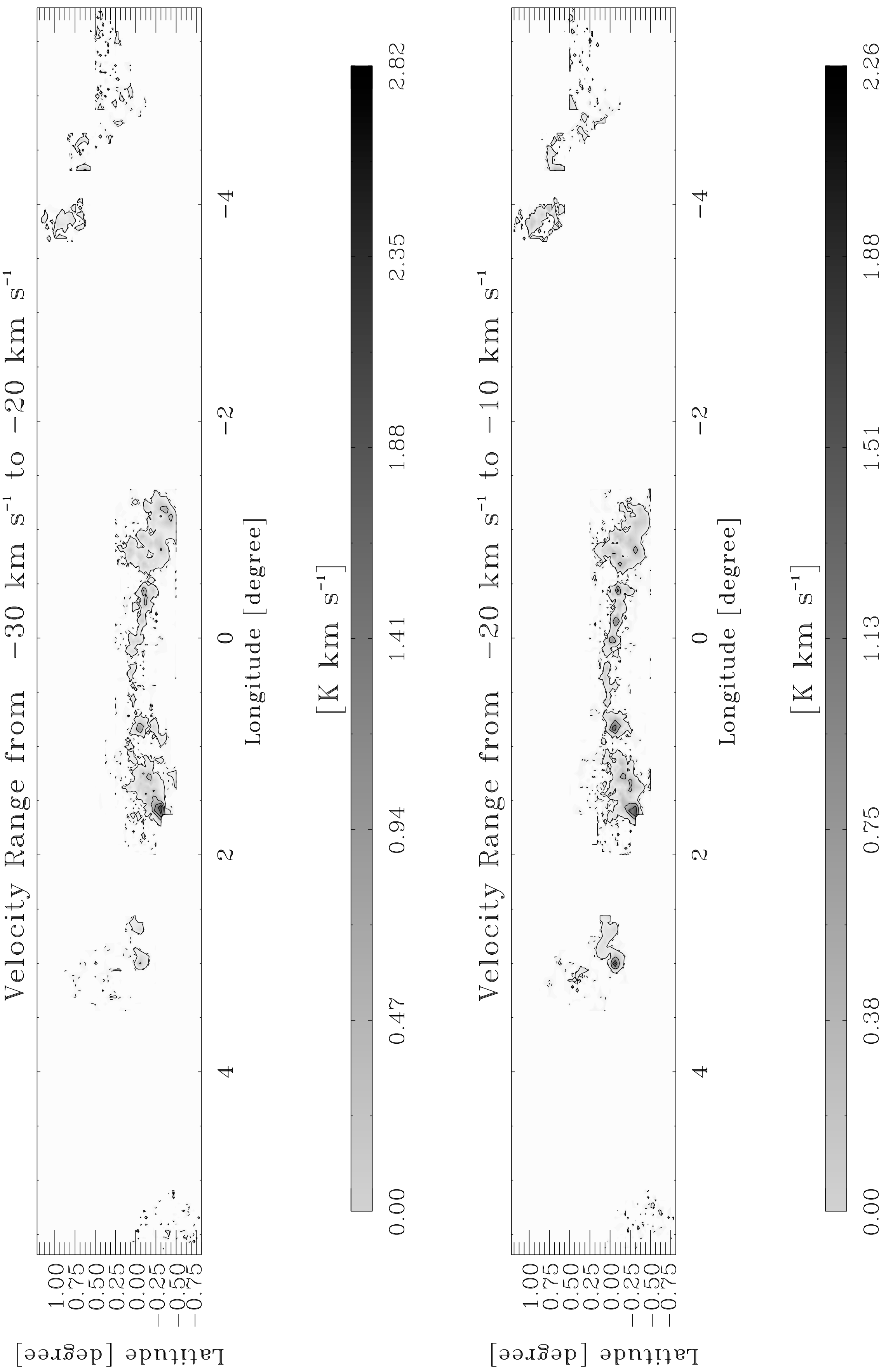

Fig. C1.12. continued.

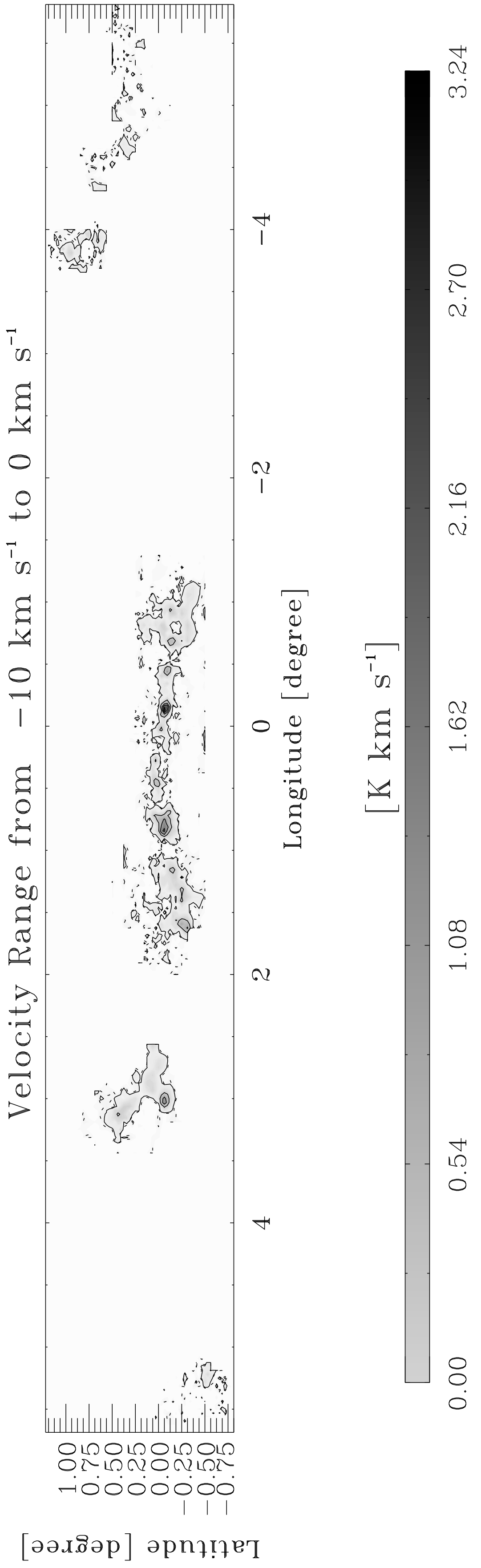

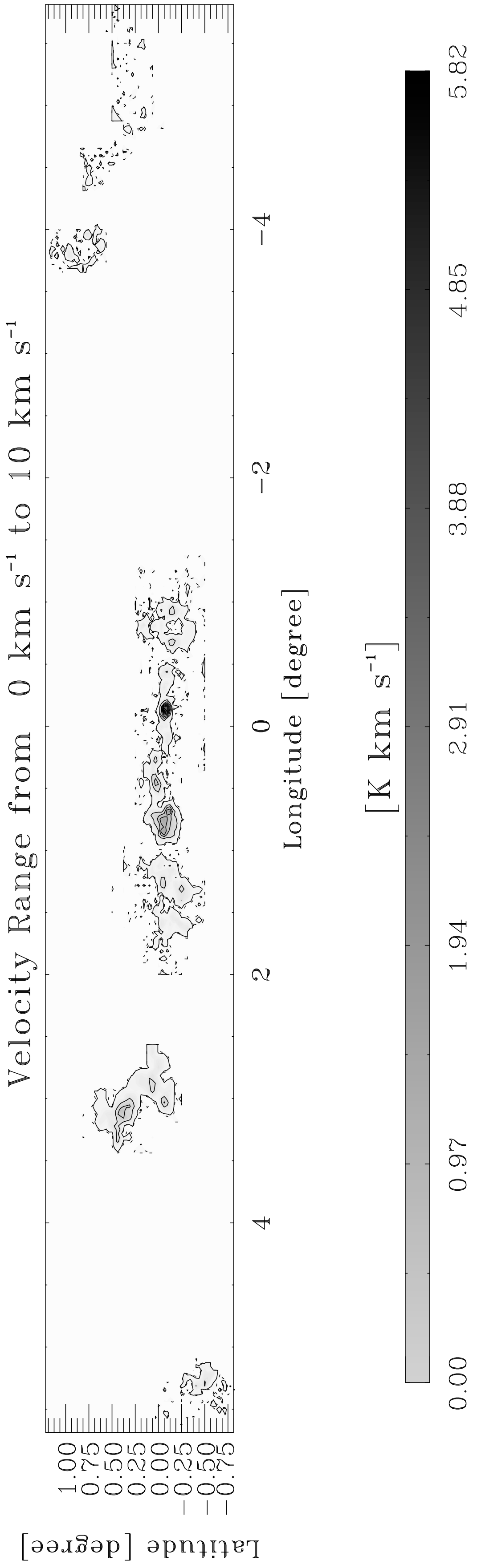

Fig. C1.13. continued.

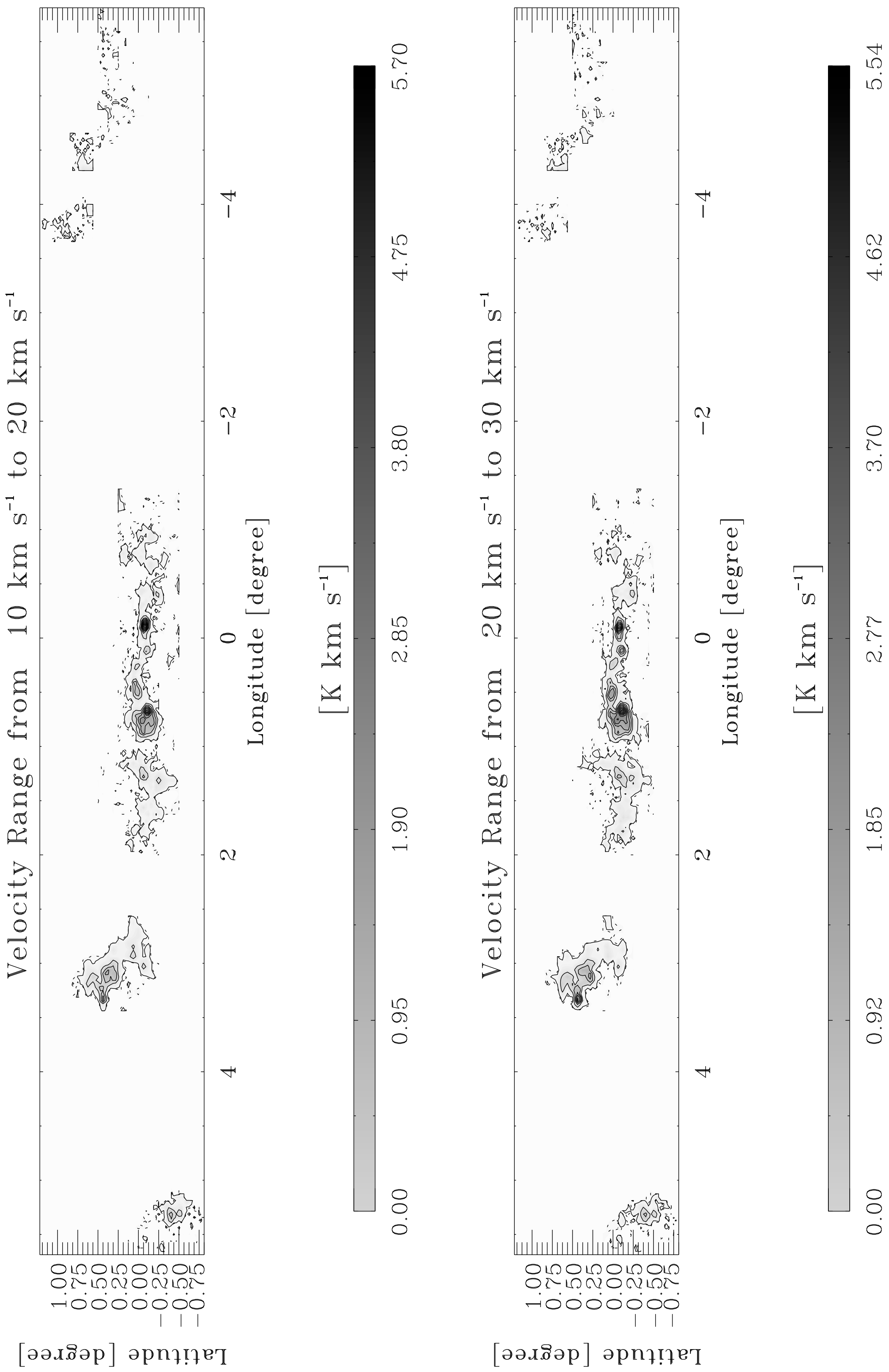

Fig. C1.14. continued.

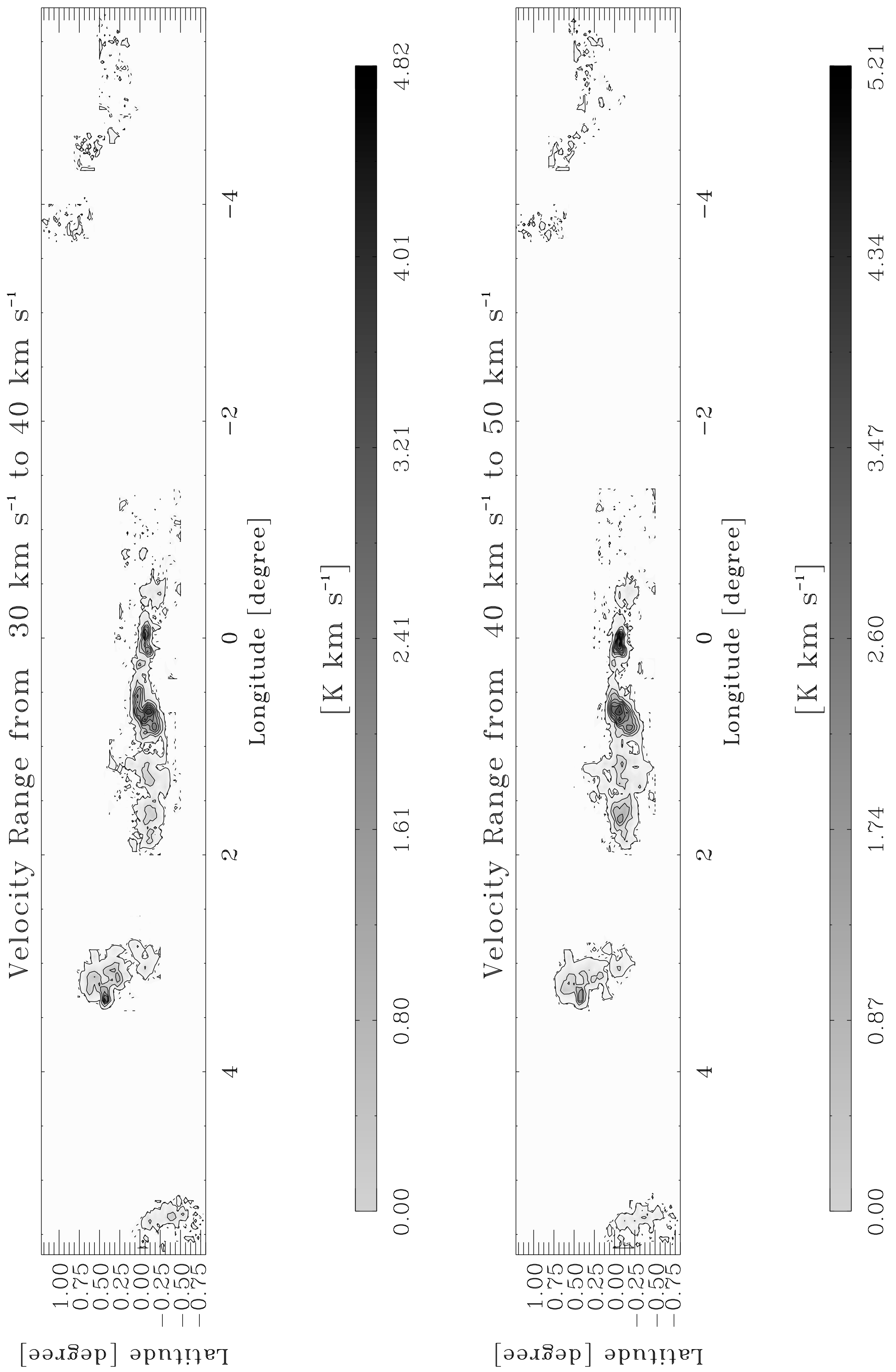

Fig. C1.15. continued.

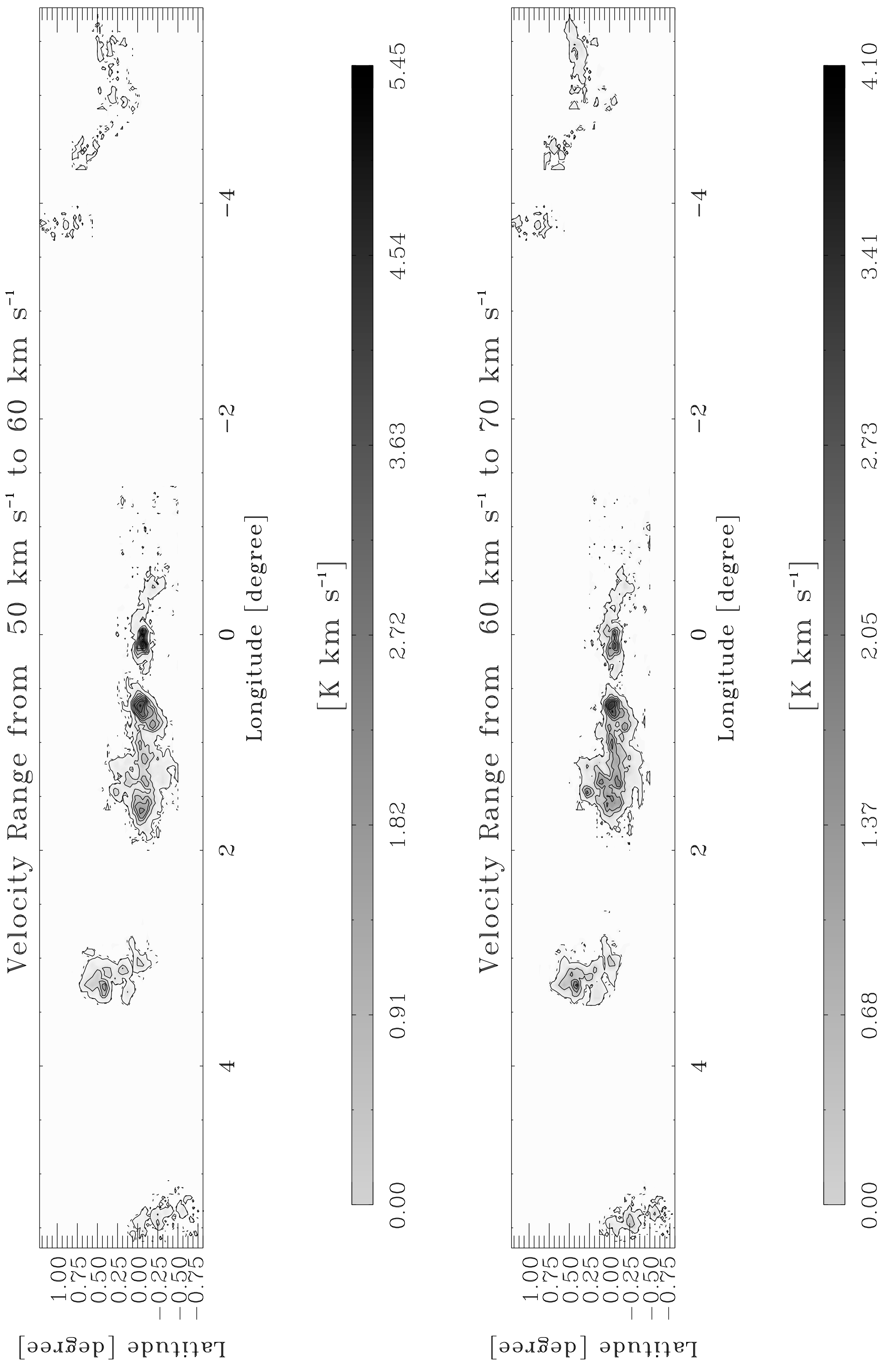

Fig. C1.16. continued.

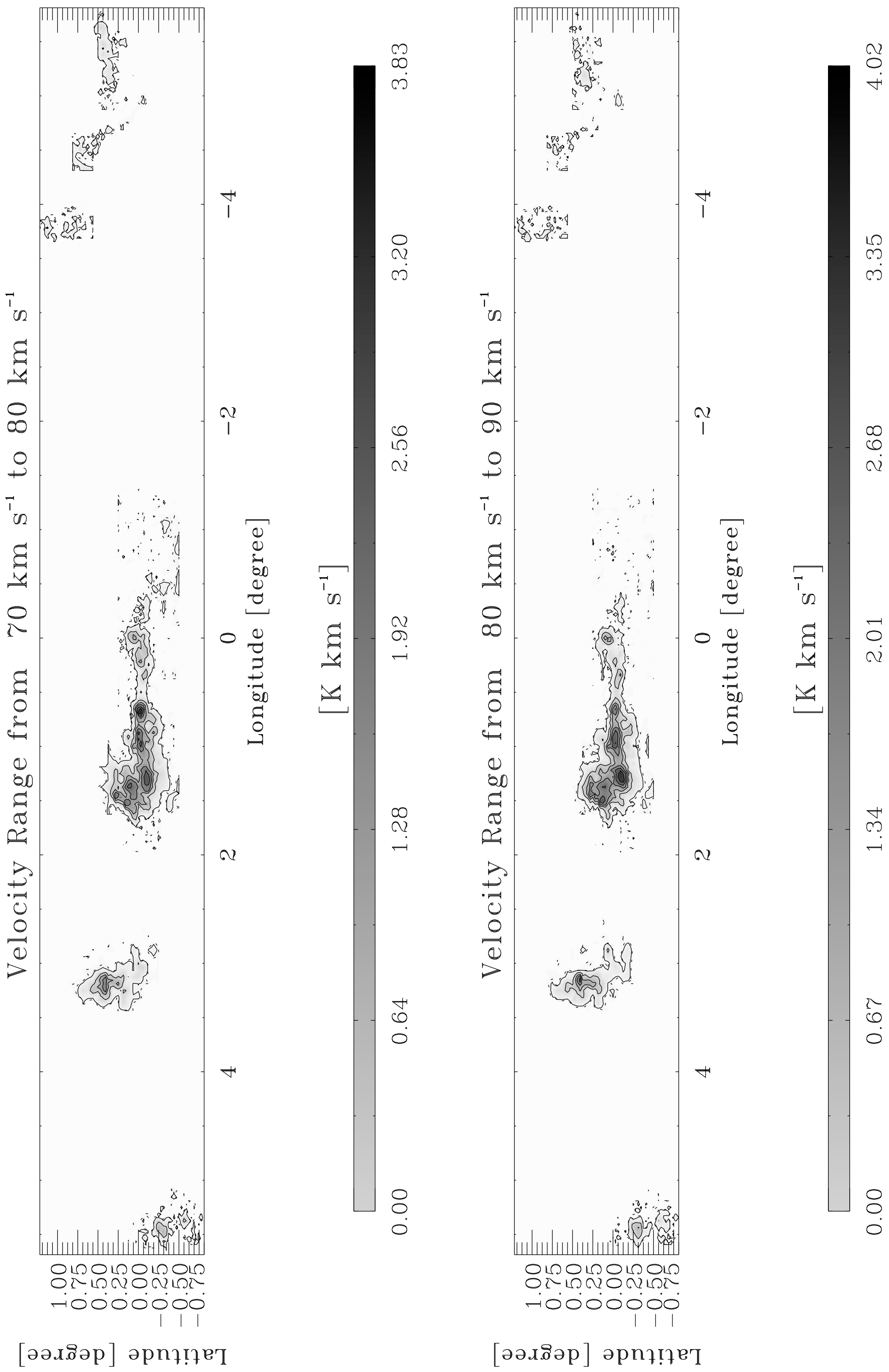

Fig. C1.17. continued.

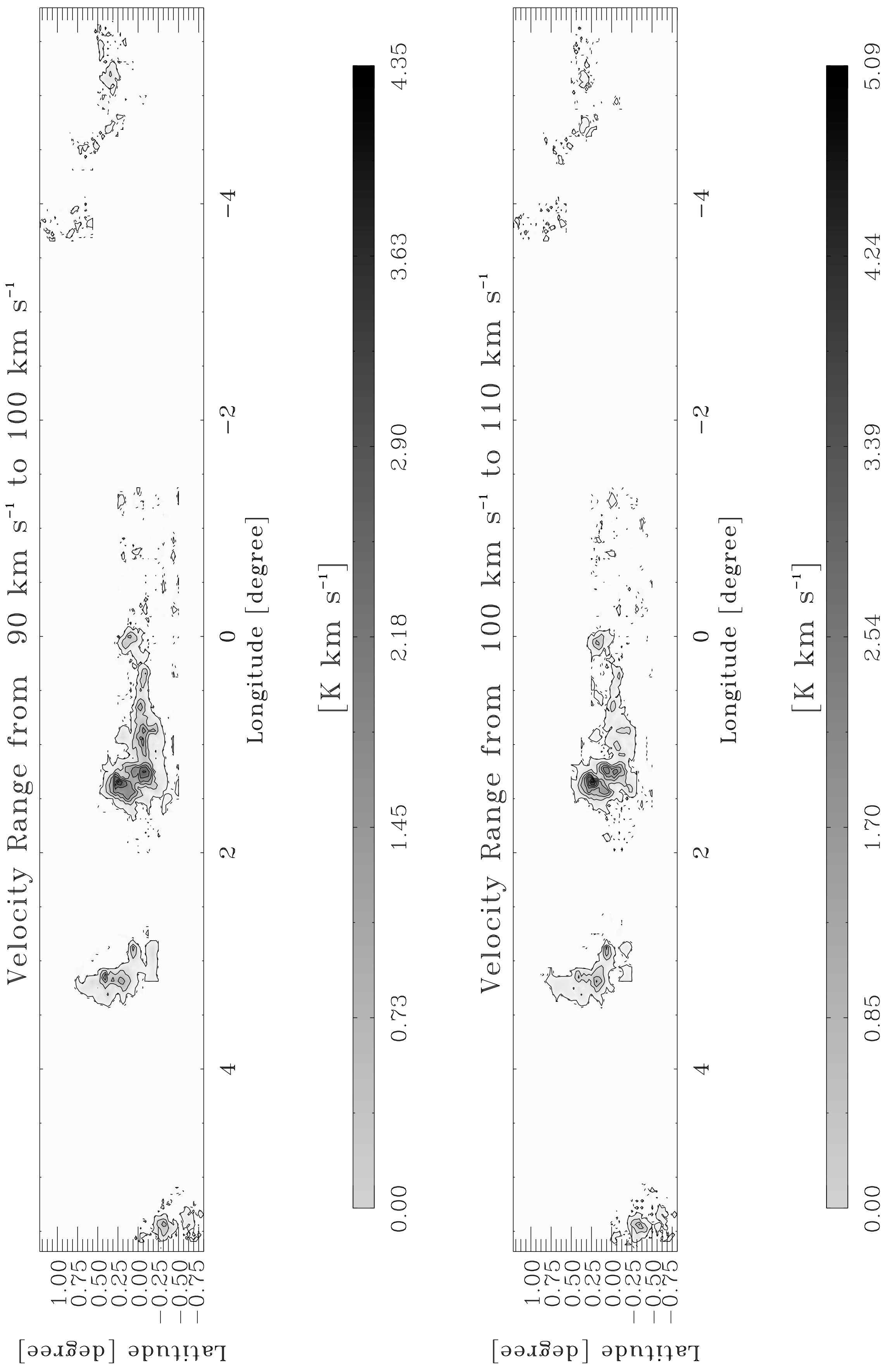

Fig. C1.18. continued.

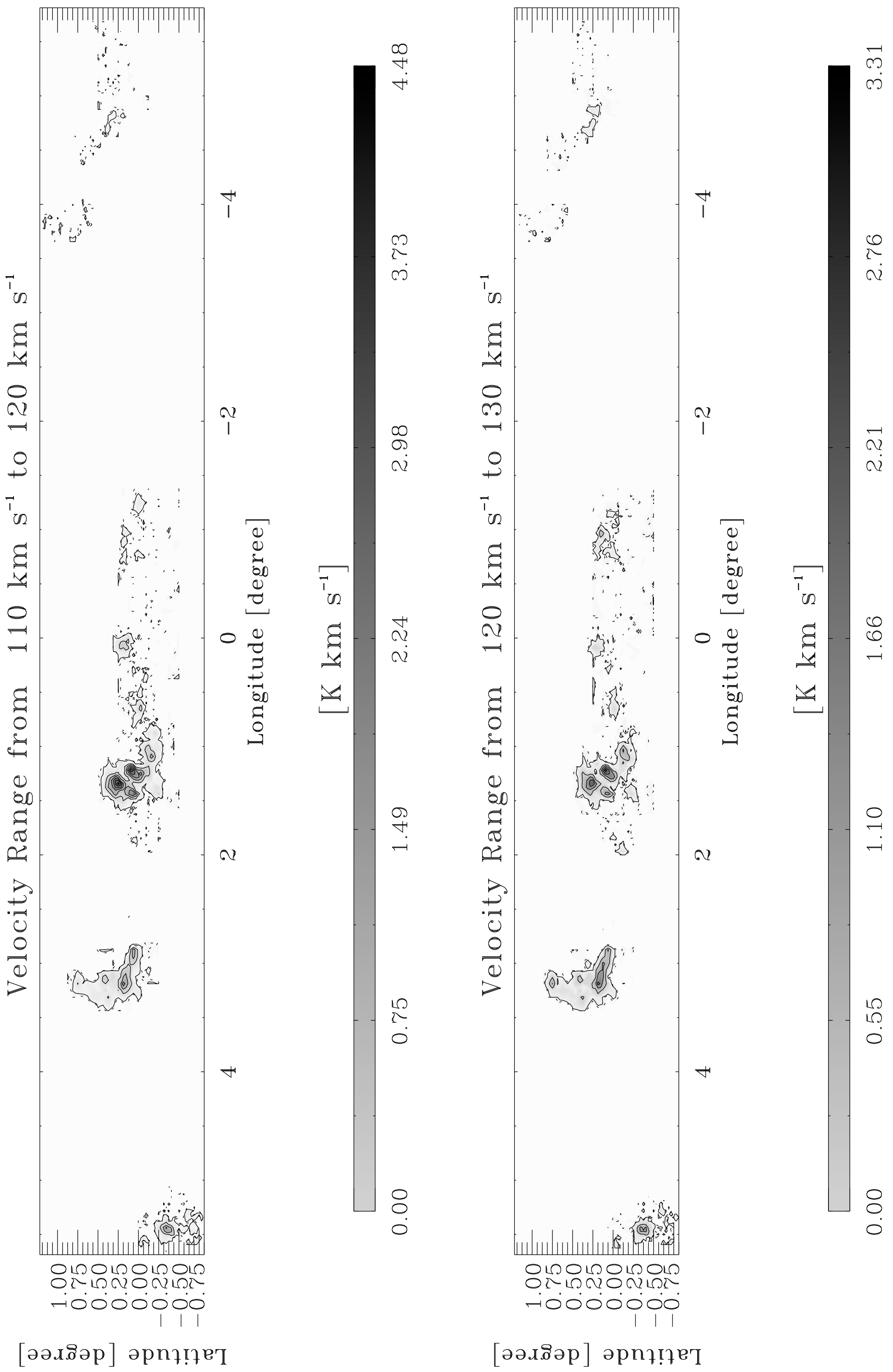

Fig. C1.19. continued.

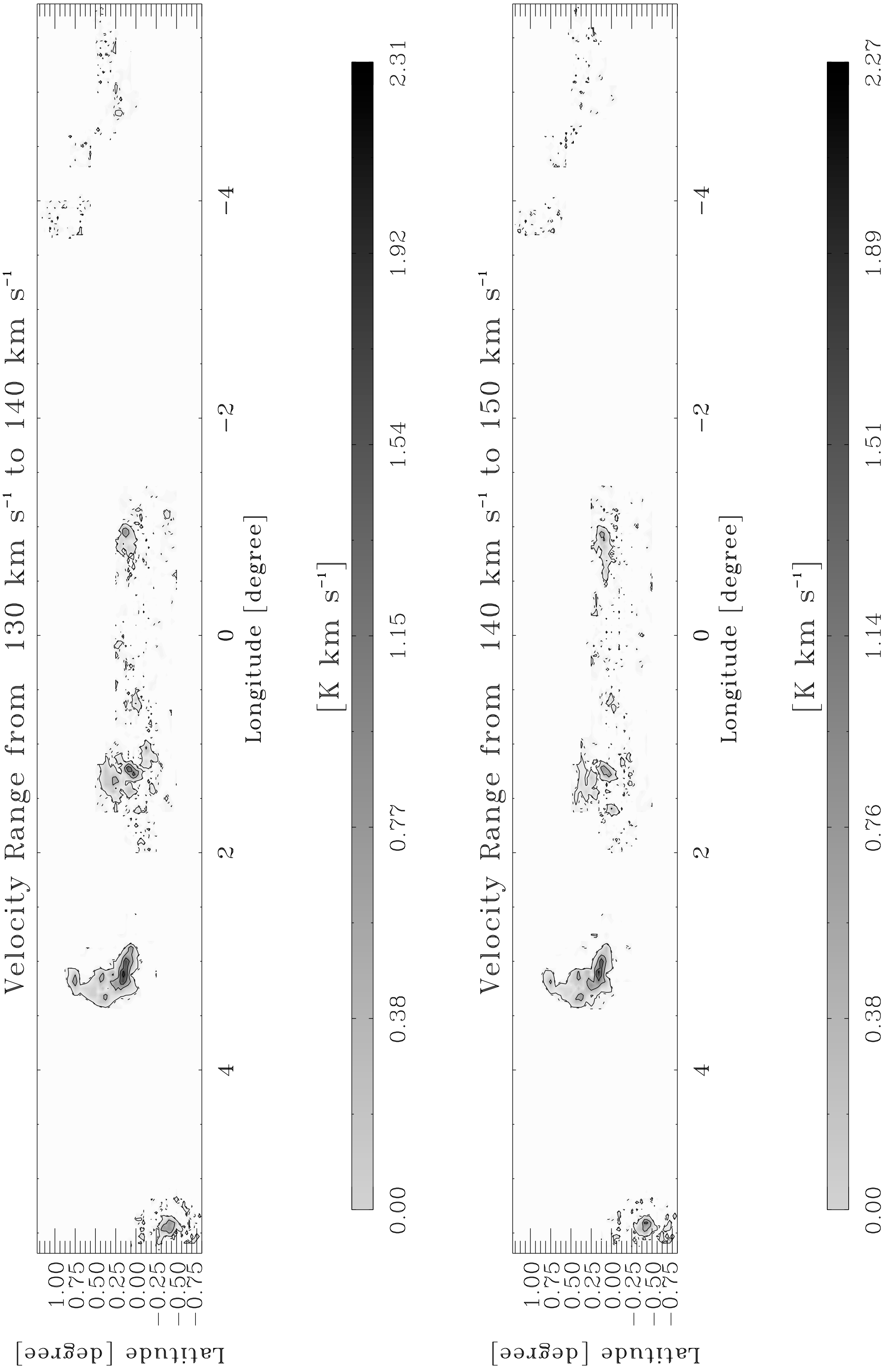

Fig. C1.20. continued.

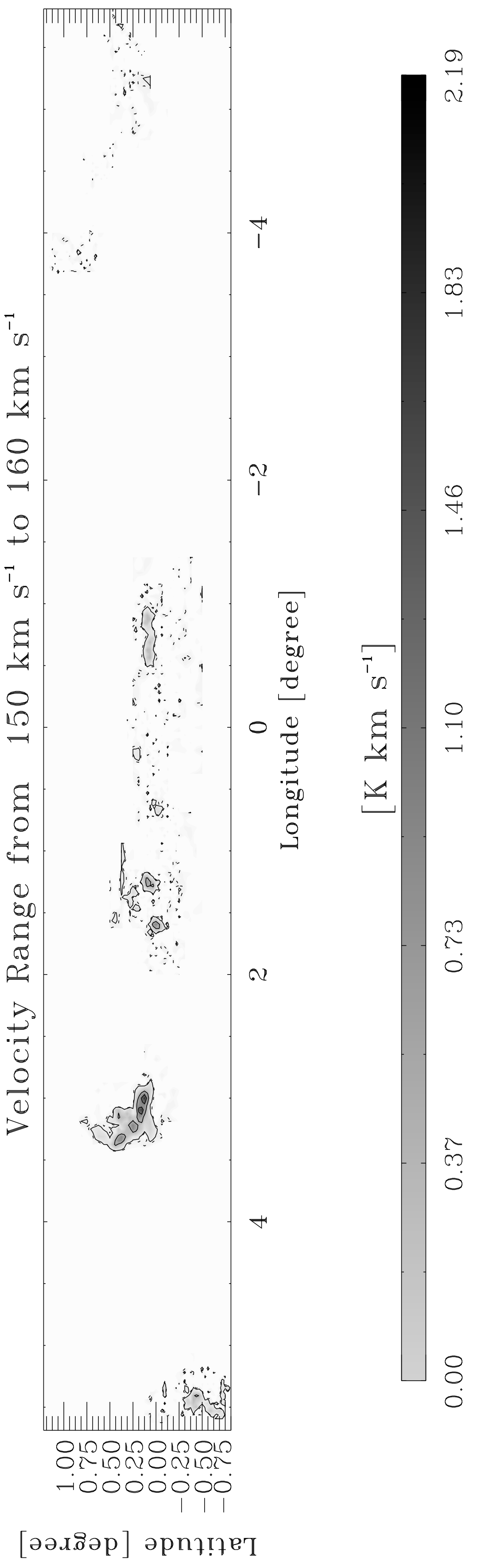

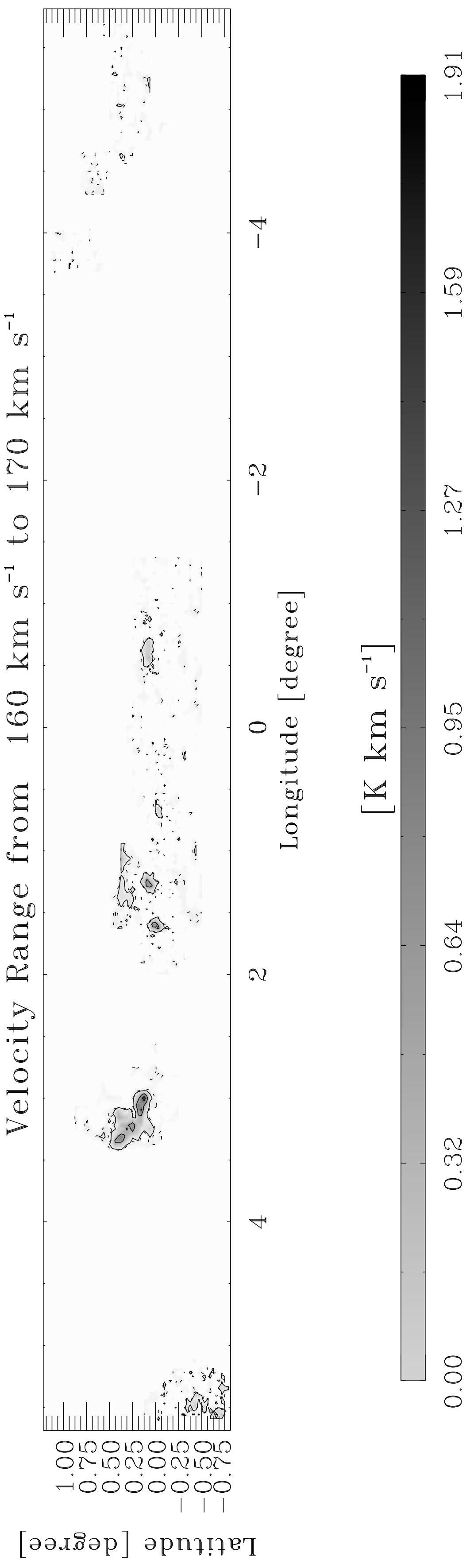

Fig. C1.21. continued.

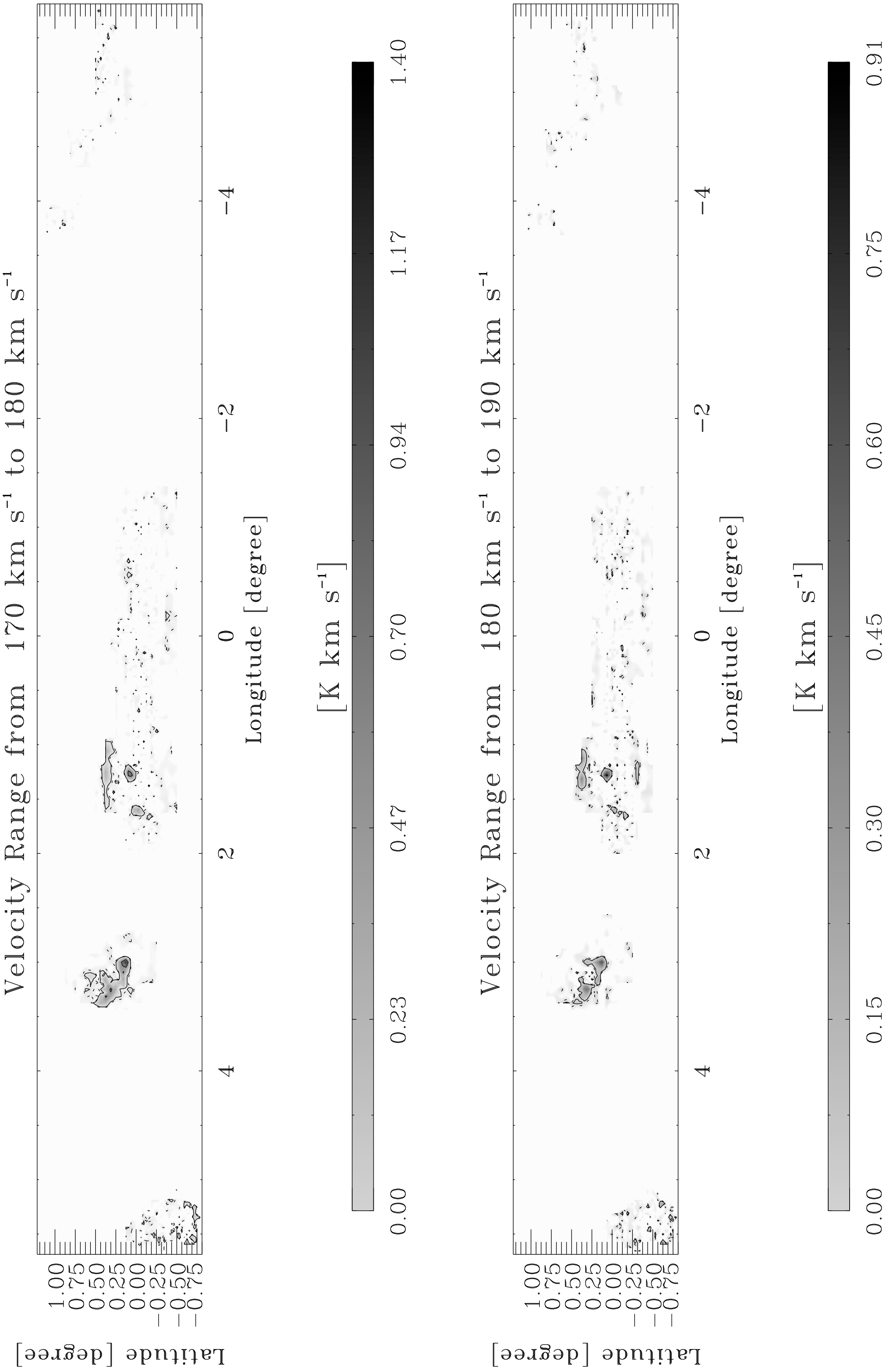

Fig. C1.22. continued.

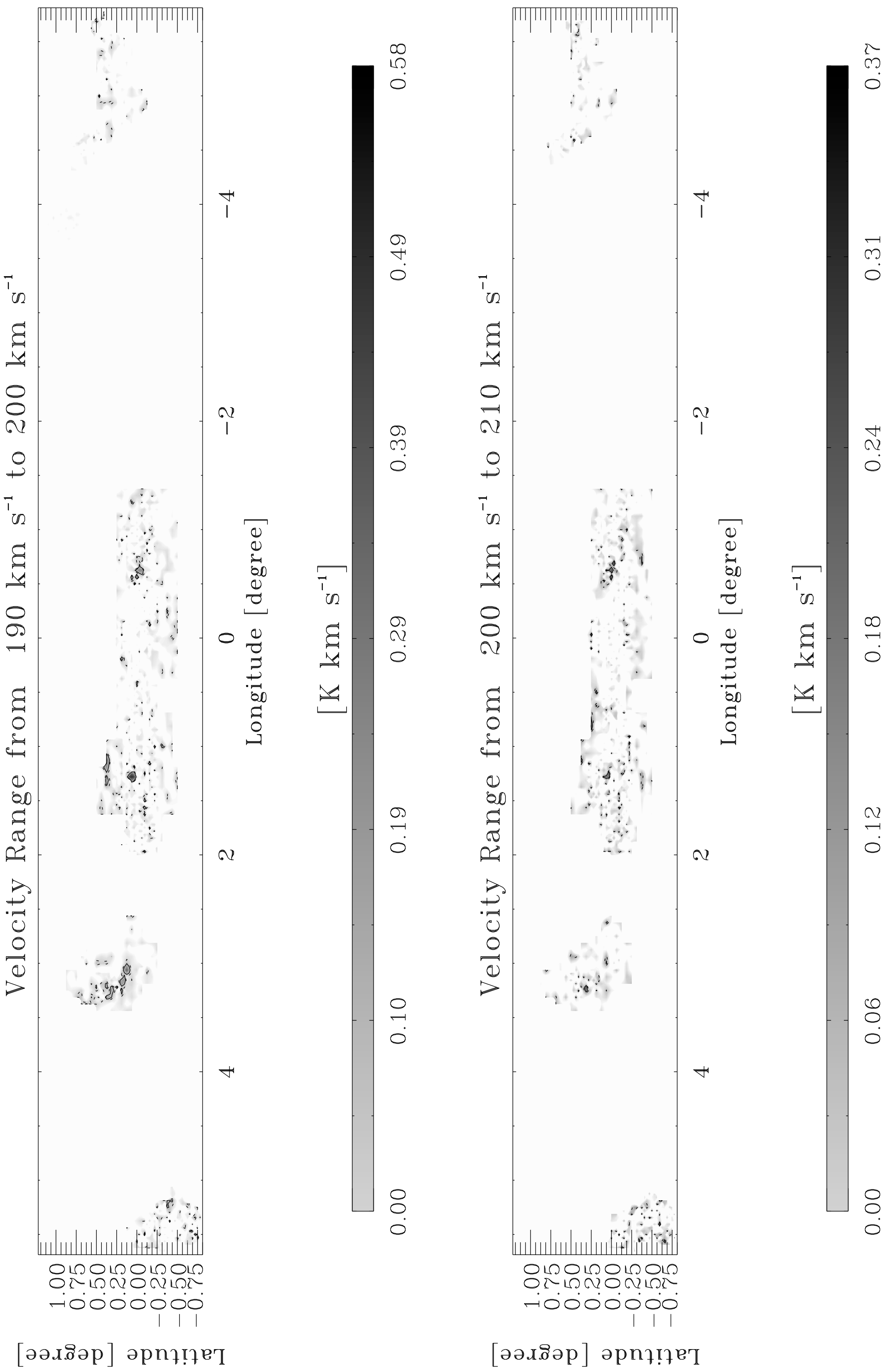

Fig. C1.23. continued.

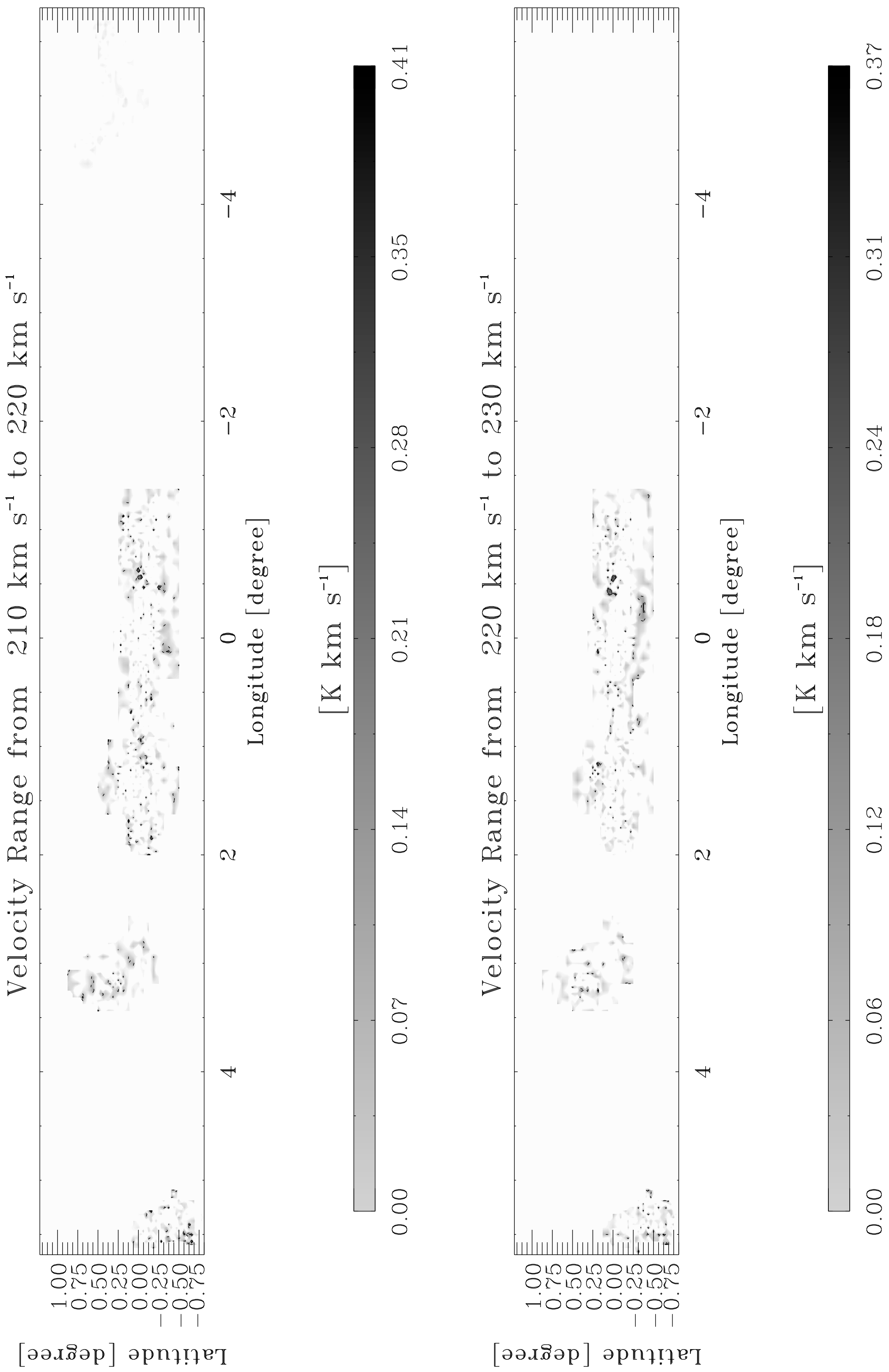

Fig. C1.24. continued.

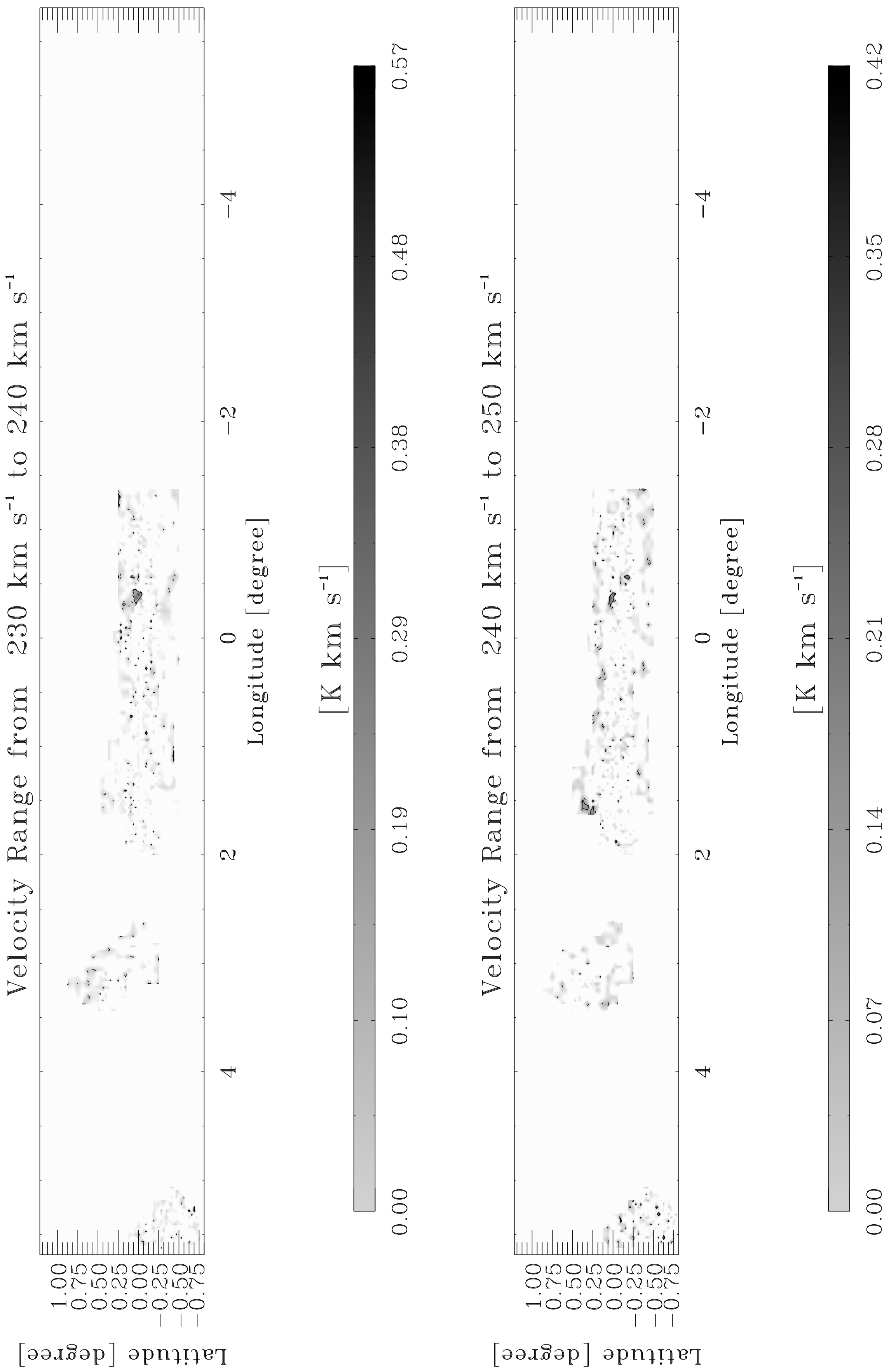

Fig. C1.25. continued.

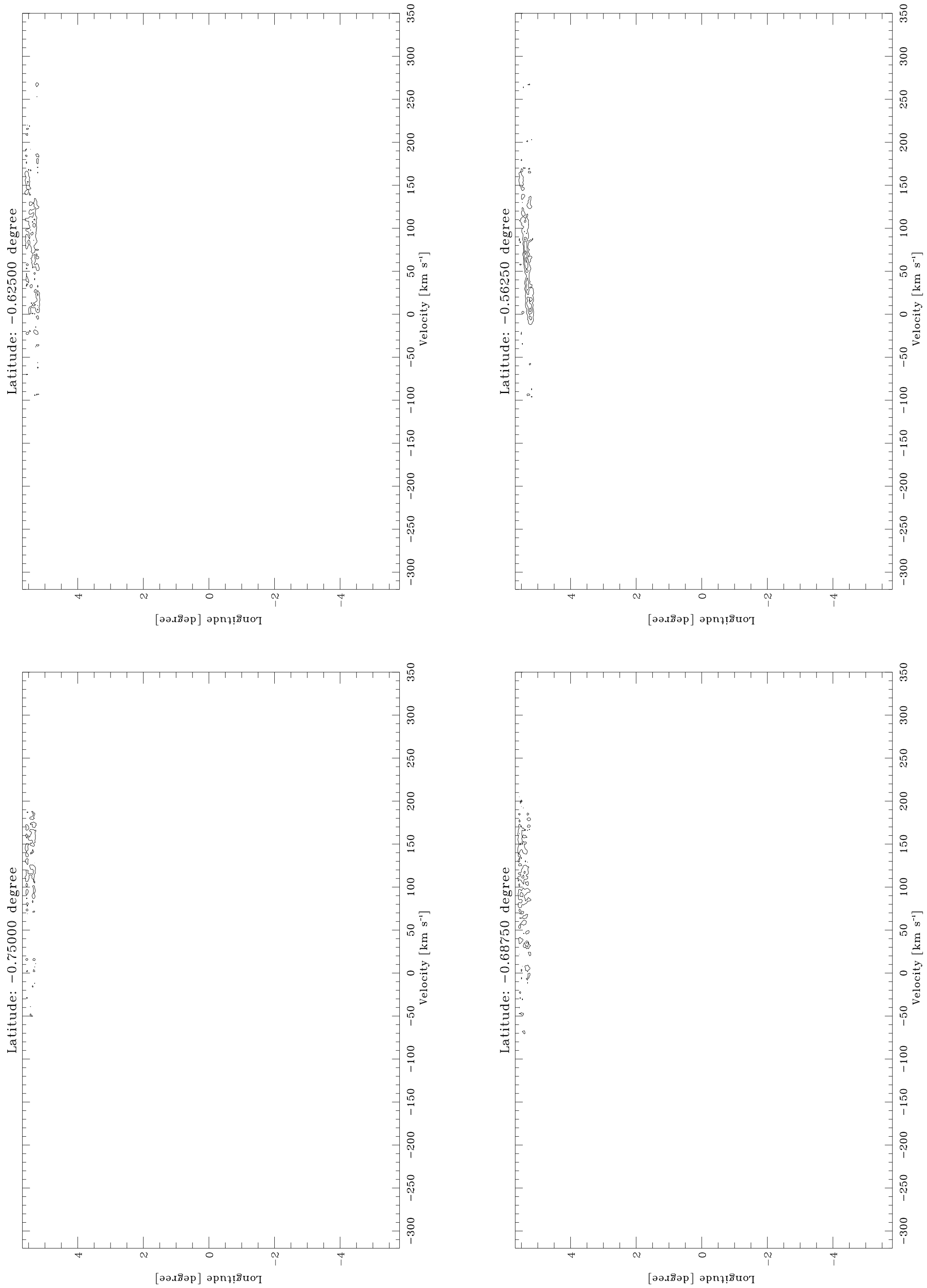

Fig. C2.1. Longitude-velocidad contour diagrams integrated in latitude in step of 0°.0625 in SiO. The lowest contour is at 0.0013 K (3σ). The following contours increase them in step of 0.0018 K, which correspond to 4σ.

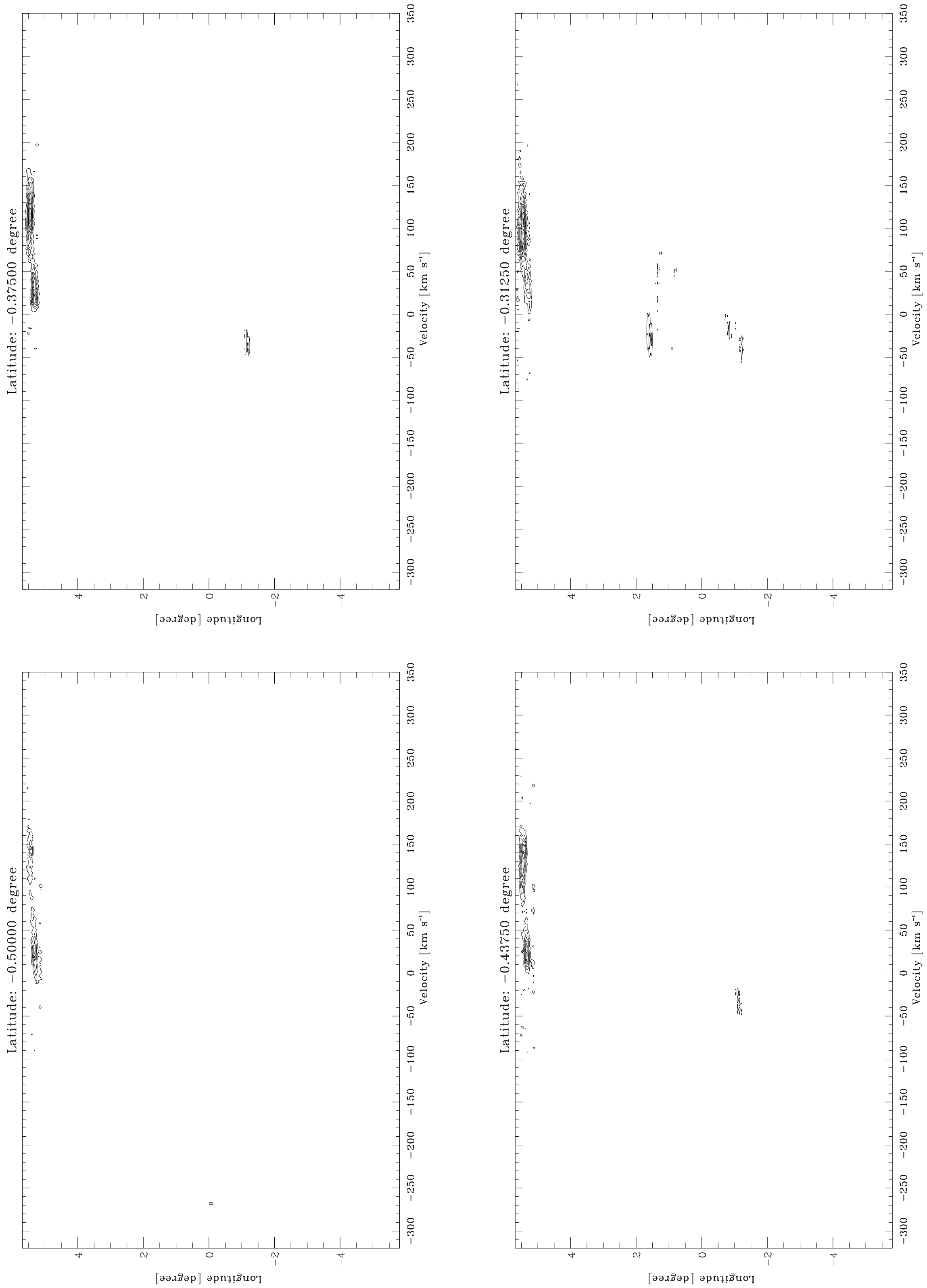

Fig. C2.2. continued.

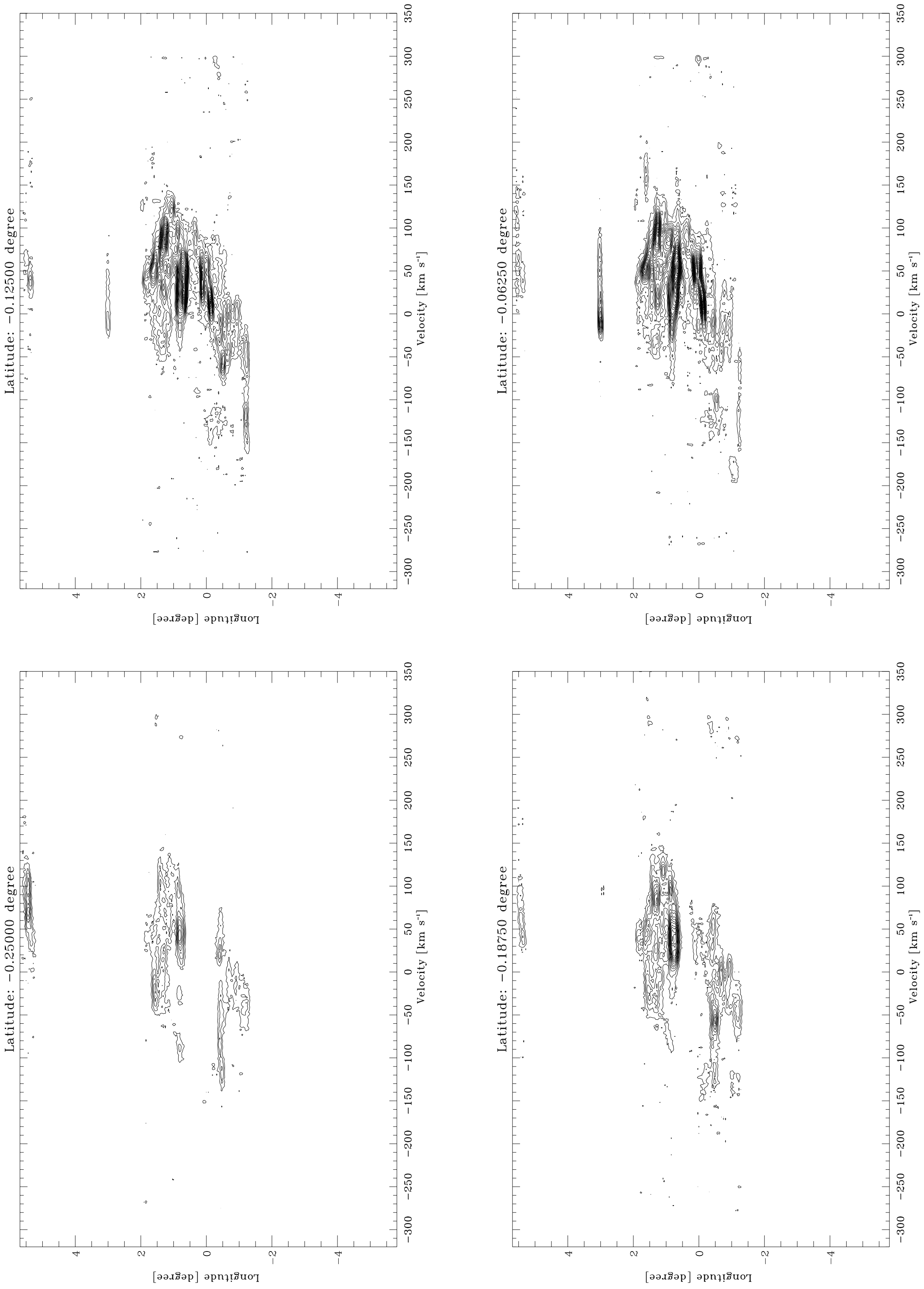

Fig. C2.3. continued.

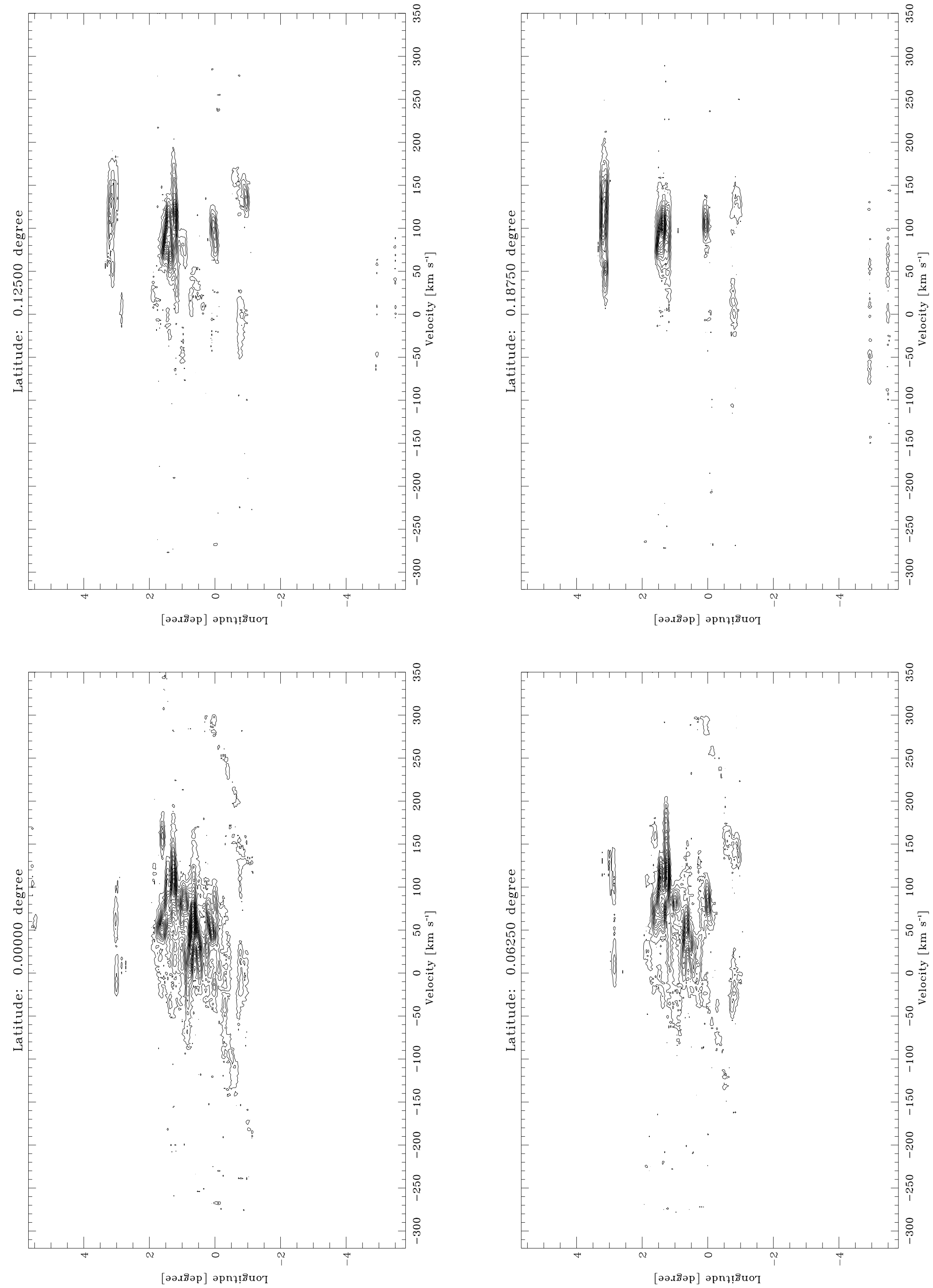

Fig. C2.4. continued.

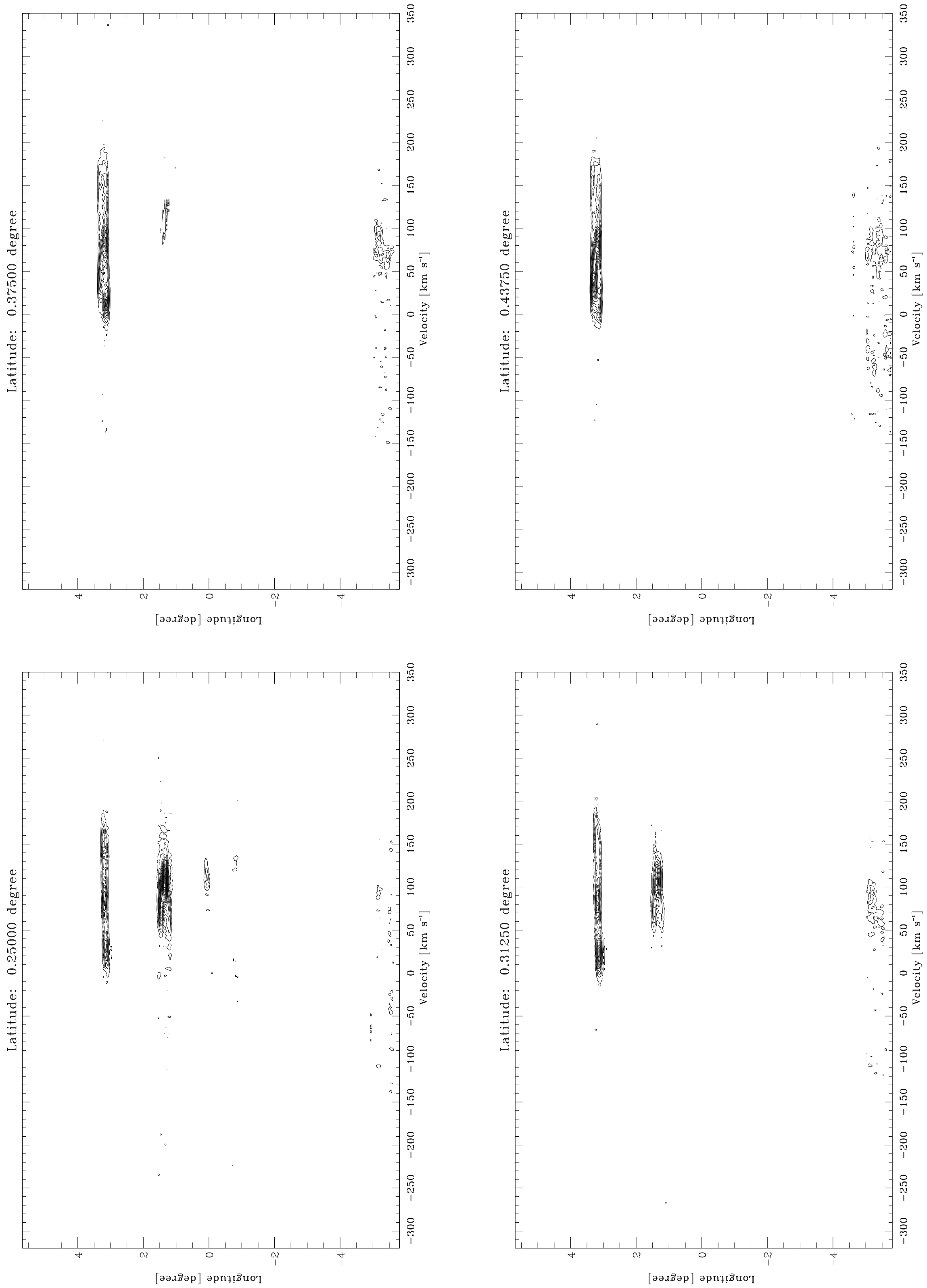

Fig. C2.5. continued.

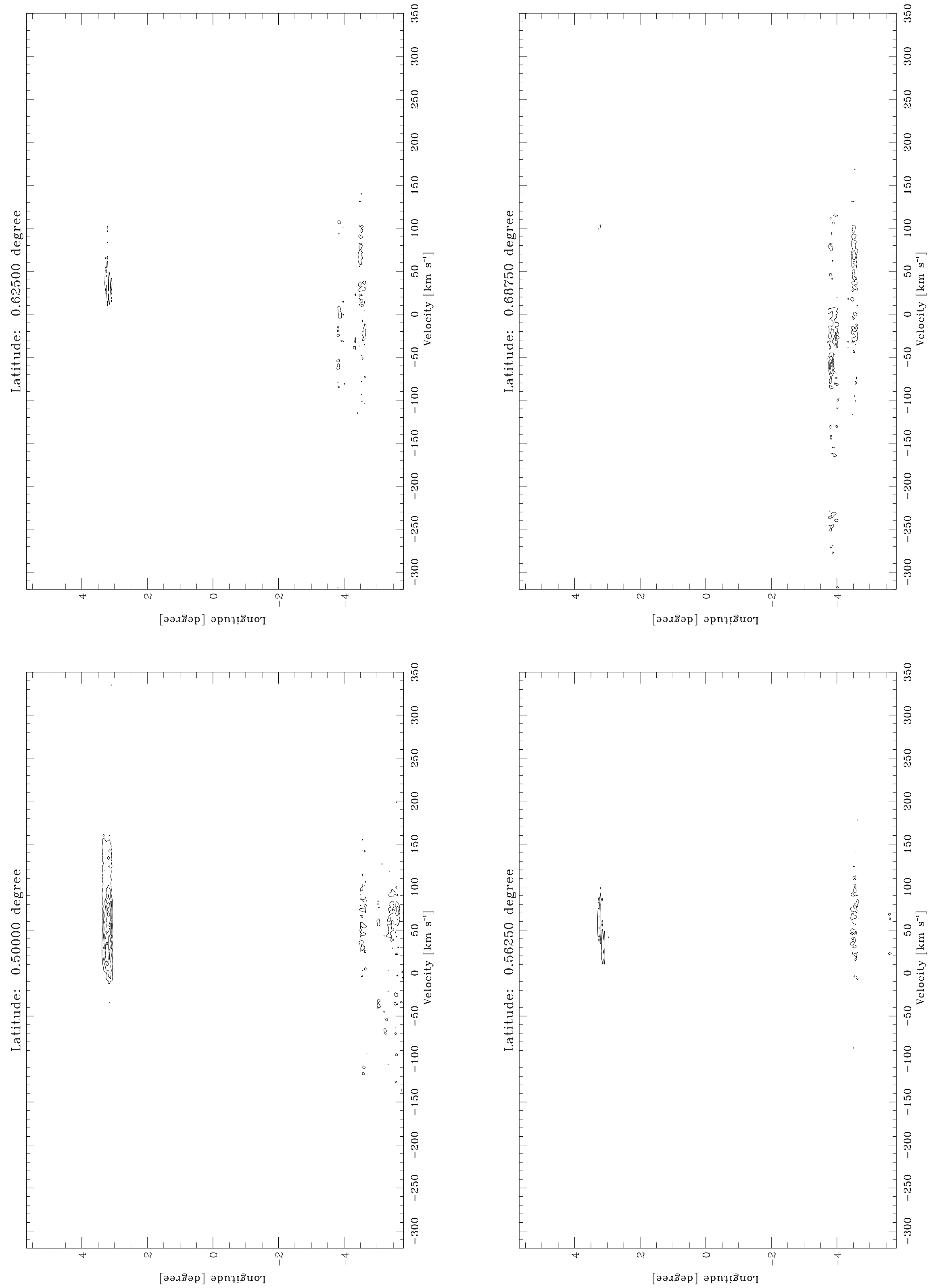

Fig. C2.6. continued.

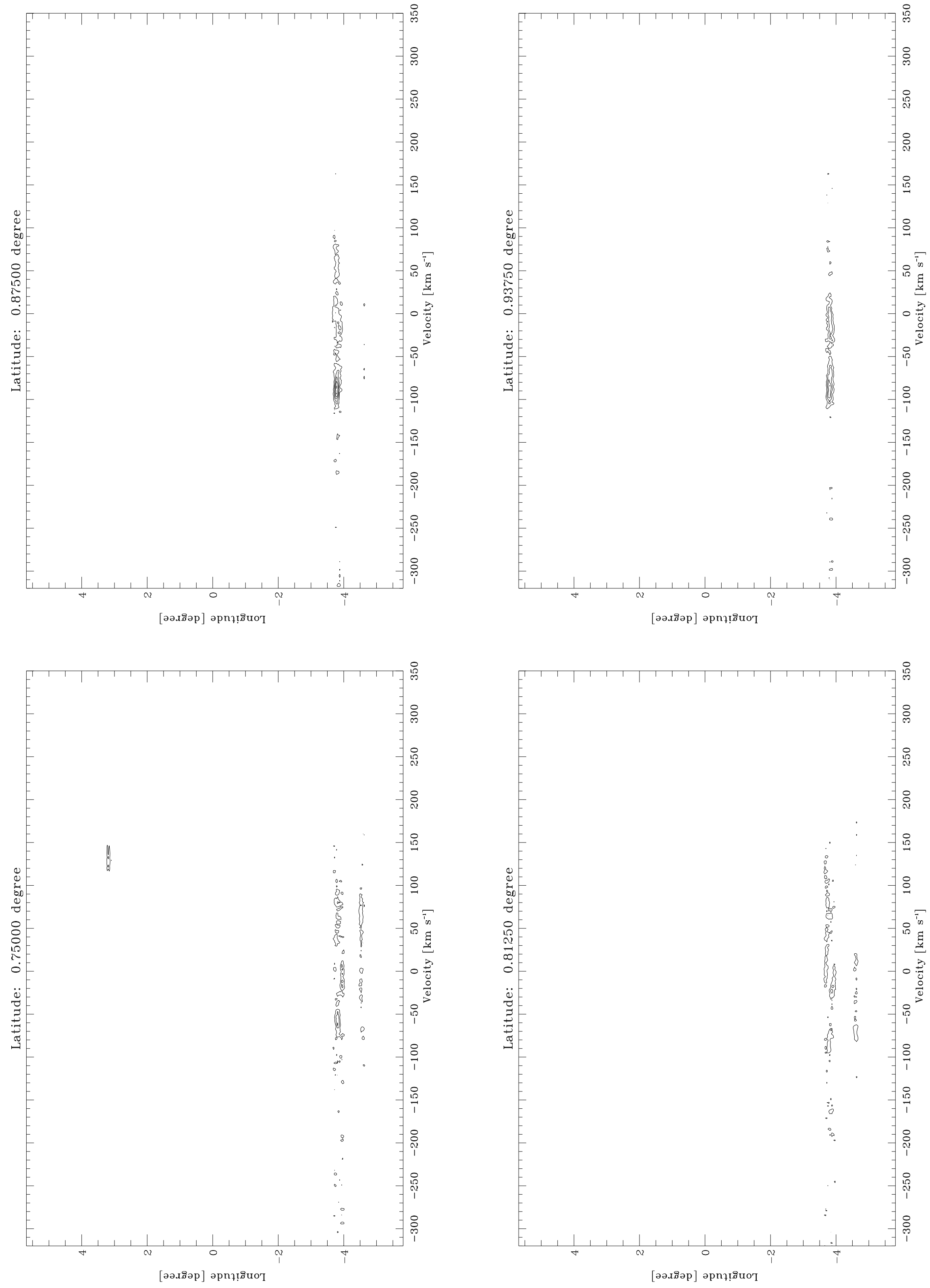

Fig. C2.7. continued.

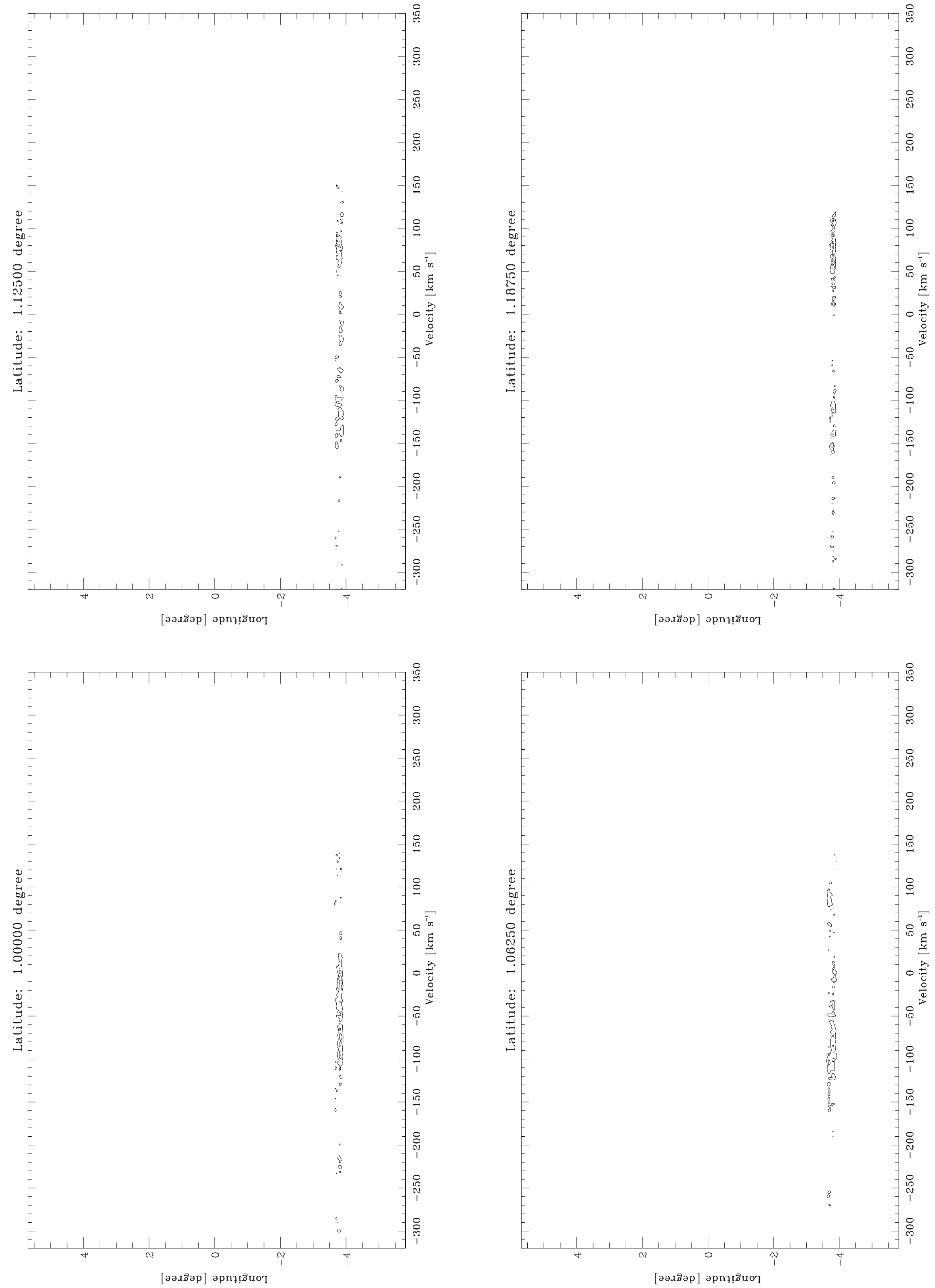

Fig. C2.8. continued.

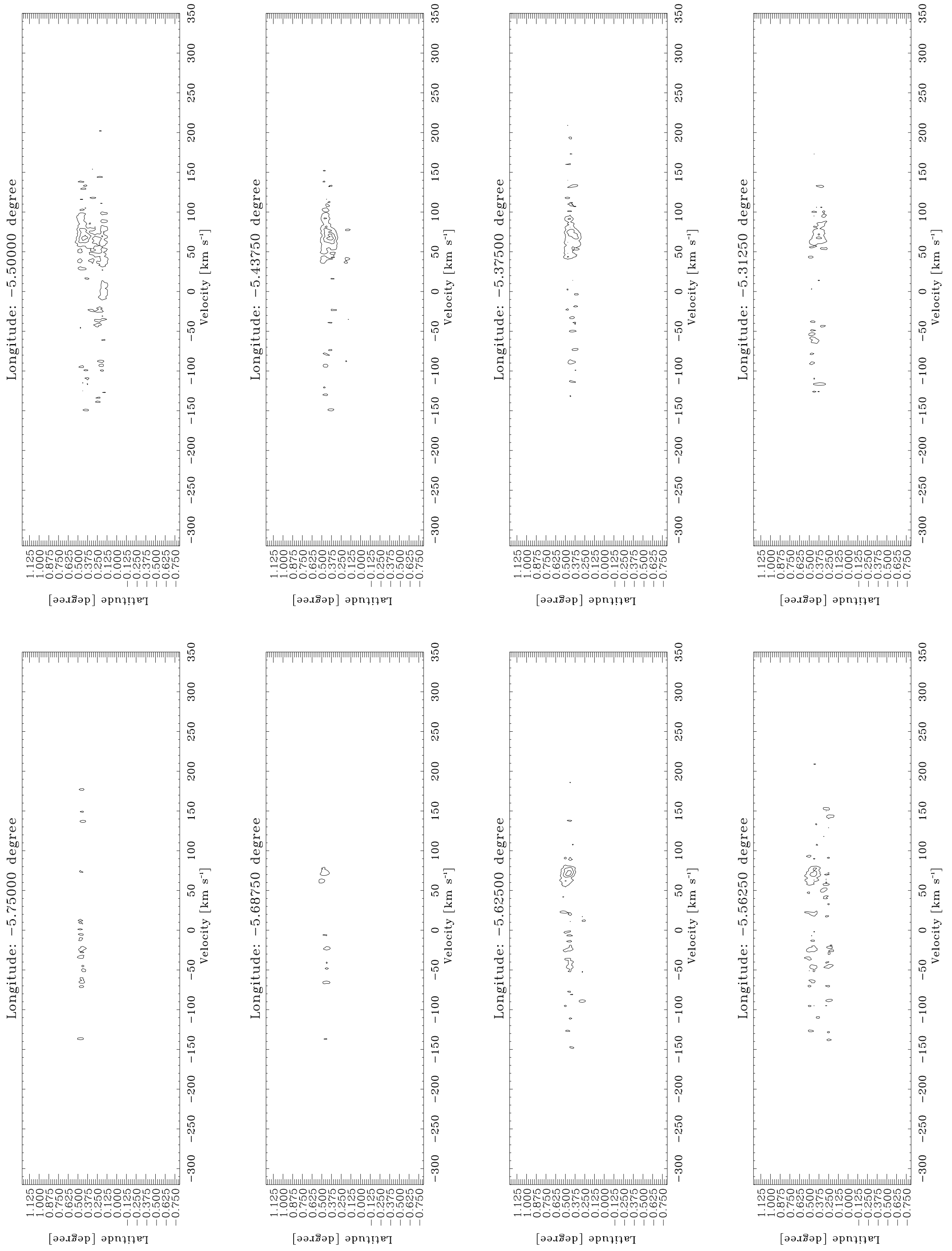

Fig. C3.1. Latitude-Velocity diagrams integrated in longitude in step of 0.°0625 for SiO. The lowest contour is at 0.0013 K (3σ). The following contours increase them in step of 0.0026 K, which correspond to 6σ.

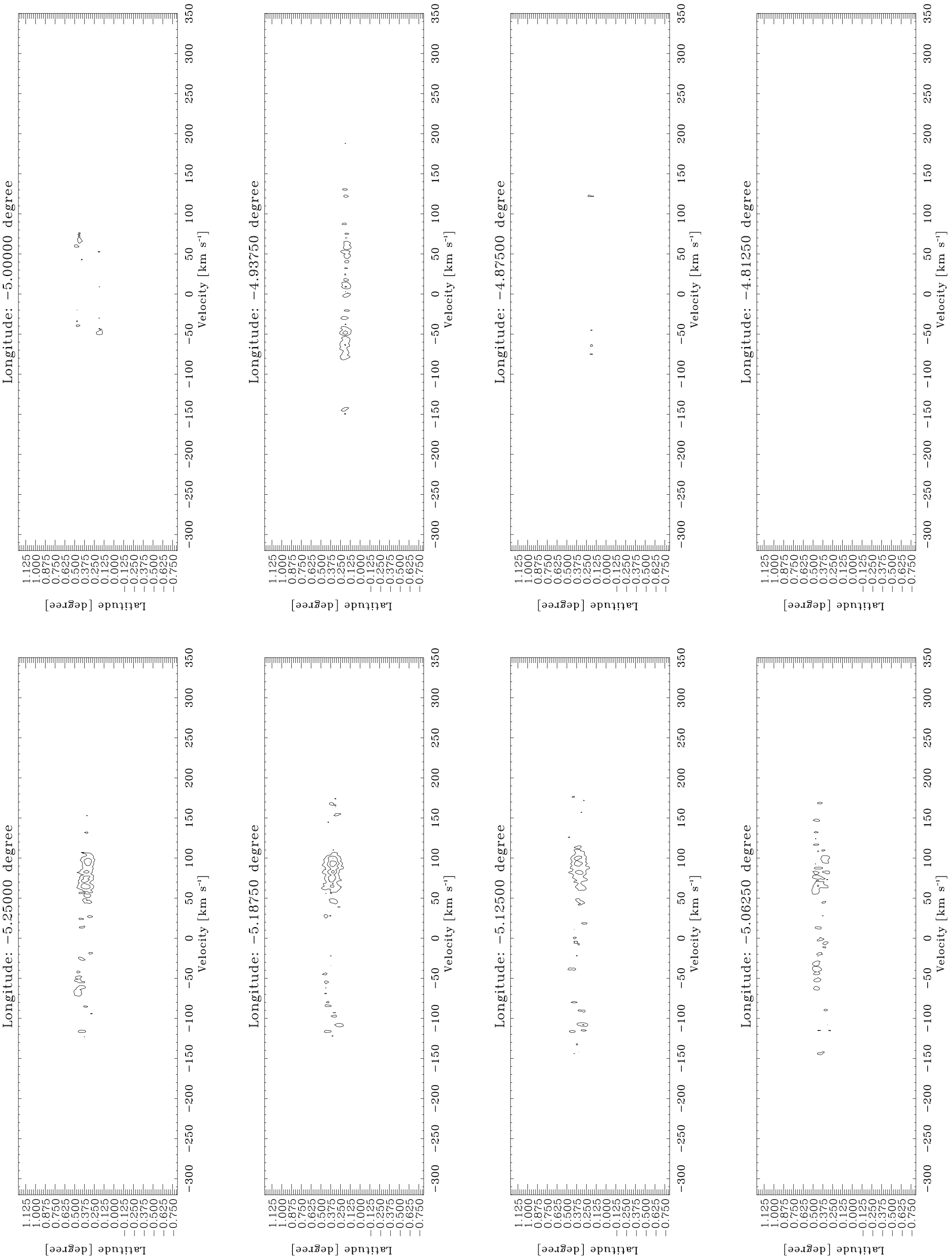

Fig. C3.2. continued.

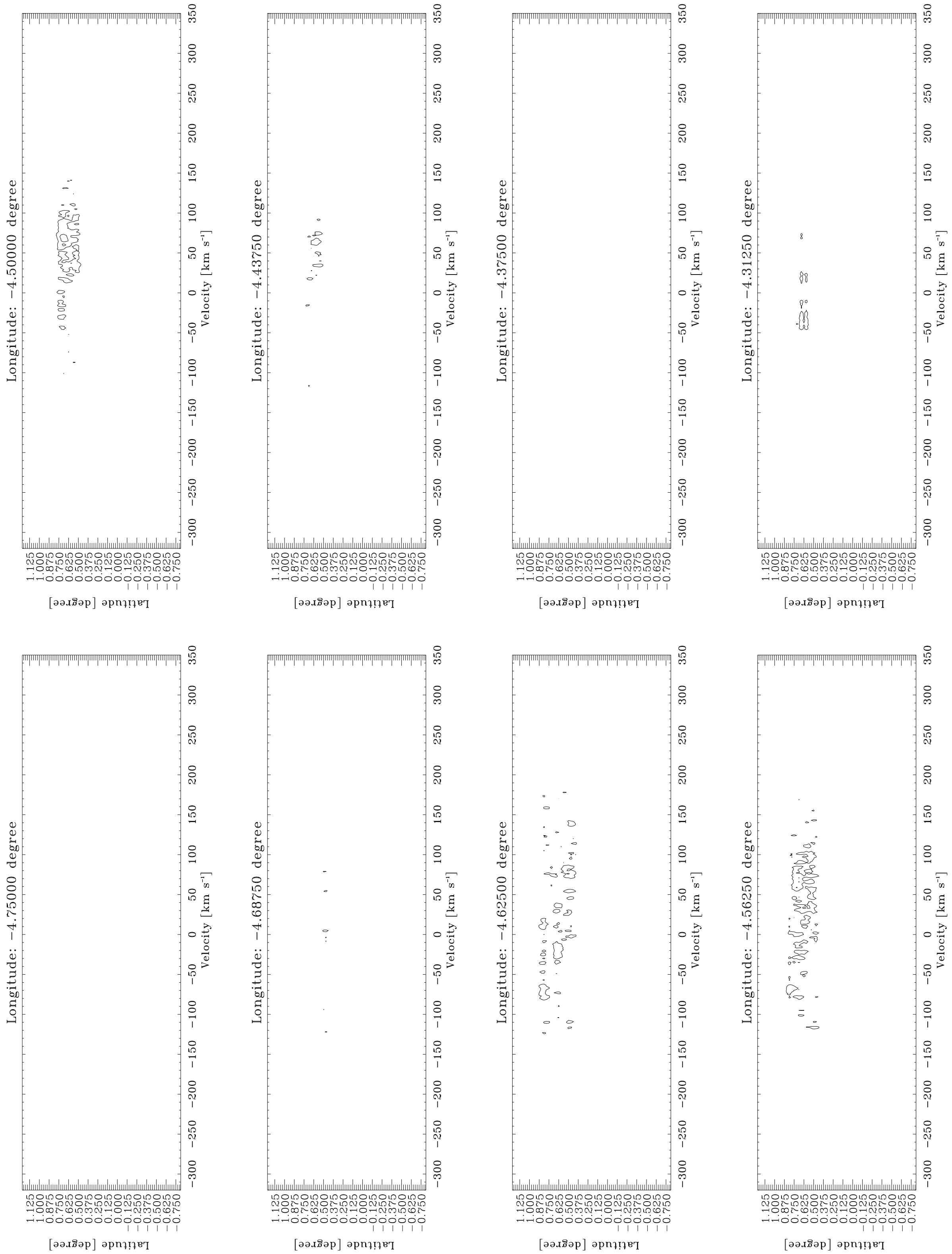

Fig. C3.3. continued.

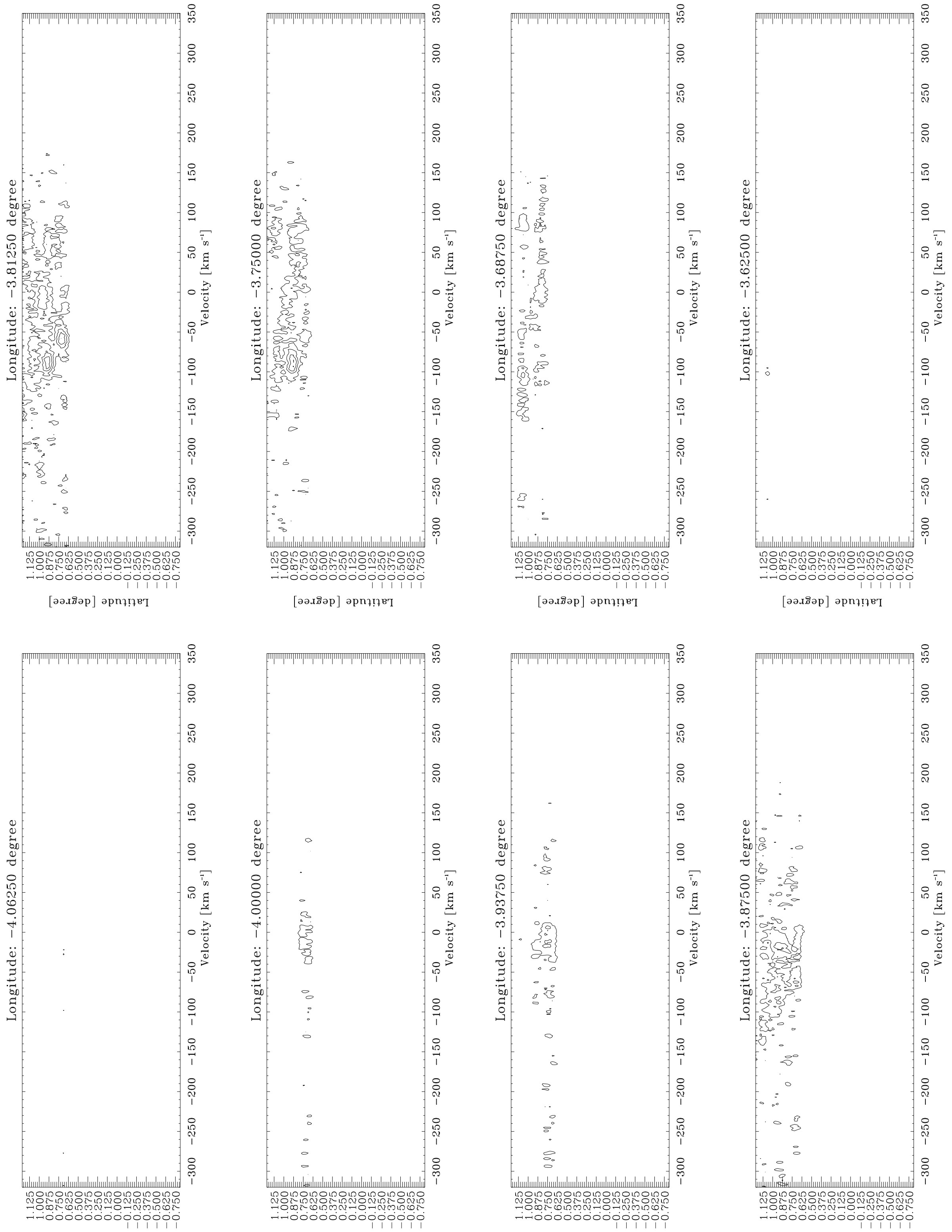

Fig. C3.4. continued.

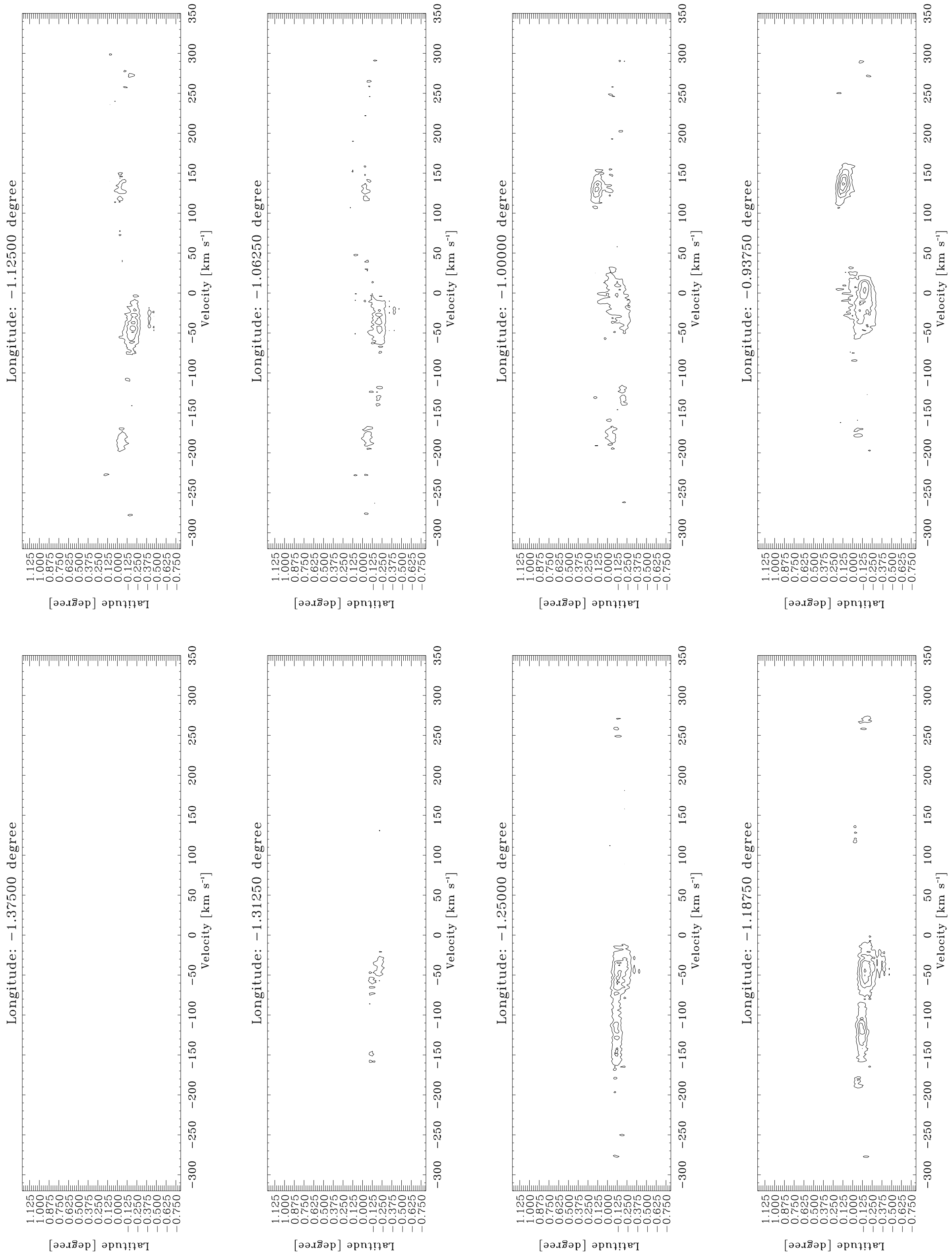

Fig. C3.5. continued.

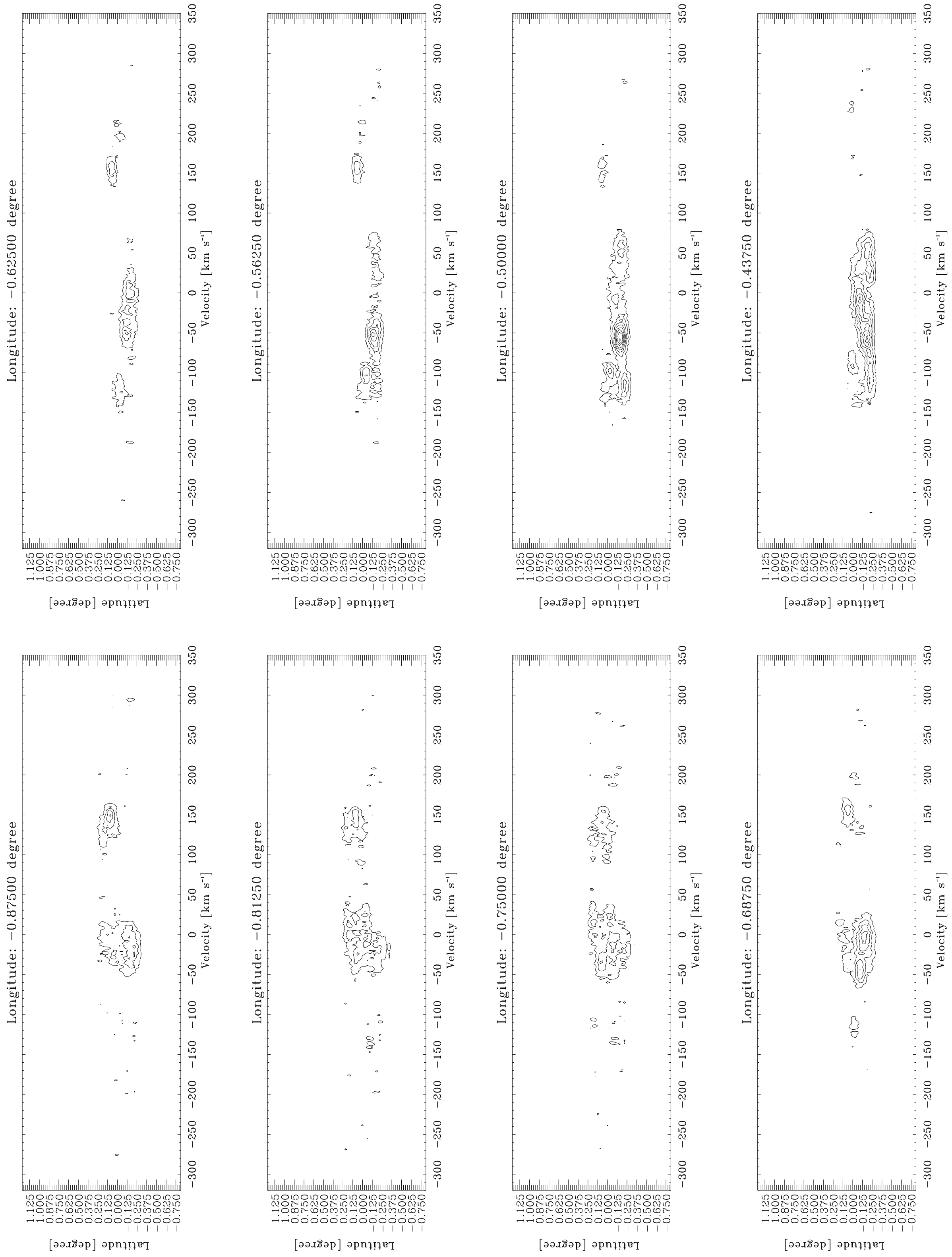

Fig. C3.6. continued.

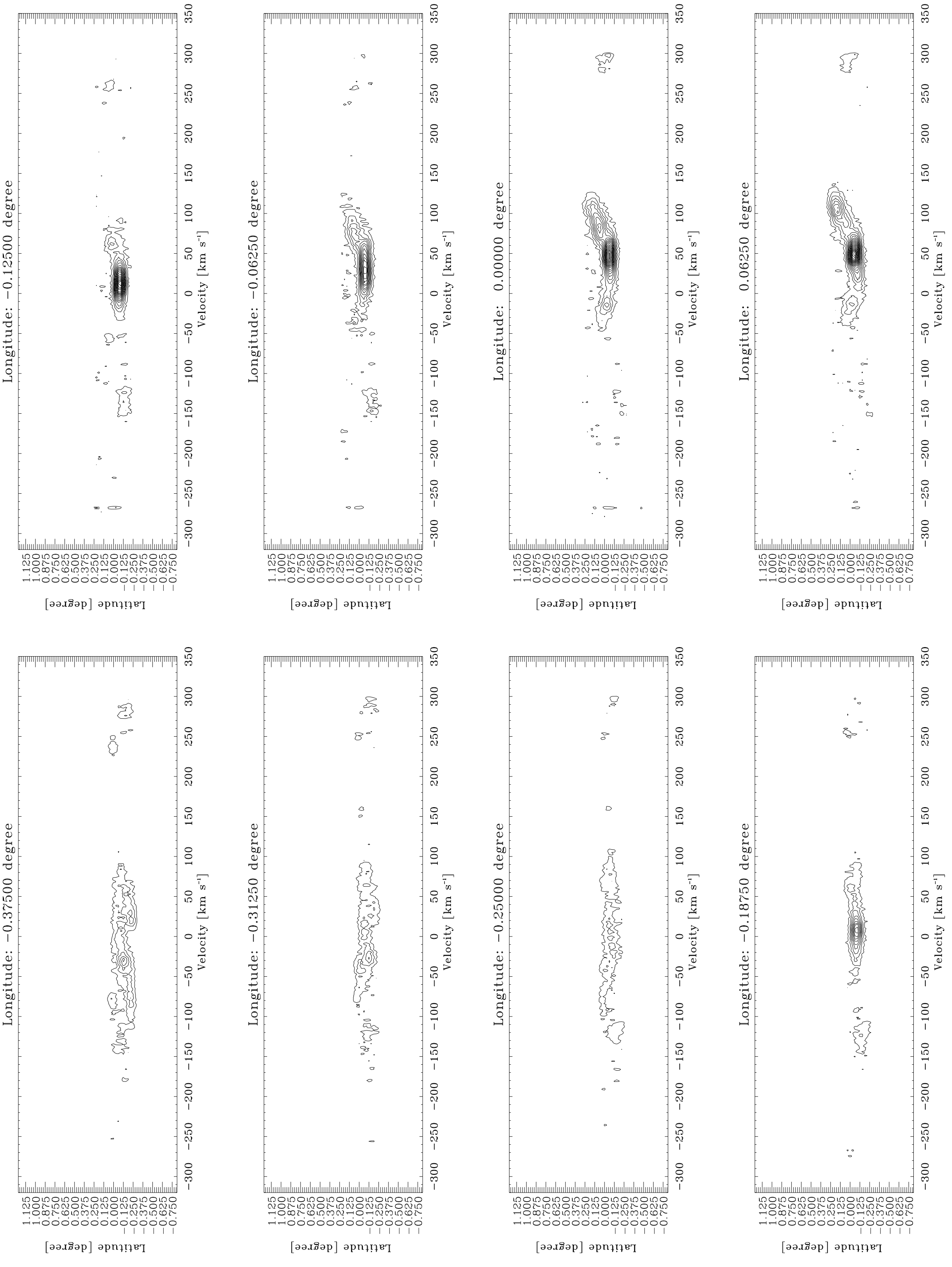

Fig. C3.7. continued.

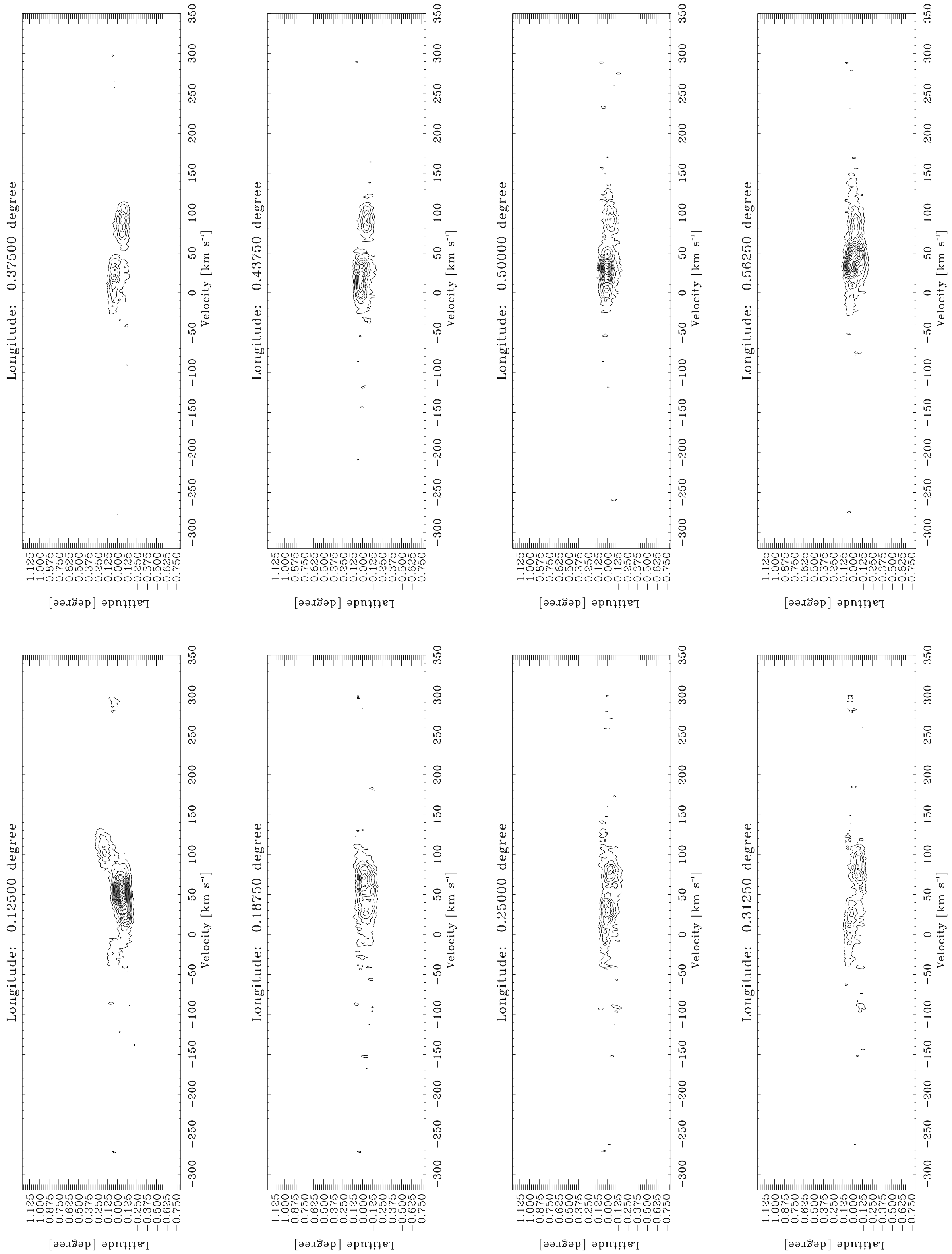

Fig. C3.8. continued.

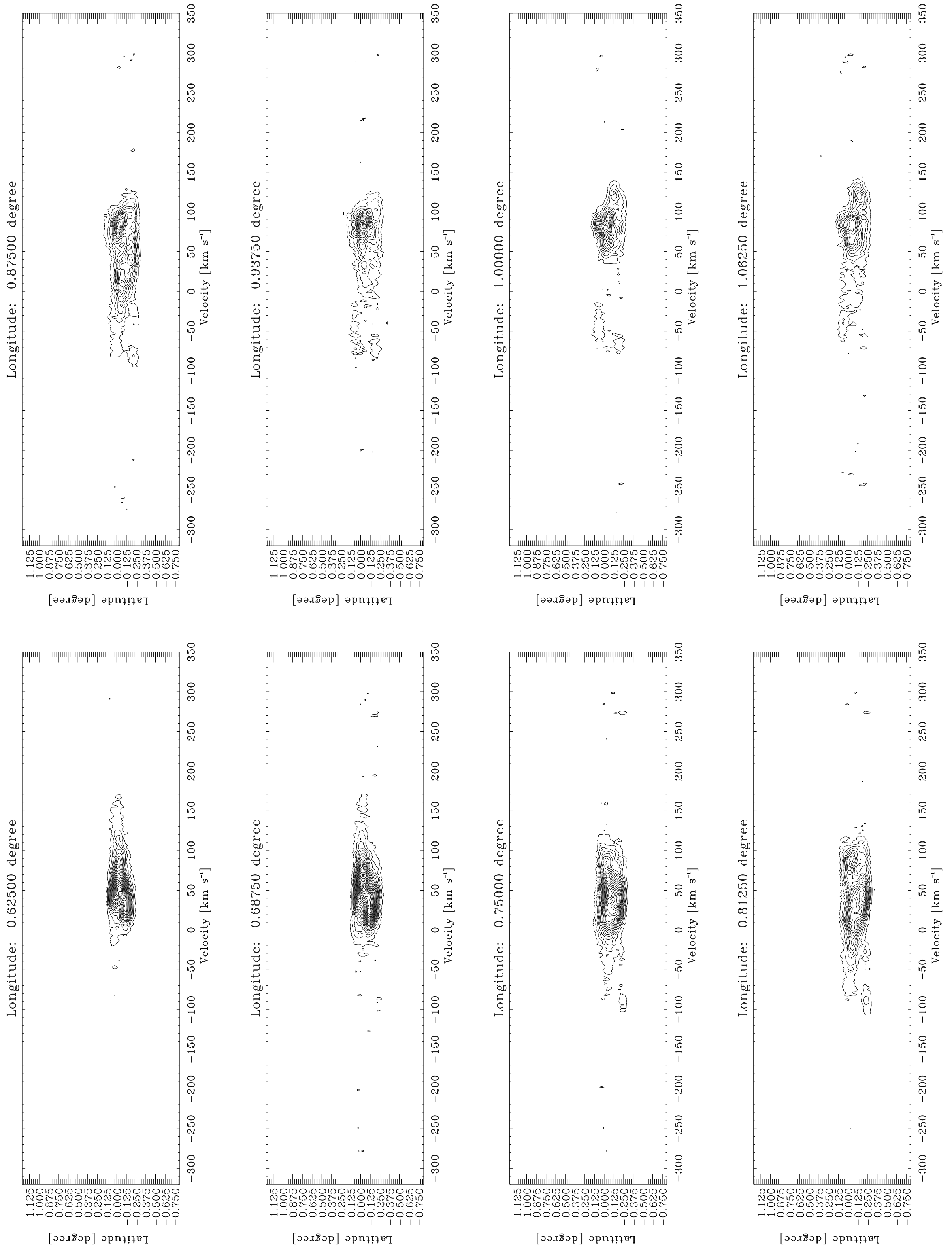

Fig. C3.9. continued.

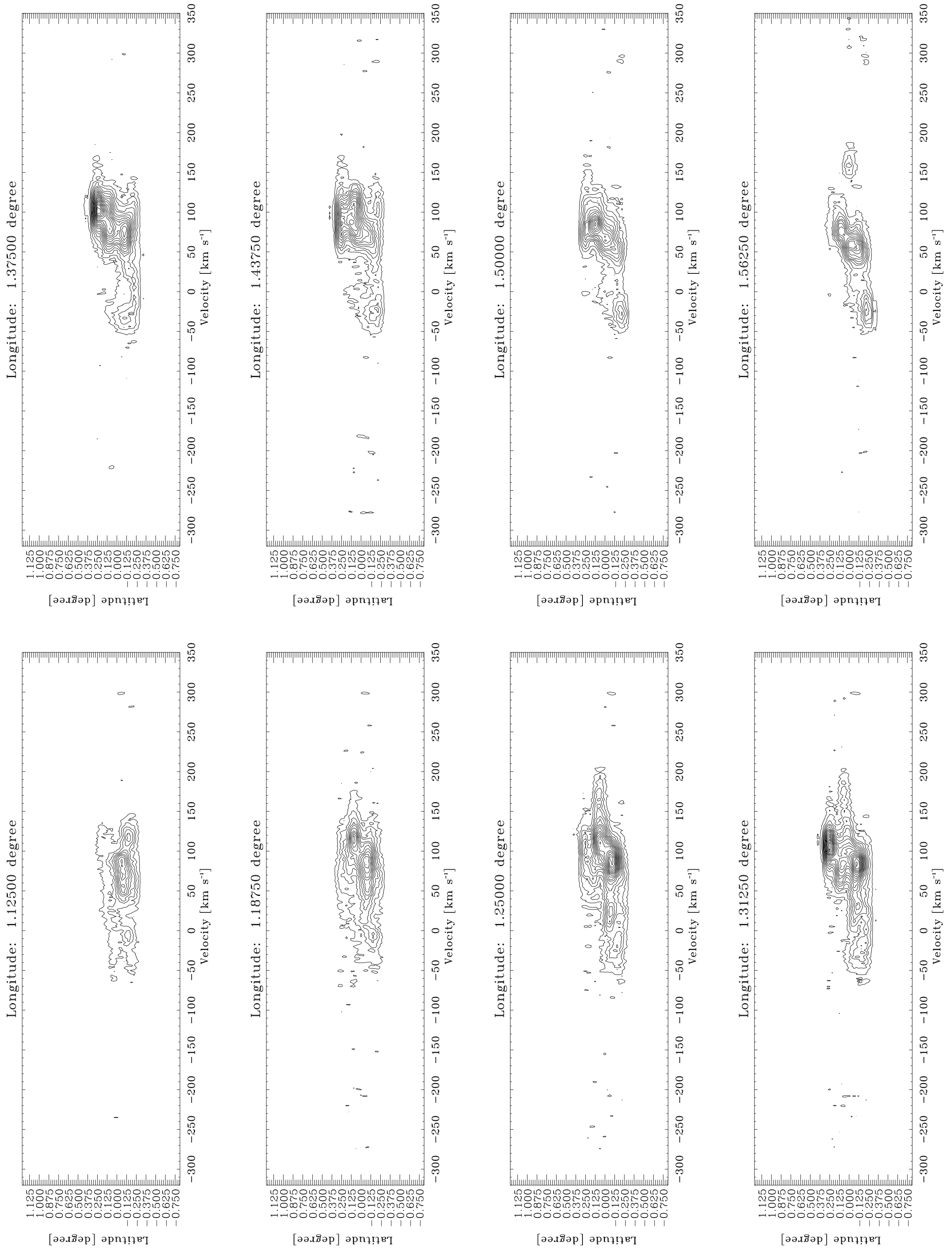

Fig. C3.10. continued.

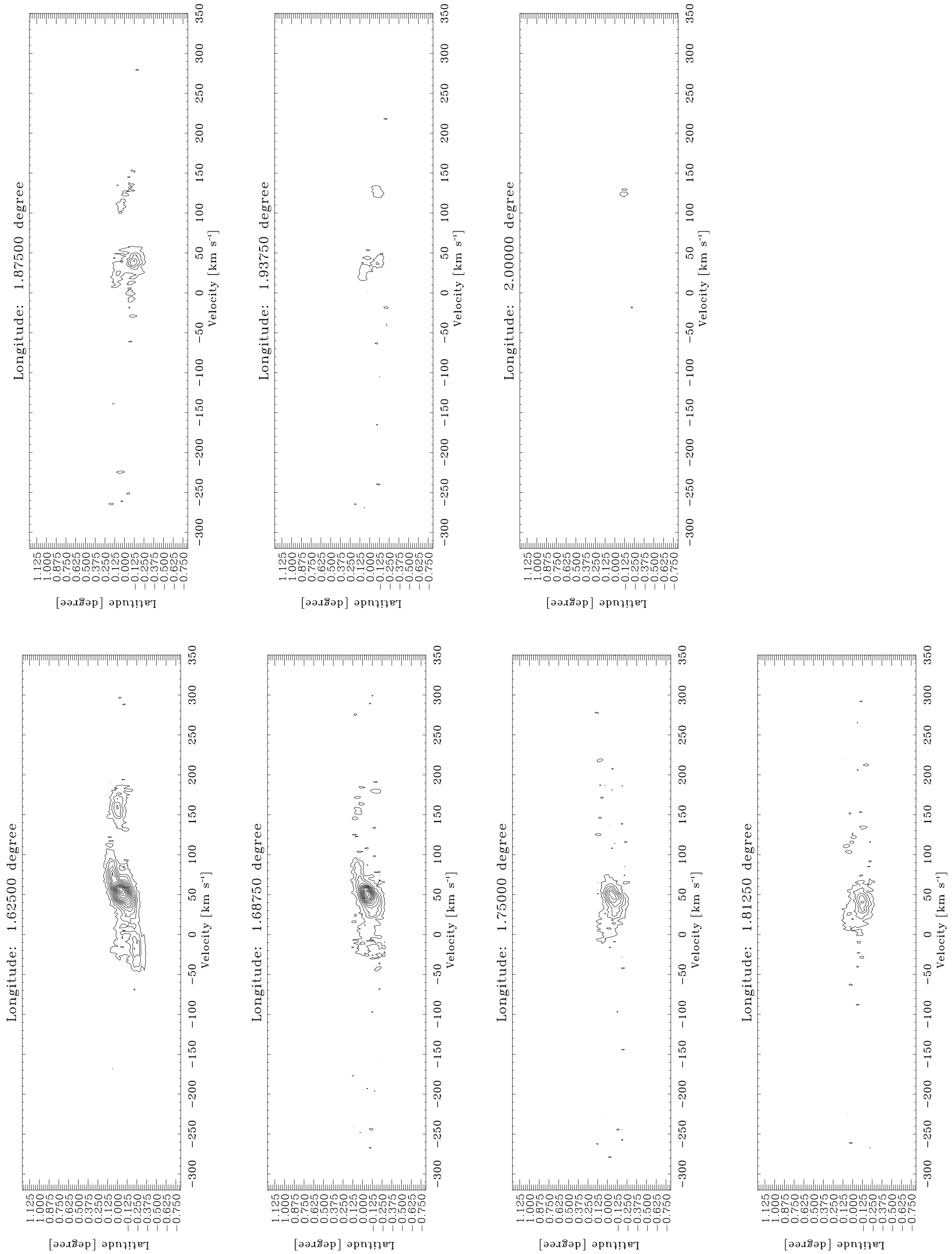

Fig. C3.11. continued.

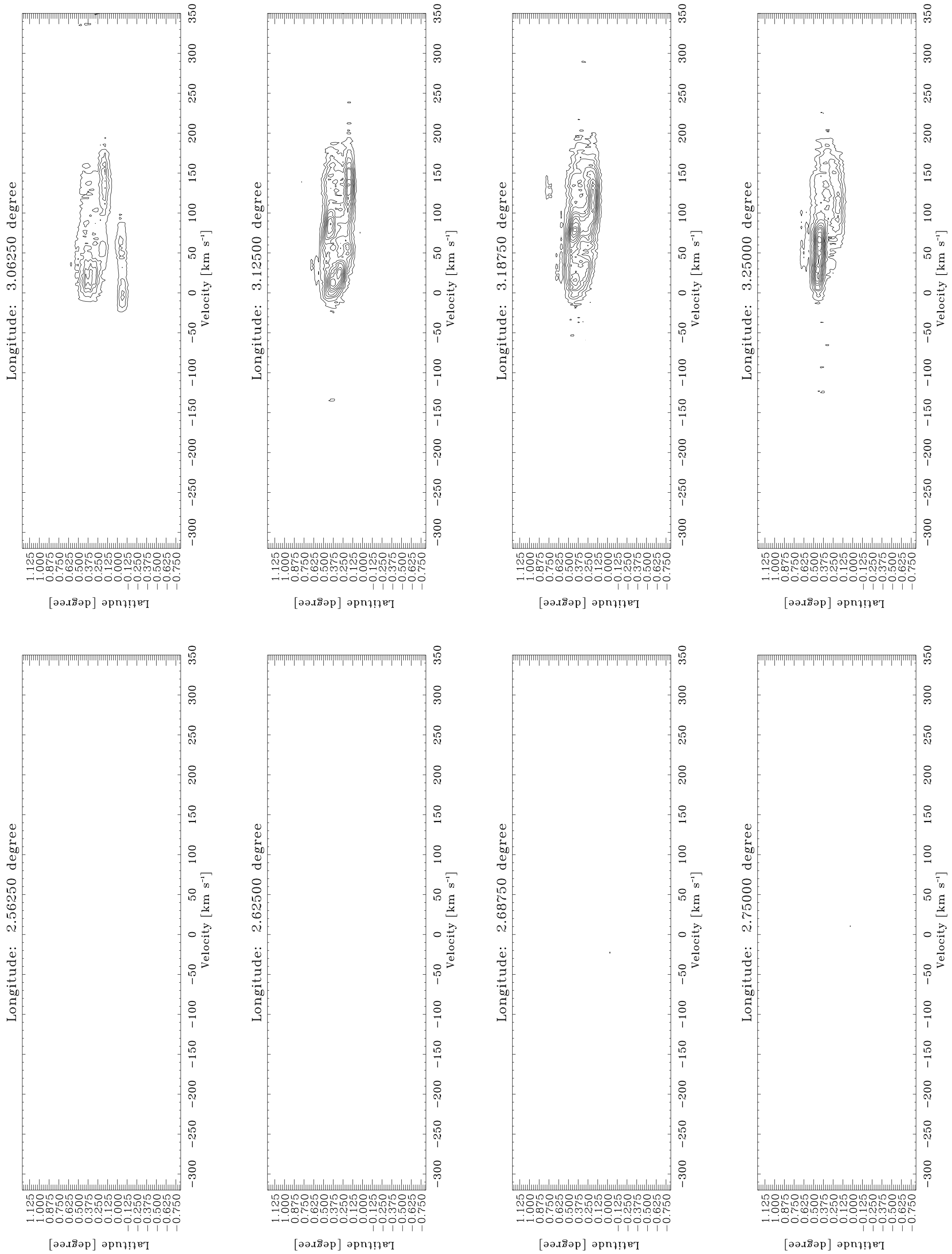

Fig. C3.12. continued.

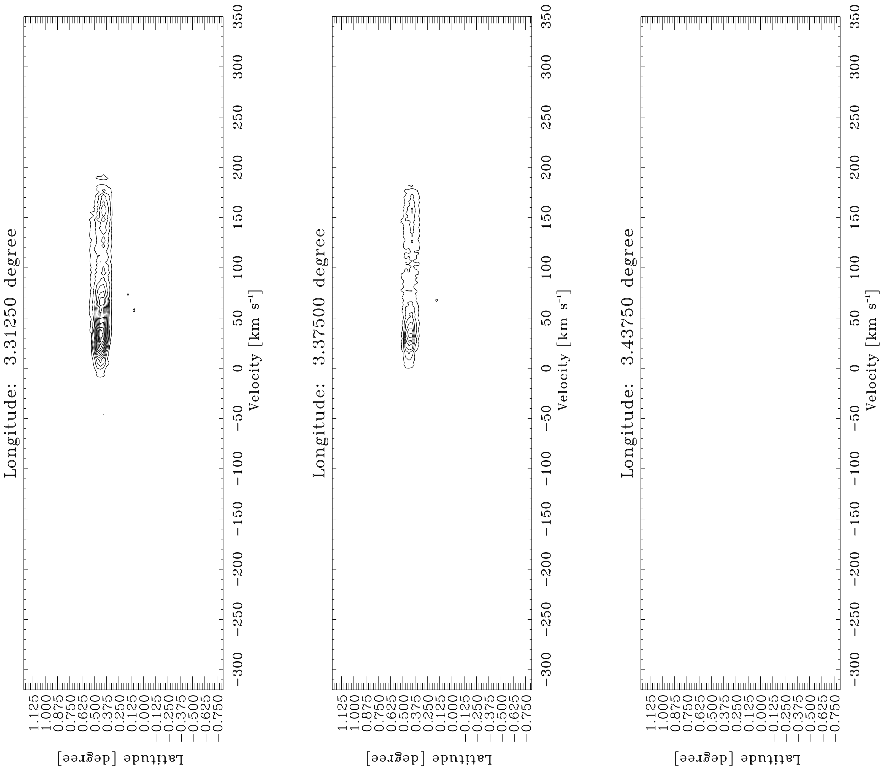

Fig. C3.13. continued.

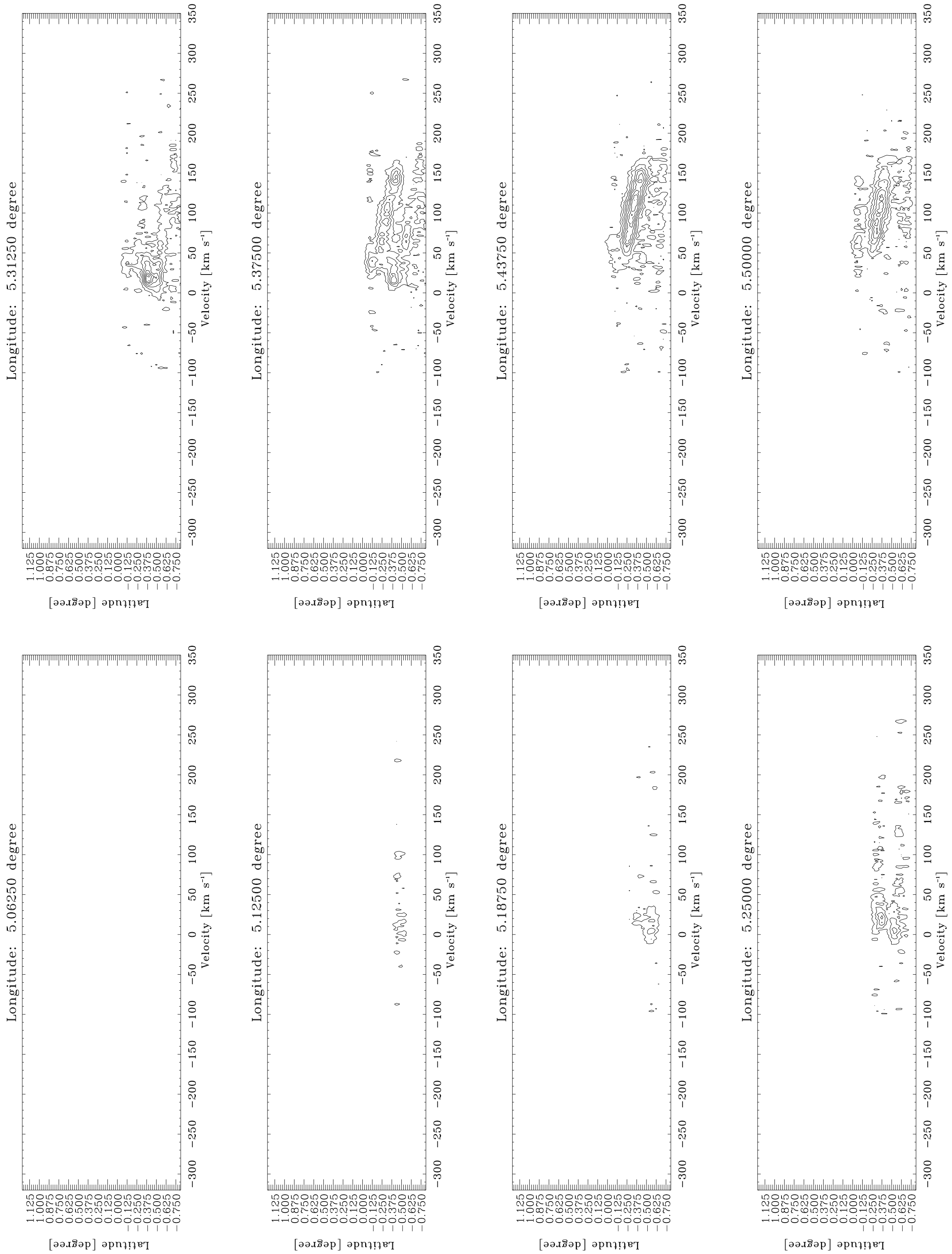

Fig. C3.14. continued.

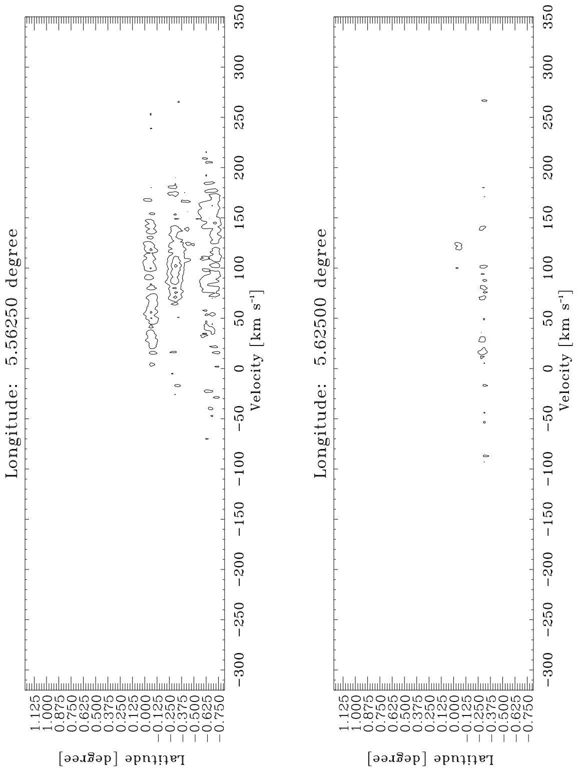

Fig. C3.15. continued.

Appendix D: $H^{13}CO^+$ Galactic center survey

In Fig. D.1, we present the channel map of the $H^{13}CO^+$ emission in the Galactic center region integrated in velocity widh of 10 km s^{-1}.

Figure D.2 presents the $l-v$ diagram integrated in latitude in steps of $0\overset{\circ}{.}0625$ in $H^{13}CO^+$. The contours levels start at 0.0013 K (3σ) and increase them in steps of 0.0018 K (4σ).

Figure D.3 is a set of latitude-velocity diagrams integrated in steps of $0\overset{\circ}{.}0625$. The contours levels start at 0.0013 K (3σ) and increase them in step of 0.0026 K (6σ).

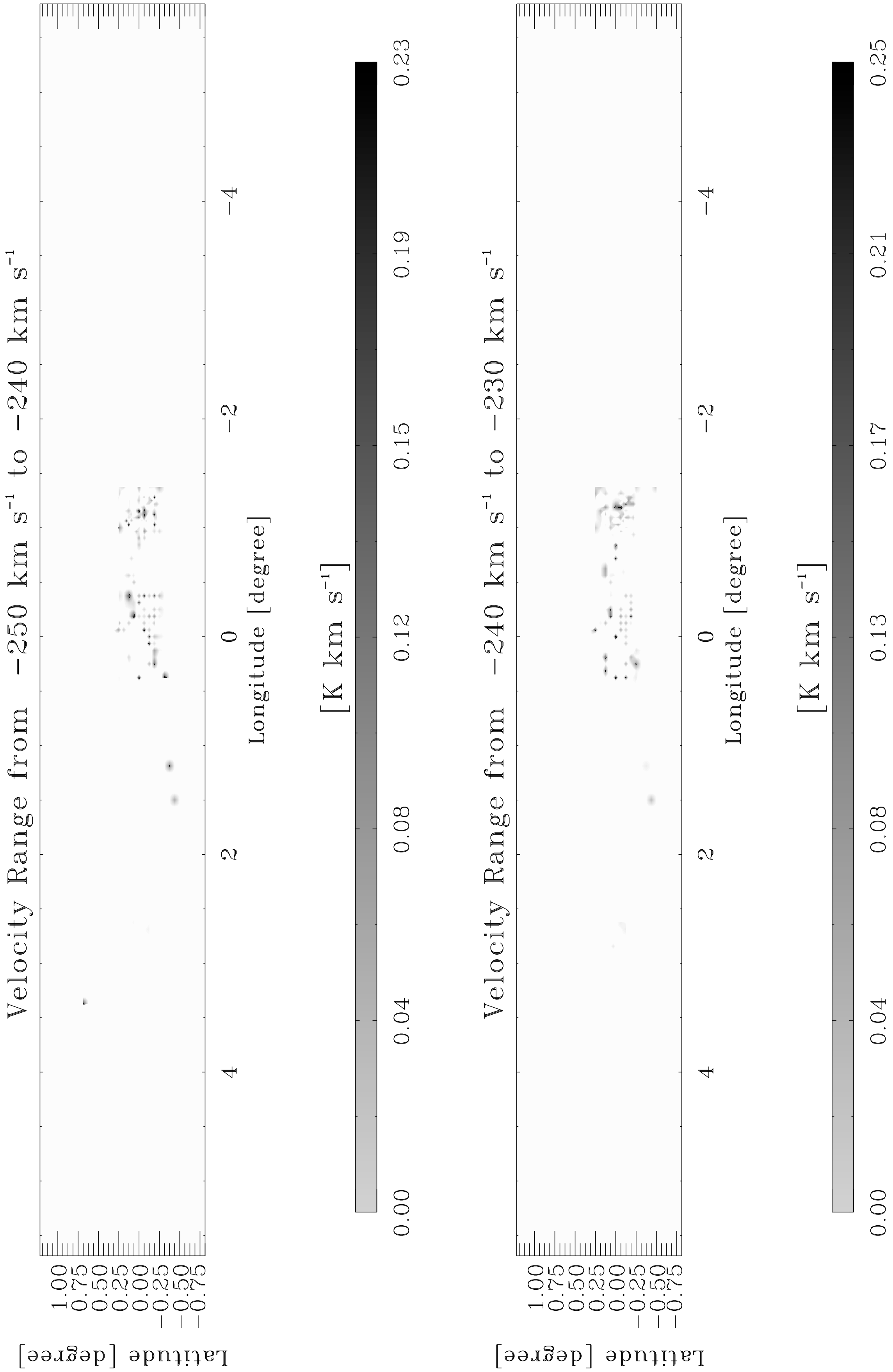

Fig. D1.1. The integrated intensity of the Galactic center region in $H^{13}CO^+$ (1−0) in velocity intervals of 10 km s^{-1} width. The solid contour levels start at 0.2 K km s^{-1}, which is the 3σ level, and increase in steps of 0.33 K km s^{-1} (5σ). The dotted contours is at 0.13 K km s^{-1} (2σ).

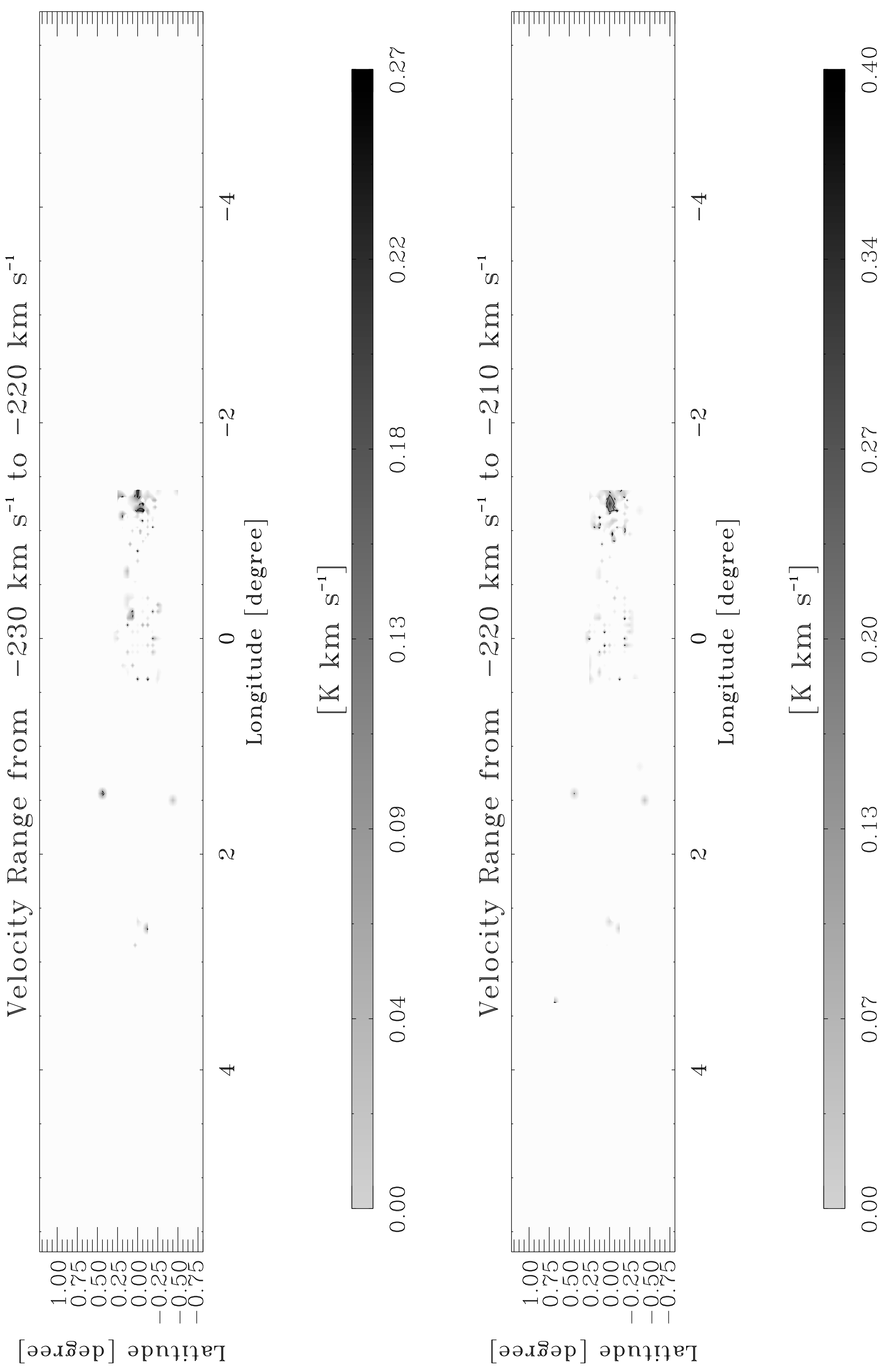

Fig. D1.2. continued.

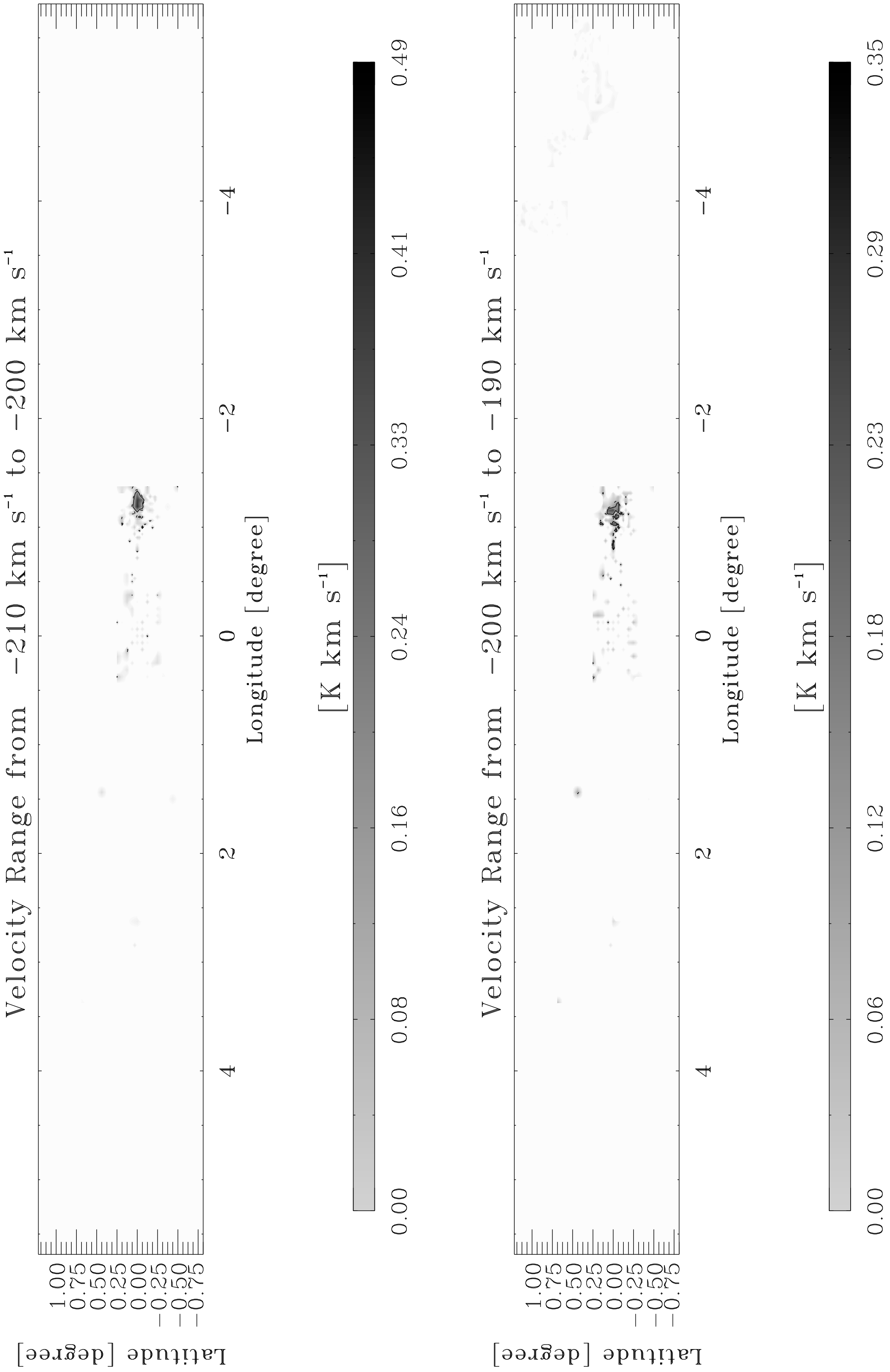

Fig. D1.3. continued.

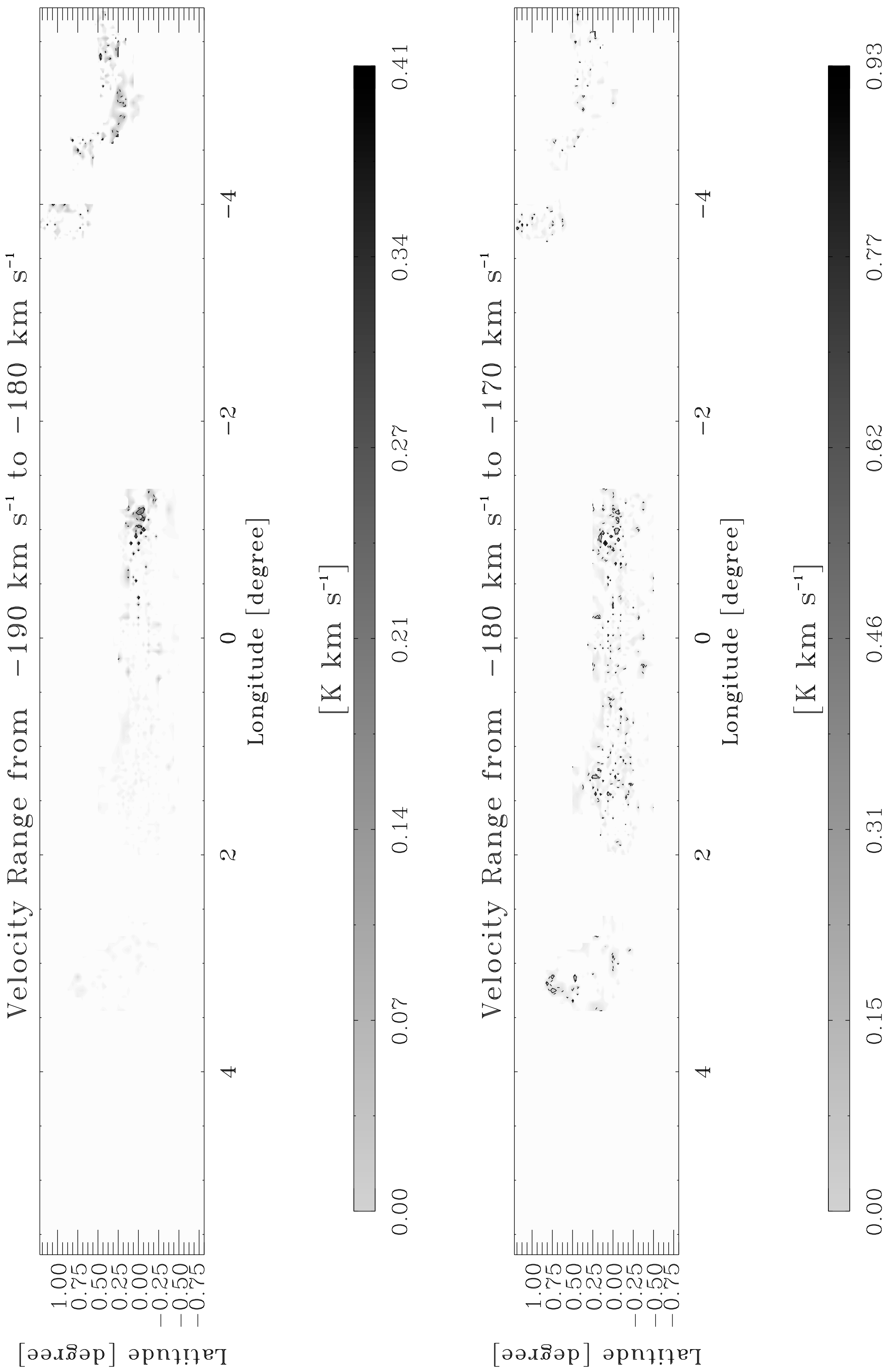

Fig. D1.4. continued.

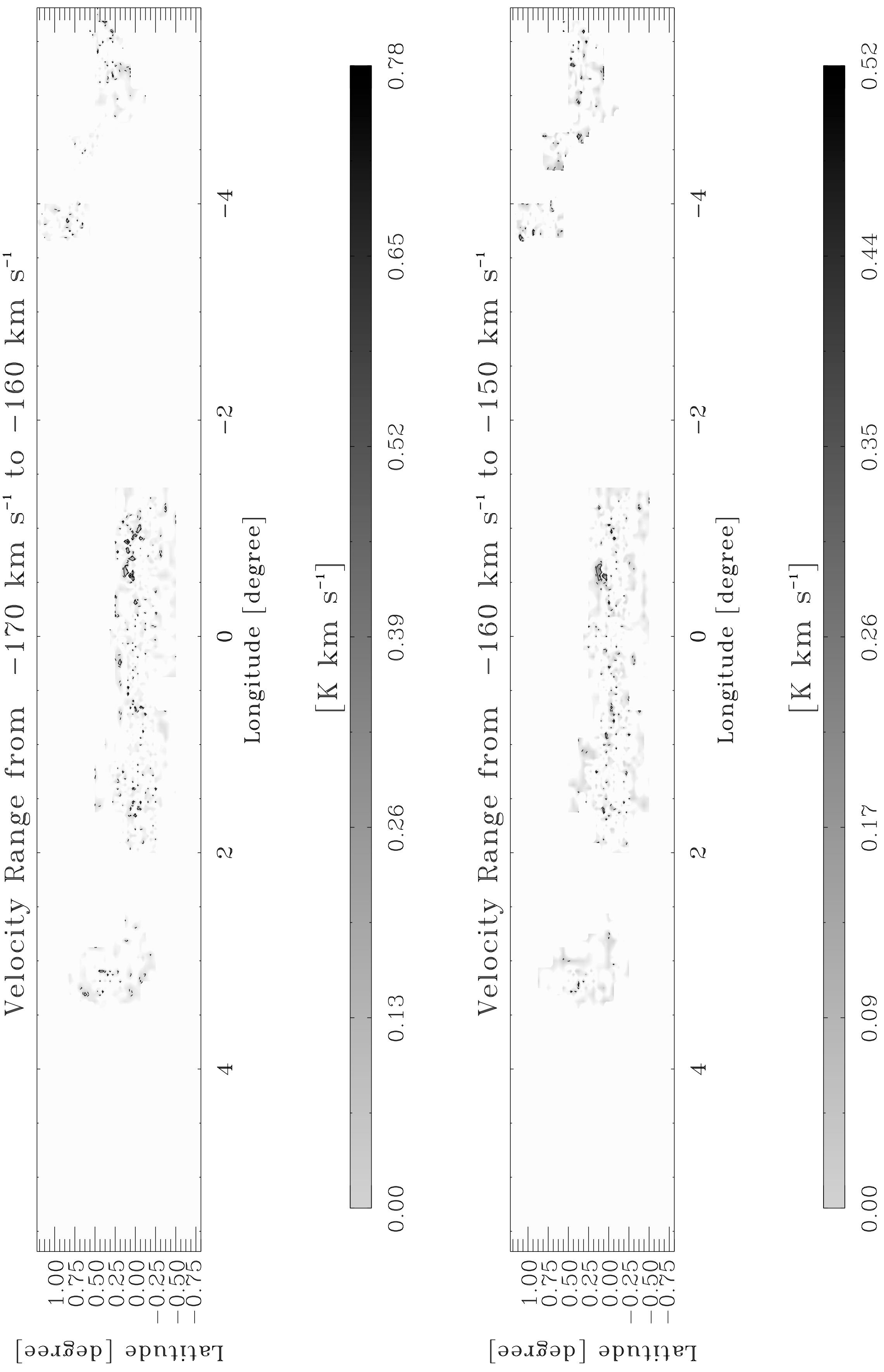

Fig. D1.5. continued.

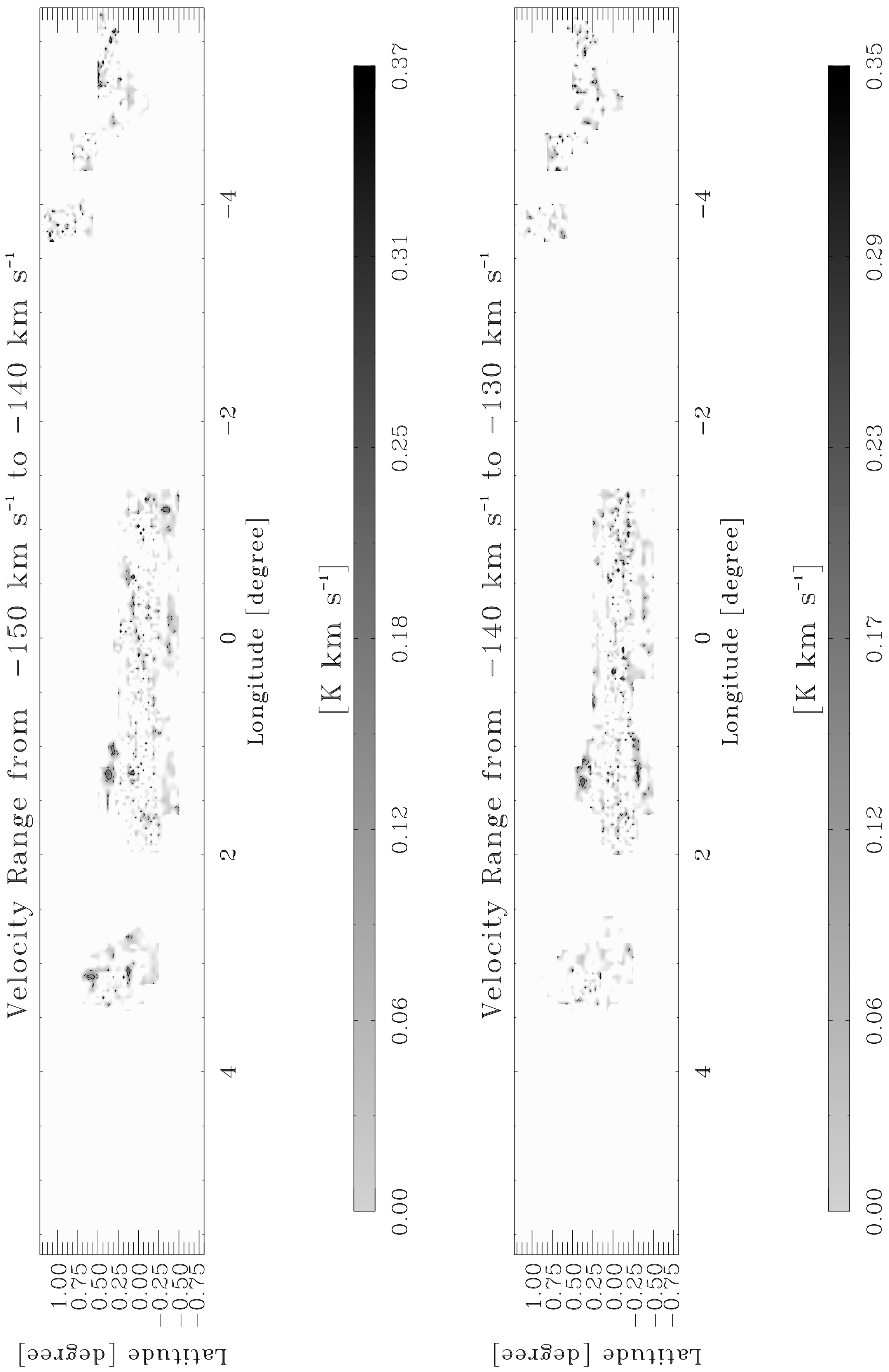

Fig. D1.6. continued.

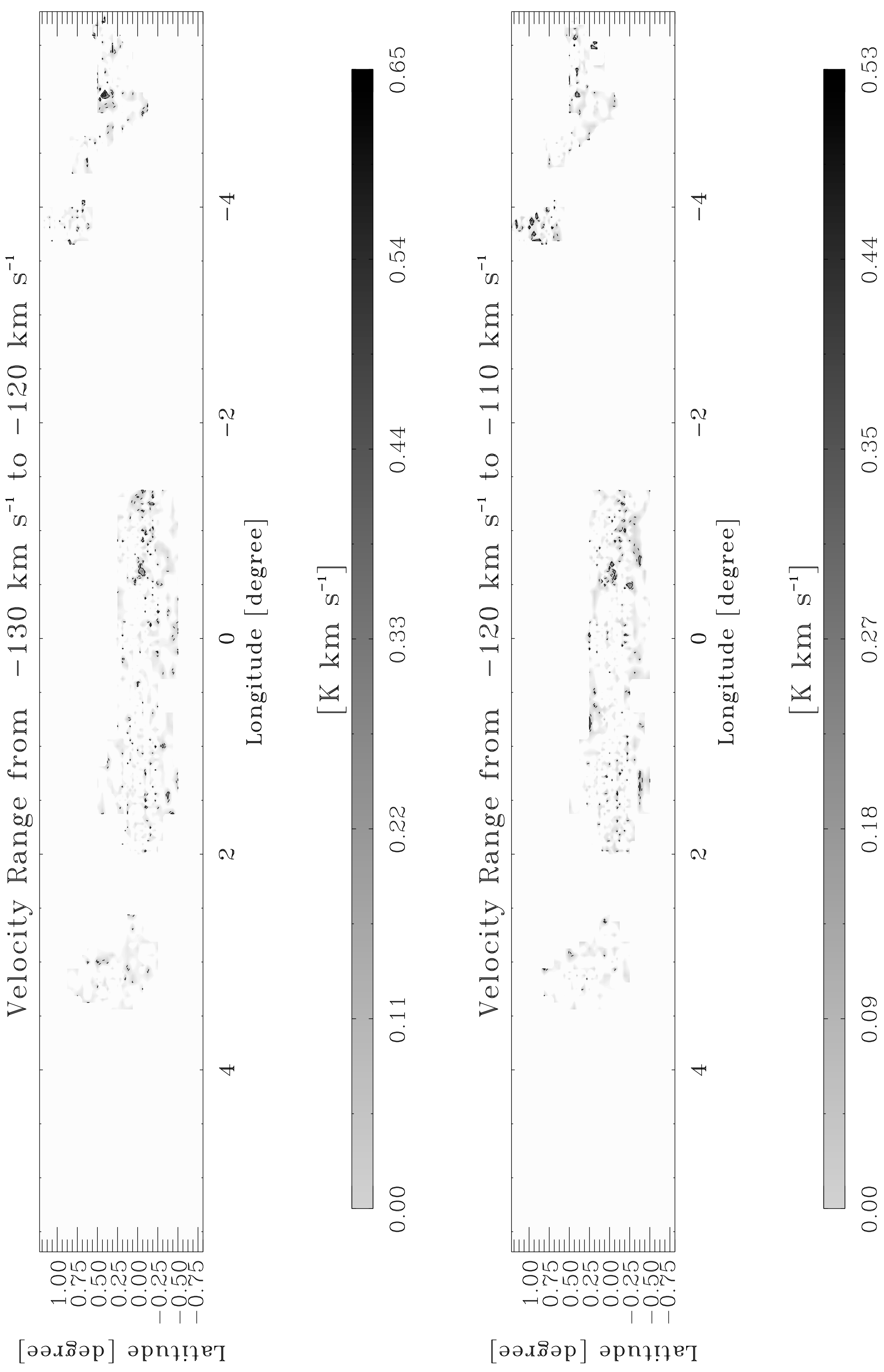

Fig. D1.7. continued.

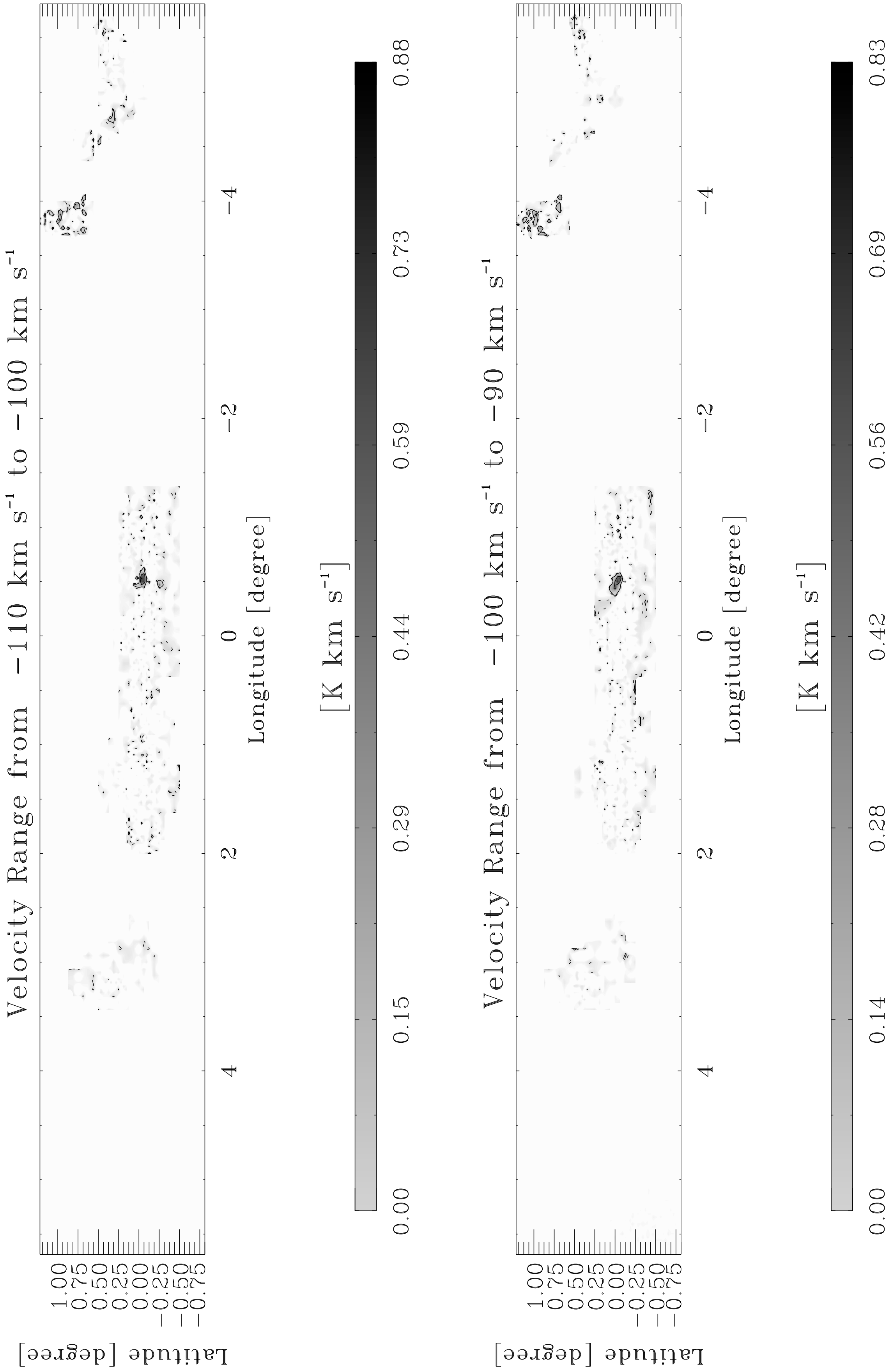

Fig. D1.8. continued.

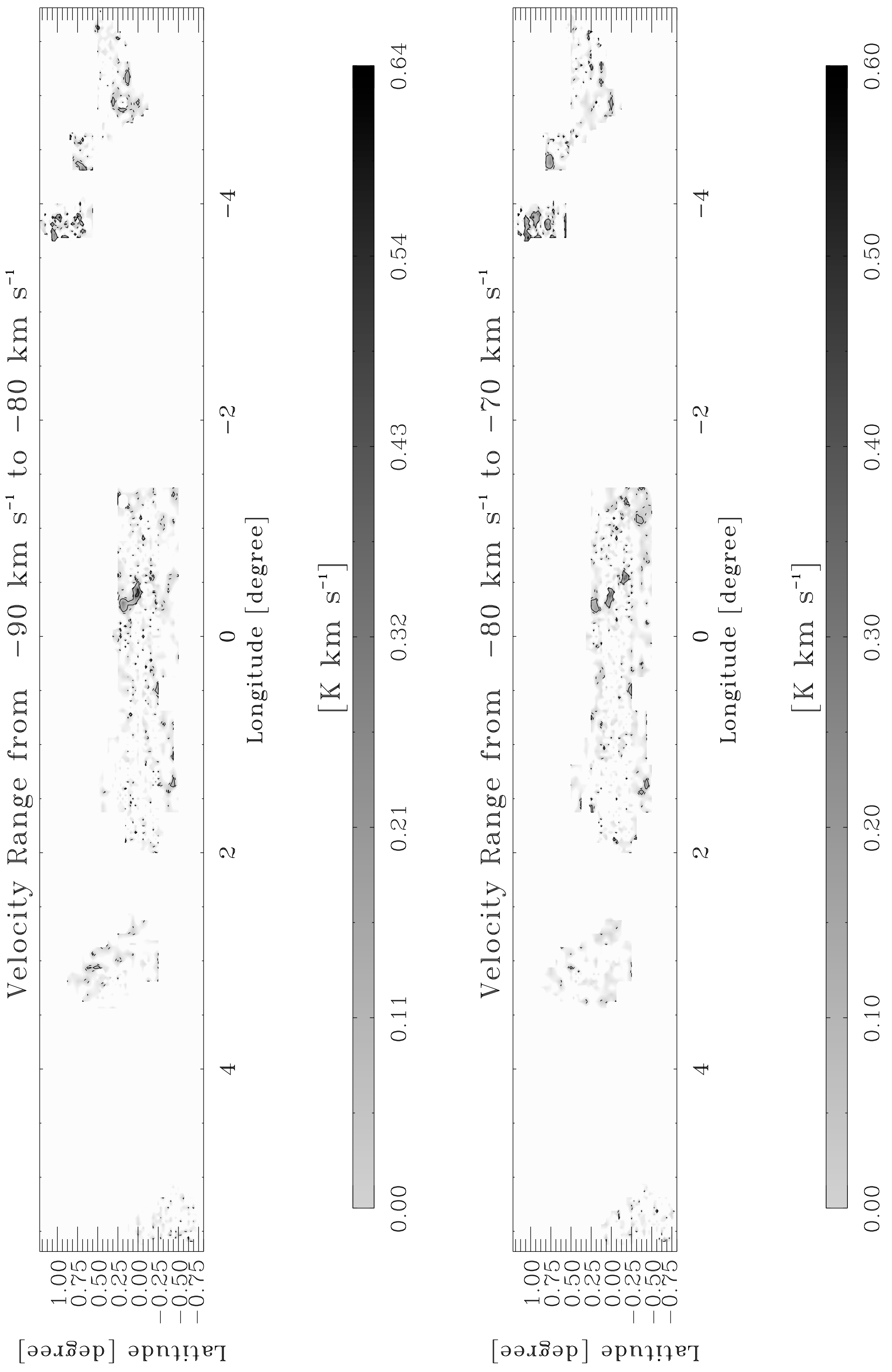

Fig. D1.9. continued.

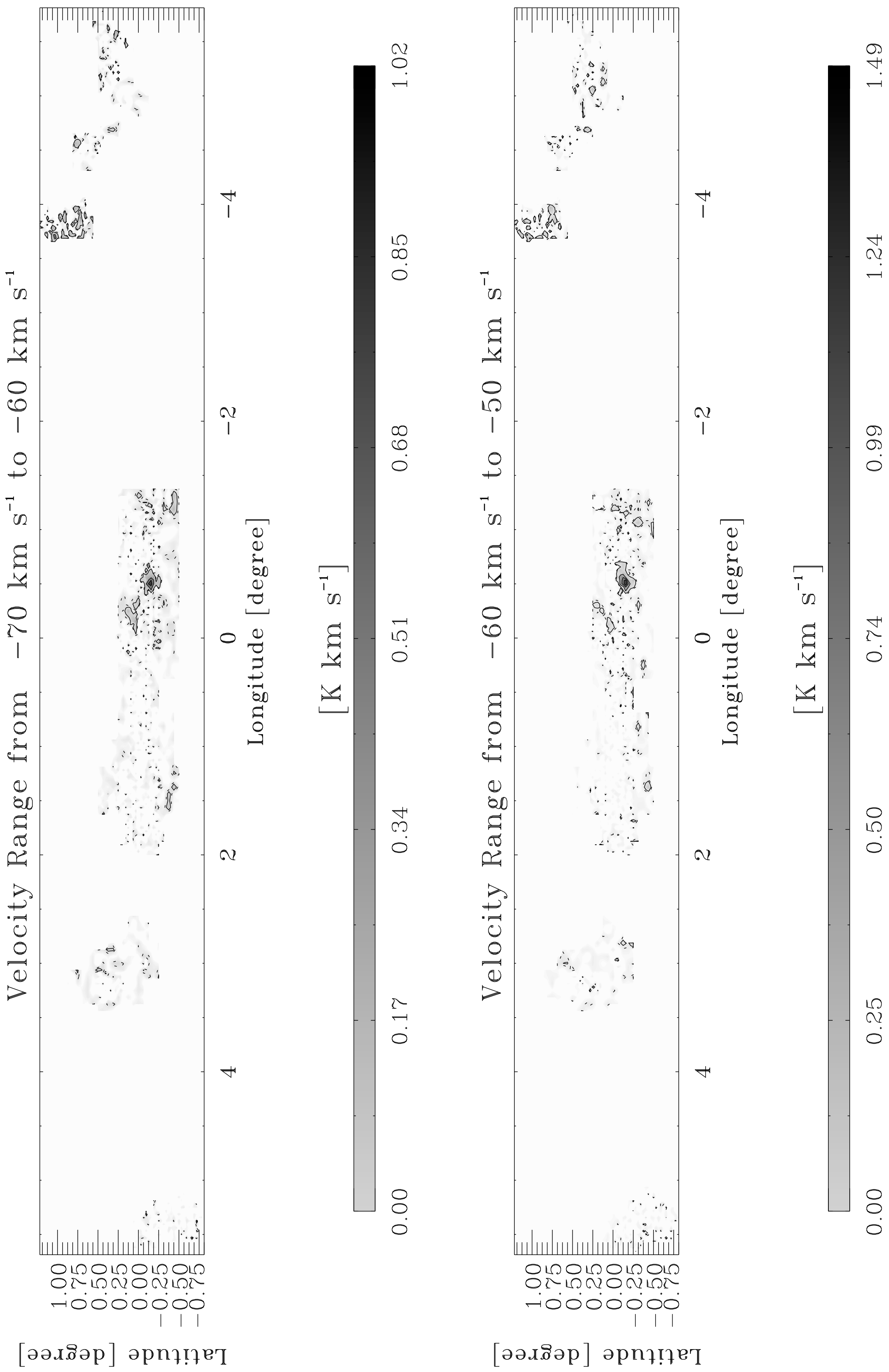

Fig. D1.10. continued.

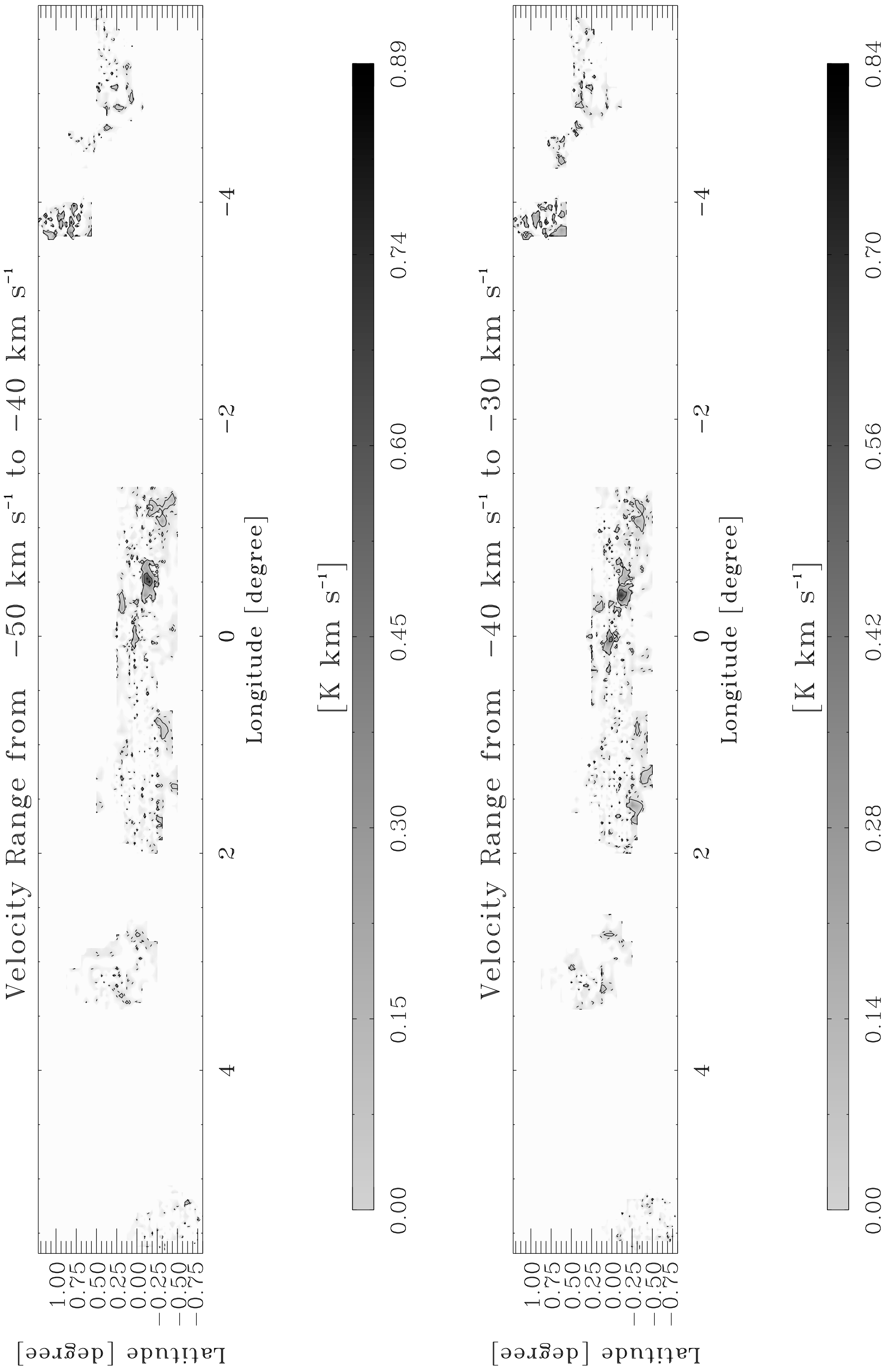

Fig. D1.11. continued.

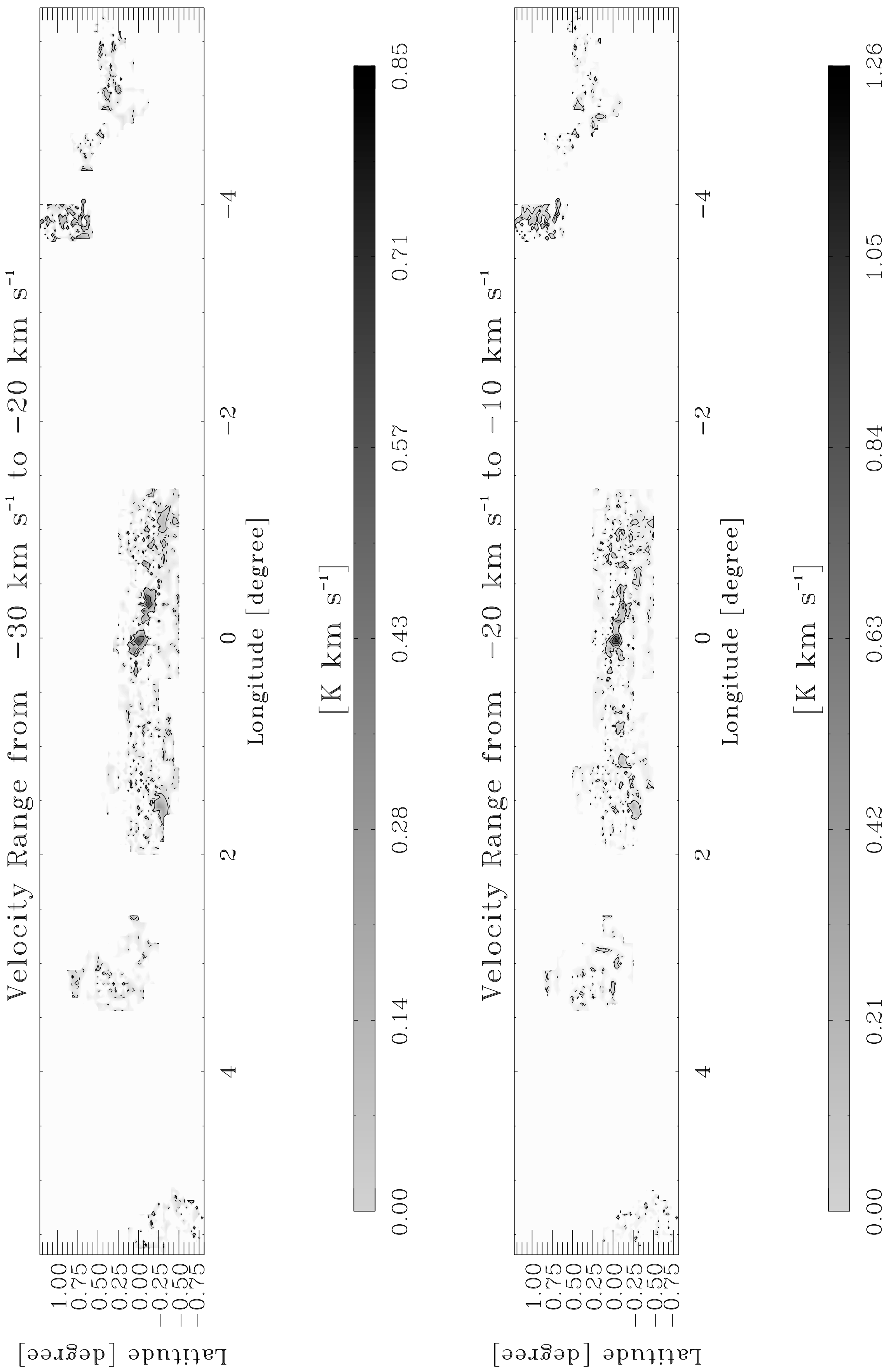

Fig. D1.12. continued.

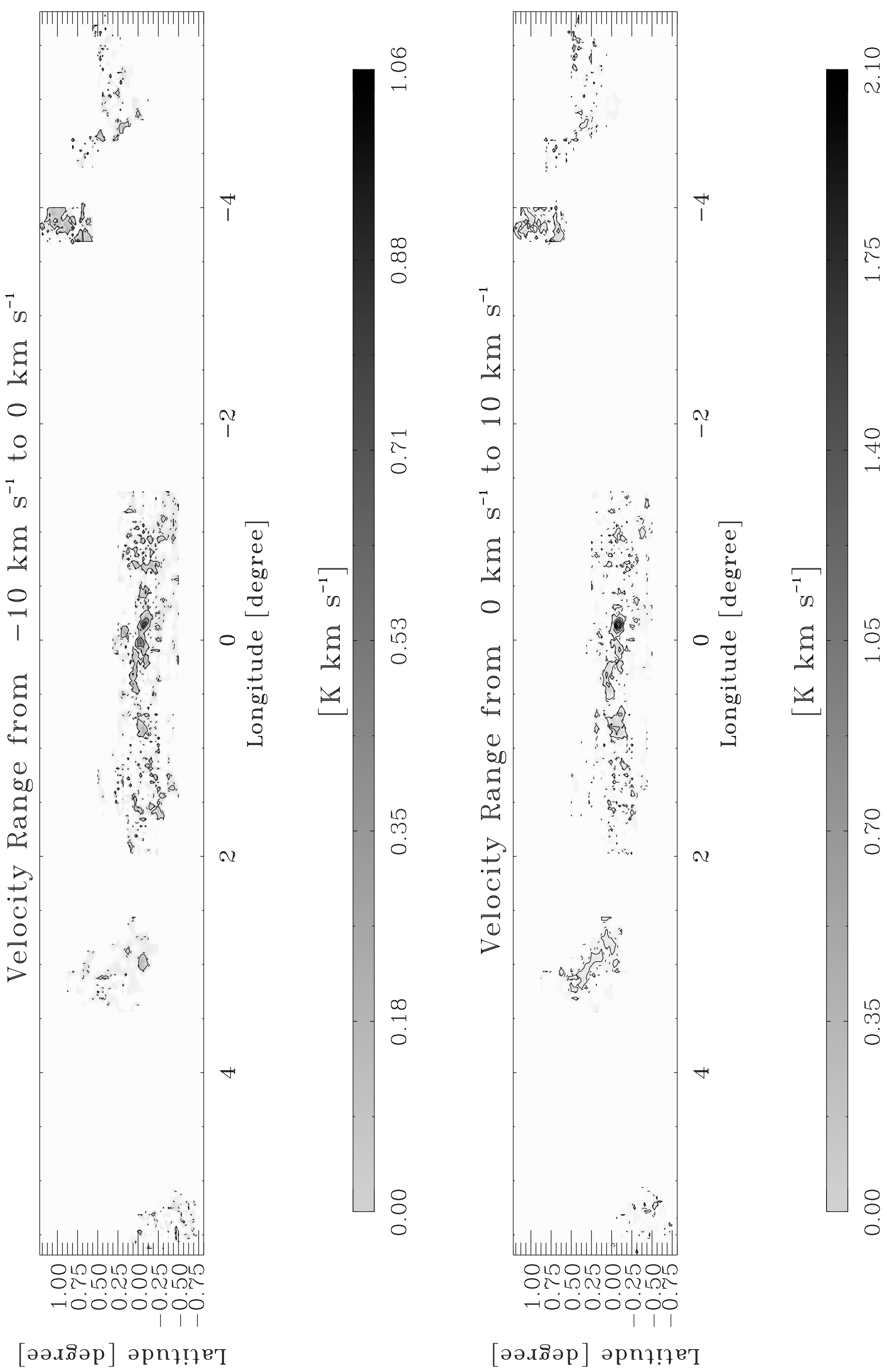

Fig. D1.13. continued.

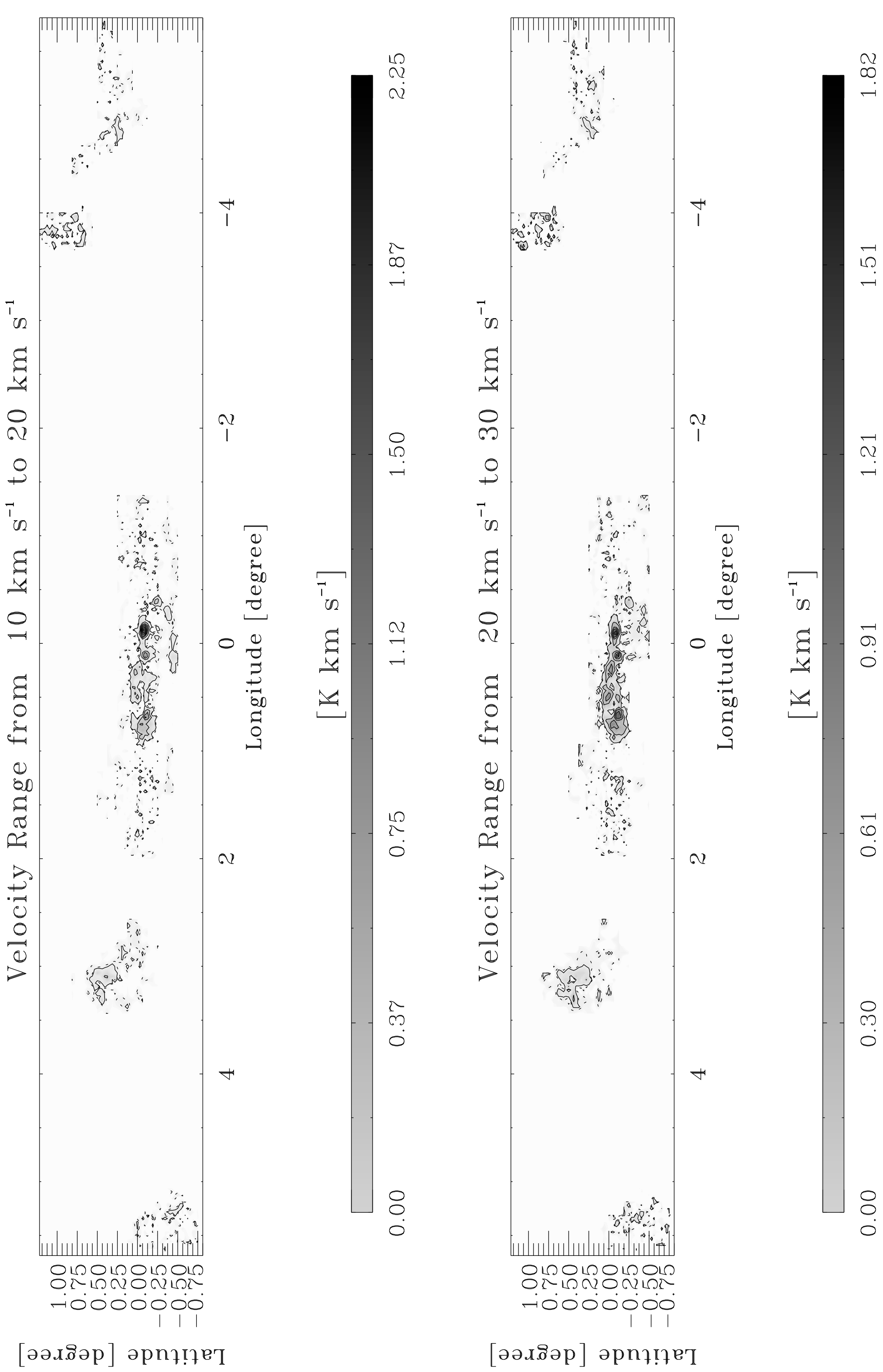

Fig. D1.14. continued.

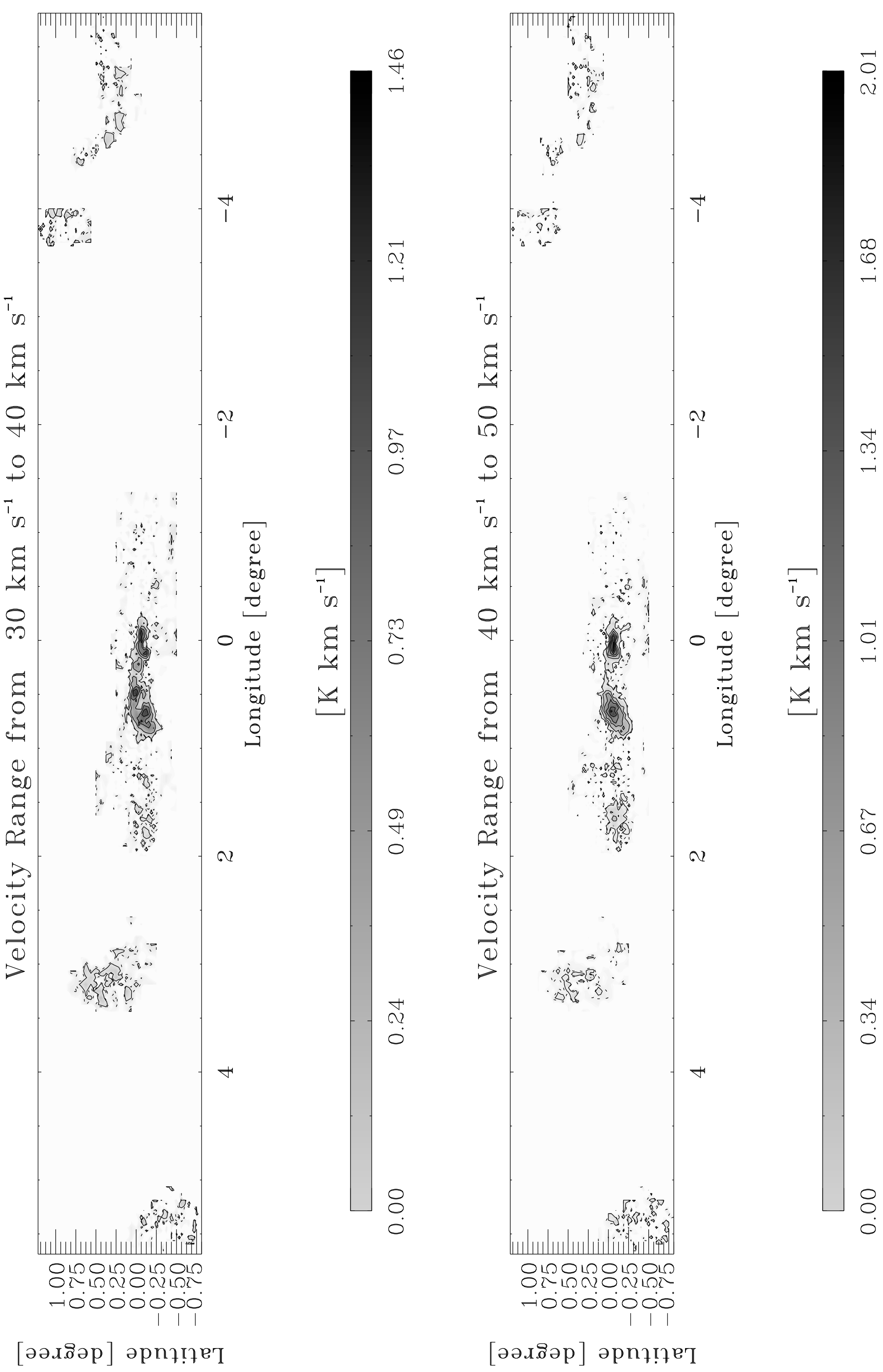

Fig. D1.15. continued.

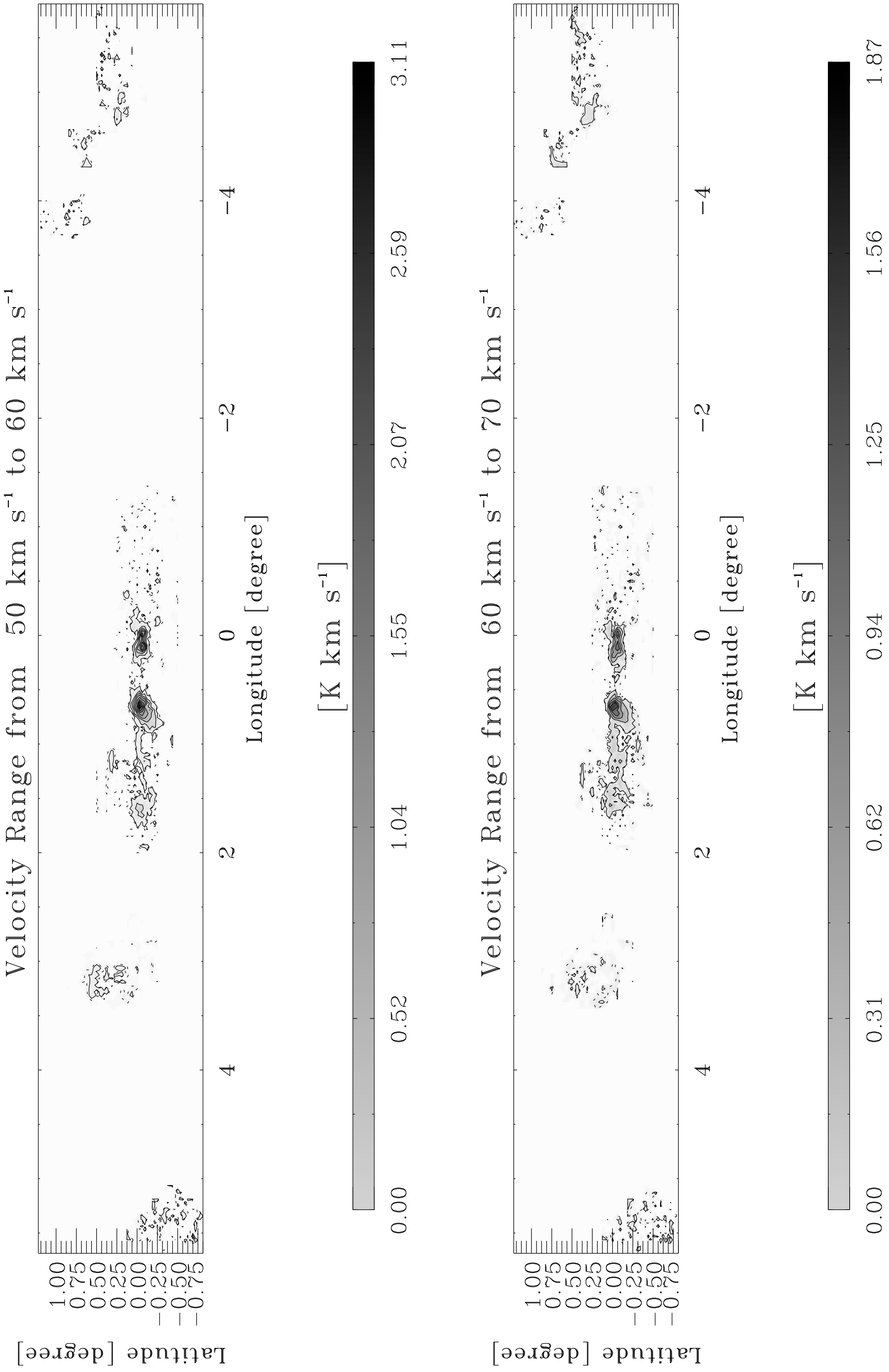

Fig. D1.16. continued.

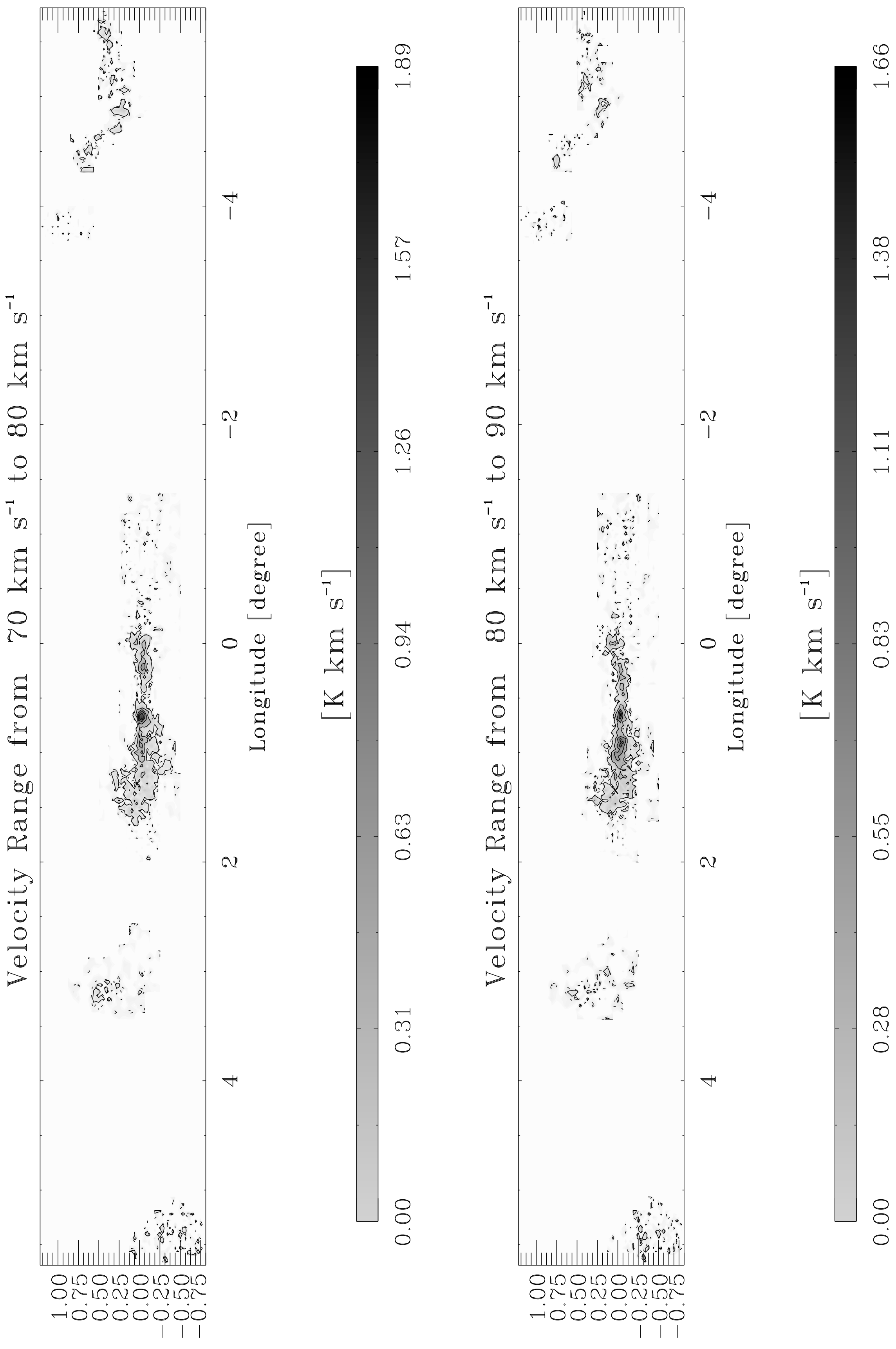

Fig. D1.17. continued.

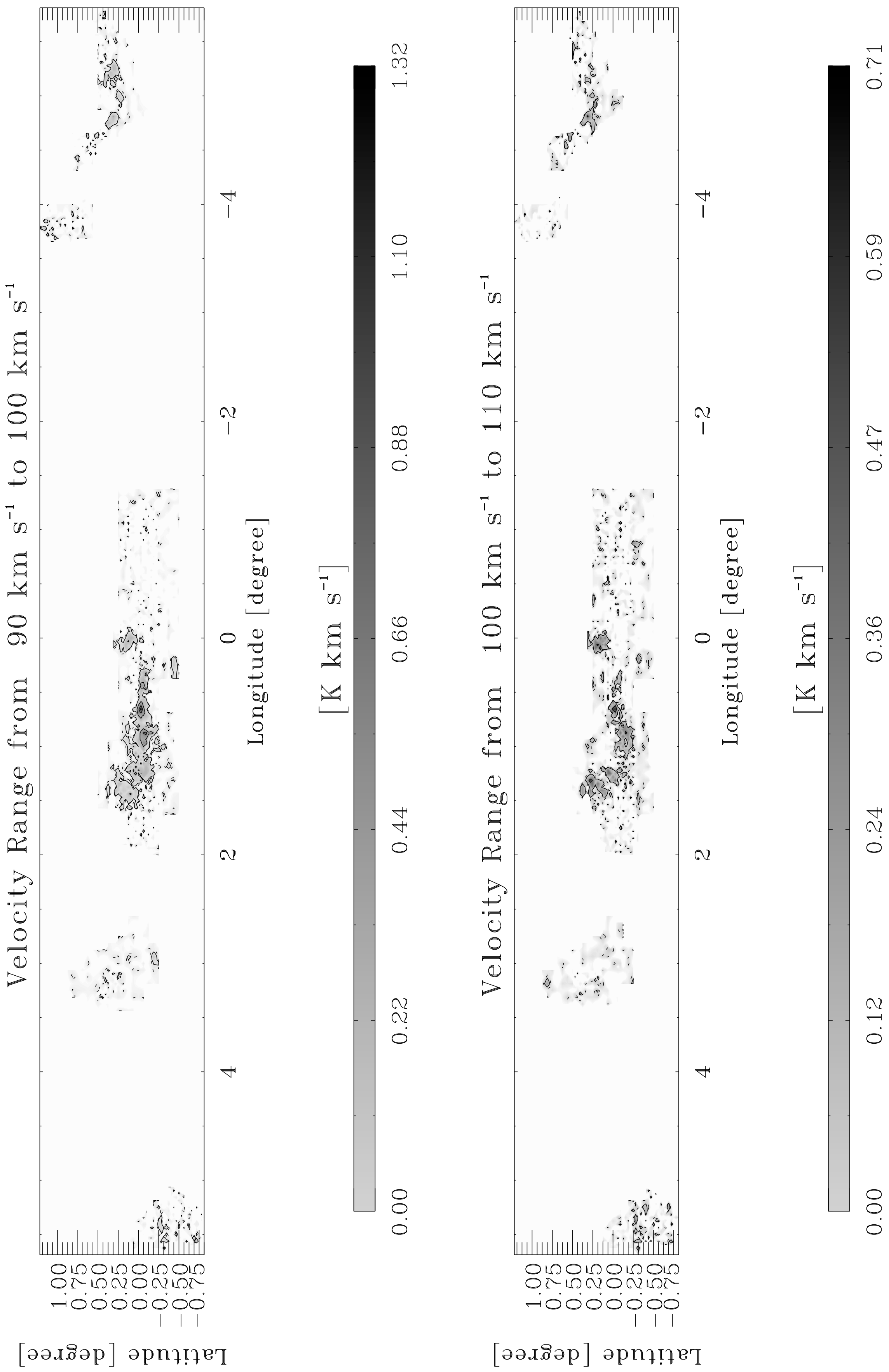

Fig. D1.18. continued.

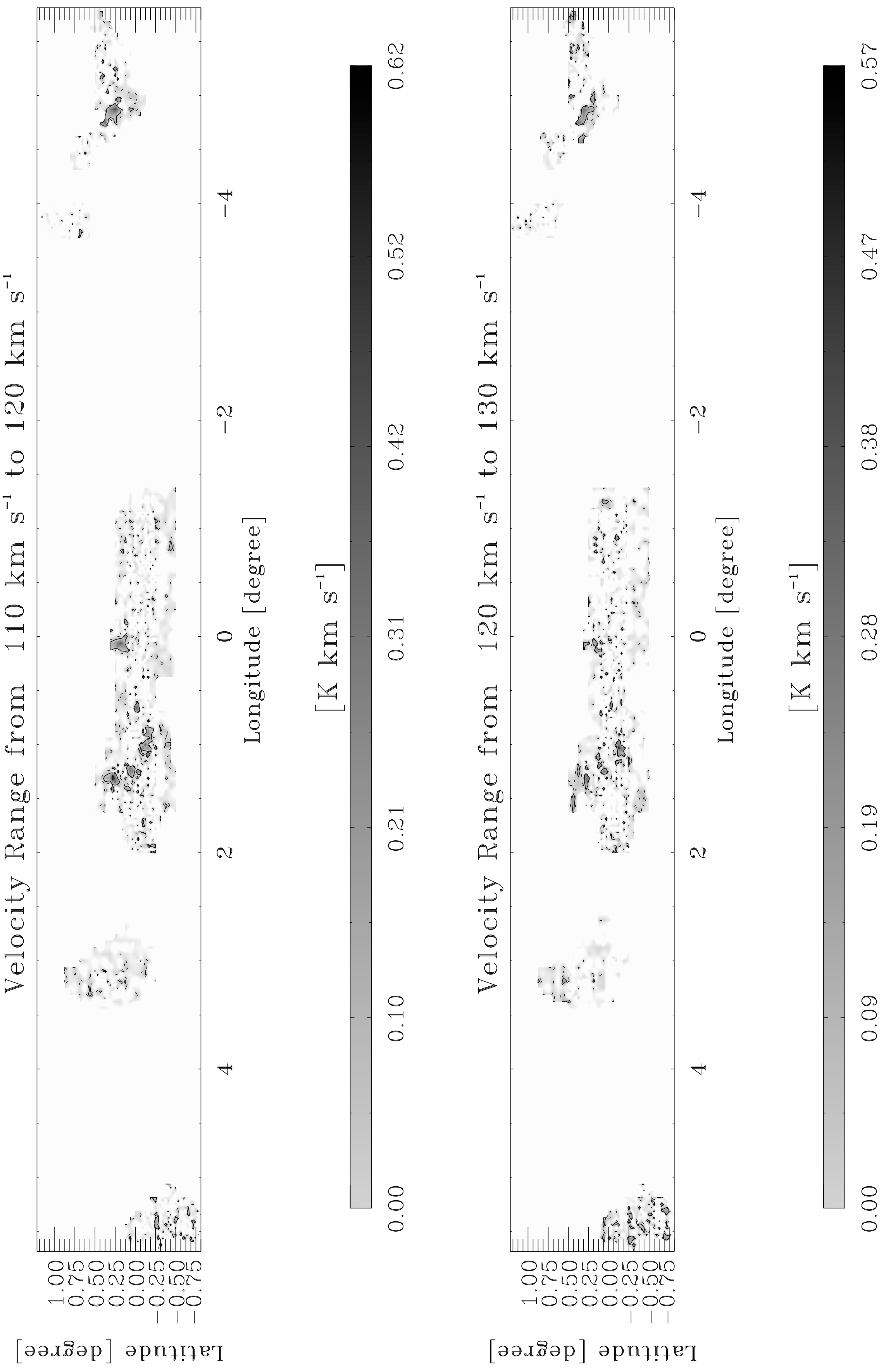

Fig. D1.19. continued.

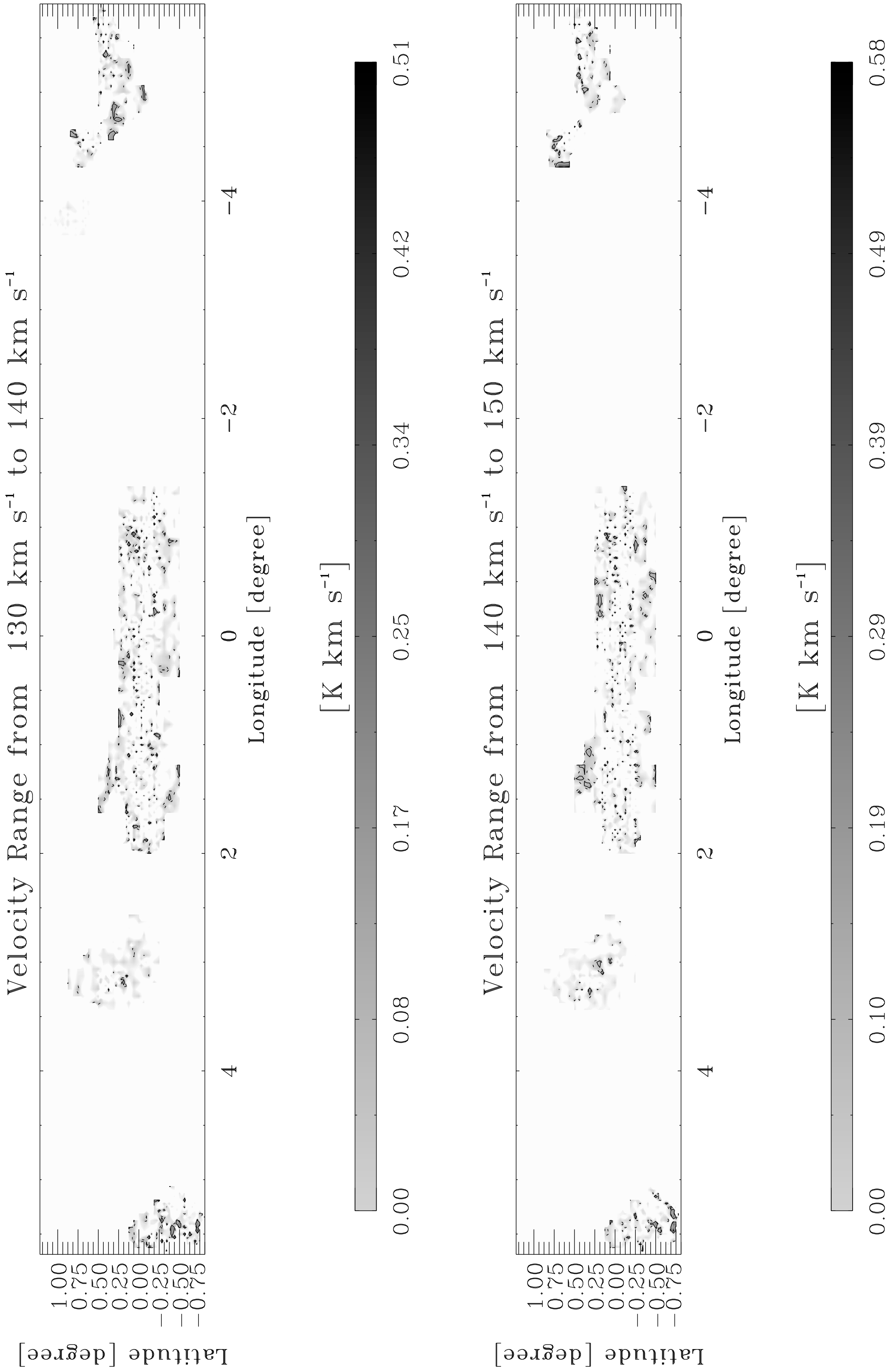

Fig. D1.20. continued.

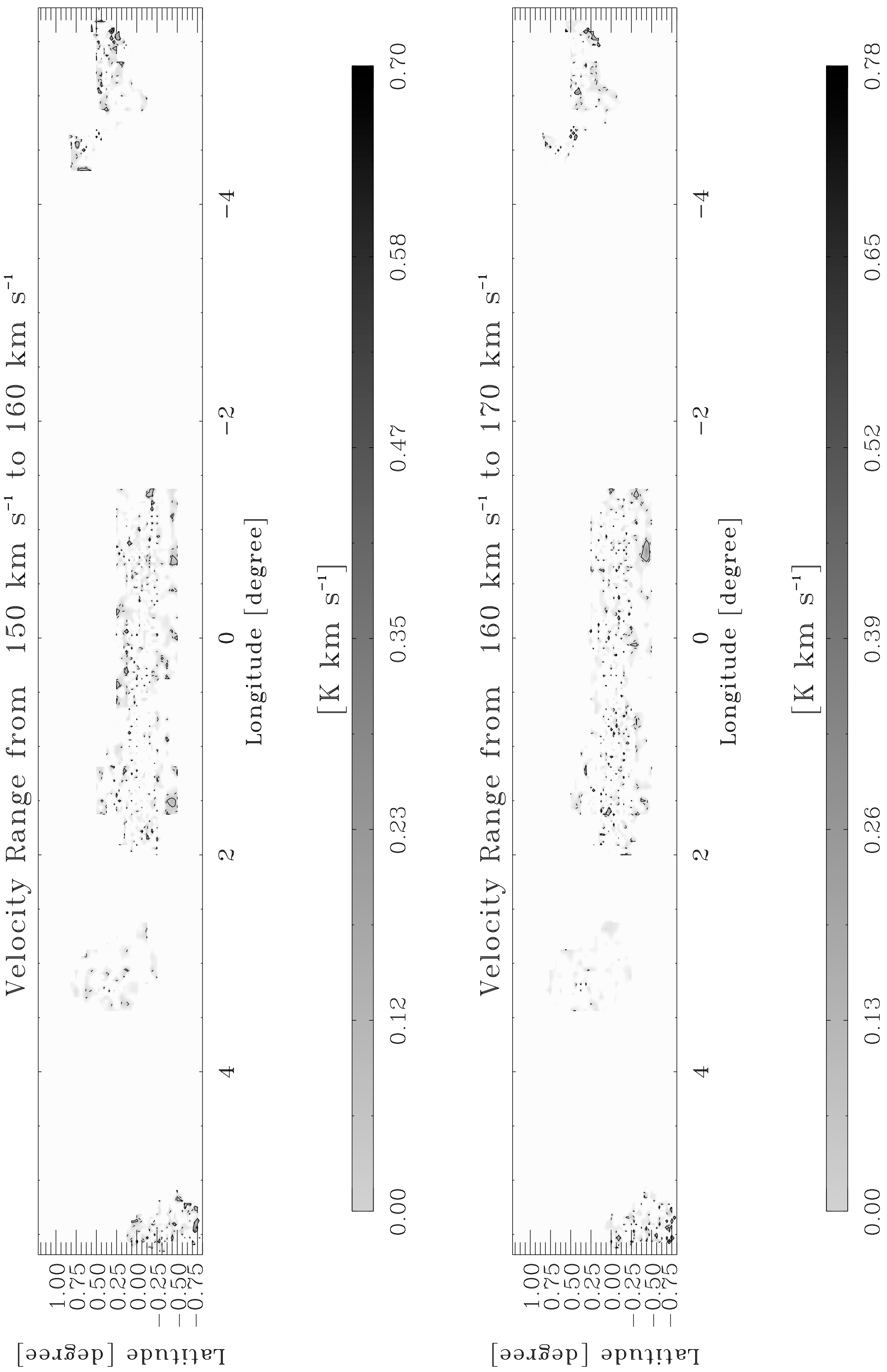

Fig. D1.21. continued.

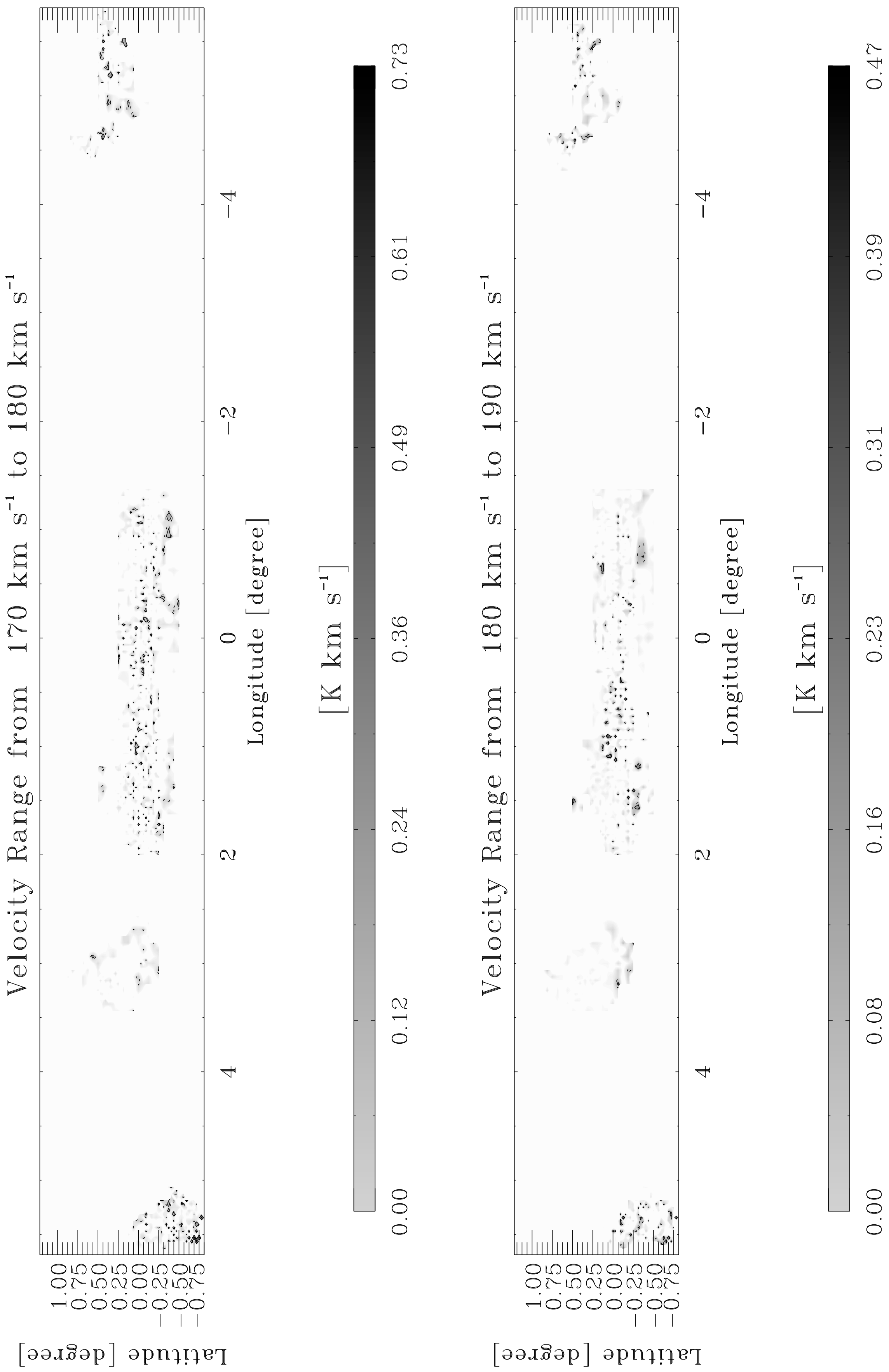

Fig. D1.22. continued.

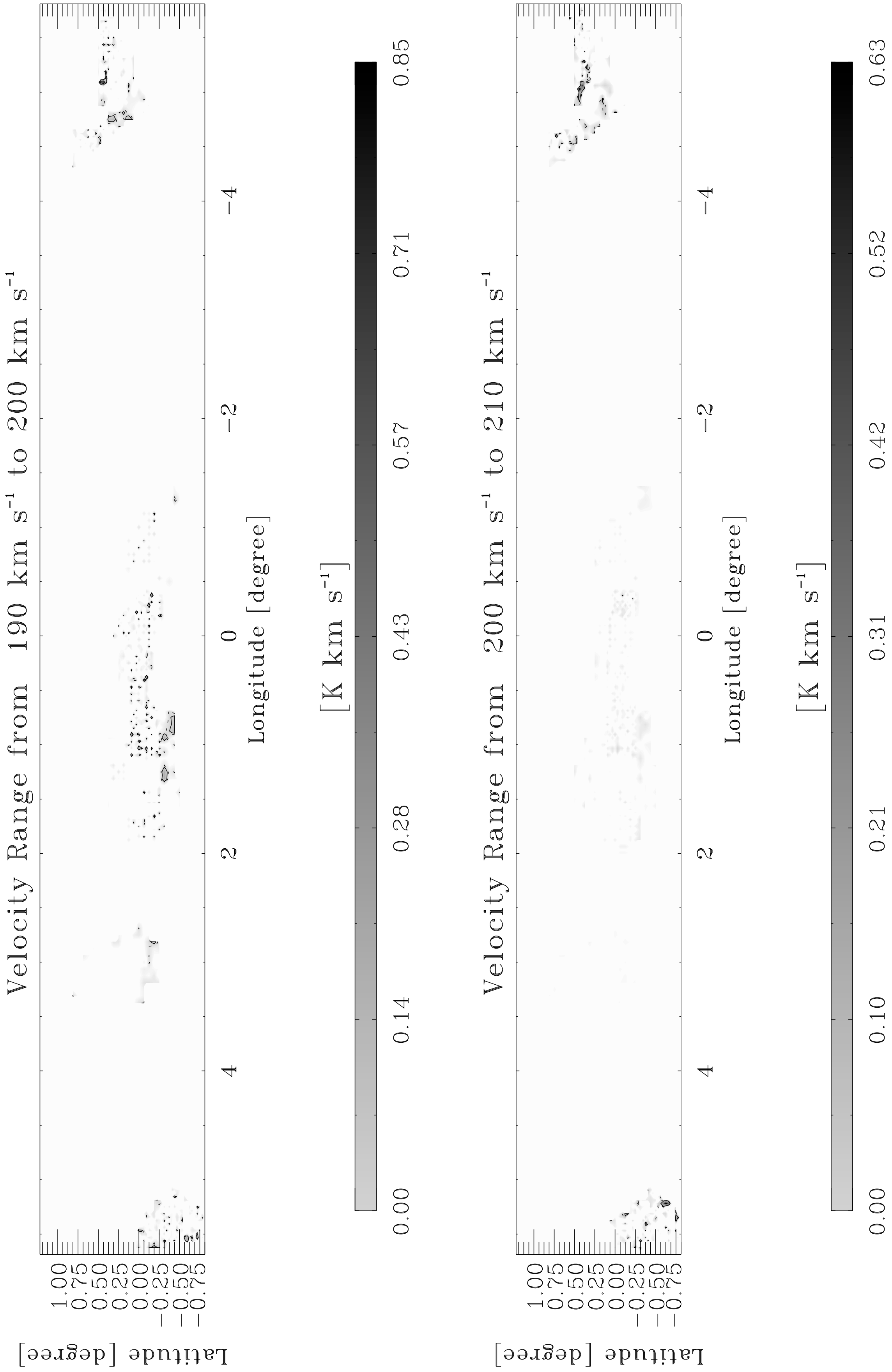

Fig. D1.23. continued.

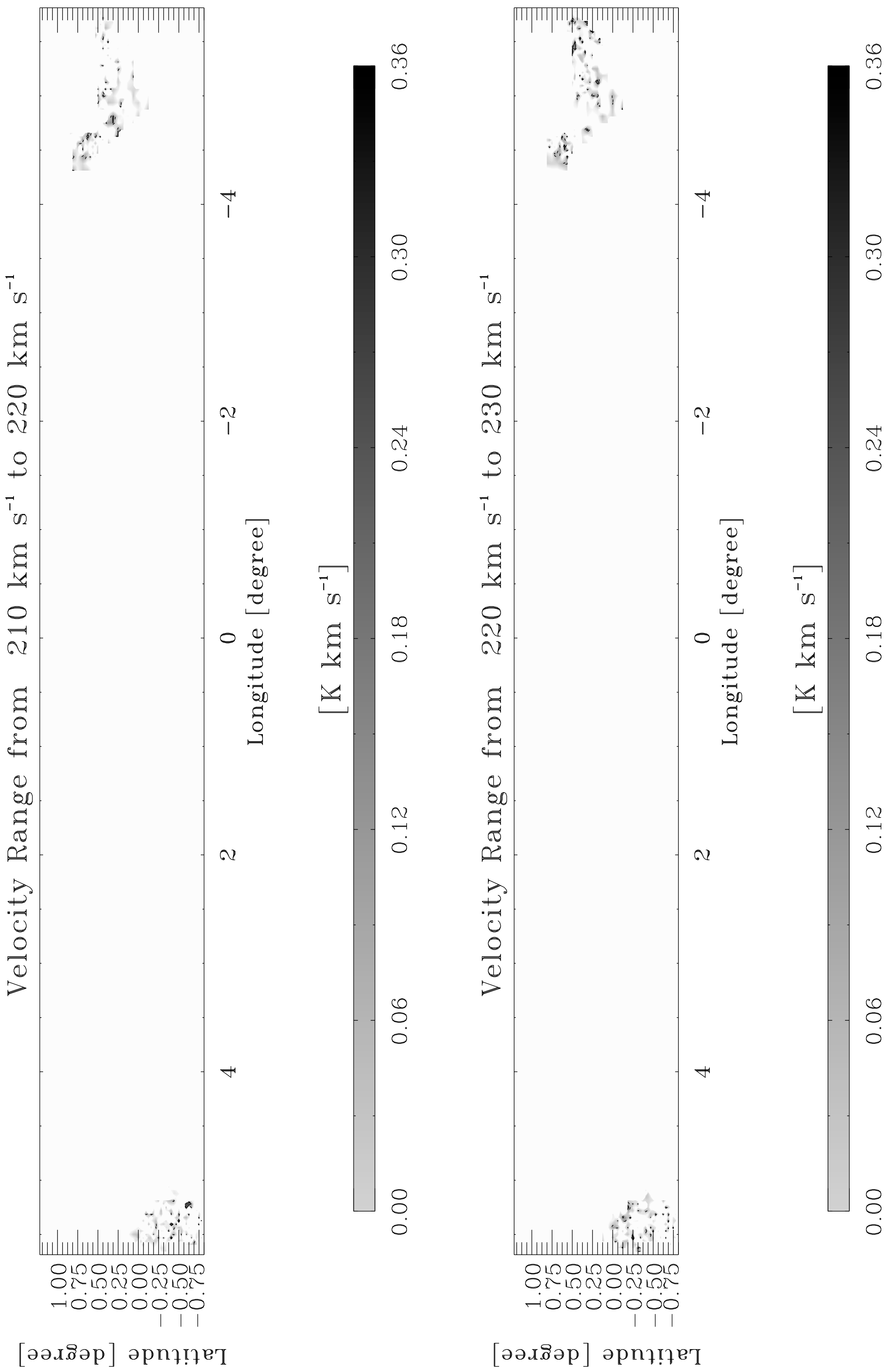

Fig. D1.24. continued.

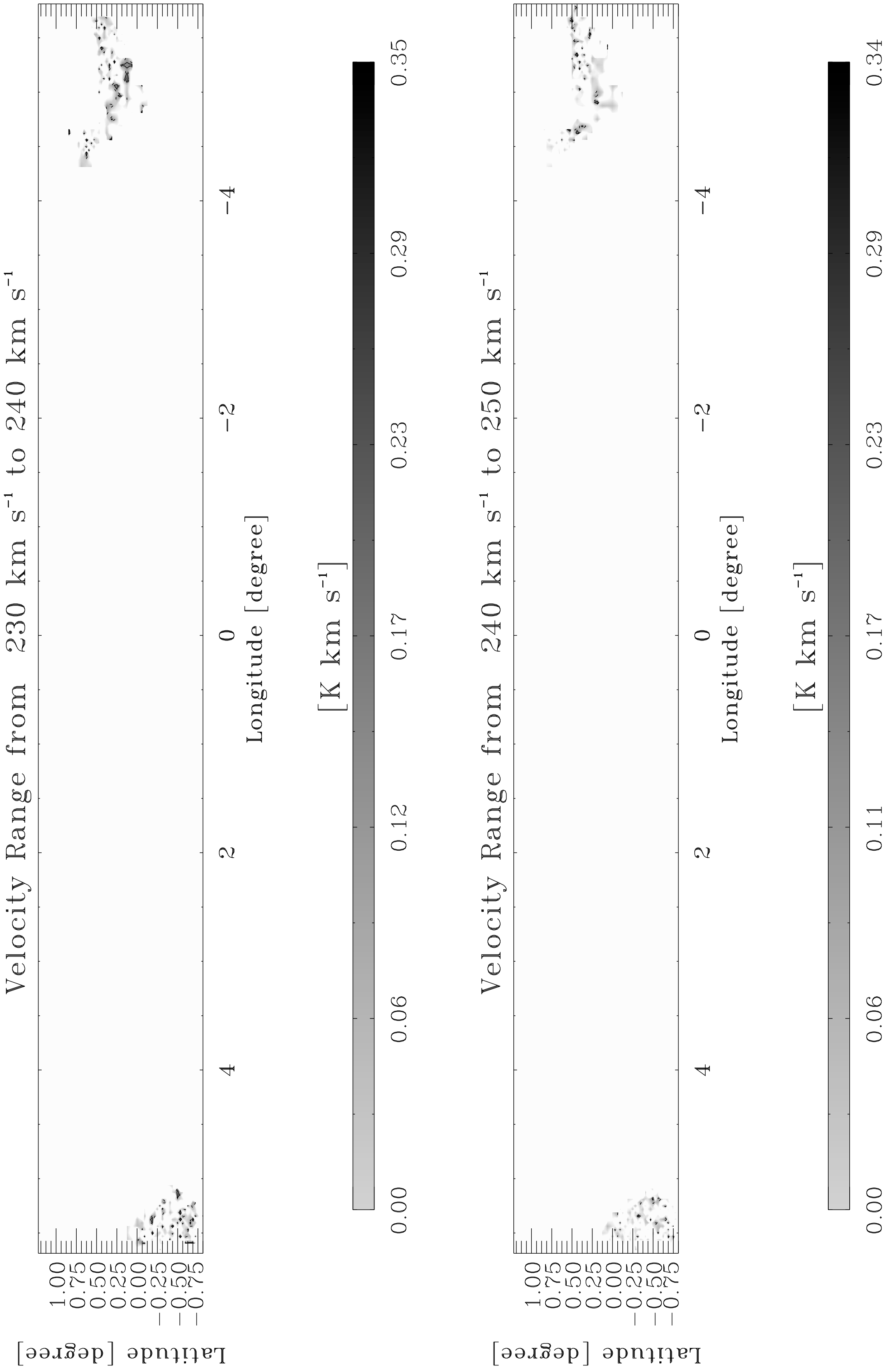

Fig. D1.25. continued.

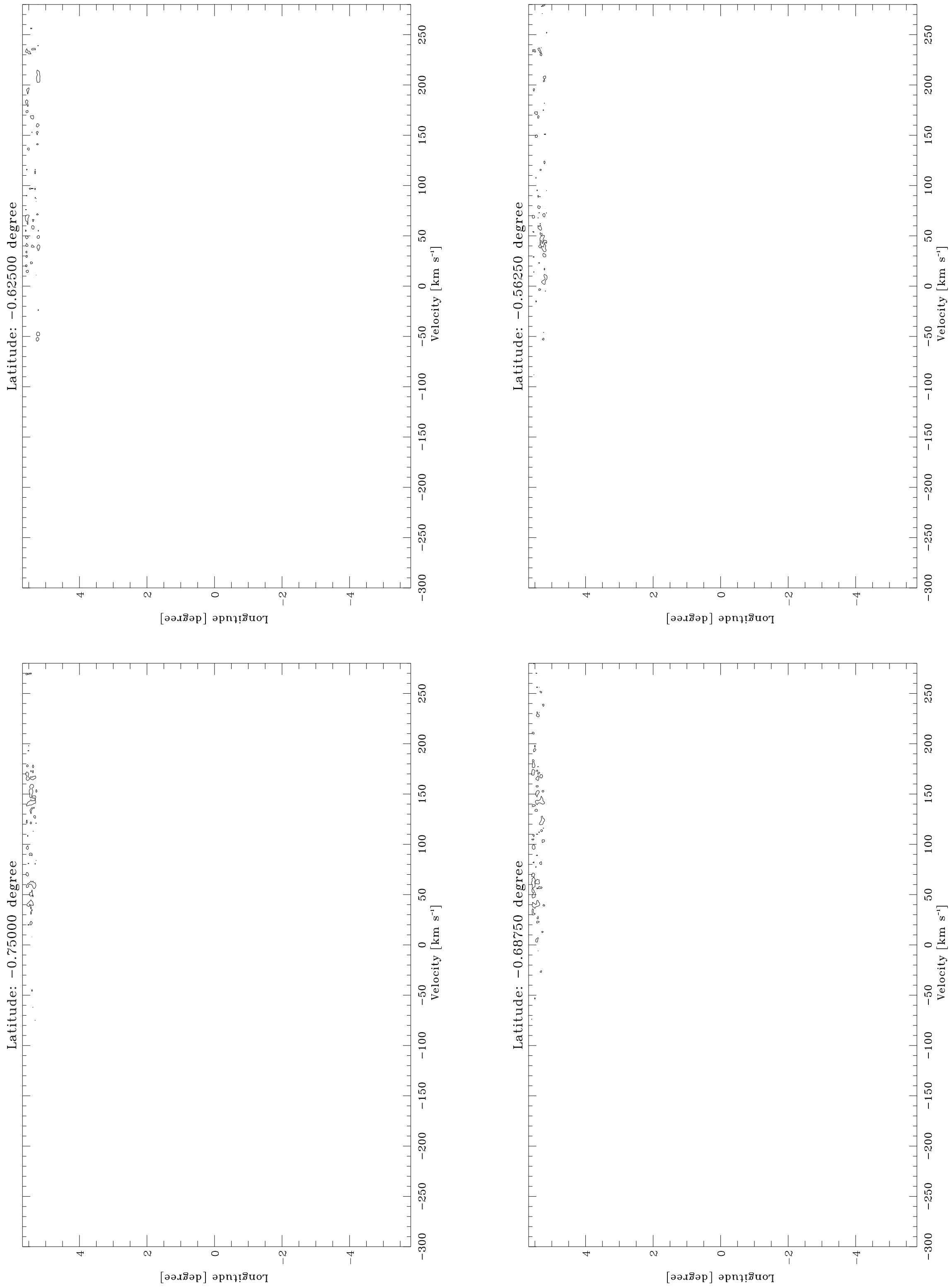

Fig. D2.1. Longitude-velocidad contour diagrams integrated in latitude in step of 0$^\circ\!\!.$0625 in H13CO+. The lowest contour is at 0.0013 K (3σ). The following contours increase them in step of 0.0018 K, which correspond to 4σ.

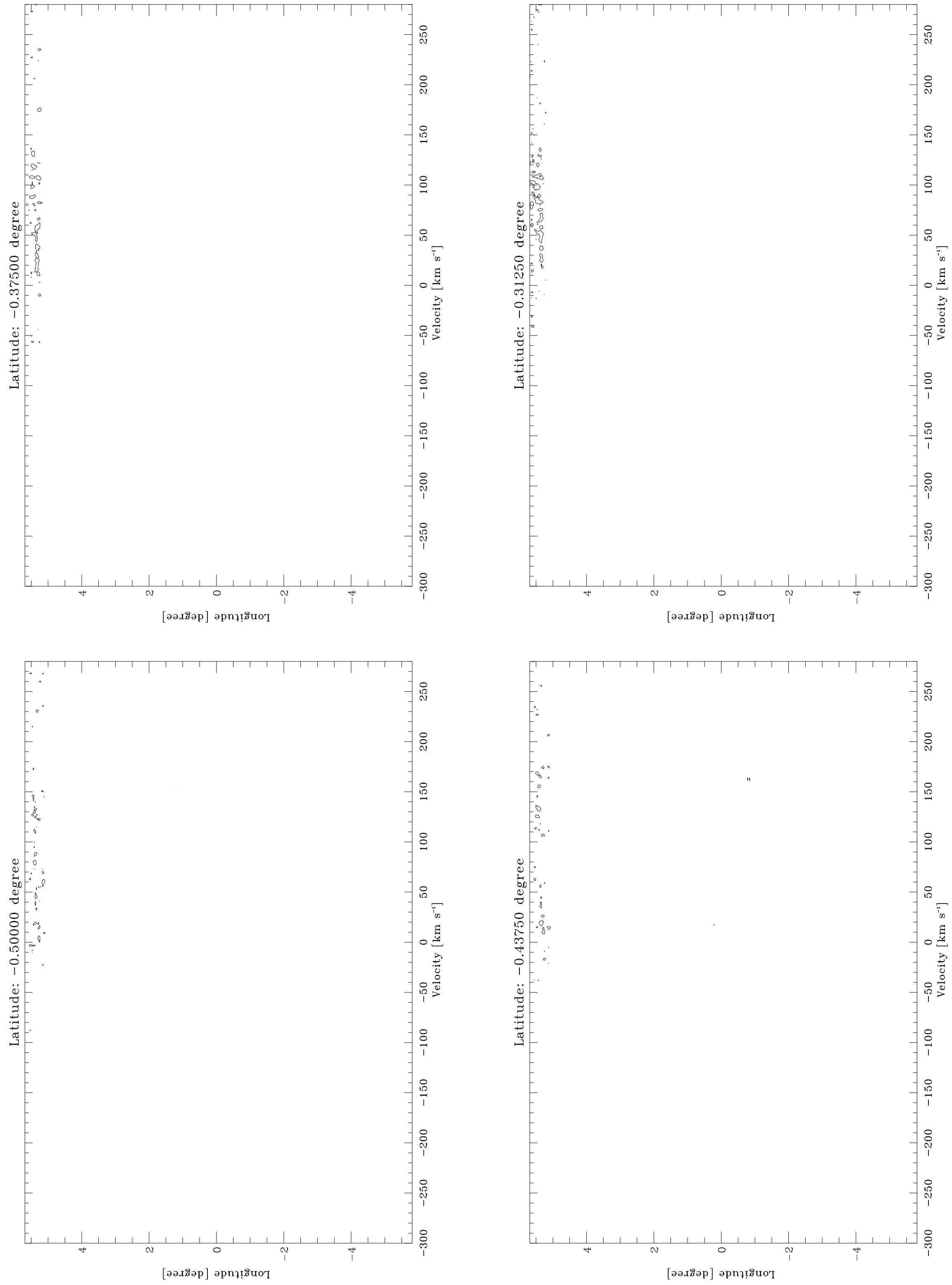

Fig. D2.2. continued.

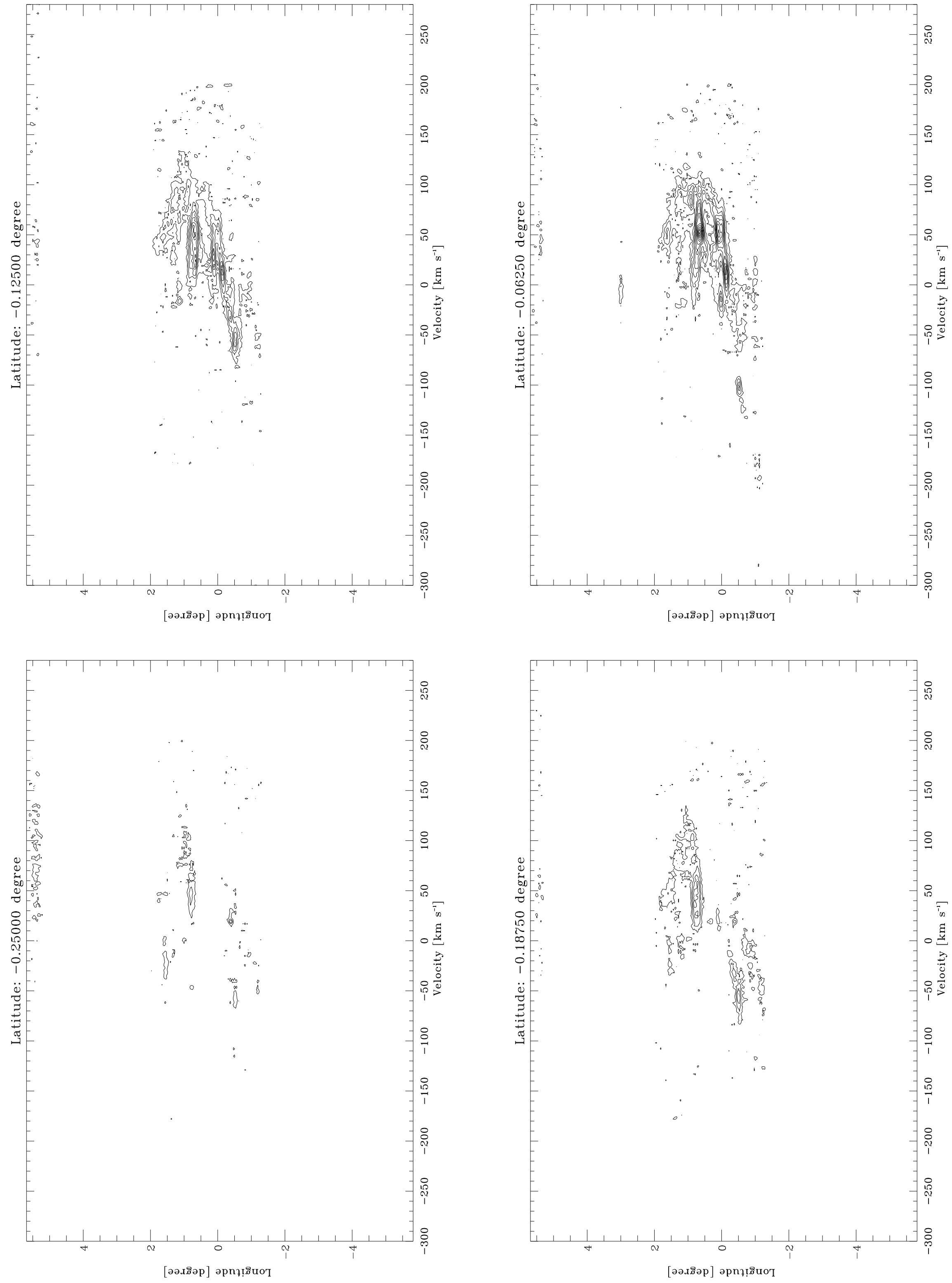

Fig. D2.3. continued.

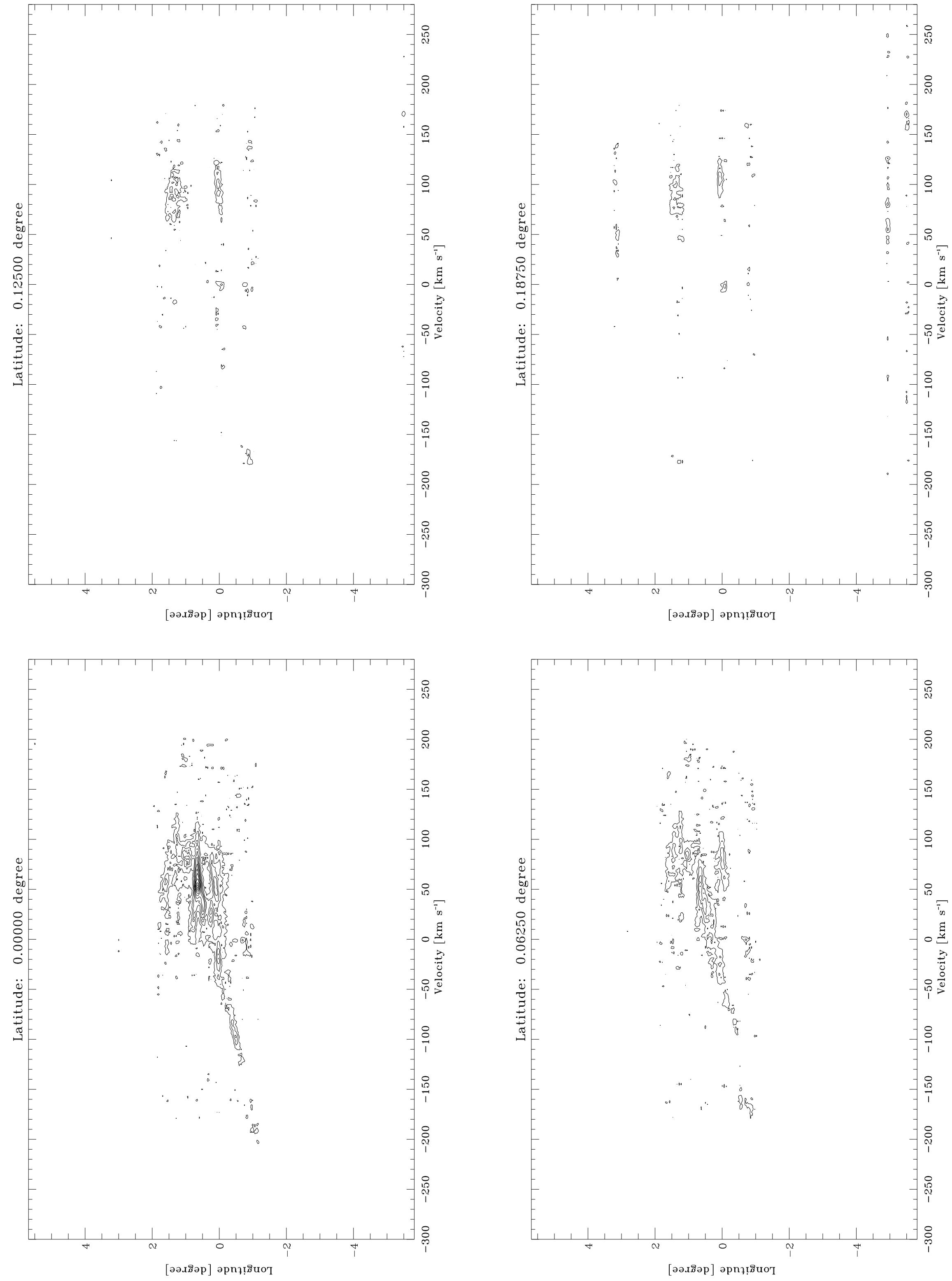

Fig. D2.4. continued.

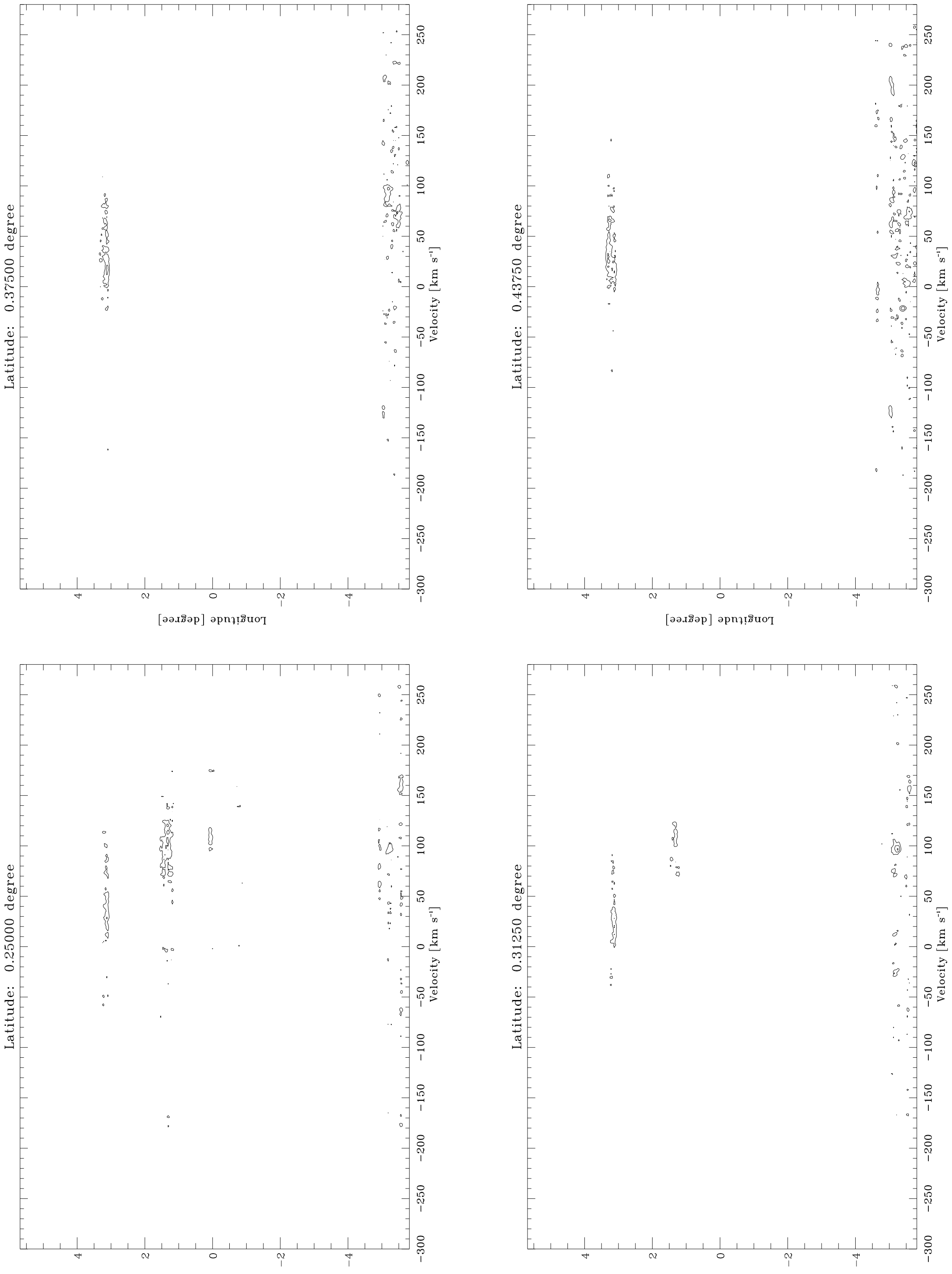

Fig. D2.5. continued.

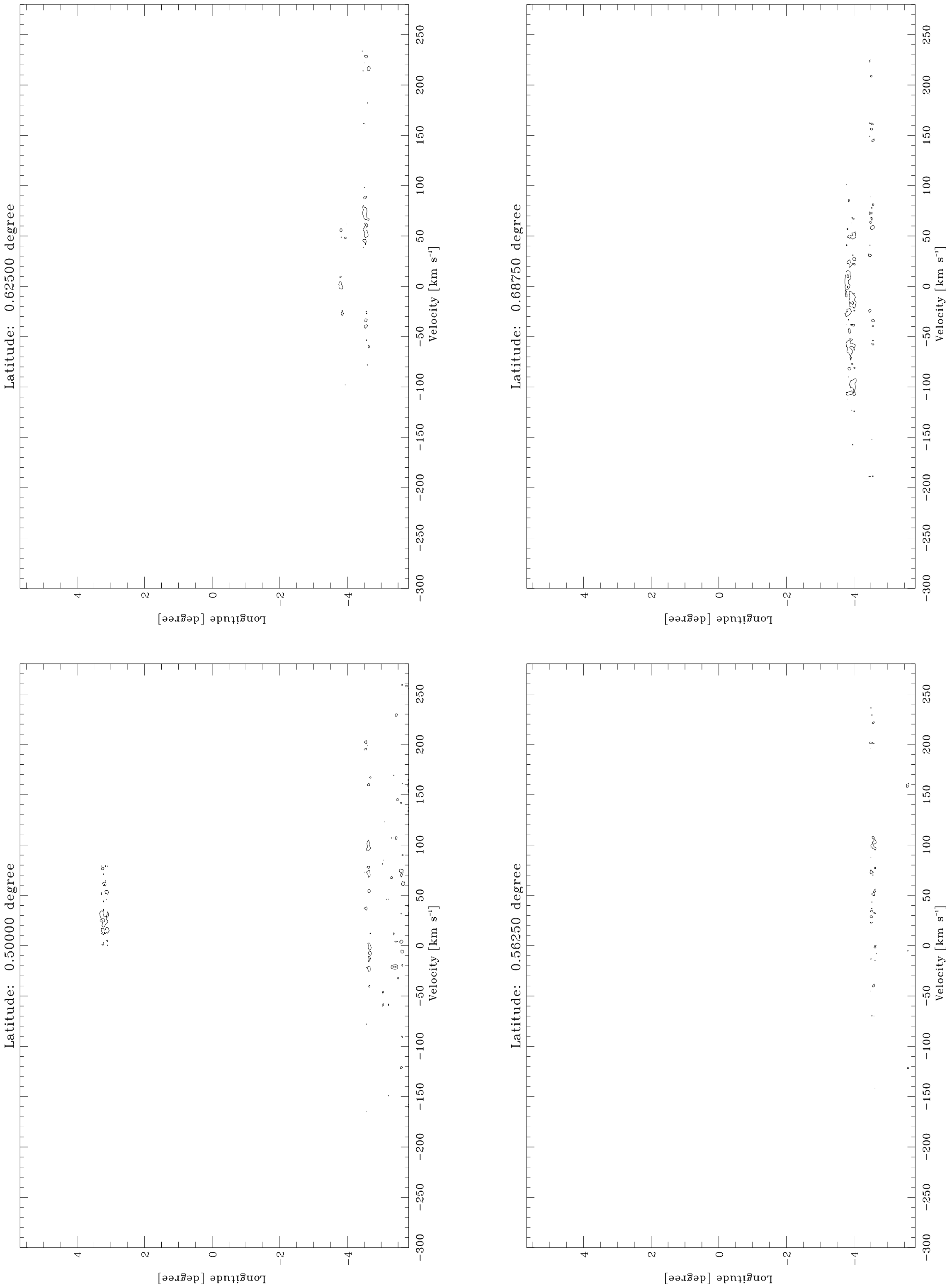

Fig. D2.6. continued.

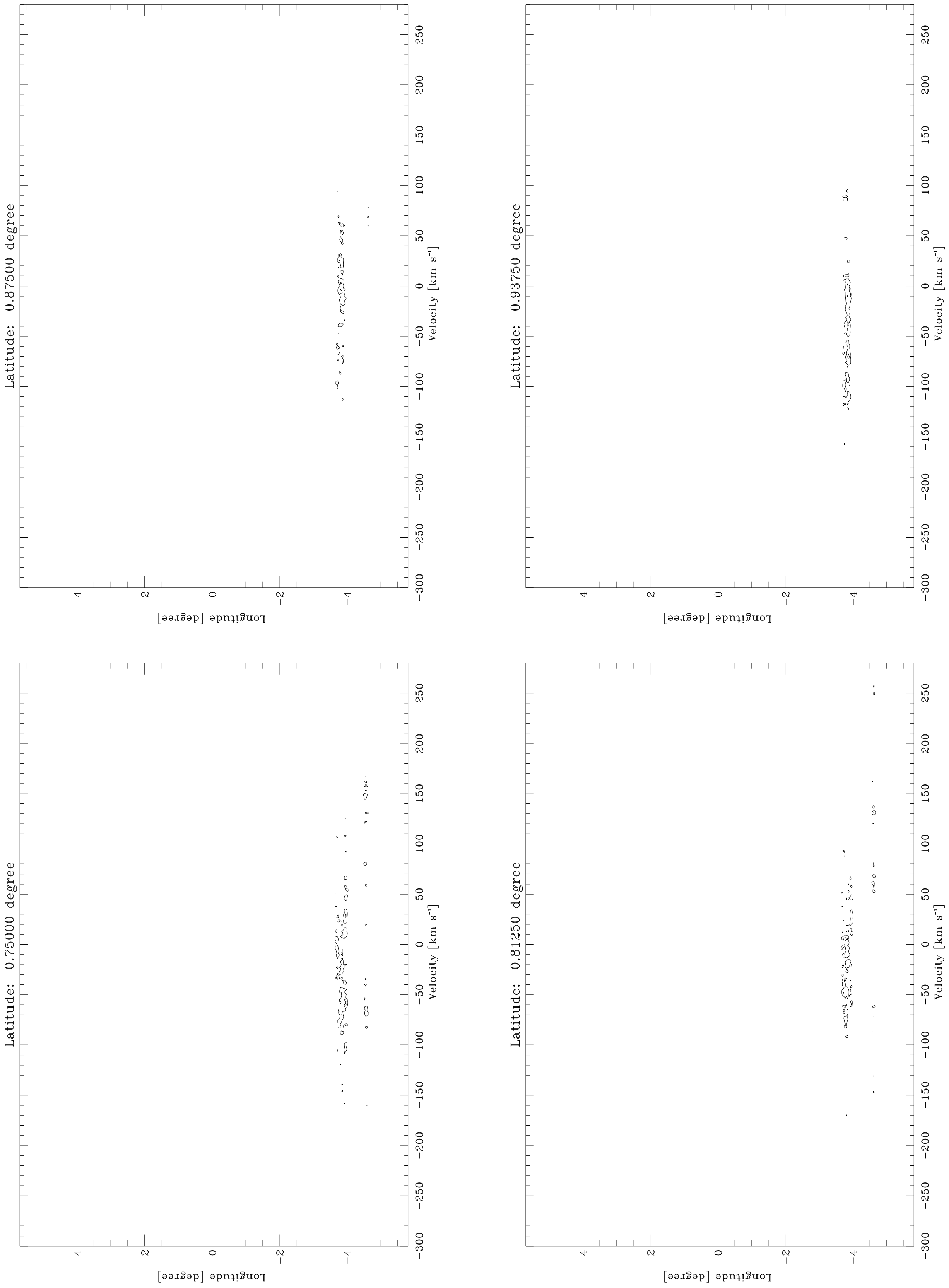

Fig. D2.7. continued.

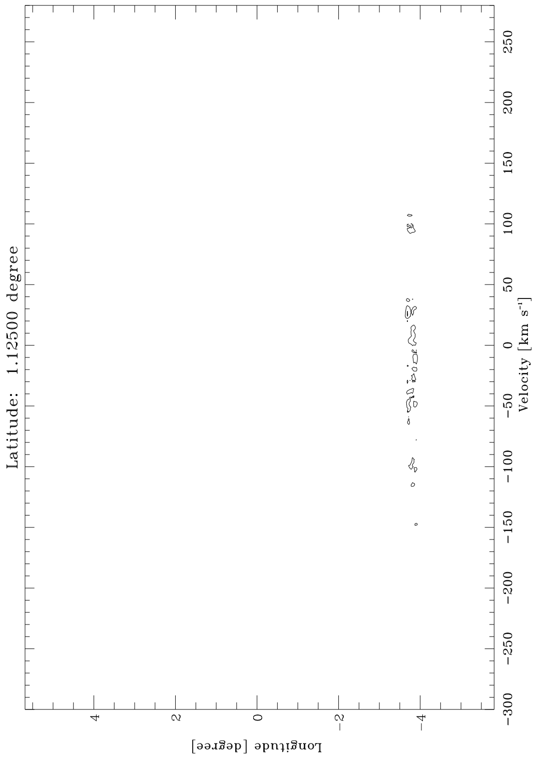

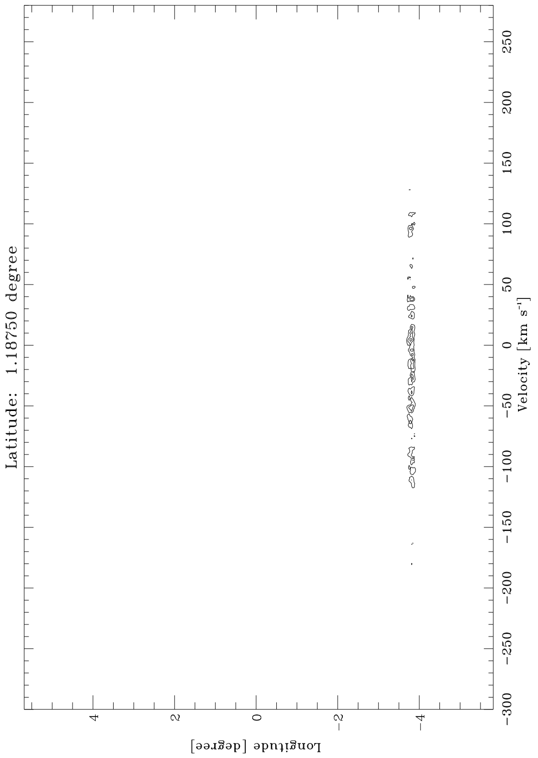

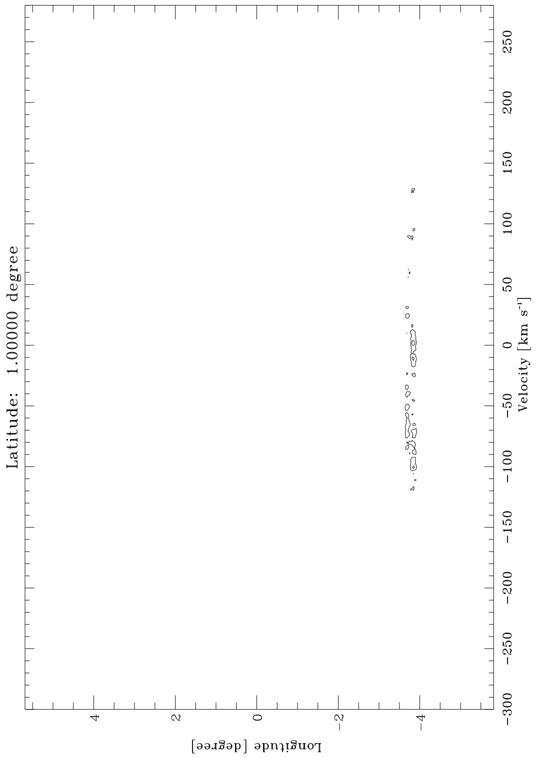

Fig. D2.8. continued.

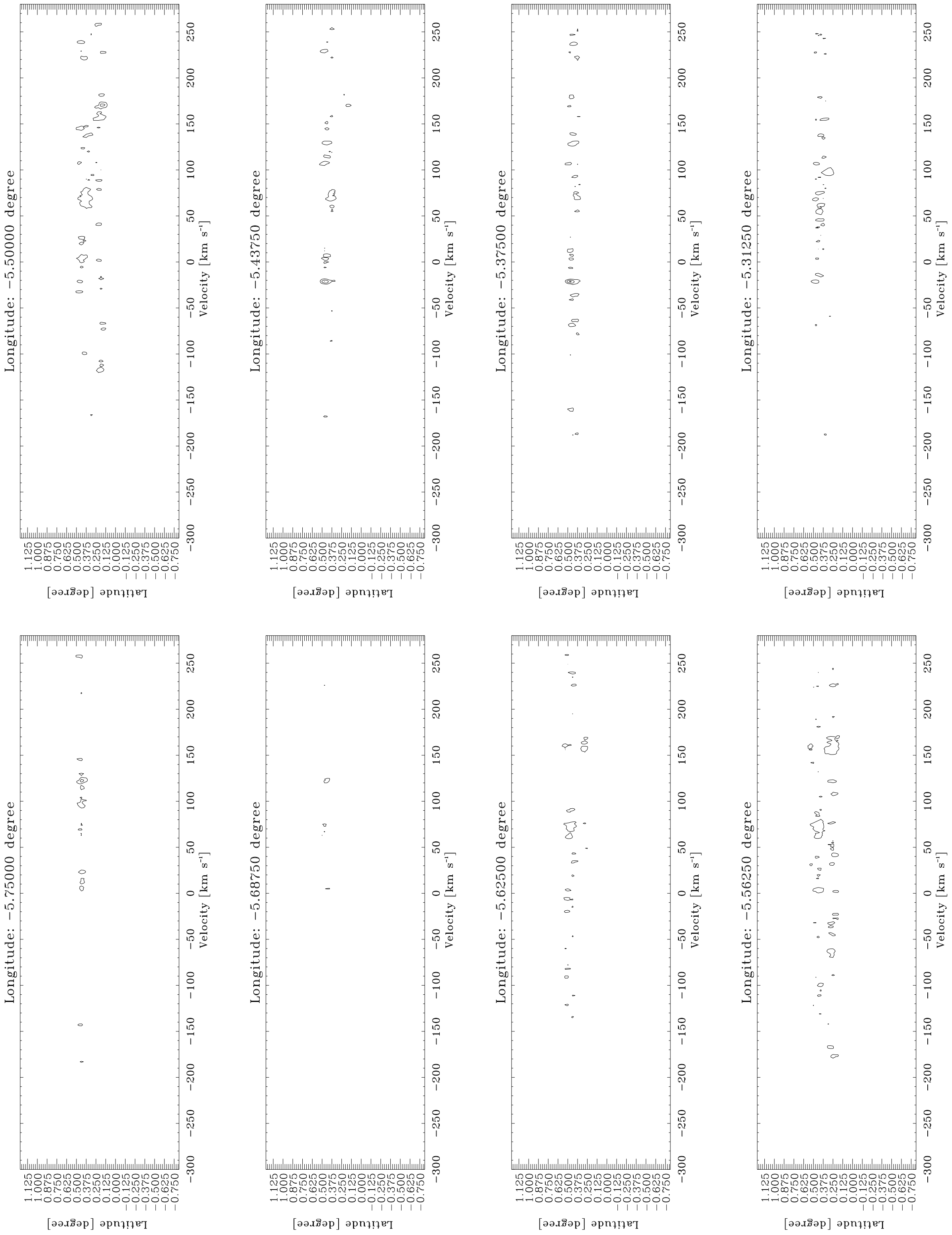

Fig. D3.1. Latitude-Velocity diagrams integrated in longitude in step of 0.°0625 for H13CO+. The lowest contour is at 0.0013 K (3σ). The following contours increase them in step of 0.0026 K, which correspond to 6σ.

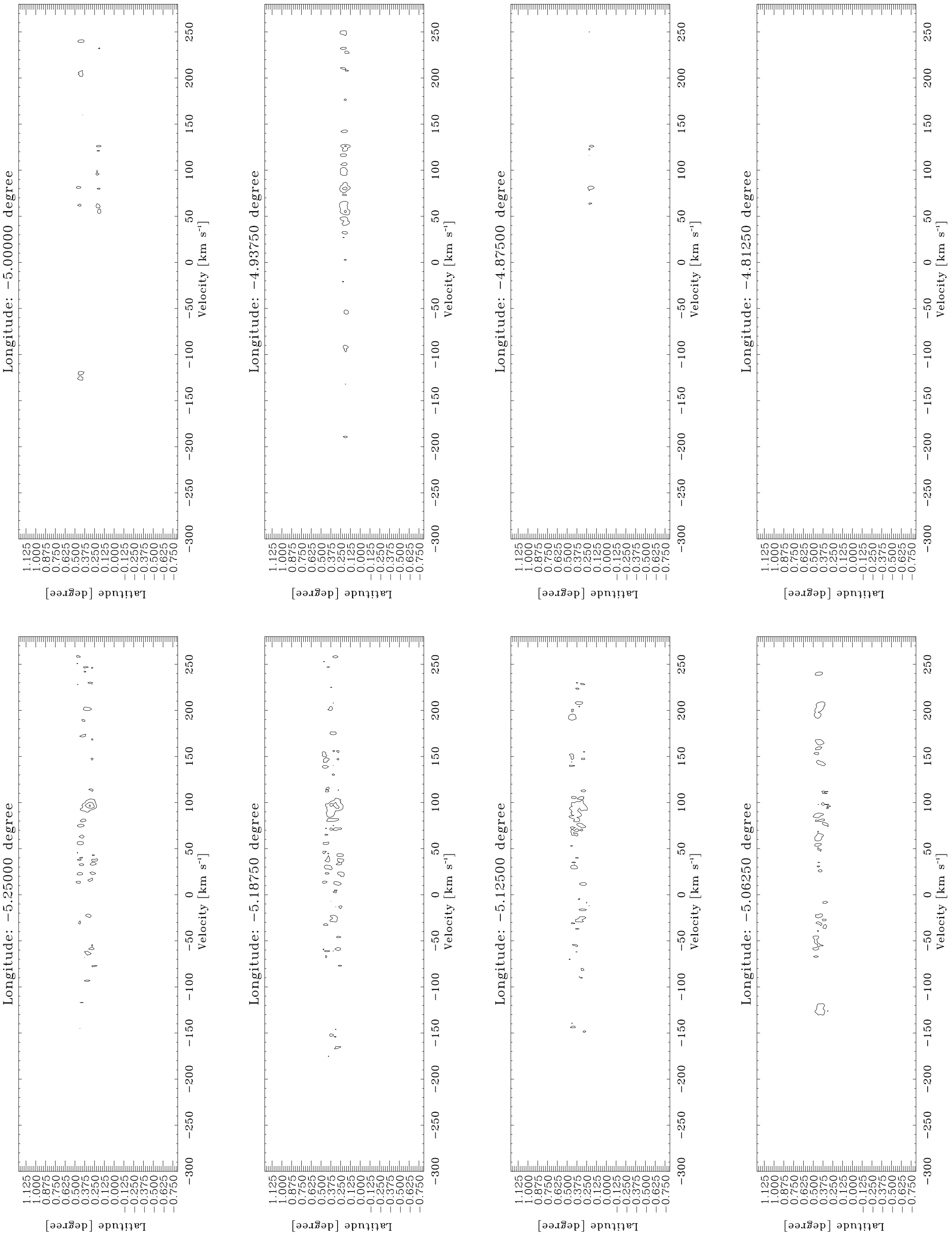

Fig. D3.2. continued.

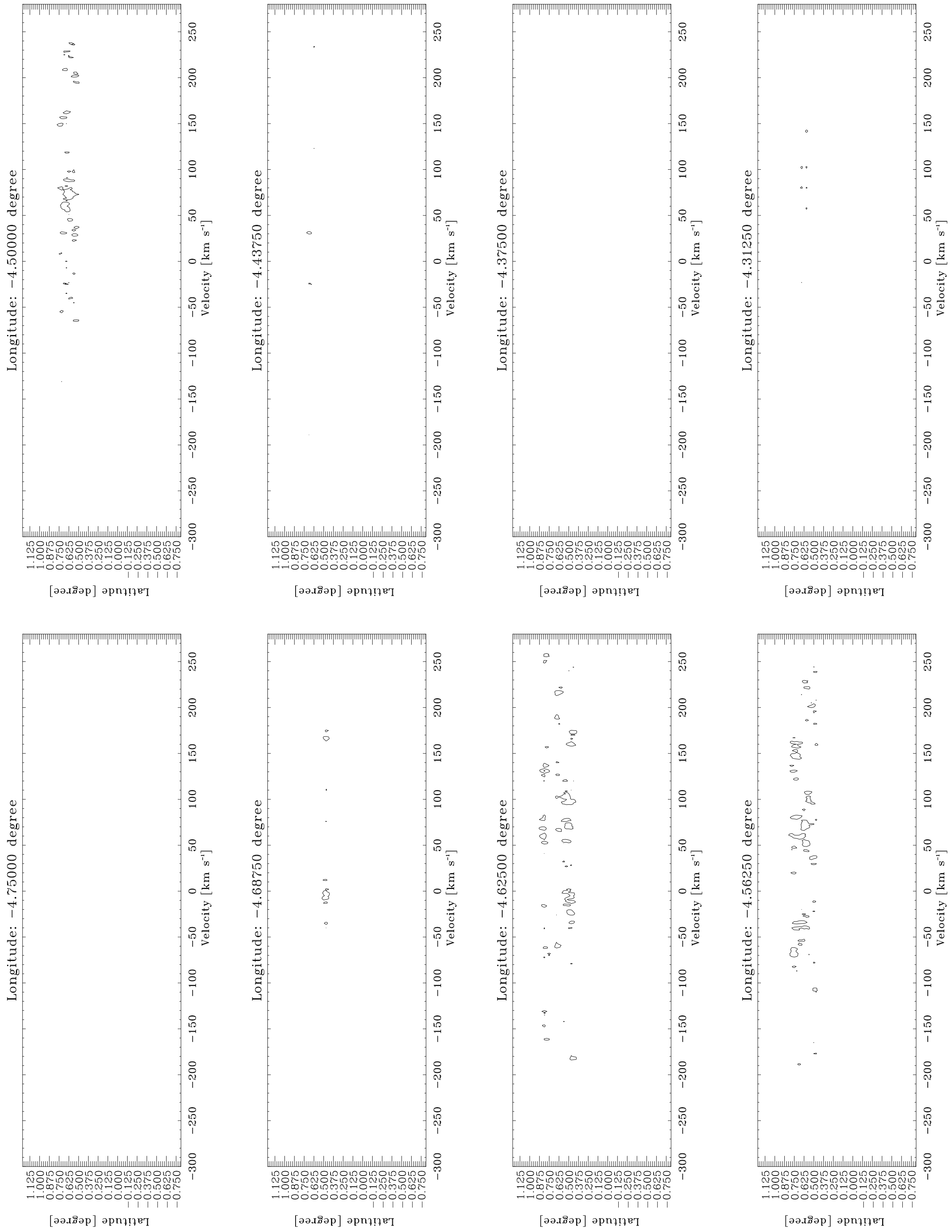

Fig. D3.3. continued.

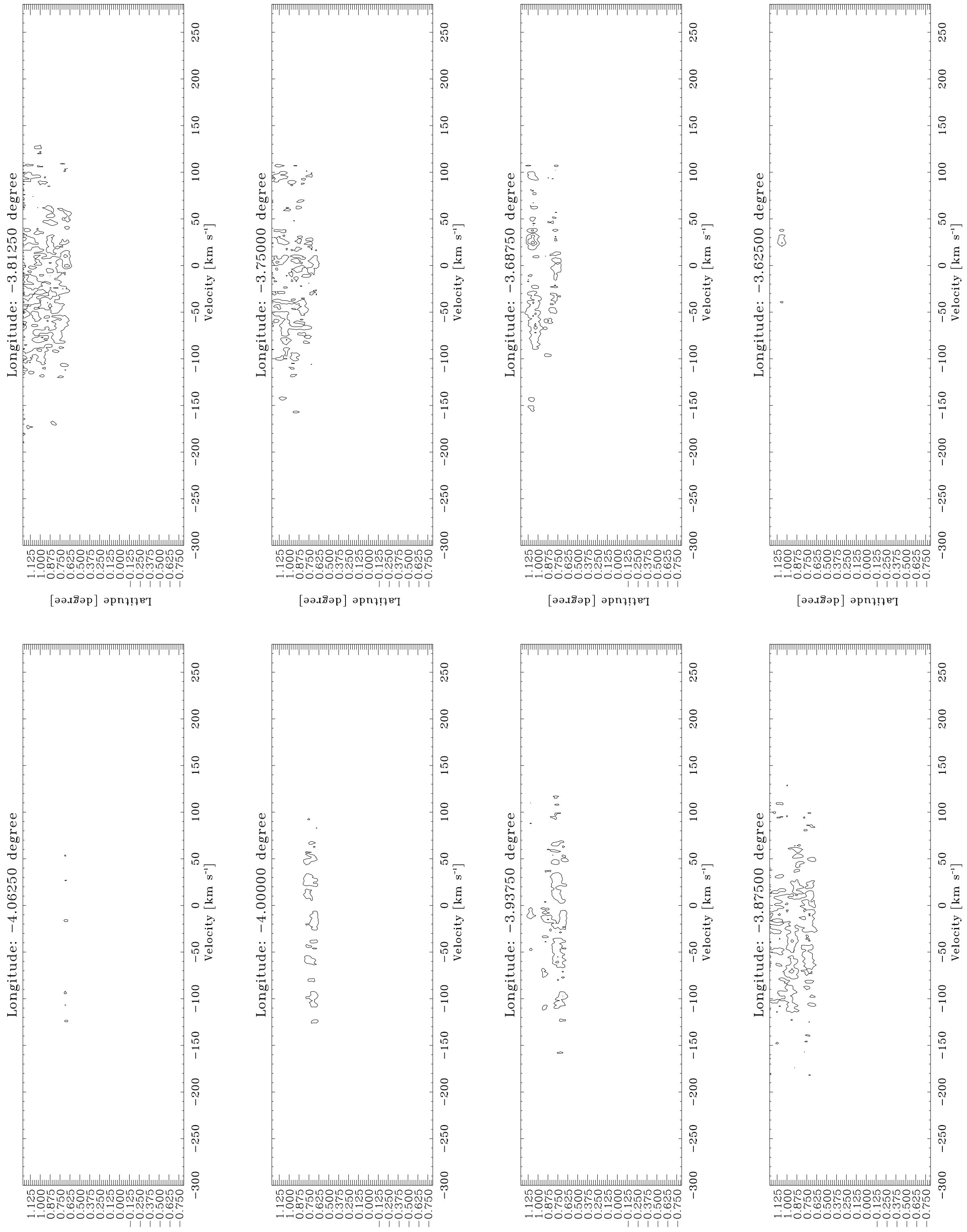

Fig. D3.4. continued.

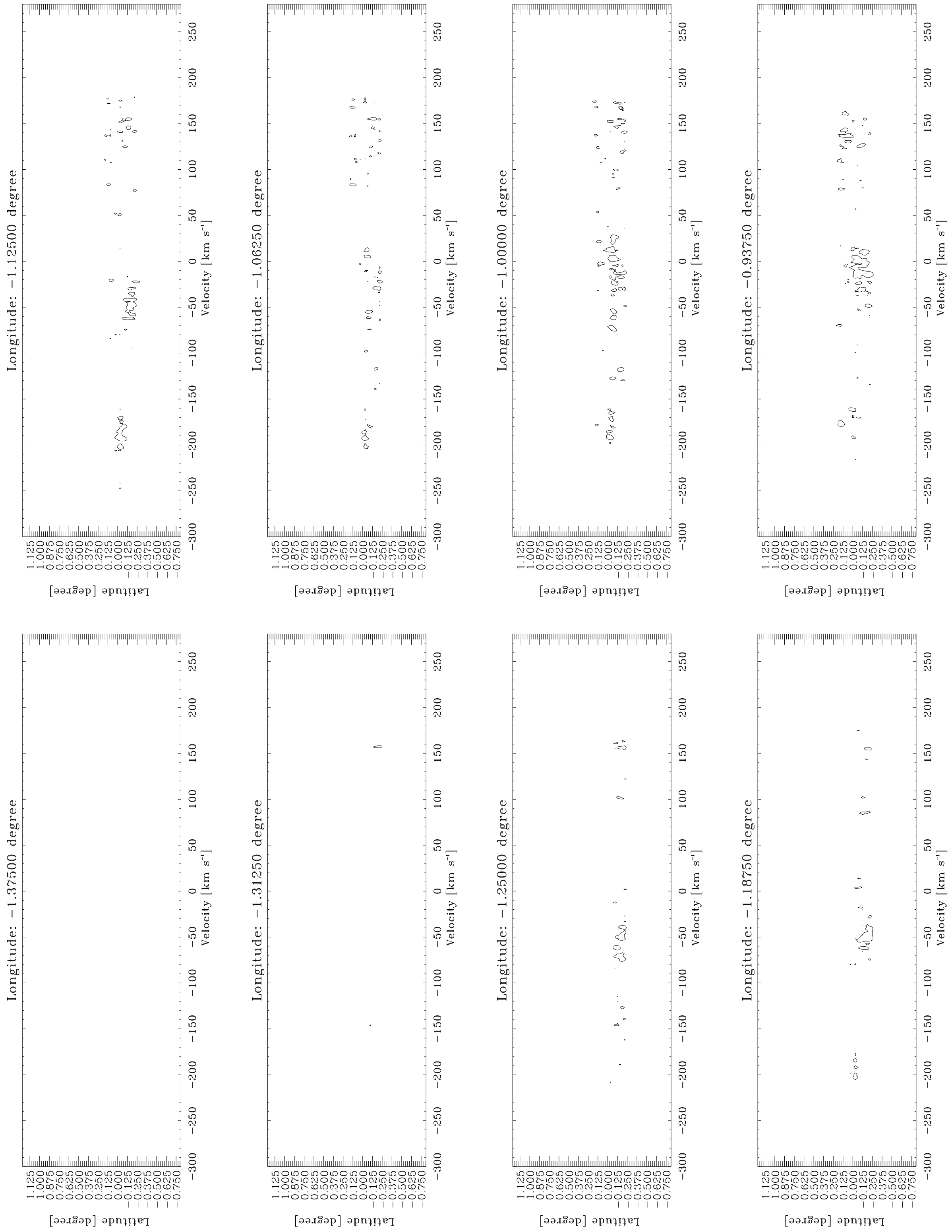

Fig. D3.5. continued.

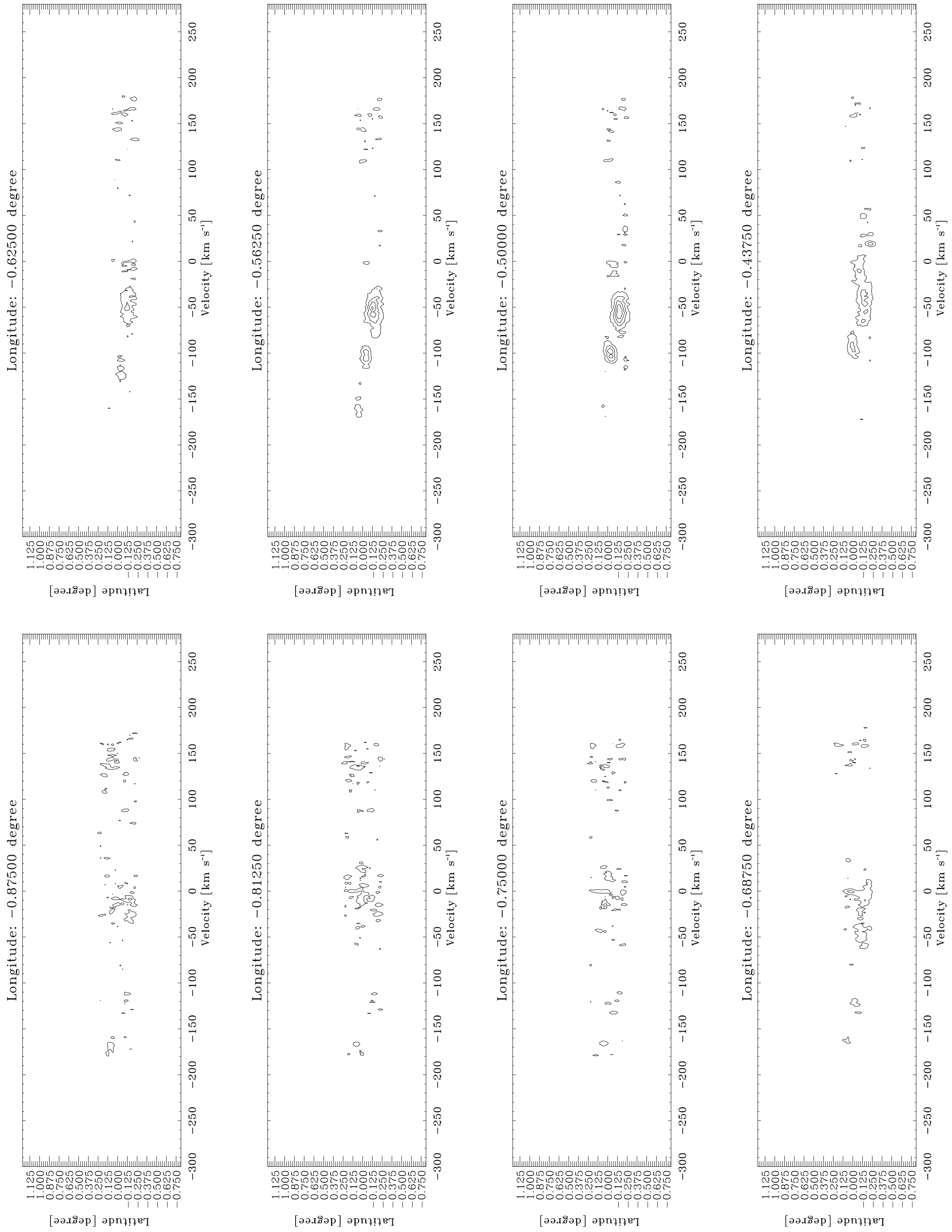

Fig. D3.6. continued.

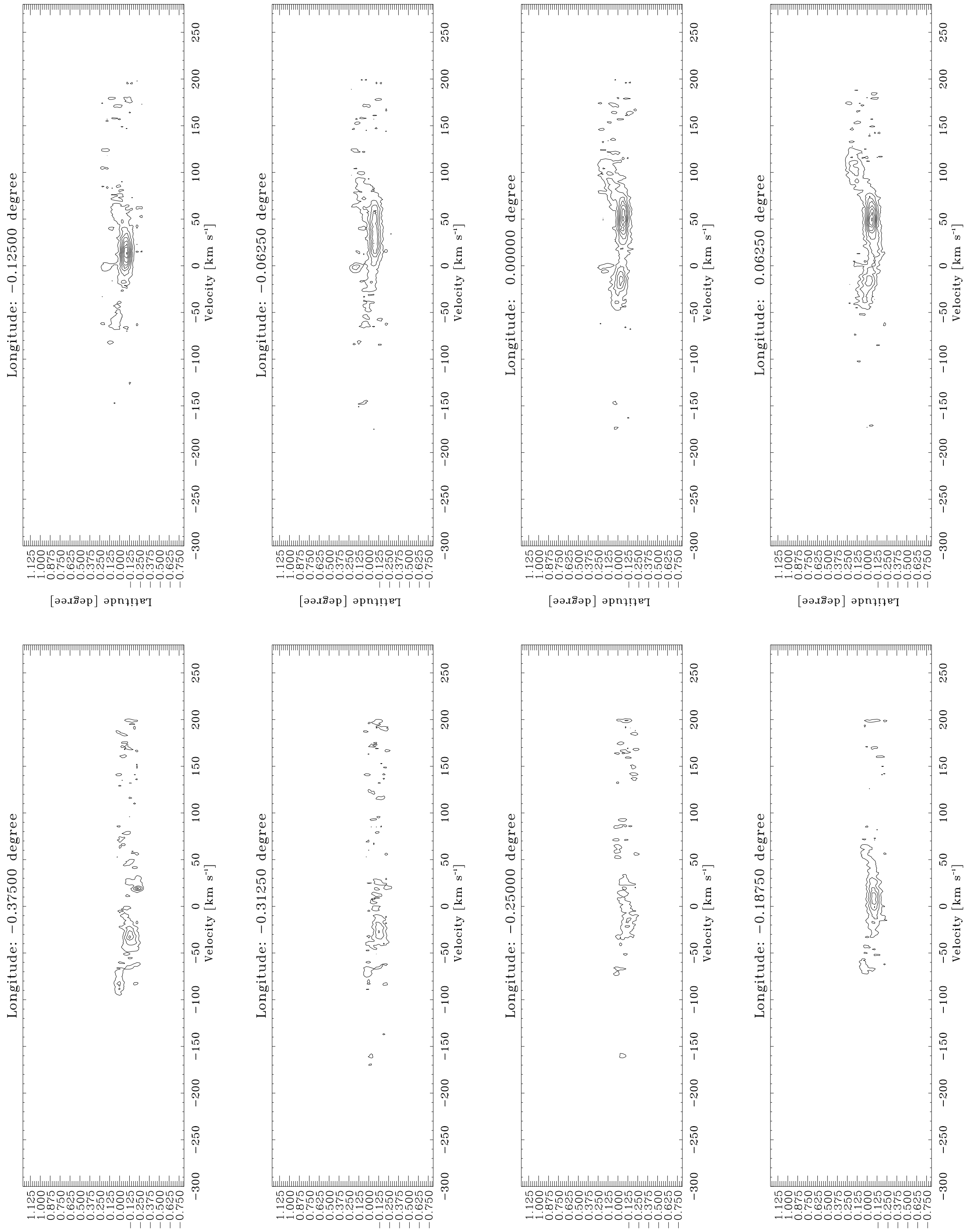

Fig. D3.7. continued.

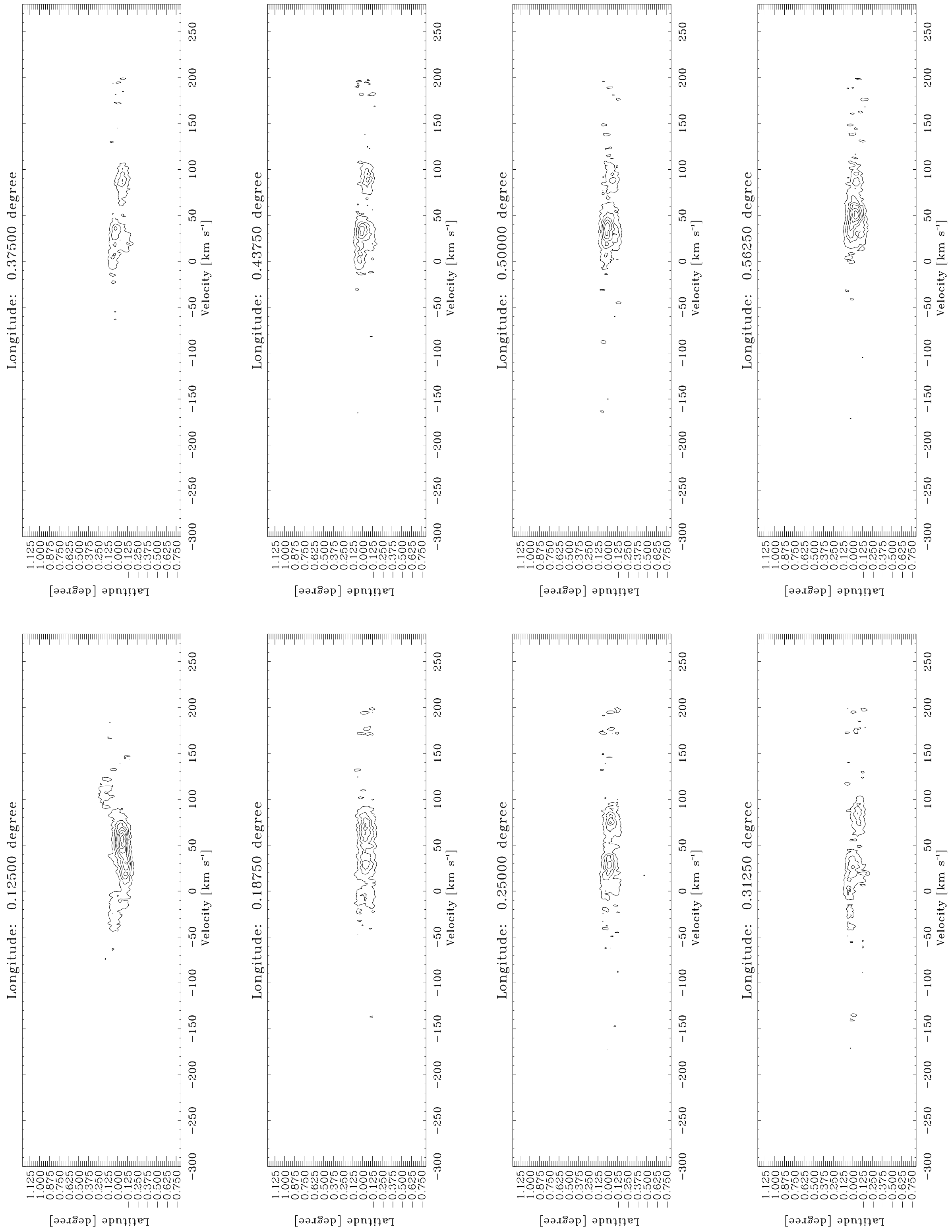

Fig. D3.8. continued.

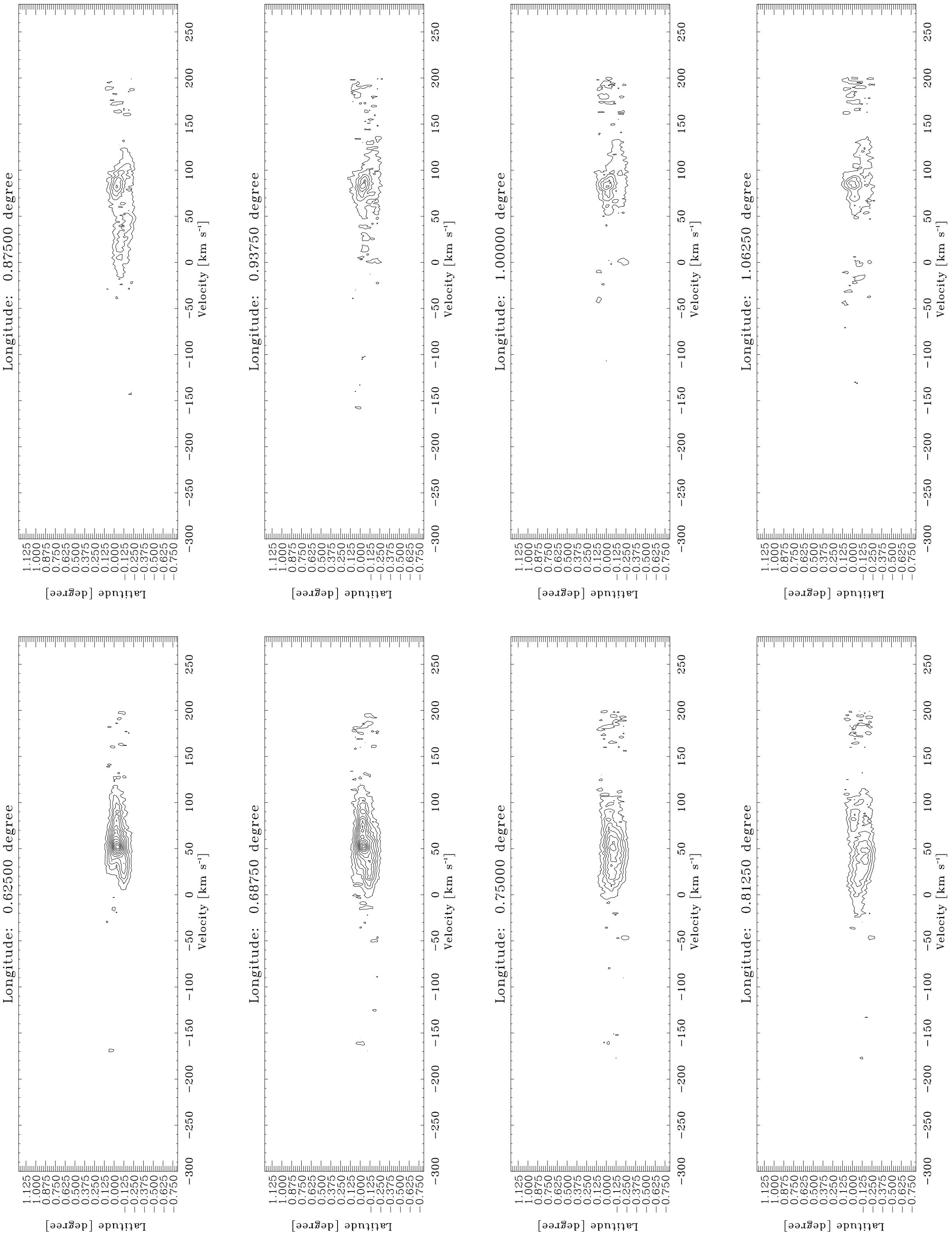

Fig. D3.9. continued.

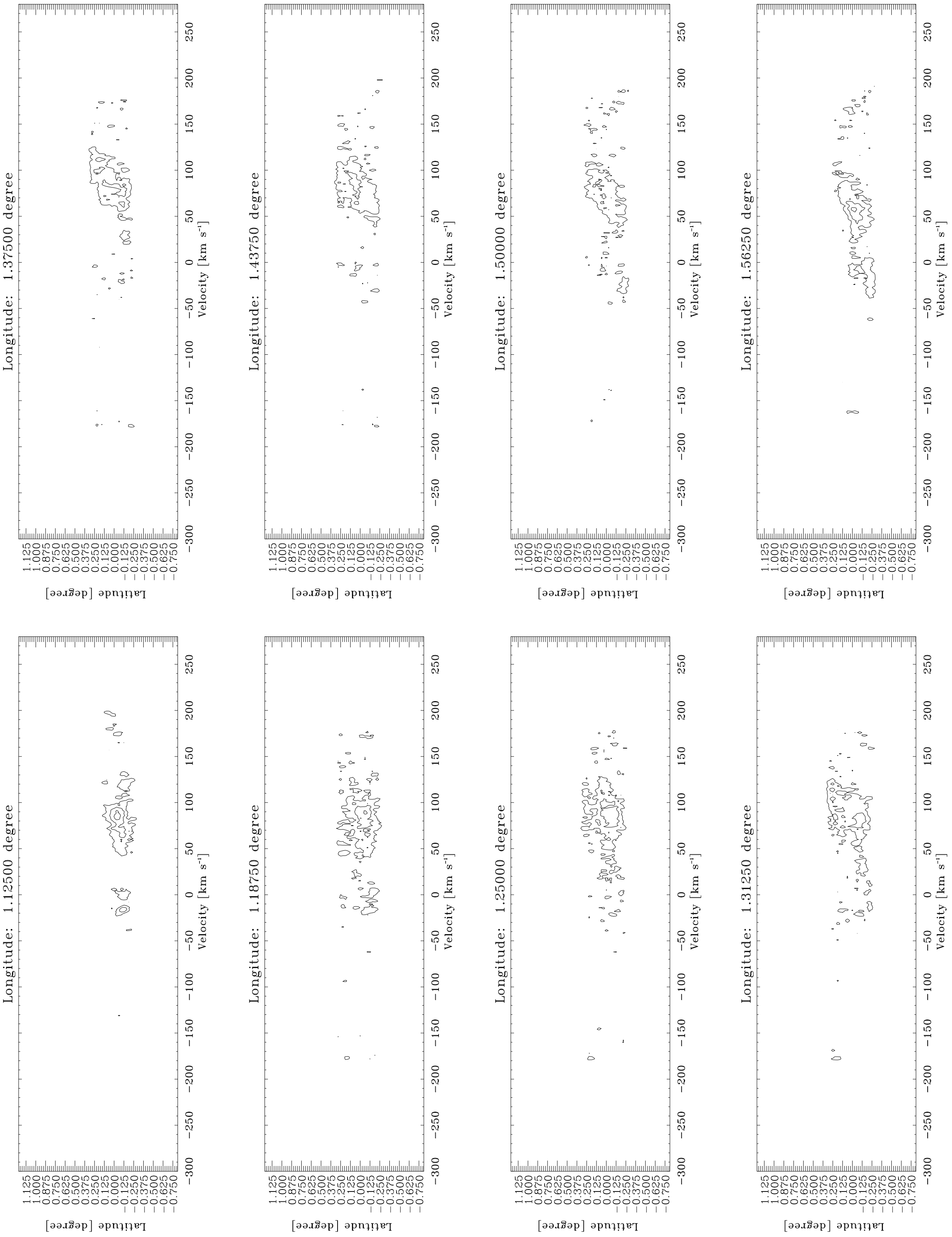

Fig. D3.10. continued.

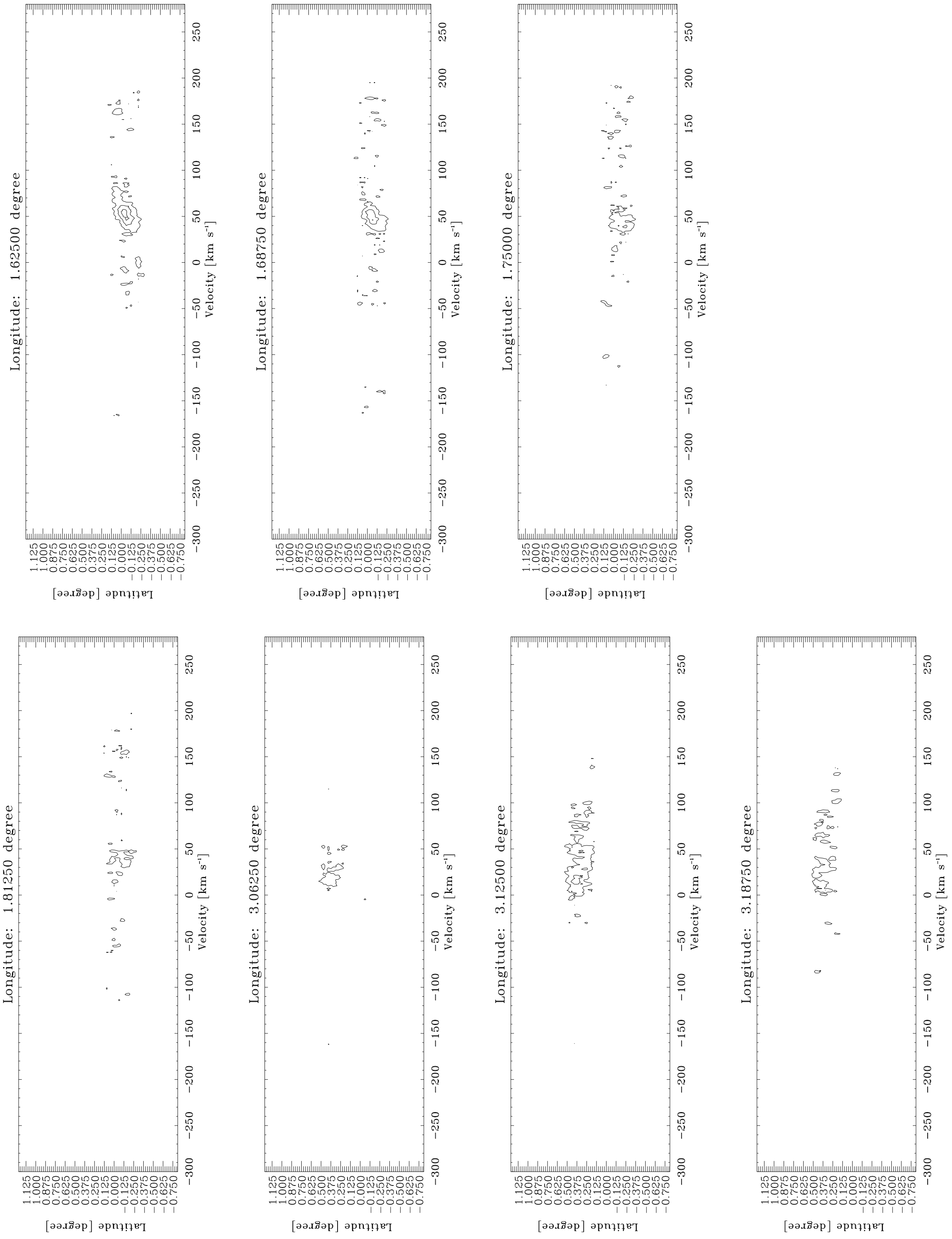

Fig. D3.11. continued.

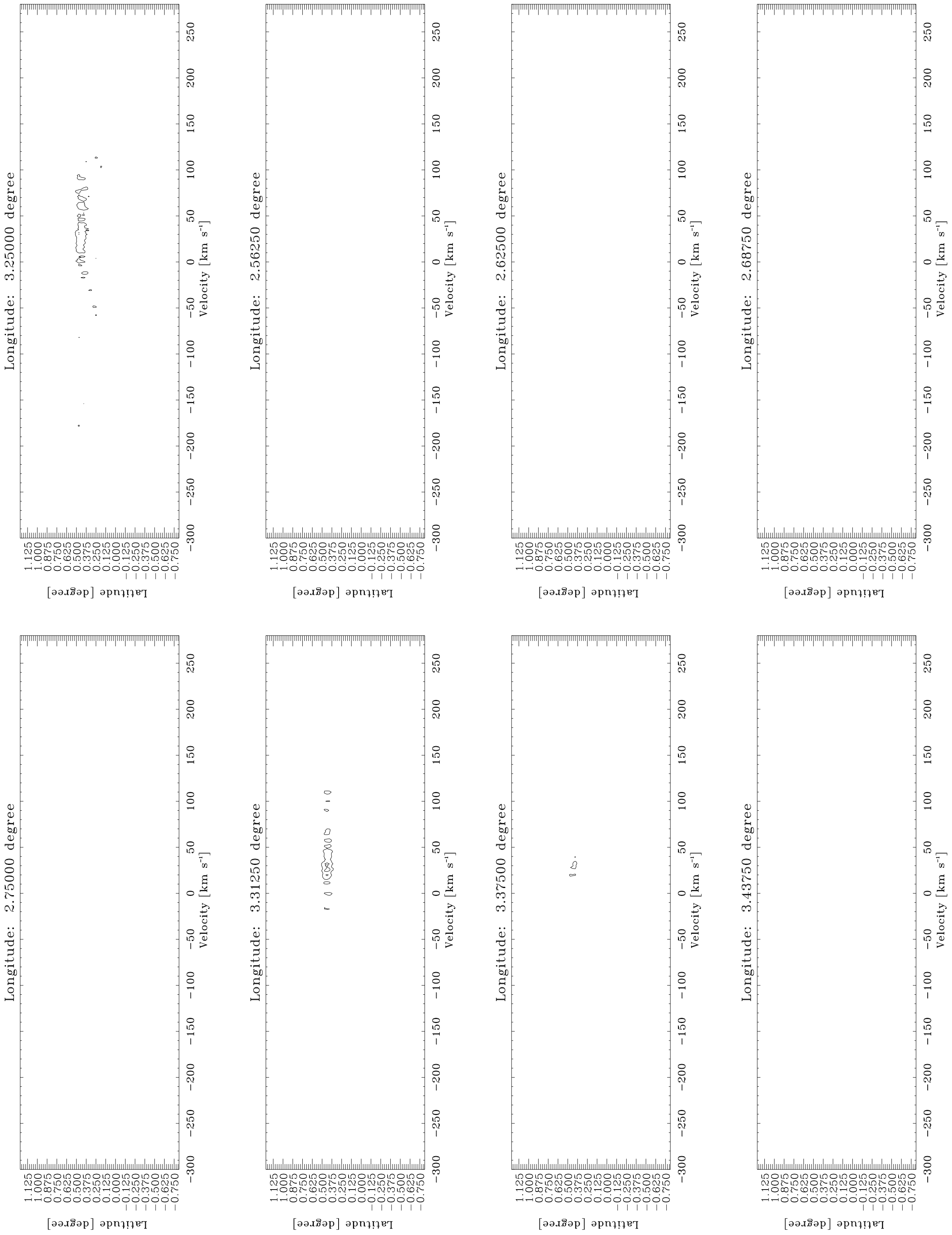

Fig. D3.12. continued.

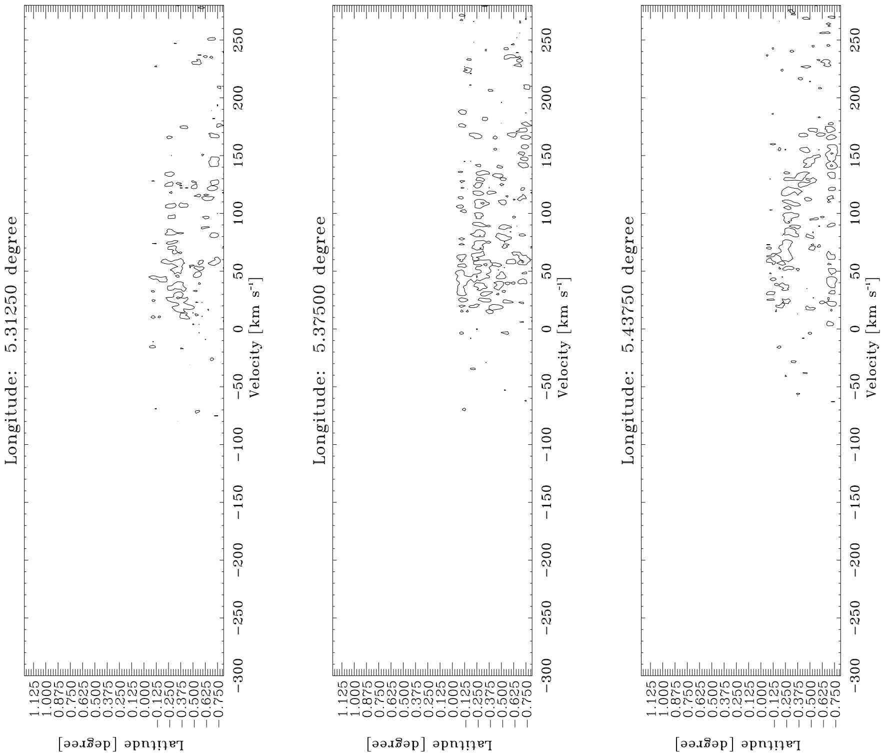

Fig. D3.13. continued.

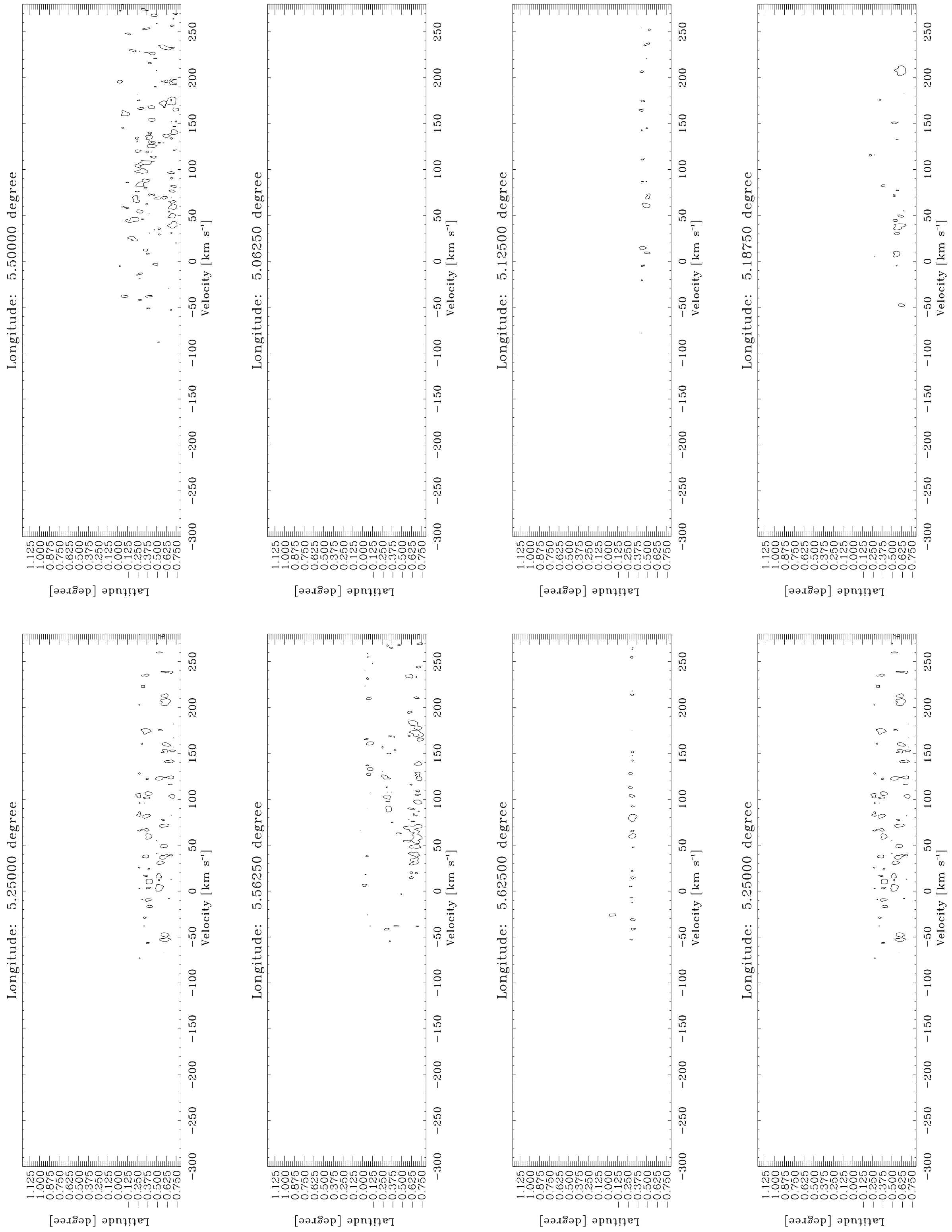

Fig. D3.14. continued.

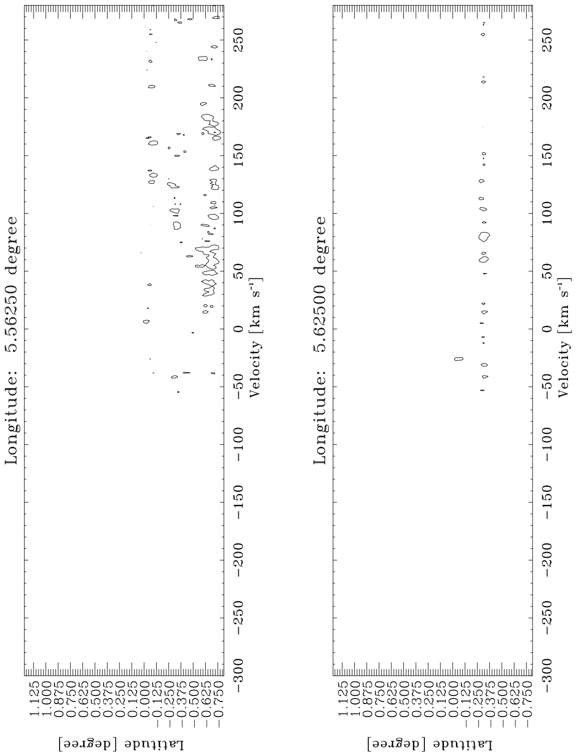

Fig. D3.15. continued.

Appendix E: Gaussian fits

We present the Gaussian fits of the average spectrum over the angular size of each region, as defined in Table 4.

Figure E.1 shows the average spectra toward the Sgr A complex. At negative velocities, we can see the EMR, in the HCO$^+$ and SiO and CO spectra. At v 0 km s^{-1}, we can see material strongly contaminated by the absorption produced by spiral arms, which can be clearly seen in the HCO$^+$ spectra. The ~50 km s^{-1} component correspond to the "Sgr A cloud", which is well identifying in all molecules. Finally, toward positive velocities, in HCO$^+$ and CO the positive part of the EMR is visible.

Figure E.2 we show the average spectra toward Sgr B complex. Both, in HCO$^+$ and CO we can see the EMR toward high positive and negative velocities. The "Sgr B cloud" correspond to the component in $v \sim 50$ km s^{-1}.

In Fig. E.3 the EMR appears very strong both in its positive and negative velocity component in all the molecular lines, less in H^{13}CO$^+$. The component corresponding to Sgr C cloud is found toward negative velocities, and both CO and HCO$^+$ appears very contaminated by the spiral arms, but it is clearly seeing in SiO and H^{13}CO$^+$.

The Fig. E.4 shows the average spectra toward Sgr D. The main component is at $v \sim 90$ km s^{-1}.

The Fig. E.5 shows the average spectra toward Sgr D. The main component is at $v \sim 210$ km s^{-1}.

Figure E.6, show the average spectra for the region toward the 1.3° complex. The main cloud is at $v \sim 80$ km s^{-1}, and in this longitude we can see the positive velocity of the EMR at $v \sim 200$ km s^{-1}.

In Fig. E.7 we show the average spectra for the region toward M+3.2+0,3. The main cloud identify by Bitran (1987) is found in $v \sim 100$ km s^{-1} ("Clump 2"), but the 3 wide velocity component belong to the Galactic center region. In the CO spectrum, we can see the spiral arms in emission at negative velocities and at high positive velocities we see the end of the EMR.

Figure E.8 shows the average spectra toward the M−5.3+0.4 region, where the main cloud is at $v \sim 80$ km s^{-1}. In the four plots, we can clearly identify the spiral arm in emission. We can see that the Galactic center component have a wide width velocity in comparison to the material from the disk.

Figure E.9 presents the average spectra toward the M−4.4+0.6 region. The main component is at ~70 km s^{-1}, and the we can see the spiral arm as narrow velocity features.

In Fig. E.10 we can see the average spectra toward the M−3.8+0.9 region. The main cloud is found at negative velocities ($v \sim -80$ km s^{-1}). The SiO and HCO$^+$ emission show an increase in the intensity in the main cloud in comparison with the CO emission, with respect to other components within the Galactic disk.

Finally, Fig. E.11 shows the average spectra toward the M+5.3−0.3 region. Like in the previous case, the SiO emission in the Galactic center clouds is high in comparison with the other complex, suggesting that in both complex (main clouds of M−3.8+0.9 and M+5.3−0.3) could be subjected to shocks.

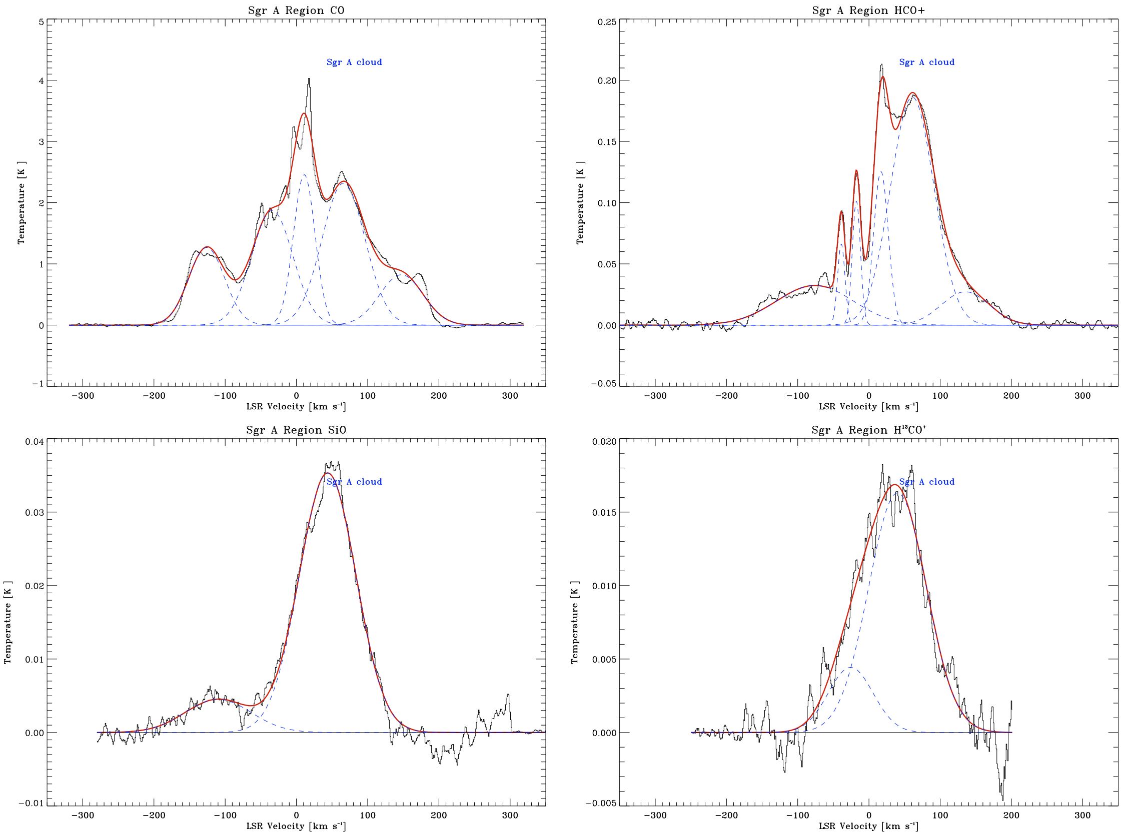

Fig. E.1. CO, HCO$^+$, SiO y H^{13}CO$^+$ average spectrum over the angular size of Sgr A region (from l = −0.3125 to −0.3125, and from b = −0.5 to 0.5). In all the figures, the red lines indicate the Gaussian fit for the complete region and blue dashed lines show the Gaussian fits of each velocity components.

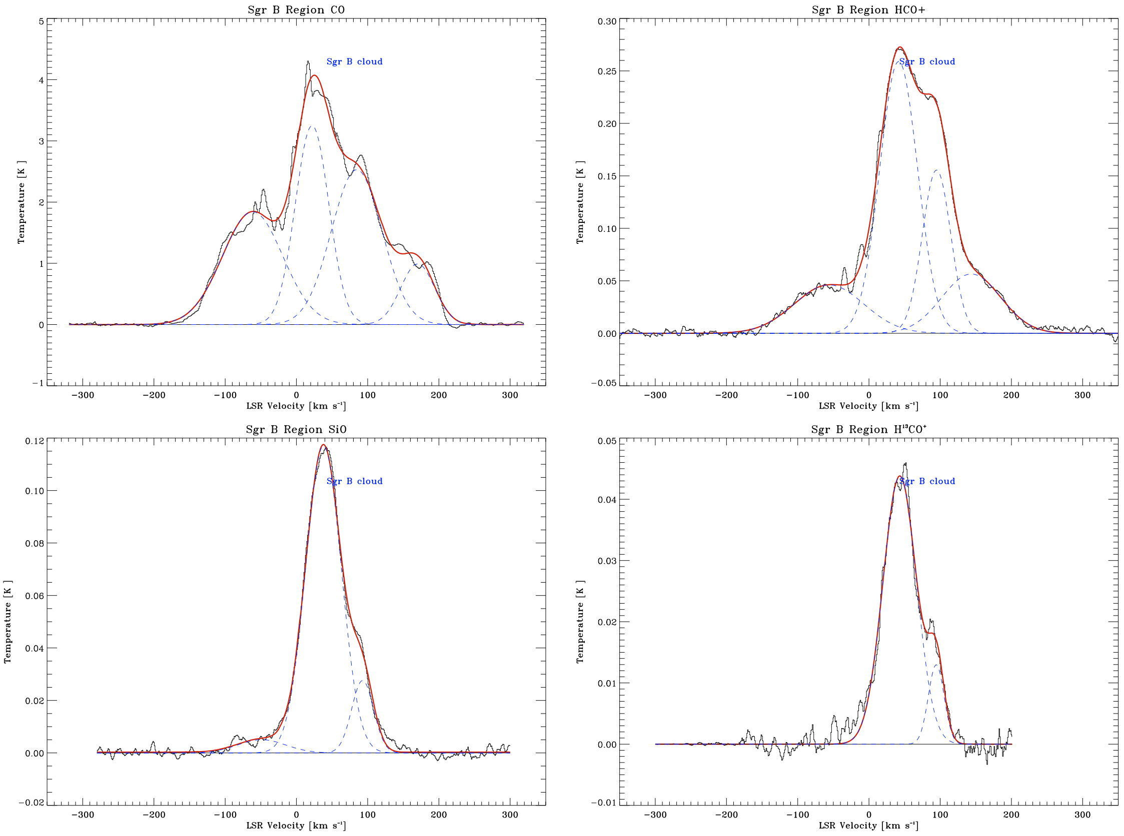

Fig. E.2. CO, HCO$^+$, SiO y H^{13}CO$^+$ average spectrum over the angular size of Sgr B region (from l = 0.375 to 0.8125, and from b = −0.5 to 0.5).

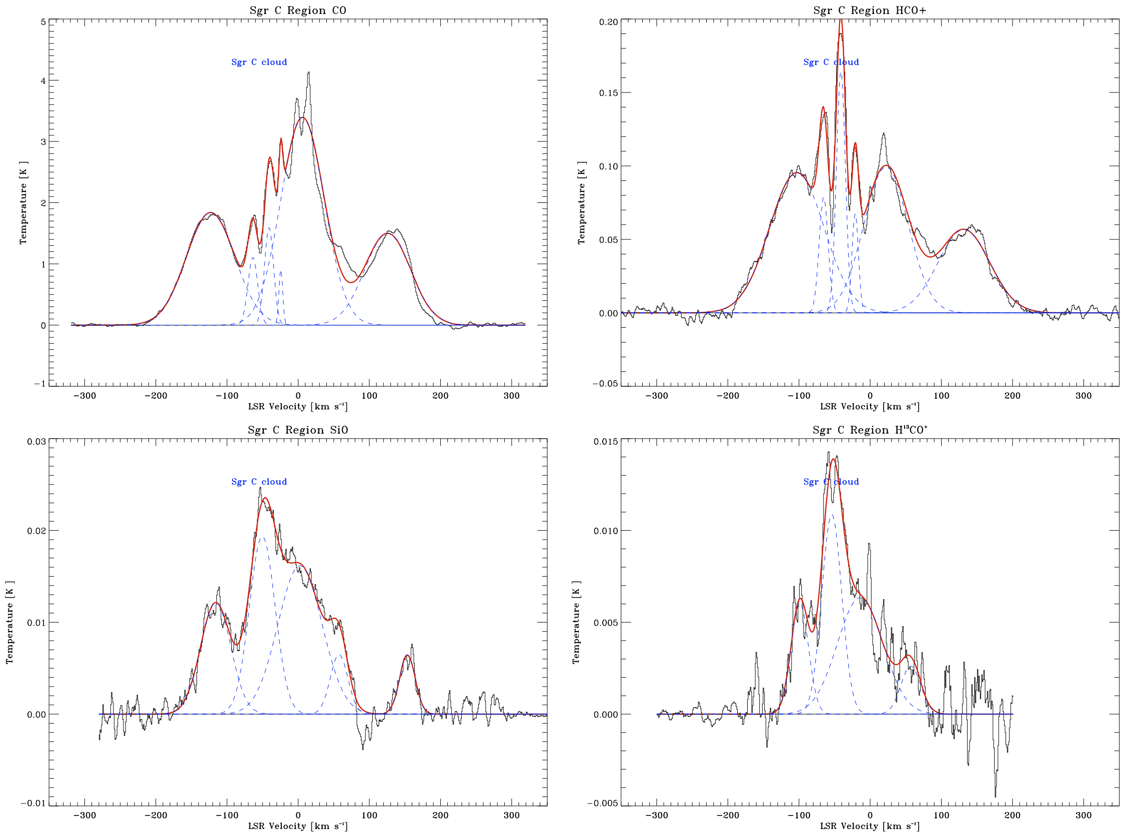

Fig. E.3. CO, HCO$^+$, SiO y H^{13}CO$^+$ average spectrum over the angular size of Sgr C region (from l = −0.6875 to −0.375, and from b = −0.5 to 0.5).

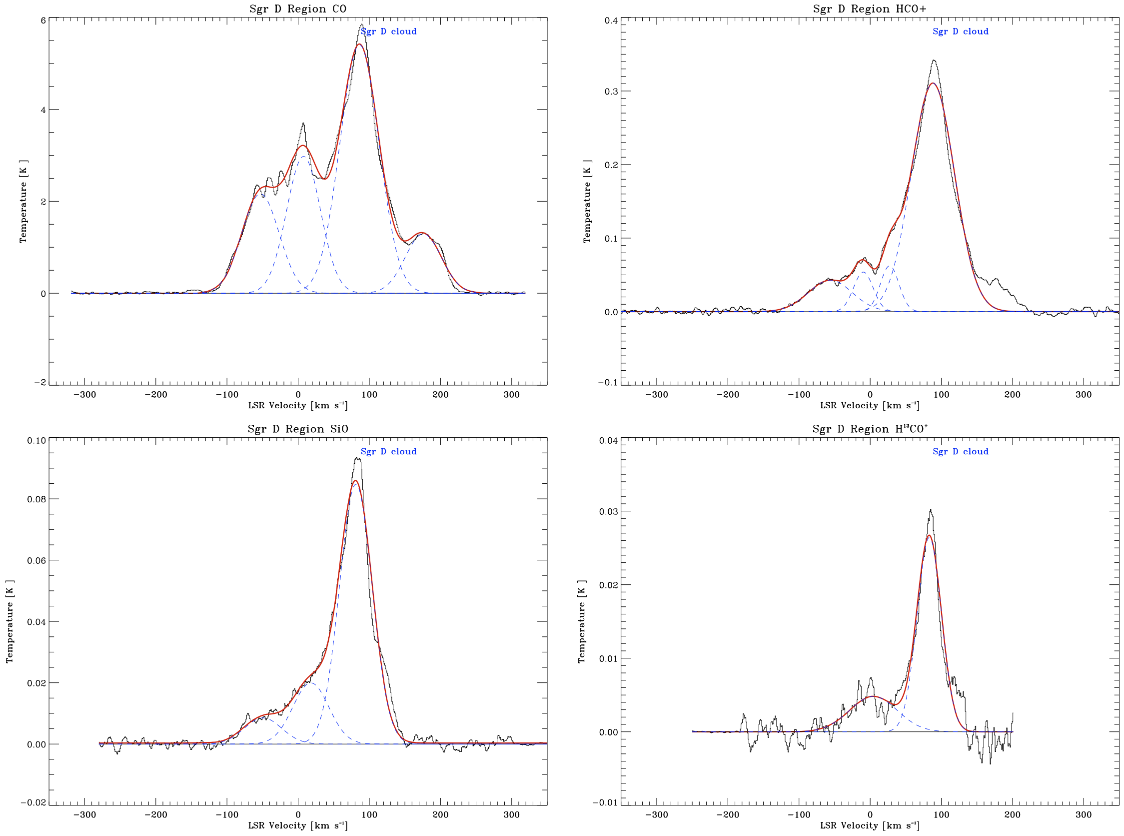

Fig. E.4. CO, HCO$^+$, SiO y H^{13}CO$^+$ average spectrum over the angular size of Sgr D region (from l = 0.875 to 1.1875, and from b = −0.5625 to 0.5625).

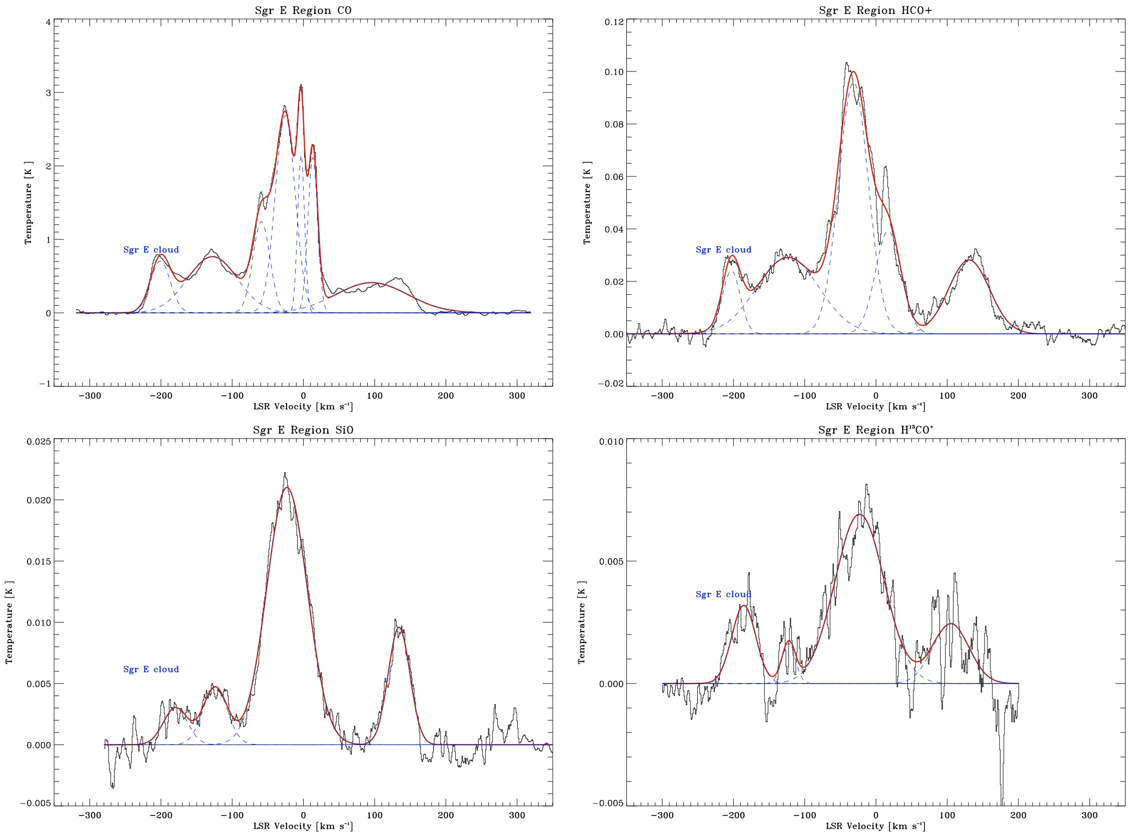

Fig. E.5. CO, HCO$^+$, SiO y H^{13}CO$^+$ average spectrum over the angular size of Sgr E region (from $l = -1.5$ to -0.75, and from $b = -0.5$ to 0.5).

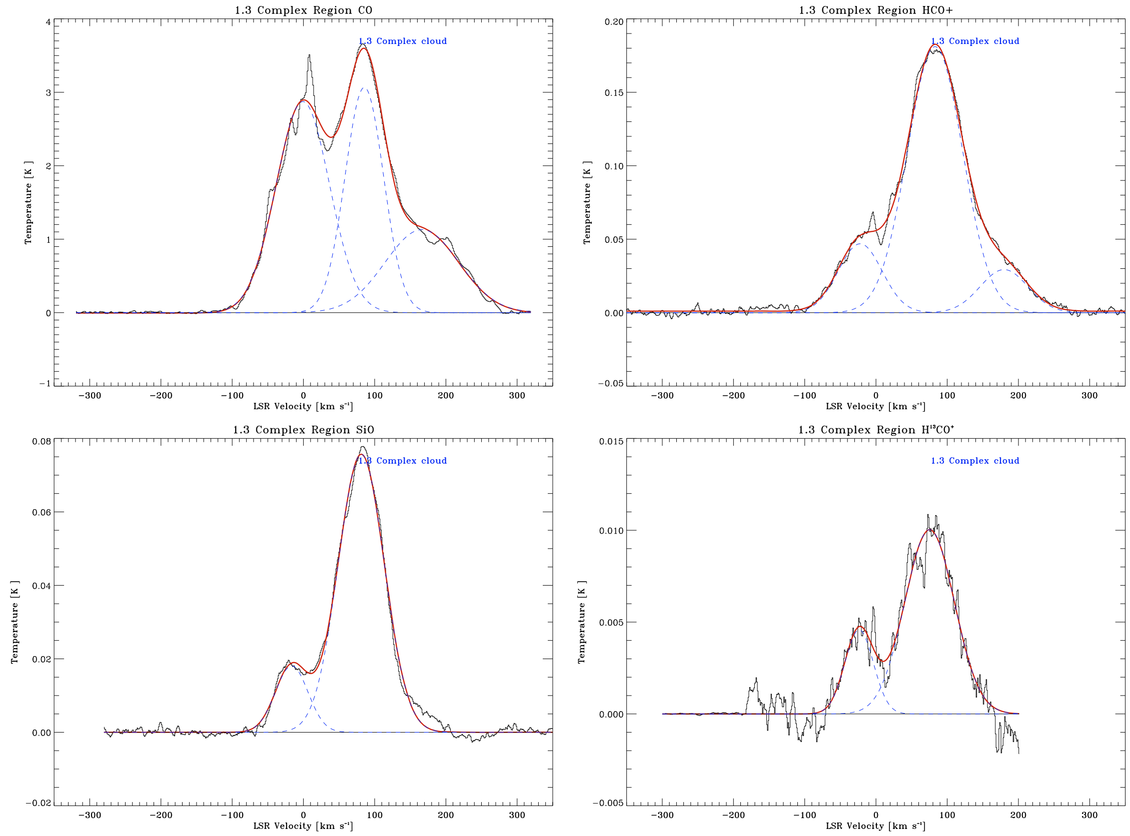

Fig. E.6. CO, HCO$^+$, SiO y H^{13}CO$^+$ average spectrum over the angular size of 1.3 complex region (from $l = 1.25$ to 2.0, and from $b = -0.5625$ to 0.5625).

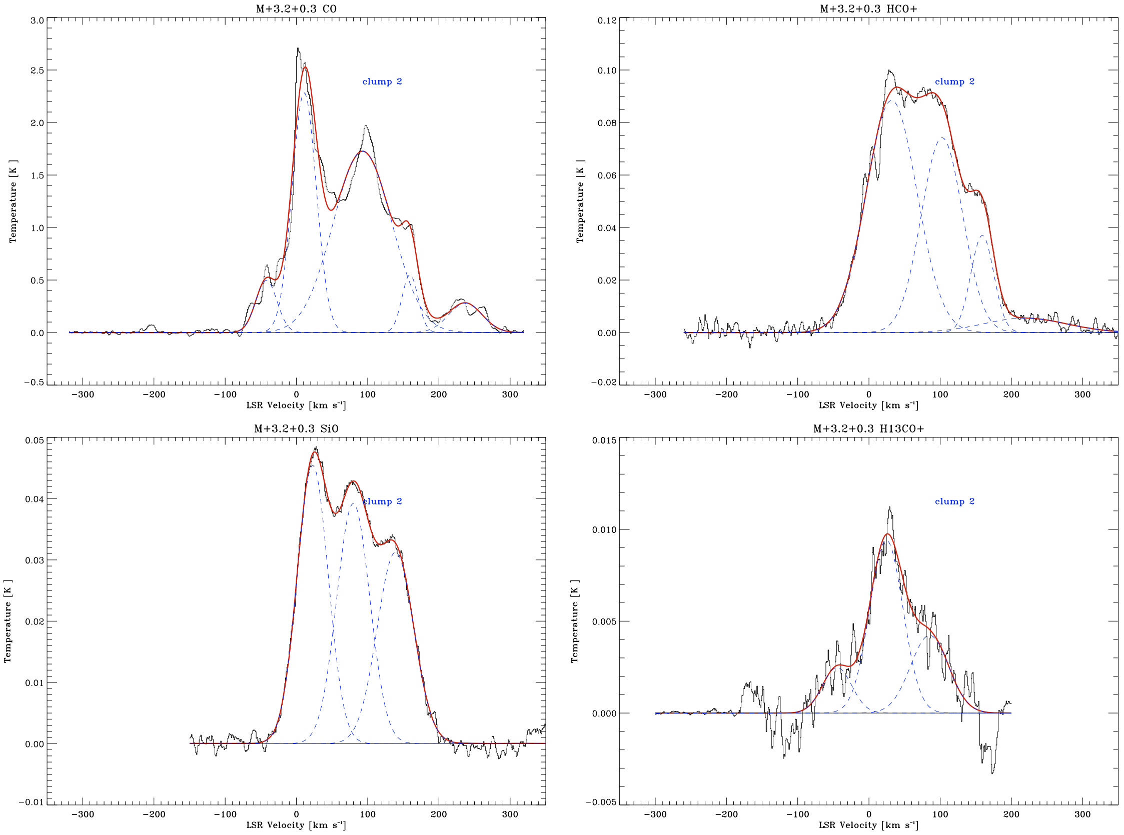

Fig. E.7. CO, HCO$^+$, SiO y H^{13}CO$^+$ average spectrum over the angular size of M+3.2+0.3 region (l, b, v) = (3.2, 0.3, 104) (from l = 2.5625 to 3.5, and from b = −0.25 to 0.875).

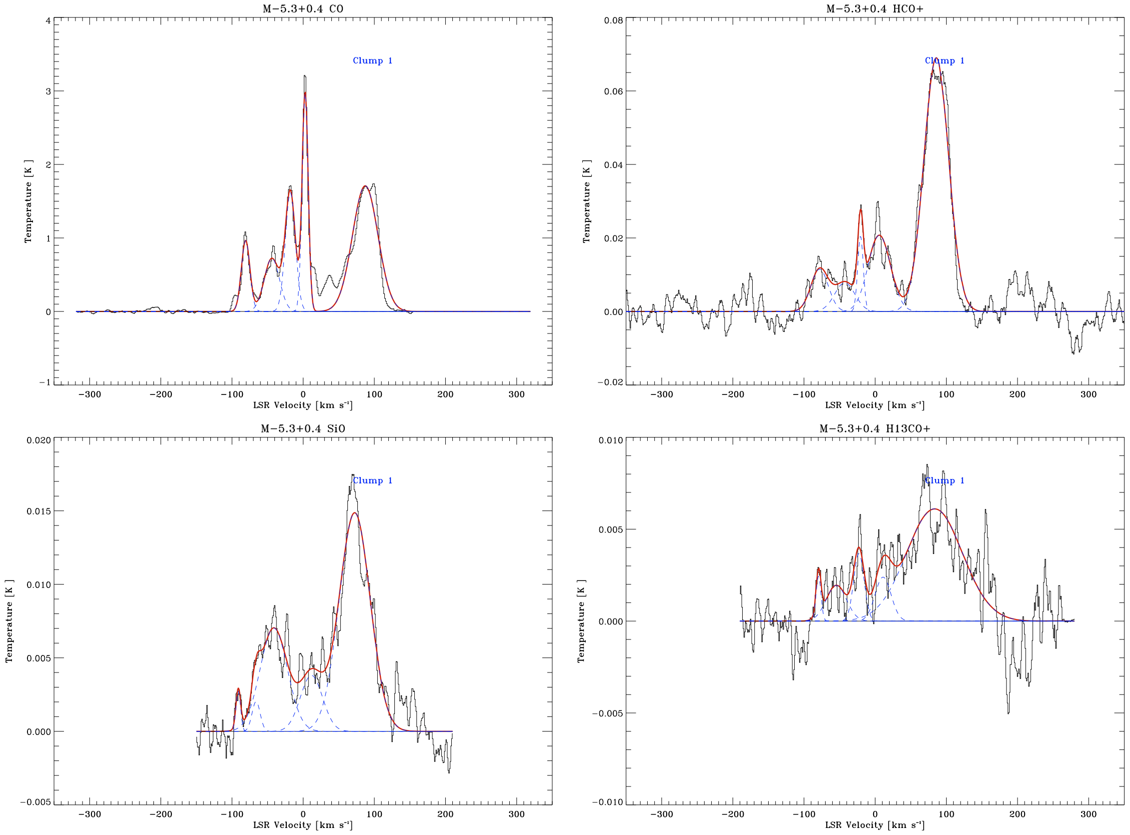

Fig. E.8. CO, HCO$^+$, SiO y H^{13}CO$^+$ average spectrum over the angular size of M−5.3+0.4 region (l, b, v) = (−5.3, 0.4, 84) (from l = −5.75 to −4.75, and from b = −0.125 to 0.5625).

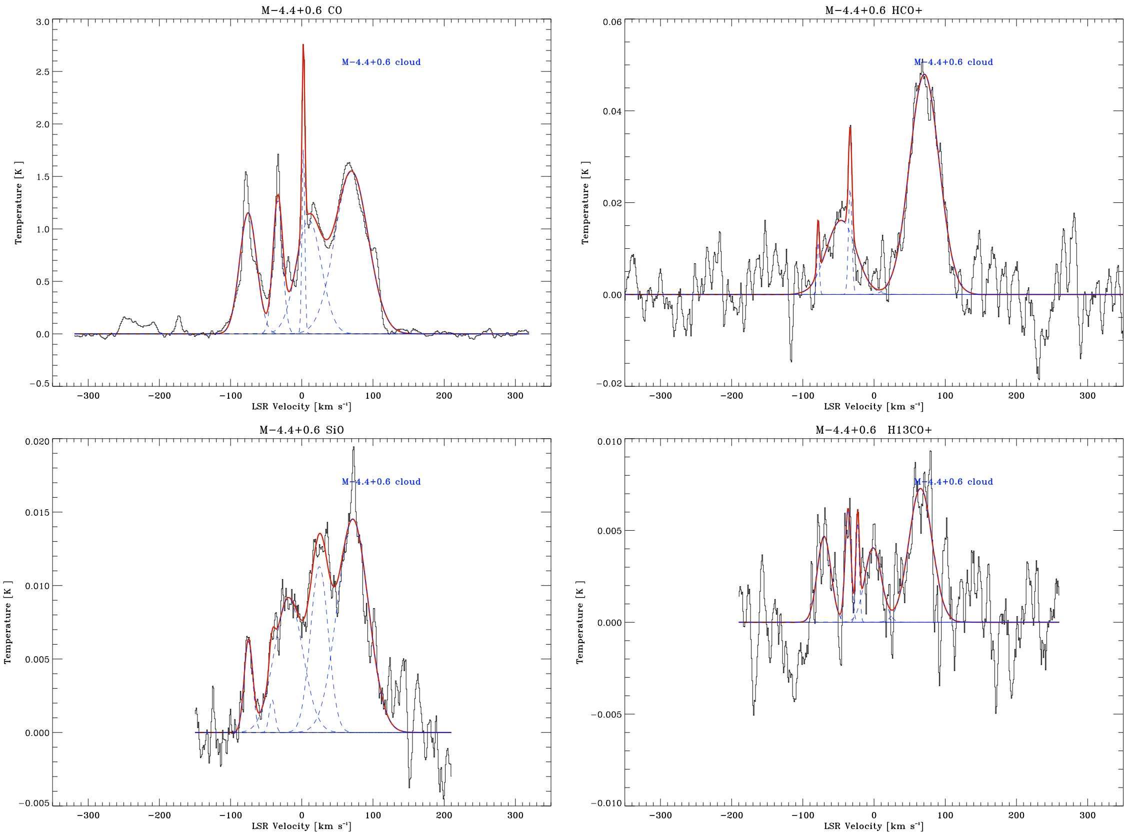

Fig. E.9. CO, HCO$^+$, SiO y H^{13}CO$^+$ average spectrum over the angular size of M−4.4+0.6 region $(l, b, v) = (-4.4, 0.6, 72)$ (from $l = -4.6875$ to -4.3125, and from $b = 0.4375$ to 0.8125).

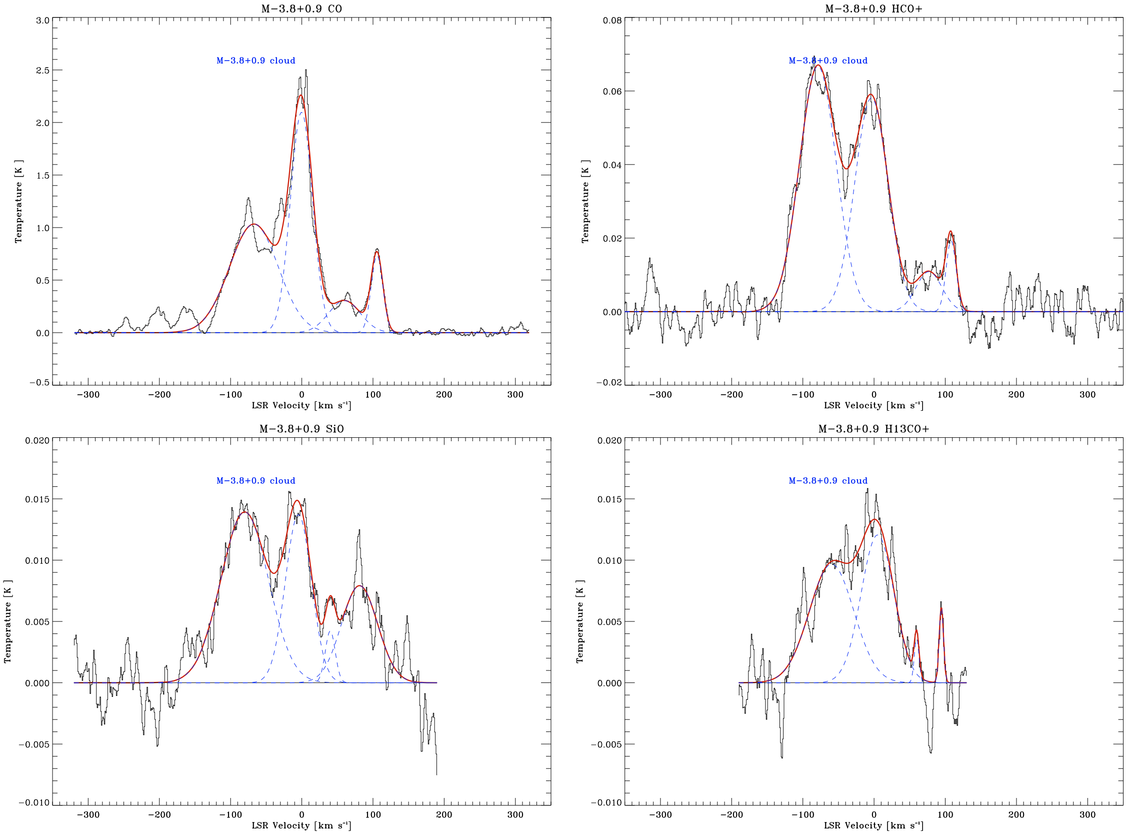

Fig. E.10. CO, HCO$^+$, SiO y H^{13}CO$^+$ average spectrum over the angular size of M−3.8+0.9 $(l, b, v) = (-3.8, 0.9, -83)$ (from $l = -4.0$ to -3.6875, and from $b = 0.5625$ to 1.1875).

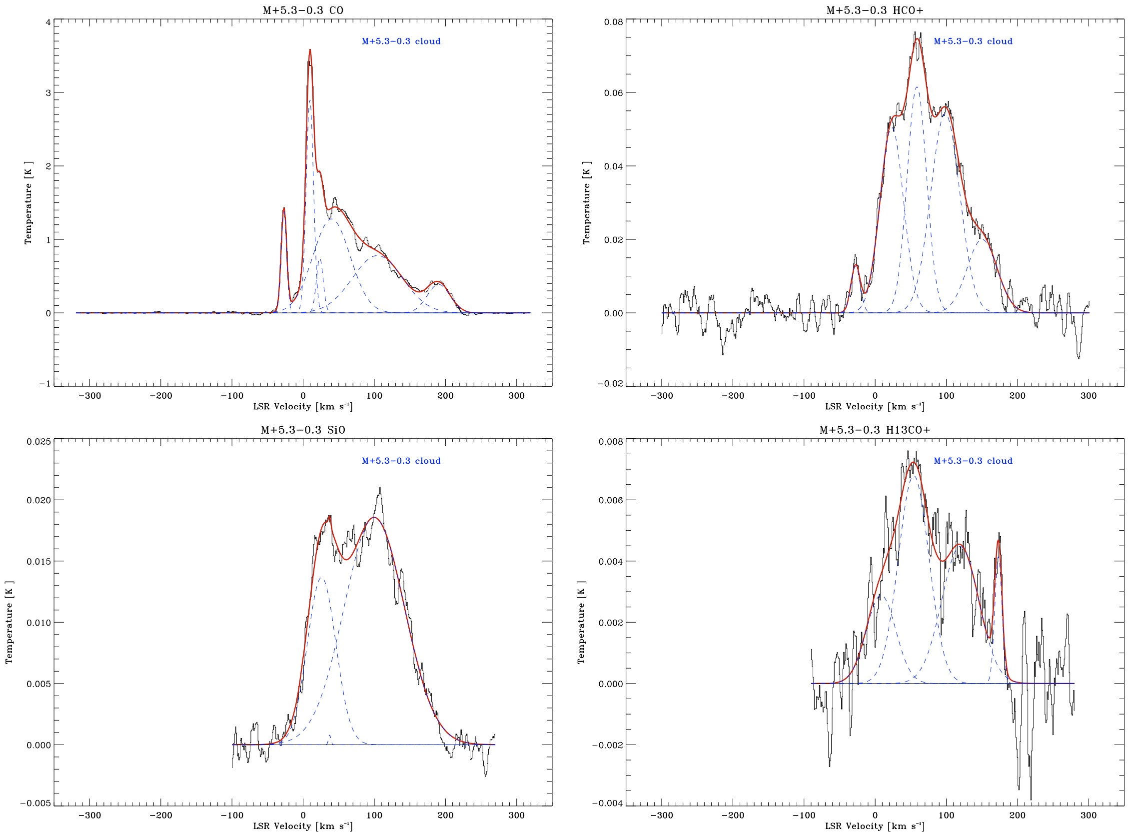

Fig. E.11. CO, HCO$^+$, SiO y H^{13}CO$^+$ average spectrum over the angular size of M+5.3-0.3 $(l, b, v) = (5.3, -0.3, 95)$ (from $l = 5.125$ to 5.5625, and from $b = -0.6875$ to 0.125).